

AD-A061 464

IIT RESEARCH INST CHICAGO ILL
THEORETICAL INVESTIGATION OF LOADS ON BURIED STRUCTURES. VOLUME--ETC(U)
AUG 78 R R ROBINSON

F/G 18/3

F29601-76-C-0124

UNCLASSIFIED

IITRI-J6378-VOL-1

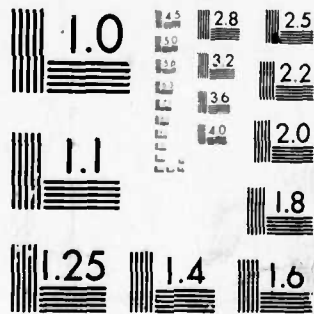
AFWL-TR-78-6-VOL-1

NL

1 OF 3
AD
A061454



06148



MICROCOPY RESOLUTION TEST CHART
NATIONAL BUREAU OF STANDARDS-1963-A

LEVEL II

(2)

AD A061464

DDC FILE COPY



THEORETICAL INVESTIGATION OF LOADS ON BURIED STRUCTURES.

Volume I of II
Results of Discussion.

(10) R. R. / Robinson

IIT Research Institute
Chicago, Illinois 60616

(12) 234p.

(11)

August 1978



(9)

Final Report.

(15) F29601-76-C-0124

Approved for public release; distribution unlimited.

(14) IITRI-56378-VOL-1

(16) This research was funded by the Defense Nuclear Agency under Subtask Y99QAXSC157, Work Unit 07, Work Unit Title: Parametric Investigation of Structure-Medium Interaction.

(17) C157

Prepared for
DIRECTOR
DEFENSE NUCLEAR AGENCY
Washington, DC 20305

(18) AFWL

(19) TR-78-6-VOL-1

AIR FORCE WEAPONS LABORATORY
Air Force Systems Command
Kirtland Air Force Base, NM 87117

JOB

175 350 78 11 16 023

This final report was prepared by the IIT Research Institute, Chicago, Illinois, under Contract F29601-76-C-0124, Job Order WDNS3427 with the Air Force Weapons Laboratory, Kirtland Air Force Base, New Mexico. Capt Stanton A. Chang (DES-S) was the Laboratory Project Officer-in-Charge.

When US Government drawings, specifications, or other data are used for any purpose other than a definitely related Government procurement operation, the Government thereby incurs no responsibility nor any obligation whatsoever, and the fact that the Government may have formulated, furnished, or in any way supplied the said drawings, specifications, or other data is not to be regarded by implication or otherwise as in any manner licensing the holder or any other person or corporation or conveying any rights or permission to manufacture, use, or sell any patented invention that may in any way be related thereto.

This report has been authored by a contractor of the US Government. Accordingly, the US Government retains a nonexclusive royalty-free license to publish or reproduce material contained herein, or allow others to do so for the Government purposes.

This report has been reviewed by the Office of Information (OI) and is releasable to the National Technical Information Service (NTIS). At NTIS it will be available to the general public, including foreign nations.

This technical report has been reviewed and is approved for publication.

Stanton A. Chang

STANTON A. CHANG
Captain, USAF
Project Officer

FOR THE COMMANDER

Gary P. Ganong

GARY P. GANONG
Major, USAF
Ch, Technology & Applications Br

Stewart W. Johnson

STEWART W. JOHNSON
Lt Colonel, USAF
Ch, Civil Engr Rsch Div

DO NOT RETURN THIS COPY. RETAIN OR DESTROY.



UNCLASSIFIED

SECURITY CLASSIFICATION OF THIS PAGE (When Data Entered)

REPORT DOCUMENTATION PAGE		READ INSTRUCTIONS BEFORE COMPLETING FORM
1. REPORT NUMBER AFWL-TR-78-6, Vol I of II ✓	2. GOVT ACCESSION NO.	3. RECIPIENT'S CATALOG NUMBER
4. TITLE (and Subtitle) THEORETICAL INVESTIGATION OF LOADS ON BURIED STRUCTURES Volume I: Results of Discussion ✓	5. TYPE OF REPORT & PERIOD COVERED Final Report	
7. AUTHOR(s) R. R. Robinson	6. PERFORMING ORG. REPORT NUMBER J6378	
9. PERFORMING ORGANIZATION NAME AND ADDRESS IIT Research Institute Chicago, IL 60616 ✓	8. CONTRACT OR GRANT NUMBER(s) F29601-76-C-0124 <i>new add</i>	
11. CONTROLLING OFFICE NAME AND ADDRESS Director Defense Nuclear Agency Washington D C 20305	10. PROGRAM ELEMENT, PROJECT, TASK AREA & WORK UNIT NUMBERS 62704H Y99QAXSC157, 07	
14. MONITORING AGENCY NAME & ADDRESS (if different from Controlling Office) Air Force Weapons Laboratory (DES) Kirtland Air Force Base, NM 87117	12. REPORT DATE August 1978 ✓	
	13. NUMBER OF PAGES 234	
	15. SECURITY CLASS. (of this report) UNCLASSIFIED	
16. DISTRIBUTION STATEMENT (of this Report) Approved for public release; distribution unlimited.		
17. DISTRIBUTION STATEMENT (of the abstract entered in Block 20, if different from Report)		
18. SUPPLEMENTARY NOTES This research was funded by the Defense Nuclear Agency under Subtask Y99QAXSC157, Work Unit 07, Work Unit Title: Parametric Investigation of Structure-Medium Interaction. (Volume II: Tables and Plots)		
19. KEY WORDS (Continue on reverse side if necessary and identify by block number) Soil-Structure Interaction Structure-Media Interaction Buried Cylinders Finite Element Calculations Two-Dimensional Calculations		
20. ABSTRACT (Continue on reverse side if necessary and identify by block number) The objective of this project was to develop simplified techniques for determining loads on buried structures of cylindrical geometry subjected to severe dynamic airblast load environments. The data forming the basis for these design loads have been primarily derived from numerical, finite element analyses for a wide range of loading, soil, and structural parameters. The numerical results were generated exclusively during this research investigation. ✓		

DD FORM 1 JAN 73 1473

EDITION OF 1 NOV 65 IS OBSOLETE

UNCLASSIFIED

SECURITY CLASSIFICATION OF THIS PAGE (When Data Entered)

78 11 16 020

UNCLASSIFIED

SECURITY CLASSIFICATION OF THIS PAGE(When Data Entered)

The primary effort during the program was the generation of soil structure interaction loads and internal cylinder forces for horizontally oriented cylinders. Both static and dynamic solutions were obtained to study in a more or less systematic manner the loads and internal cylinder forces for variations of the structural stiffness, depth of burial, and soil media parameters. Depths of burial ranged from one-half the tunnel radius to two tunnel diameters. A concrete tunnel liner with radius to thickness ratios varying from 4 to 15 were used and two nonlinear soil materials were incorporated in the dynamic solutions. Simple triangular airblast loads with peak overpressures of 500 and 1500 psi (3.45 and 10.34 MPa) and durations of 0.015 to 0.060 sec were incorporated with the dynamic solutions.

Dynamic free-field solutions were obtained using the triangular airblast loading waveforms and the two nonlinear soil materials, and also for certain variations to the soil parameters. A simplified method for determining loads on buried structures was defined by N. M. Newmark Consulting Engineering Services early in the project, based on methods that have been used prior to this project.

The major conclusion drawn from the project is that the concept of using a few of the soil structure interaction modal loads to arrive at a simplified method of loading appears to have a great deal of merit. In fact, it appears that it is generally sufficient to use only modes 0 through 2 to obtain a sufficiently detailed definition of the loading to satisfactorily compute the internal tunnel liner forces.

ACCESSION for	
NTIS	Write Section <input checked="" type="checkbox"/>
DDC	B. H. Smith <input type="checkbox"/>
UNCLASSIFIED	
JUL 1 1977	
BY	
DISPATCH/10/10/10	
A	

UNCLASSIFIED

SECURITY CLASSIFICATION OF THIS PAGE(When Data Entered)

PREFACE

This is the final report on IIT Research Institute (IITRI) Project J6378 entitled, "Theoretical Investigation of Loads on Buried Structures". This research project was performed for the Air Force Weapons Laboratory (AFWL) under contract F29601-76-C-0124 during the period 1 June 1967 to 31 December 1977.

The AFWL Project Officer was Capt. Stanton A. Chang, Structural Dynamics, Survivability Branch. The project was initially under the direction of R. E. Welch (1 June 1976 to 31 December 1976) and completed by R. R. Robinson under the general supervision of A. Longinow Structural Analysis Section and K. E. McKee Director, Engineering Division. IITRI personnel who made significant technical contributions include A. K. Gupta, R. R. Robinson and R. E. Welch. Professors N. M. Newmark, W. J. Hall and J. D. Haltiwanger of N. M. Newmark Consulting Engineering Services acted as consultants throughout the project and provided a simplified procedure for determining loads on buried structures during the early phases of the project. M. A. Plamondon of the AFWL Survivability Branch provided a good deal of the incentive associated with the attempts to characterize dynamic loads on buried structures by a few of the modal components.

CONTENTS

<u>Section</u>	<u>Page</u>
I INTRODUCTION	1
1. Background	1
2. Objectives	7
3. Scope of Work	7
II STATIC ANALYSES	11
1. Infinite Media Analyses	11
2. Soil Media Stress Analysis	12
3. Cylinder Force Resultant Analysis	18
4. Depth of Burial Analysis	31
III DYNAMIC ANALYSES	42
1. Run Matrix of Dynamic Cases	44
2. Dynamic Finite Element Solution Analysis	48
a. Automatic Generation of Mesh Data	48
b. Pressure and Force Loadings	48
c. Materials	49
d. Damping	55
e. Finite Element Model	57
f. SAMSON Modifications	60
3. Results of Dynamic (SAMSON) Solutions	62
a. Peak Response Results	63
b. Modal History Results	63
c. Crown, Springline, Invert Results	95
4. Analysis of Cylindrical Shell to SSI Loading	122
a. Displacements	122
b. Exact Circular Frequencies	123
c. Approximate Frequencies	123
d. Radial and Tangential Shear Loads	123
e. Equations of Motion	124
f. Cylinder Force Resultants	125
g. Nondimensional Moment Modal Amplitudes	127
h. Nondimensional Thrust Modal Amplitudes	128
i. Application of Method	128
j. Discussion of Results	137
IV CONCLUSIONS AND RECOMMENDATIONS	150
1. Conclusions	150
2. Recommendations	153
REFERENCES	160
APPENDIX A: Free Field Vertical Stress Wave Investigations	165
APPENDIX B: Loading Functions on Buried Cylinders	181
APPENDIX C: Dynamic Interaction Between Elastic Media	205

ILLUSTRATIONS

<u>Figure</u>	<u>Page</u>
1 Static Analysis Notation	13
2a Nondimensional Soil Stress Variation - Case A ($R/t = 15, 8$)	16
2b Nondimensional Soil Stress Variation - Case A ($R/t = 6, 4$)	17
3a Nondimensional SSI Stresses, NS Case A ($\alpha = 0.0096, k = 1/3, \nu = 1/4$)	21
3b Nondimensional Cylinder Internal Forces, NS Case A	22
4a Nondimensional SSI Stresses, NS Case B ($\alpha = 0.0096, k = 0, \nu = 1/4$)	24
4b Nondimensional Cylinder Internal Forces NS Case B	25
5a Nondimensional SSI Stresses, NS Case C ($\alpha = 0.096, k = 0, \nu = 1/4$)	26
5b Nondimensional Cylinder Internal Forces NS Case C	27
6a Nondimensional SSI Stresses, NS Case D ($\alpha = 0.96, k = 0, \nu = 1/4$)	28
6b Nondimensional Cylinder Internal Forces NS Case D	29
7 Finite Element Mesh for SAP4 Static Analysis, $h/R = 0.5$	33
8 Finite Element Mesh for SAP4 Static Analysis, $h/R = 1.0$	34
9 Finite Element Mesh for SAP4 Static Analysis, $h/R = 2.0$	35
10 Finite Element Mesh for SAP4 Static Analysis, $h/R = 4.0$	36
11a Nondimensional Soil Stress Variation for Various Depths of Burial ($R/t = 15, 8$)	38
11b Nondimensional Soil Stress Variation for Various Depths of Burial ($R/t = 6, 4$)	39
12 Dynamic Analysis Parameters	43
13 Nonlinear ROCKMT3 Soil Media Properties	46
14 Dynamic Uniaxial Data - Dense Dry Sand	51
15 Coulomb-Mohr Shear Strength Parameters Compared with ROCKMT3 Parameters	53
16 Nonlinear R/C Liner (1% Steel), ROCKMT3 Parameters	56
17 Finite Element Mesh of Soil for SAMSON Dynamic Analysis ($h/R = 0.5$)	58

ILLUSTRATIONS (Contd)

<u>Figure</u>		<u>Page</u>
18	Finite Element Mesh of Soil for SAMSON Dynamic Analysis ($h/R = 4.0$)	59
19	Tunnel Liner Mesh for SAMSON Dynamic Analysis ($R/t = 15$)	61
20a	Minimum and Maximum Nondimensional Thrust Variation Around Liner, Case 5	65
20b	Minimum and Maximum Nondimensional Moment Variation Around Liner, Case 5	66
20c	Minimum and Maximum Nondimensional Shear Variation Around Liner, Case 5	67
20d	Minimum and Maximum SSI Nondimensional Radial Stress Variation Around Liner, Case 5	68
20e	Minimum and Maximum SSI Nondimensional Circumferential Stress Variation Around Liner, Case 5	69
20f	Minimum and Maximum SSI Nondimensional Shear Stress Variation Around Liner, Case 5	70
21	Notation for Modal Amplitudes from Dynamic (SAMSON) Results	72
22a	Nondimensional Thrust History, Mode 0, Case 5	74
22b	Nondimensional Thrust History, Mode 1, Case 5	75
22c	Nondimensional Thrust History, Mode 2, Case 5	76
22d	Nondimensional Thrust History, Mode 3, Case 5	77
22e	Nondimensional Thrust History, Mode 4, Case 5	78
22f	Nondimensional Thrust History, Mode 5, Case 5	79
22g	Nondimensional Thrust History, Mode 6, Case 5	80
23a	Nondimensional Moment History, Mode 0, Case 5	81
23b	Nondimensional Moment History, Mode 1, Case 5	82
23c	Nondimensional Moment History, Mode 2, Case 5	83
23d	Nondimensional Moment History, Mode 3, Case 5	84
23e	Nondimensional Moment History, Mode 4, Case 5	85
23f	Nondimensional Moment History, Mode 5, Case 5	86
23g	Nondimensional Moment History, Mode 6, Case 5	87
24a	Nondimensional SSI Radial Stress, Mode 0, Case 5	88
24b	Nondimensional SSI Radial Stress, Mode 1, Case 5	89
24c	Nondimensional SSI Radial Stress, Mode 2, Case 5	90
24d	Nondimensional SSI Radial Stress, Mode 3, Case 5	91

ILLUSTRATIONS (Contd)

<u>Figure</u>		<u>Page</u>
24e	Nondimensional SSI Radial Stress, Mode 4, Case 5	92
24f	Nondimensional SSI Radial Stress, Mode 5, Case 5	93
24g	Nondimensional SSI Radial Stress, Mode 6, Case 5	94
25a	Nondimensional Liner Shear, Mode 1, Case 5	96
25b	Nondimensional Liner Shear, Mode 2, Case 5	97
25c	Nondimensional Liner Shear, Mode 3, Case 5	98
25d	Nondimensional Liner Shear, Mode 4, Case 5	99
25e	Nondimensional Liner Shear, Mode 5, Case 5	100
25f	Nondimensional Liner Shear, Mode 6, Case 5	101
26a	Nondimensional SSI Shear Stress, Mode 1, Case 5	102
26b	Nondimensional SSI Shear Stress, Mode 2, Case 5	103
26c	Nondimensional SSI Shear Stress, Mode 3, Case 5	104
26d	Nondimensional SSI Shear Stress, Mode 4, Case 5	105
26e	Nondimensional SSI Shear Stress, Mode 5, Case 5	106
26f	Nondimensional SSI Shear Stress, Mode 6, Case 5	107
27a	Nondimensional Crown Thrust History, Case 5	109
27b	Nondimensional Crown Moment History, Case 5	110
27c	Nondimensional Crown SSI Radial Stress History, Case 5	111
28a	Nondimensional Springline Thrust History, Case 5	113
28b	Nondimensional Springline Moment History, Case 5	114
28c	Nondimensional Springline Radial Stress History, Case 5	115
29a	Nondimensional Invert Thrust History, Case 5	116
29b	Nondimensional Invert Moment History, Case 5	117
29c	Nondimensional Invert SSI Radial Stress History, Case 5	118
30a	Comparison of Analytical Thrust Mode Variation with SAMSON Result, Case 5	139
30b	Comparison of Analytical Thrust Mode Variation with SAMSON Result, Case 5	140
31	Comparison of Analytical Moment Mode Variation with SAMSON Result, Case 5	141
32	Comparison of Analytical Thrust Mode Variation with SAMSON Result, Case 13	142

ILLUSTRATIONS (Contd)

<u>Figure</u>		<u>Page</u>
33	Comparison of Analytical Moment Mode Variation with SAMSON Result, Case 13	143
34	Nondimensional Mode 2 Moment Variation Computed from SAMSON Mode 2 SSI Shear and Radial Stress, Case 13	145
35	Nondimensional Mode 2 Moment Variation Computed from Mode 2 SSI Shear and Radial Stresses Derived by Inverse Method, Case 13	147
36a	Nondimensional Mode 2 SSI Radial Stress Variation from Inverse Method, Case 13	148
36b	Nondimensional Mode 2 SSI Shear Stress Variation from Inverse Method, Case 13	149
37a	Approximations to Mode 0 SSI Radial Stress Variation, Cases 5 and 13	156
37b	Approximations to Mode 1 SSI Radial Stress Variation, Cases 5 and 13	157
A1	Soil Media Mesh to Fill In Tunnel Liner Cavity	168
A2	Comparison of 2D and 1D Free Field Vertical Stress Waves Soil B, $p_o = 500$ psi, $t_d = 0.015$ sec	169
A3	Comparison of 2D and 1D Free Field Vertical Stress Waves Soil B, $p_o = 1500$ psi, $t_d = 0.06$ sec	172
A4	Response of Trilinear Loading ROCKMT3 Soil B ($K_{L1} = 16,700$ $K_{L2} = 38,900$ $K_{L3} = K_u = 166,700$) 1D Finite Element Model	175
A5	Response of Bilinear Loading ROCKMT3 Soil ($K_{L1} = 16,700$ $K_{L2} = 38,900$ $K_u = 166,700$)	176
A6	Response of Linear Loading ROCKMT3 Soil ($K_L = 16,700$ $K_u = 166,700$)	177
A7	Response to Bilinear Loading ROCKMT3 Soil ($K_{L1} = 16,700$ $K_{L2} = 38,900$ $K_u = 38,900$)	178
A8	Free Field Response of Trilinear Loading ROCKMT3 Soil A ($K_{L1} = 16,700$, $K_{L2} = 38,900$, $K_{L3} = K_u = 166,700$) 1D Finite Element Model	179
A9	Response of Linear Elastic Soil with Damping	180
B1	Maximum Thrust versus Depth of Burial in Sand, $p_z r^3 / EI = 0-2$	183
B2	Maximum Thrust versus Depth of Burial in Sand, $p_z r^3 / EI = 2-3$	184
B3	Maximum Thrust versus Depth of Burial in Sand, $p_z r^3 / EI = 3-4$	185
B4	Maximum Thrust versus Depth of Burial in Sand, $p_z r^3 / EI = 4-6$	186

ILLUSTRATIONS (Concl)

<u>Figure</u>		<u>Page</u>
B5	Crown and Invert Moments versus Normalized Overpressure, $h_z = 0$ in Sand	187
B6	Crown and Invert Moments versus Normalized Overpressure, $h_z = D/8$ in Sand	188
B7	Crown and Invert Moments versus Normalized Overpressure, $h_z = D/4$ in Sand	189
B8	Crown and Invert Moments versus Normalized Overpressure, $h_z = D/2$ in Sand	190
B9	Loading Functions for Underground Cylinders	192
B10	Representation of Underground Iso-impulse Curves	193
B11	Approximate Underground Iso-impulse Curves (High Impulse Region)	200
B12	Approximate Underground Iso-impulse Curves (Low Impulse Region)	201
B13	Representation of Underground Vertical Airblast-Induced Pressure Pulses	203
C1	Simplified Soil Structure Finite Element Model	206

TABLES

<u>Table</u>	<u>Page</u>
I Nondimensional SSI and Cylinder Force and Displacement Components	30
II Cylinder Nondimensional Thrust and Moment for Various Depths of Burial - SAP4 Results	37
III Approximate Equivalent Trilangular Pulse Airblast Overpressure Duration (msec)	44
IV Run Matrix for (SAMSON) Dynamic Solutions	47
V Minimum and Maximum Nondimensional Liner Force Resultants (T,M,V) and SSI Stresses ($\sigma_r, \sigma_\theta, \tau_{r\theta}$) Case 5	64
VI Minimum and Maximum Fourier Modal Amplitudes of Nondimensional Liner Force Resultants (T,M,V) and SSI Stresses ($\sigma_r, \tau_{r\theta}$), Case 5	108
VII Comparison of Modal History Approximation with SAMSON Solution History (Input Variables)	119
VIII Modal Vibration Parameters (R/t = 4) Case 5	130
IX Modal Vibration Parameters (R/t = 15) Case 13	131
X Comparison of Peak Thrusts from Analytical Modes with SAMSON Results, Case 5	133
XI Comparison of Peak Moments from Analytical Modes with SAMSON Results, Case 5	134
XII Comparison of Peak Thrusts from Analytical Modes with SAMSON Results, Case 13	135
XIII Comparison of Peak Moments from Analytical Modes with SAMSON Results, Case 13	136
AI Free Field Study Run Matrix	166

SECTION I

INTRODUCTION

1. BACKGROUND

It is a well established fact that the structural response of hardened weapon system facilities to nuclear airblast and ground shock loading is significantly affected by the manner in which the structure is founded upon or buried within the soil media. Although there is an acknowledged awareness that the structure interacts with the adjacent medium, the exact nature of this interaction is imprecisely defined.

These phenomena and related aspects have generally been referred to as soil structure interaction (SSI). SSI has been investigated extensively for a number of years from different points of view, and the determination of loads on buried structures is an integral part of the subject.

The subject of SSI constantly recurs in connection with facility response problems simply because there is no logical and consistent way of avoiding it. The dynamic characteristics of a structure in contact with an extended material (i.e., the earth) differ substantially from its dynamic characteristics in vacuo. The surrounding medium has the effect of providing:

- Resistance, stiffening the structure in both rigid body and flexible modes of motion;
- An apparent damping of the structural motions by transporting energy in the form of a dynamic disturbance away from the structure (i.e., radiation damping);
- Additional, real damping due to the dissipative effects in the medium;
- Shock mitigation or amplification at the soil-structure interface depending on the properties of the medium; and
- Arching action above and around the structure.

In terms of the free field, the inclusion response consists of a perturbation of free field stress waves to the extent that the inclusion displays stiffness or mass properties which differ from the material for which the free field stress waves are

defined. This perturbation also displays the described characteristic effects.

Despite previous research efforts in SSI, it remains difficult to distinguish and identify such effects in real structures. One reason for this is that in most real structures the gross motions (rigid body) tend to follow the associated free field displacement fields with relatively small displacement perturbations. However, the fact that interaction effects are relatively small in terms of displacement fields means only that they have their greatest influence in terms of velocities, accelerations and, structural deformation (i.e., stresses and strains) which are more difficult to analyze and observe. In this connection note that:

- If a structure closely follows the free field, this implies that there is enough damping, real or apparent, in the interaction process to suppress any major oscillation about the free field motions.
- If there were a strictly imposed condition that the structure follow the free field, the stress-strain field throughout the whole or part of the structure would be known from compatibility and, except for very flexible structures, these would be completely unrealistic.

Although the subject of SSI and loads on buried structures has been studied to some extent in connection with such applications as culvert design and mining operations, early attempts to design hardened ground facilities gave great impetus to the field; and for the last 20 years it has been the subject of extensive research in connection with military facilities and, more recently, with the seismic design of nuclear power plants. The literature associated with the field is so substantial and widely scattered that only some brief comments on the development of the field with an emphasis on the generation of sources of data and the application of such data to the design process are given here. References 1 through 57 are cited for potential application to the subject investigation. The results presented in these references have either been used directly or reviewed for possible use in this research program. Several attempts at a detailed literature review have been made including those in references 1 through 6.

Numerous research investigations have been undertaken to study and quantify various phenomena associated with buried structures under dynamic loads in connection with the need to design or harden military facilities against nuclear attack. These early studies employed data from nuclear tests, small-scale laboratory experiments, existing solutions for classical inclusion problems, and a design rationale largely adopted from soil mechanics. Early centers for studies of this type were at IIT Research Institute (IITRI), then Armour Research Foundation, the University of Illinois, and the Massachusetts Institute of Technology. This phase of research culminated with the appearance of a variety of handbooks and technical summaries such as the early Air Force Design Manual (Ref. 5), the Compendium of Airblast Effects (Ref. 6) and a series of Corps of Engineers manuals entitled Design of Structures to Resist the Effects of Atomic Weapons (Ref. 7). These documents generally, and the Air Force Design Manual in particular, took a conventional and somewhat conservative approach to the question of loads on buried structures. The design process employed was basically quasi-static and the structure was essentially designed for the estimated free field pressure wave. The beneficial effects of soil arching above and around the structure were also taken into account; however, the possibility of load magnification on the structure due to reflection of the soil stress wave at the interface was generally dismissed on the grounds that little or no evidence for such phenomena could be found in the available test data.

Subsequent activity saw the decreased reliance on full-scale test data (the moratorium on aboveground testing had come into effect), the increased use of medium-scale field simulations, and especially, the increased use of large-scale computations and computer programs. Early computer work involved the extension of more or less classical approaches (i.e., series and modal solutions) as in references 8,9 and 10, and the development of so-called SSI models in which effects at the structure-soil interface were represented by stiffness and damping terms. An early model of this type was developed at IITRI (Ref. 11, 12, and 13) in which the

normal stress σ_s (i.e., unit load) on the surface of the structure was represented as

$$\sigma_s = \sigma_f + k(u_f - u_s) + s(\dot{u}_f - \dot{u}_s) \quad (1)$$

where σ_f is the normal stress in the free field (i.e., in the soil if the structure were not present); u_f and u_s are corresponding normal displacements of the free field and the structure; and \dot{u}_f and \dot{u}_s are the velocities. Such representations were for a time extensively used by IITRI and others in the evaluation and design of facilities including the MINUTEMAN and SAFEGUARD system structures (see Ref. 14 through 19 for instance). The approach was developed as a generalization of fairly old techniques related to culvert and tunnel design; and while it has fallen into disuse in recent years due to theoretical objections and the development of finite element and other techniques, it remains a potentially valuable tool for the evaluation of loads on buried structures and known classical solutions can be set up in this form. The method displays several known ingredients of the inclusion response solution, namely, the explicit dependence on the free field stress, the recognition that the surrounding medium has stiffness, and the incorporation of wave dispersion or interface reflection in the damping term.

The solution to classical inclusion problems has been the subject of numerous investigations throughout the most active period of SSI research. The response to spherical, elastic inclusions to steady state dilatational wave strains has been studied with respect to stress concentrations in the surrounding medium (Ref. 20) and scattering phenomena (Ref. 21). In both cases the numerical results are few and apply principally to the limiting cases of rigid and hollow spheres. The analogous acoustic inclusion problem (i.e., acoustic sphere in acoustic medium) has been solved in reference 22. The rigid spherical inclusion has also been studied by C. C. Mow in references 23 through 25, with emphasis on the inclusion response for a transient compressive pulse with exponential decay. These papers, especially reference 24, contain the principal qualitative information derivable from the classic inclusion literature in terms useful for the structural inclusion problem.

Briefly these findings are:

- The velocity of the inclusion exceeds the incident free field particle velocity only when the inclusion is heavier than the same volume of the surrounding medium.
- The solution contains a free vibration term which decays exponentially as energy is carried away from the inclusion response by wave action.
- The velocity and acceleration response of the inclusion may differ substantially from the corresponding free field motions even though the differences in displacement components are not great.

The first of these observations is often cited as an argument that there can be no amplification in the gross motion of a structural inclusion since these are inherently hollow, lined cavities and therefore of lower average density than the surrounding media.

The corresponding two-dimensional inclusion problems have been more extensively studied although they generally remain limited to elastic materials and simple geometries. References 26 through 31 are concerned with the impingement of plane waves on cylindrical cavities. Stress concentrations are obtained in reference 30 for harmonic dilatational wave trains as functions of wavelength and Poisson's ratio. References 27, 28, and 29 consider the response of cylindrical cavities for transient compression pulses and generate influence functions which are subsequently used in obtaining the response of a cylindrical shell used as a cavity liner (Ref. 32 and 33). The equivalent problem for a cylindrical shell in an acoustic medium is given in references 34 and 35.

The rigid circular inclusion is treated for harmonic dilatational waves in references 36 and 37, with reference 36 providing information on the relation of inclusion response to wavelength and inclusion mass (similar to that given in Ref. 24), and reference 37 giving stress concentration data. Exact elasticity solutions for thick cylindrical inclusions are given in reference 38 for harmonic dilatational waves and in reference 39 for incident shear waves. References 40 and 41 consider the response of

cylindrical cavities and shells to plane waves which are obliquely incident (i.e., propagate along, in addition to across, the axis of the cylinder).

A class of problems that can be called the surface inclusion or footing problem involves the response of various types of slabs resting on the surface of a semi-infinite, and perhaps layered, elastic medium. These differ from the spherical and cylindrical classical problems only in that the slab does not replace any of the surrounding medium. The classic papers for this problem are by Bycroft (Ref. 42 and 43) and deal with the forced harmonic vibration of a rigid, circular surface footing in four distinct modes. The solutions consist of driving force versus frequency, amplitude, and dimensionless constants and have proved useful in the analysis of the response of surface structures. Reference 44 provides similar solutions for the rectangular slab and indicates that these results are similar over a range of footing aspect ratios to those for the circular slab. Unlike fully buried structures, heavy surface structures can display significant amplification effects since they are not limited by a displaced volume of soil and can generate significant surface mass densities.

More recent activity in the SSI research has seen the increased reliance on large-scale computations and simulations of the response of buried structures. This is due almost entirely to the emergence of the finite element analysis technique as a powerful tool making such simulation possible. Although a wide variety of programs and techniques have been used for the analysis of buried structures, some programs which have been developed and used specifically for this purpose include INDEPS (Ref. 45), NOFEAR (Ref. 46) and DYNAX (Ref. 47), and SAMSON (Ref. 48); the last two were developed at IITRI.

It is noteworthy that throughout these later developments comparatively little effort has been devoted to extract design type data on loads and response or to the preparation of summaries and systematic simplified procedures. The new edition of the Air Force Design Manual (Ref. 49) presents little new data relating to the loads on buried structures over that which were available

in the earlier editions. In fact, the manual treats this phase of design almost exclusively in terms of response of rigid structures with soil response represented by dissipative terms of the form ρcV corresponding to plane elastic wave propagation. This is equivalent to the simplest form of the SSI model described in equation (1) with $k=0$ and $s=\rho c$.

2. OBJECTIVES

This research project has been directed toward the development of simplified techniques for determining loads on buried structures of cylindrical geometry subjected to severe dynamic blast load environments. The data forming the basis for these design loads have been primarily derived from numerical, finite element analyses for a wide range of loading, soil, and structural parameters. The numerical results presented herein have been generated exclusively from this research investigation.

The primary objective of this program has been to generate SSI loads and internal cylinder forces for horizontally oriented cylinders. Both static and dynamic solutions have been obtained in order to study in a more or less systematic manner the SSI loads and internal cylinder forces for variations of the structural stiffness, depth of burial, and soil media parameters.

During the course of this project, a concept was postulated that air blast induced SSI loads could be represented by only a few components of the modal representation of the SSI loads. For example, a buried cylinder in an infinite elastic medium is subjected to only the uniform (mode 0) and ovaling (mode 2) load components for a statically applied biaxial state of free field stress. With this concept in mind, various static and dynamic buried structure analyses were performed to determine the appropriateness of characterizing SSI loads by a few modes for a wide range of structure, soil, depth of burial and loading parameters.

3. SCOPE OF WORK

Attempts have been made throughout the project to cover a rather wide range of loading, structure, and soil media parameters.

However, the depths of burial of the structure that were considered are relatively shallow since it has been postulated that ground surface effects can be generally ignored for depths of burial greater than two times the cylinder diameter. Most of the results are presented in nondimensional form; however, if any specific dimensions were required, such as the diameter of the cylinder, then a 4 meter inside diameter has been employed. The cylinder has also been idealized throughout the study as an elastic material with thicknesses and material parameters corresponding to concrete.

The initial phase of the project was devoted to a brief review of the literature which was summarized in section I.1. Other activities required early in the project were to establish a communication link with the AFWL computer facilities at Kirtland AFB, New Mexico. This effort was required since the majority of the numerical calculations were to be performed on the CDC 6600 and 7600 computers at Kirtland AFB through a remote batch configuration via a dial-up terminal at IITRI in Chicago.

Several simplified methods of analysis for determining loads on buried structures have been developed in the past. One such technique that is based on experimental results, analytical investigations, and engineering judgement was defined early in this project by N. M. Newmark Consulting Engineering Services and is presented in appendix II. This method does not reflect the numerical results of the analyses conducted in this investigation.

The early numerical results were devoted to the generation of some elastic material, static load solutions for variations of the cylinder and soil media parameters. The results of these studies are given in section II.

There are some indications that the principal components of SSI loading on a horizontally oriented cylinder can be represented by a relatively few modal components of the loading. This simplified loading concept appeared to be plausible since the uniform component (mode 0) and ovaling component (mode 2) are the only sources of loading for an elastic cylinder embedded in an isotropic

elastic media of infinite extent subjected to a free field biaxial state of static loading. The major effort undertaken during the project was devoted to the generation of dynamic finite element numerical results in an effort to ascertain whether or not a few modes can be selected which will adequately represent the loading on a structure. The SAMSON computer code was used for these analyses to obtain solutions to a basic set of structure, soil, and loading parameters. A total of 32 cases was defined to represent what was considered to be reasonable extreme values of the parameters that were varied. The five parameters considered were:

- Radius to thickness ratio of cylinder
- Depth of burial
- Peak airblast overpressure
- Duration of overpressure loading
- Soil types (nonlinear material)

Two additional elementary cases were also solved using nonlinear reinforced concrete cylinder parameters. Also, two solutions were obtained using an elastic soil material in conjunction with the elastic concrete tunnel liner. These finite element SAMSON solutions and the manner in which the numerical results are processed and displayed are presented in section III.

Section III also contains the method of analysis that was used to judge the postulation that only a few of the modal components of the load are required to adequately represent the essential SSI loads. A discussion of the results of the SAMSON analyses and the problems encountered in determining which modal load components are important is given in section III. Conclusions and recommendations for future work are in section IV.

Appendix A gives the results of a number of free field solutions that were generated involving the two soils considered and the four airblast loading waveforms. Appendix B presents a simple method for determining loads on buried structures that was defined by N. M. Newmark Consulting Engineering Services at the beginning

of this project. Appendix C is presented to indicate the magnitude of errors that can be expected if the stresses in the soil elements surrounding the structure are used to determine the SSI loads.

Volume II of this report contains the bulk of the SAMSON solutions for each of the cases that were run. These results include: (1) tables of maximum and minimum values of the cylinder internal forces and SSI stresses around the liner, (2) modal amplitude histories of the cylinder forces and the SSI stress, (3) time history plots of the cylinder moment and thrust and the SSI radial stress at the crown, springline, and invert points.

SECTION II

STATIC ANALYSES

This section presents the results of several static-elastic analyses that were performed to investigate the effects of depth of burial and structure and soil media stiffness on the SSI stresses and the cylinder^{*} internal forces. These investigations are limited to plane strain analyses of horizontally oriented cylinders, and hence they are applicable to the analysis of a long cylinder where the effects of the ends of the cylinder can be neglected. Both the structure and the soil media have been idealized as linear elastic materials.

1. INFINITE MEDIA ANALYSES

These analyses consider an elastic liner embedded in a homogeneous elastic soil media of infinite extent. A biaxial free field state of stress in the soil is assumed, and the interface between the soil and structure can be idealized as either free to slip (i.e., no interface friction) or fully bonded (i.e., infinite interface friction). This problem has been treated extensively in the past by Burns and Richards (Ref. 50) and Hoeg (Ref. 51 and 52). Burns and Richards restricted their investigation to the case where the biaxial free field stress state is derived from a uniaxial state of strain, and solutions are given for the calculation of the media stresses and the cylinder force resultants. The major disadvantage of the uniaxial strain case is that the biaxial stress ratio is dependent on Poisson's ratio of the soil.

Hoeg's studies are not restricted to a uniaxial strain case, and the biaxiality ratio can be arbitrarily specified. However, these investigations do not include solutions for internal force resultants of the cylinder and a typographic sign error exists in one of the equations which can lead an unsuspecting user to erroneous conclusions.

^{*} The terms cylinder, tunnel, and liner are used interchangeably to denote the right circular cylinder buried structure.

The following equations are based on appropriately modified and, where necessary, corrected results from reference 51.

2. SOIL MEDIA STRESS ANALYSIS

Referring to figure 1, the nondimensional media stresses at any nondimensional polar coordinate in the media (ρ, θ) are given by

$$\text{Radial Stress, } \bar{\sigma}_r = \sigma_r/p = \bar{\sigma}_{r0} + \bar{\sigma}_{r2} \cos 2\theta \quad (2)$$

$$\text{Circumferential Stress, } \bar{\sigma}_\theta = \sigma_\theta/p = \bar{\sigma}_{\theta0} + \bar{\sigma}_{\theta2} \cos 2\theta \quad (3)$$

$$\text{Shear Stress, } \bar{\tau}_{r\theta} = \tau_{r\theta}/p = \bar{\tau}_{r\theta2} \sin 2\theta \quad (4)$$

where

k = biaxiality ratio of free field soil stress and the subscripts 0 and 2 refer to the uniform and ovaling components.

$$\rho = R/r \quad (\leq 1.0) \quad (5a)$$

$$\bar{\sigma}_{r0} = -(1+k)(1-a_1\rho^2)/2 \quad (5b)$$

$$\bar{\sigma}_{r2} = -(1-k)(1-3a_2\rho^4 - 4a_3\rho^2)/2 \quad (5c)$$

$$\bar{\sigma}_{\theta0} = -(1+k)(1+a_1\rho^2)/2 \quad (5d)$$

$$\bar{\sigma}_{\theta2} = (1-k)(1-3a_2\rho^4)/2 \quad (5e)$$

$$\bar{\tau}_{r\theta2} = (1-k)(1+3a_2\rho^4 + 2a_3\rho^2)/2 \quad (5f)$$

The coefficients a_1, a_2, a_3 have been determined for two idealized soil-structure interface conditions; namely, the fully bonded or no slip (NS) case and the zero friction or free slip (FS) case. For the NS case the coefficients are

$$a_1 = \frac{(1-2\nu)(C-1)}{(1-2\nu)C+1} \quad (6a)$$

$$a_2 = \left[(1-2\nu)(1-C)F - (1-2\nu)^2 C/2 + 2 \right] / b \quad (6b)$$

$$a_3 = \left\{ \left[1 + (1-2\nu)C \right] F - (1-2\nu)C/2 - 2 \right\} / b \quad (6c)$$

$$\text{where } b = \left[(3-2\nu) + (1-2\nu)C \right] F + (2.5-8\nu+6\nu^2)C + 6 - 8\nu \quad (7a)$$

$$\text{and } C = \alpha(R/t)/(1-\nu), \text{ compressibility ratio} \quad (7b)$$

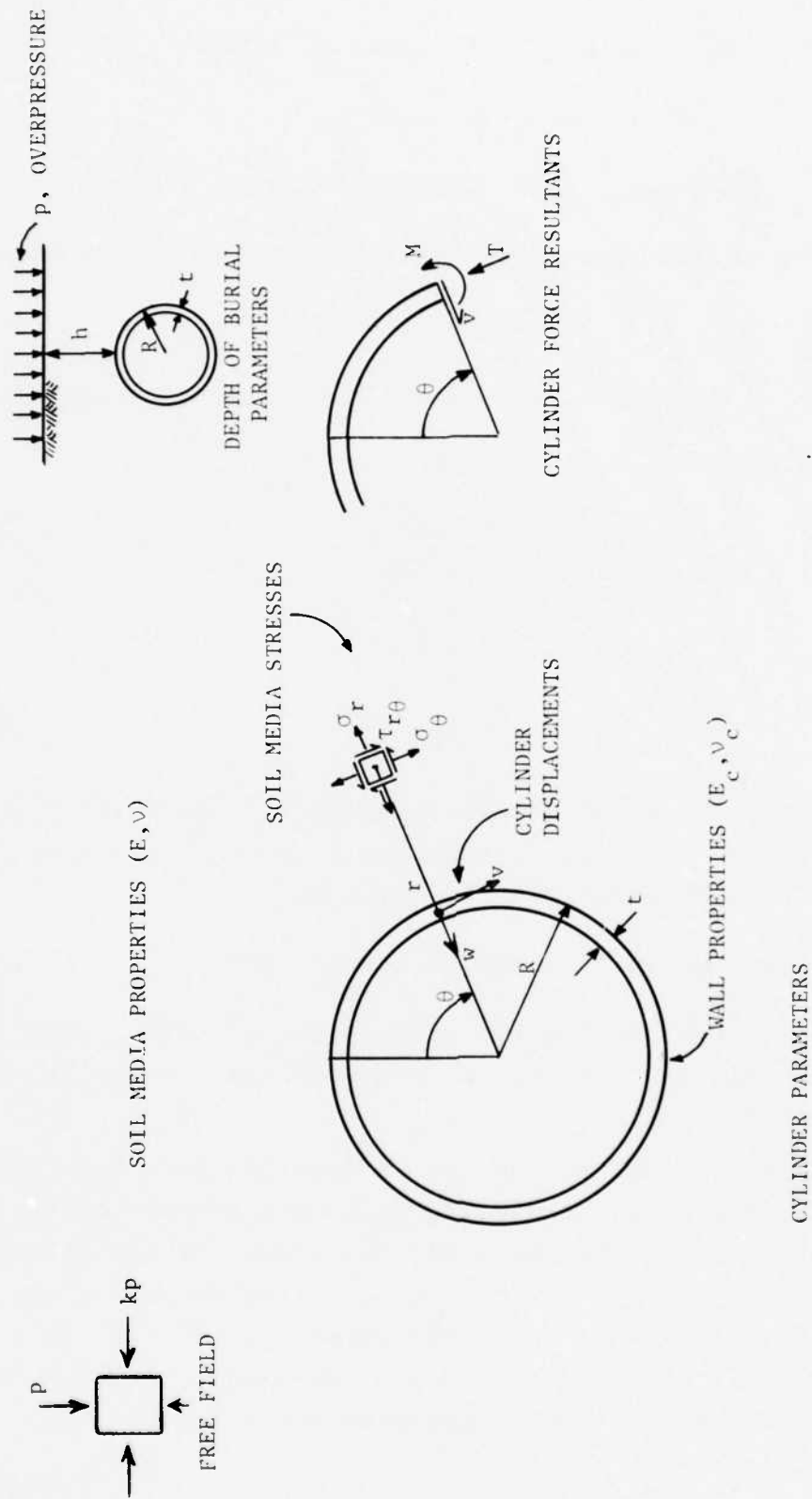


Figure 1. Static Analysis Notation

$$F = 2C(1-2\nu)(R/t)^2, \text{ flexibility ratio} \quad (7c)$$

$$\alpha = M^*/\bar{E}_c, \text{ material modulus ratio} \quad (7d)$$

$$M^* = \frac{E(1-\nu)}{(1+\nu)(1-2\nu)}, \text{ constrained modulus of soil} \quad (7e)$$

E, ν = modulus of elasticity and Poisson's ratio of soil media

$$\bar{E}_c = E_c/(1-\nu_c^2), \text{ apparent modulus of cylinder} \quad (7f)$$

E_c, ν_c = modulus of elasticity and Poisson's ratio of cylinder

For the FS case the coefficients are

$$a_1 = \frac{(1-2\nu)(C-1)}{(1-2\nu)C+1} \quad (8a)$$

$$a_2 = -\frac{2F+1-2\nu}{2F+5-6\nu} \quad (8b)$$

$$a_3 = \frac{2F-1}{2F+5-6\nu} \quad (8c)$$

If the free field is in a state of uniaxial strain, i.e., only the vertical strain is nonzero, then the biaxiality ratio is determined from Poisson's ratio of the soil as

$$k = \nu/(1-\nu), \text{ uniaxial strain case} \quad (9)$$

Equations (2) through (8) for the calculation of soil stress are independent of equation (9), and the biaxiality ratio can be any value desired.

The solutions for the FS and the NS idealizations have been used to compute the radial and circumferential stress variation in the vicinity of the cylinder along the crown ray ($\theta = 0$) and the springline ray ($\theta = 90$ deg). Since the solution is for the unbounded or infinite media case, the invert ray ($\theta = 180$ deg) stress variation is the same as for the crown ray. Results were obtained for several cylinder stiffnesses and a typical soil media with

$$E = 25 \text{ ksi (172.4 MPa) or } M^* = 30 \text{ ksi (206.9 MPa)}$$

$$\nu = 0.25$$

$$k = 1/3$$

These soil and structure parameters will be referred to as Case A. The cylinder material parameters are appropriate for a concrete tunnel liner, viz.,

$$E_c = 3000 \text{ ksi (20,700 MPa)}$$

$$\nu_c = 0.2$$

Results are shown in figure 2 for four cylinder geometries represented by radius to thickness ratios (R/t) of 15, 8, 6 and 4. For a tunnel with a 6.6 ft (2 m) inside radius, these R/t ratios correspond to cylinder thicknesses ranging from approximately 0.5 to 2 ft (0.152 to 0.610 m). For this figure, a rather unconventional method has been used to display the radial and circumferential soil stress variations in a condensed manner. Note that all of the stresses are compression (negative) except the circumferential stress near the crown for the FS case. The compressive (-) radial stresses have been displayed above the abscissa (crown or springline ray); whereas, the compressive (-) circumferential stresses are displayed below the abscissa. Hence, the tension (+) circumferential stresses at the crown are plotted above the abscissa.

An examination of the curves in this figure indicates that the soil stresses are very nearly equal to the free field stress for points approximately 1 to 1.5 diameters away from the edge of the liner. These curves also show that the soil stresses adjacent to the cylinder are significantly different for the NS and the FS solutions, especially the circumferential stresses. The NS case is considered a more realistic occurrence than the FS case. For example, it has been observed that when highway tunnel liners that have been in service for some time are excavated, soil particles are attached or bonded to the entire surface of the liner. This indicates that if relative tangential motion occurs between the

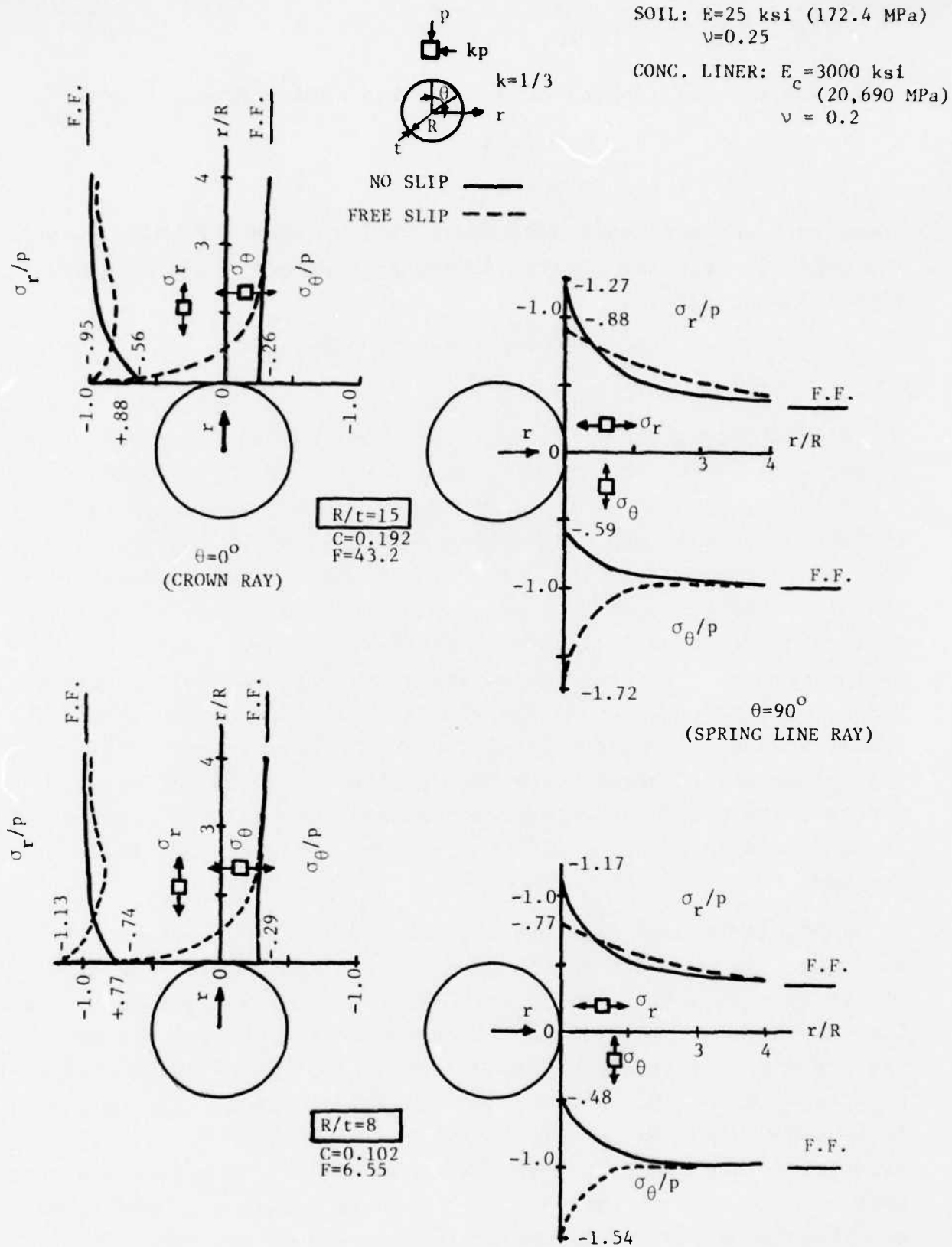


Figure 2a. Nondimensional Soil Stress Variation
 Case A ($R/t = 15, 8$)

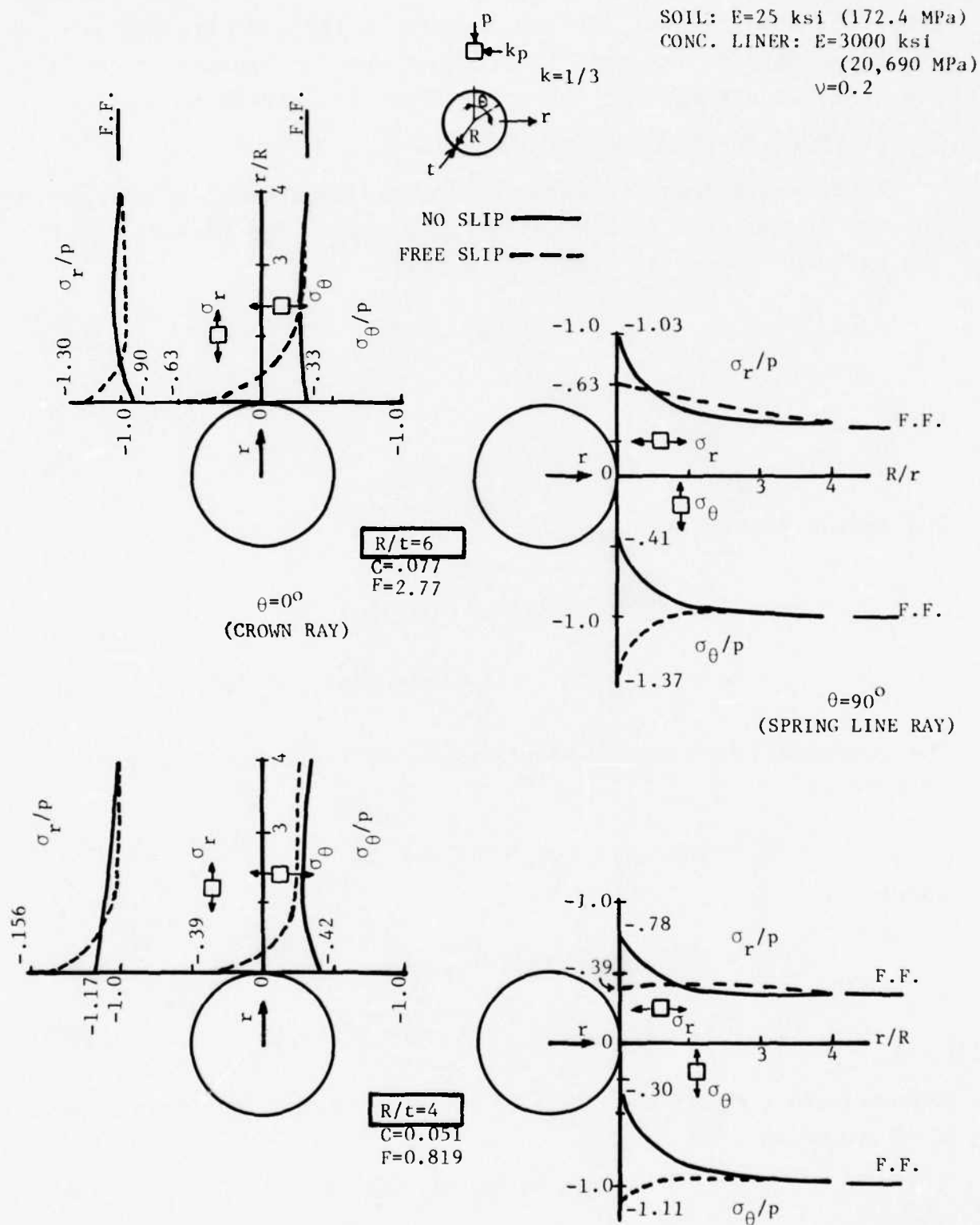


Figure 2b. Nondimensional Soil Stress Variation
 Case A ($R/t = 6, 4$)

structure and the soil, it takes place in the soil because the shear capacity of the soil is exceeded and not because there is low friction strength at the soil-structure interface.

3. CYLINDER FORCE RESULTANT ANALYSIS

The internal force resultants (moment and thrust) of the cylinder can be computed in the following manner. The elastic law for the cylinder moment is (Ref. 53, p 211)

$$M = - \frac{K}{R^2} \left(w + \frac{d^2 w}{d\theta^2} \right) \quad (10a)$$

where

$$K = \bar{E}_c t^3/12 \quad (10b)$$

The radial displacement of the cylinder is

$$w = 0.5p \frac{R}{M^*} \left\{ (1+k)(1-\nu) \left(1 + \frac{a_1}{1-2\nu} \right) + (1-k) \frac{1-\nu}{1-2\nu} \left[1 + a_2 + 4(1-\nu) a_3 \right] \cos 2\theta \right\} \quad (10c)$$

The nondimensional radial displacement of the cylinder can be written as

$$\bar{w} = wM^*/(pR) = \bar{w}_0 + \bar{w}_2 \cos 2\theta \quad (10d)$$

where

$$\bar{w}_0 = 0.5(1+k)(1-\nu) \left(1 + \frac{a_1}{1-2\nu} \right) \quad (10e)$$

$$\bar{w}_2 = 0.5(1-k) \frac{1-\nu}{1-2\nu} \left[1 + a_2 + 4(1-\nu)a_3 \right] \quad (10f)$$

From equations (10a) and (10b) the nondimensional cylinder moment is obtained as

$$\bar{M} = M/pR^2 = \bar{M}_0 + \bar{M}_2 \cos 2\theta \quad (10g)$$

where

$$\bar{M}_0 = -C_1(1+k)(1-\nu) \left(1 + \frac{a_1}{1-2\nu} \right) \quad (10h)$$

$$\bar{M}_2 = 3C_1(1-k) \frac{(1-\nu)}{1-2\nu} \left[1 + a_2 + 4(1-\nu)a_3 \right] \quad (10i)$$

$$C_1 = \frac{K}{2M^*R^3} = \frac{1}{24\alpha} \left(\frac{t}{R} \right)^3 \quad (10j)$$

The differential equation of radial equilibrium for the cylinder is (Ref. 53, p 211)

$$\frac{d^2 M}{d\theta^2} - RT = \sigma_r R^2 \quad (11)$$

The radial stress (σ_r) referred to in this equation is the inter-face SSI stress, computed from equations (2) and (5) with $\rho = 1$. Performing the indicated operations in equation (11) and solving for the nondimensional thrust yields

$$\bar{T} = T/pR = \bar{T}_0 + \bar{T}_2 \cos 2\theta \quad (11a)$$

where

$$\begin{aligned} \bar{T}_0 &= -\bar{\sigma}_{r0} \Big|_{\rho=1} \\ &= (1+k)(1-a_1)/2 \end{aligned} \quad (11b)$$

$$\begin{aligned} \bar{T}_2 &= -\bar{\sigma}_{r2} \Big|_{\rho=1} - 4 \bar{M}_2 \\ &= 0.5 (k-1) \left\{ 1 - 3a_2 - 4a_3 - 24 C_1 \left(\frac{1-\nu}{1-2\nu} \right) \left[1 + a_2 + 4(1-\nu)a_3 \right] \right\} \end{aligned} \quad (11c)$$

A very close approximation to the nondimensional cylinder force modal amplitudes can be written as a function of the non-dimensional SSI modal stresses as

$$\bar{M}_0 = \frac{\bar{\sigma}_{ro}}{12 (R/t)^2} \quad (11d)$$

$$\bar{M}_2 = (-\bar{\sigma}_{r2} + \bar{\tau}_{r\theta 2}/2)/3 \quad (11e)$$

$$\bar{T}_0 = -\bar{\sigma}_{ro} \quad (11f)$$

$$\bar{T}_2 = (\bar{\sigma}_{r2} - 2 \bar{\tau}_{r\theta 2})/3 \quad (11g)$$

The following four fundamental nondimensional parameters are sufficient to completely specify the material and geometric characteristics of the problem:

α , modulus ratio, equation (7d)

k , biaxiality ratio of free field stress

ν , soil Poisson's ratio

R/t , cylinder radius to thickness ratio

In an effort to study the nondimensional variation of the SSI stresses ($\bar{\sigma}_r, \bar{\tau}_{r\theta}$) and the cylinder internal forces (\bar{M}, \bar{T}) around the cylinder ($\theta = 0$ to 90 deg), a number of elementary solutions have been computed using the appropriate equations (2) through (11) for the NS case at the interface idealization.

As before, a typical soil medium postulated ($E = 25$ ksi = 172 MPa, $\nu = 0.25$, $k = 1/3$) and a concrete cylinder is assumed ($E_c = 3000$ ksi = $20,690$ MPa, $\nu_c = 0.2$) with the same four radius-to-thickness ratios. For this case, the fundamental parameters are

Case A: $\alpha = 0.0096$

$k = 0.333$

$\nu = 0.25$

$R/t = 15, 8, 6, 4$

The circumferential variations of the nondimensional SSI stresses and the cylinder internal forces for this case are shown in figure 3.

Solutions to three additional cases have also been obtained to indicate the influence of the parameter α on the results. For these cases, the biaxiality ratio k has been taken as zero so that the results can be used to obtain solutions for any biaxiality ratio. This can be done by transforming the $k = 0$ results by 90 deg, multiplying by the desired biaxiality ratio, and adding this solution to the original $k = 0$ solution. Only the parameter α has been varied between these three cases; the remaining fundamental parameters for each case have been taken as

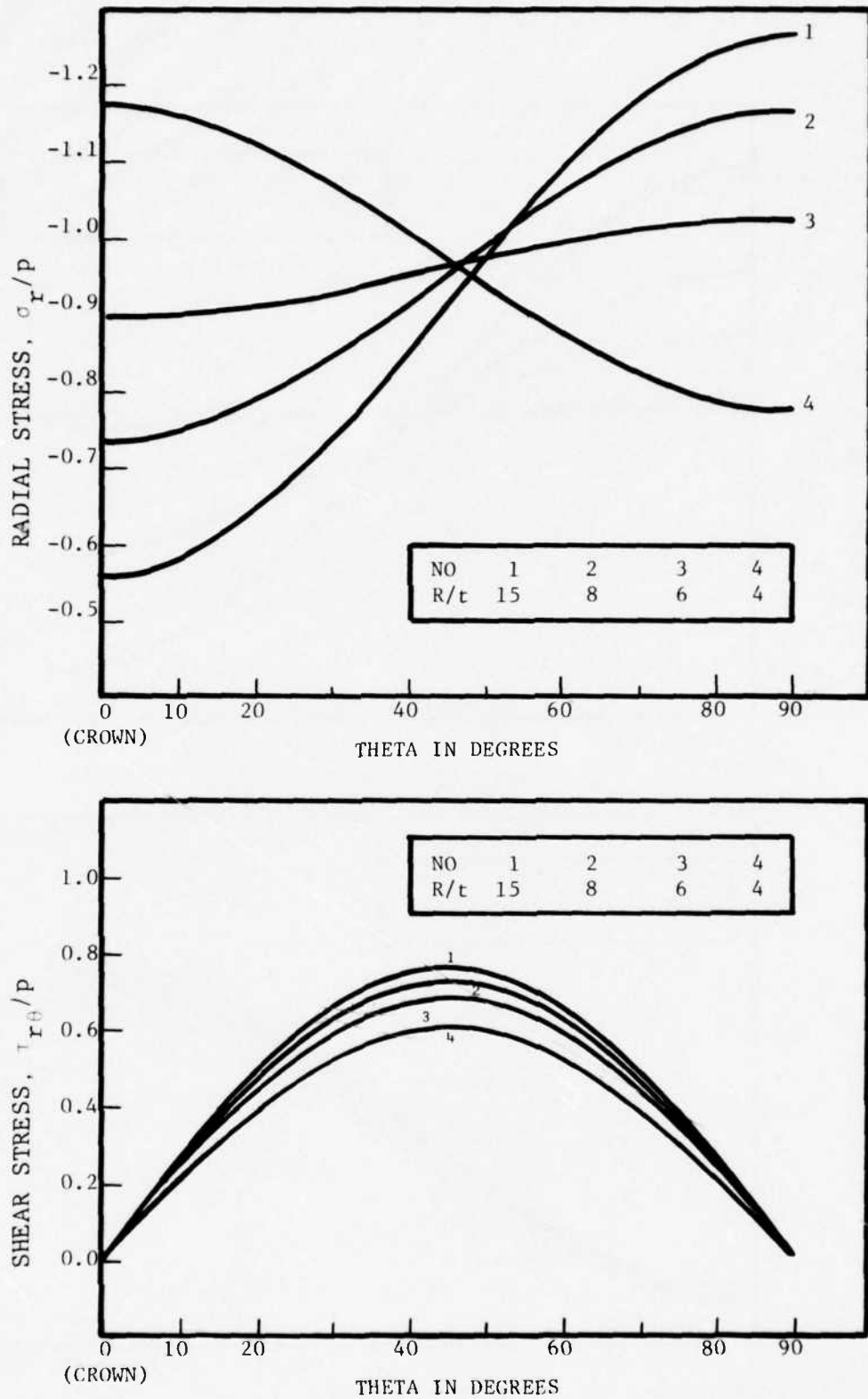


Figure 3a. Nondimensional SSI Stresses
NS Case A ($\alpha = 0.0096$, $k = 1/3$, $\nu = 1/4$)

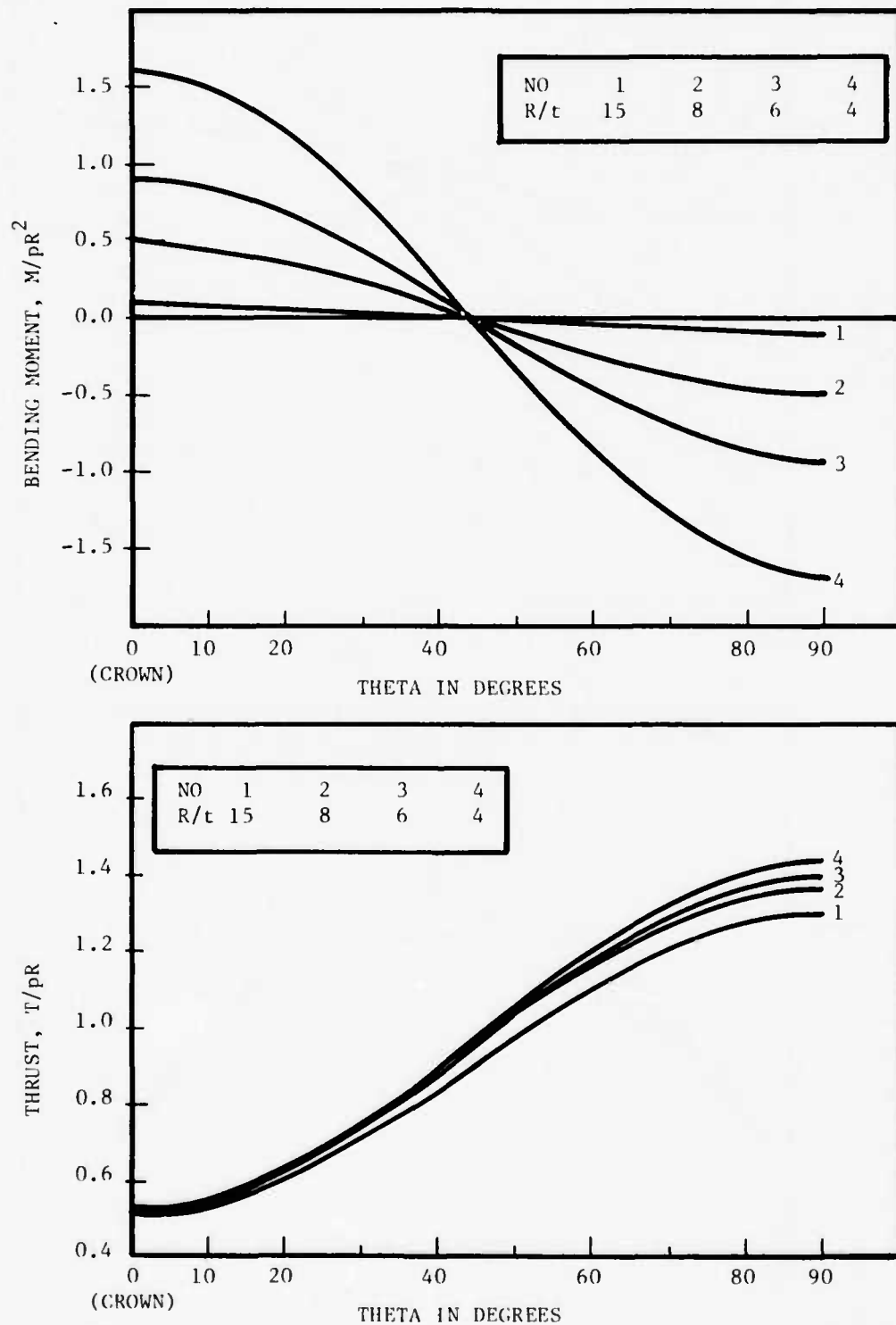


Figure 3b. Nondimensional Cylinder Internal Forces, NS Case A

$$\left. \begin{array}{l} k = 0 \\ \nu = 0.25 \\ R/t = 15, 8, 6, 4 \end{array} \right\} \text{cases B, C and D}$$

The modulus ratio and figures containing the SSI stresses and cylinder internal forces for each case are:

Case	B	C	D
α	0.0096	0.096	0.96
figure	4	5	6

Case B has the same value of α as case A, but assumes there is no horizontal free field stress. Cases C and D use values of α that are one and two orders of magnitude greater than case B. Thus, if the tunnel liner material is again assumed to be concrete, then the constrained modulus of the soil media, M^* , would be 30, 300 and 3000 ksi (206.9, 2069 and 20,690 MPa) for cases B, C and D, respectively. Case D is representative of a very competent rock-like soil media, and case C would represent a material intermediate between a typical soil and rock-like media.

Table I gives the mode 0 and mode 2 component amplitudes of the nondimensional SSI stresses and the cylinder internal forces for each of the four sets of material parameters (cases A, B, C and D). These amplitudes have been computed for each of the structure-soil media interface idealizations, i.e., the fully bonded or NS assumption and the zero friction or FS condition.

The results of cases B, C and D demonstrate a number of interesting things such as the arching action through the soil around the liner for the more flexible cylinders of case B and very high magnitudes of arching around the liner for all cylinders considered for cases C and D. Also, the SSI shear stress ($\tau_{r\theta}$) and the cylinder thrust (T) are not terribly sensitive to the cylinder stiffness (R/t) or the material modulus ratio (α) until the soil media modulus approaches that of the cylinder. As expected, the bending moments in the liner (M) are very sensitive to both the modulus ratio (α) and the cylinder stiffness (R/t).

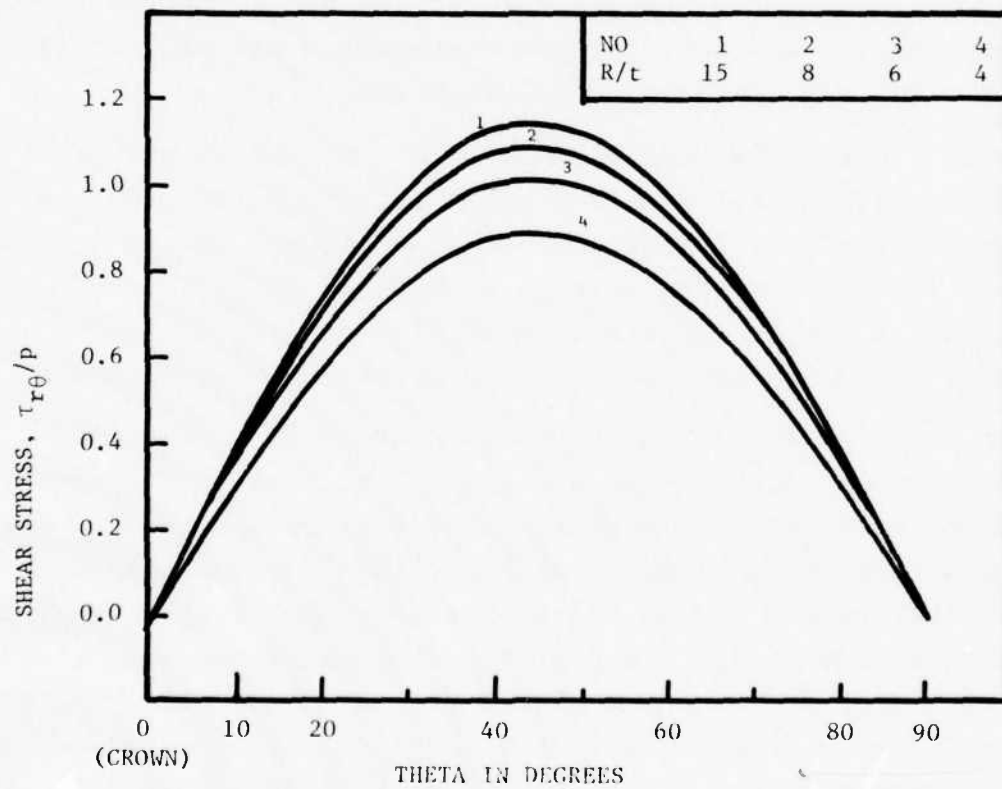
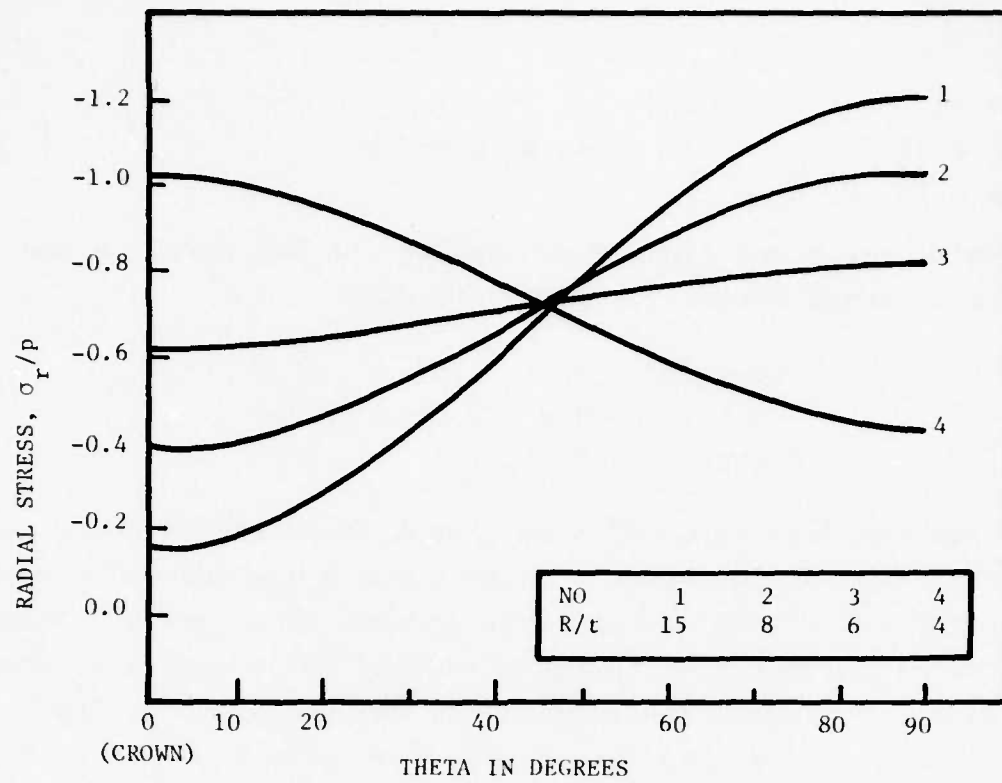


Figure 4a. Nondimensional SSI Stresses, NS Case B
 $(\alpha = 0.0096, k = 0, \nu = 1/4)$

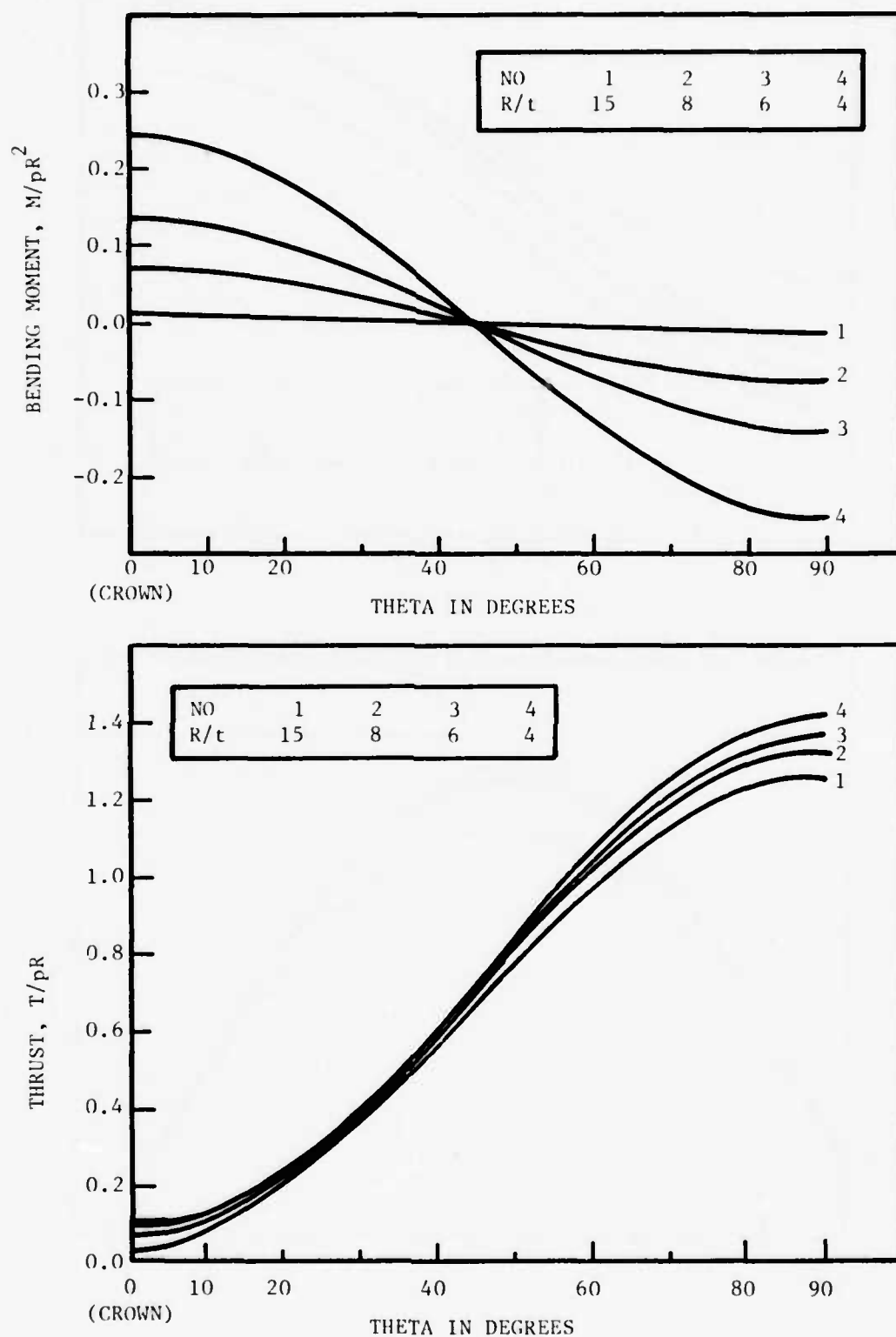


Figure 4b. Nondimensional Cylinder Internal Forces, NS Case B

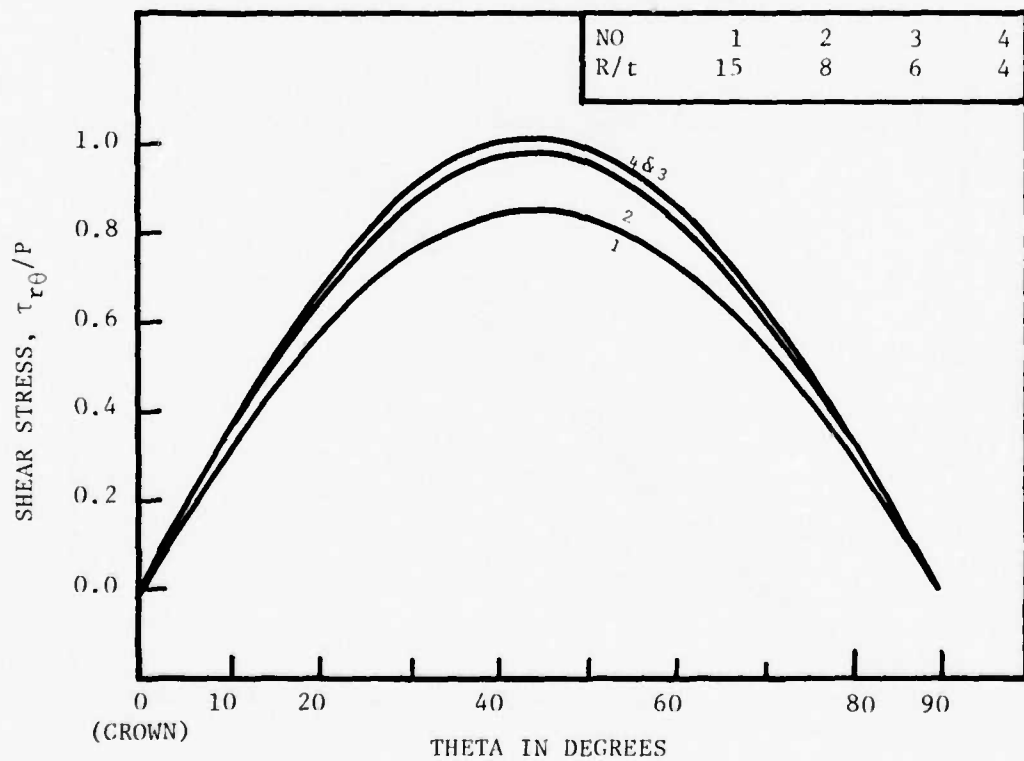
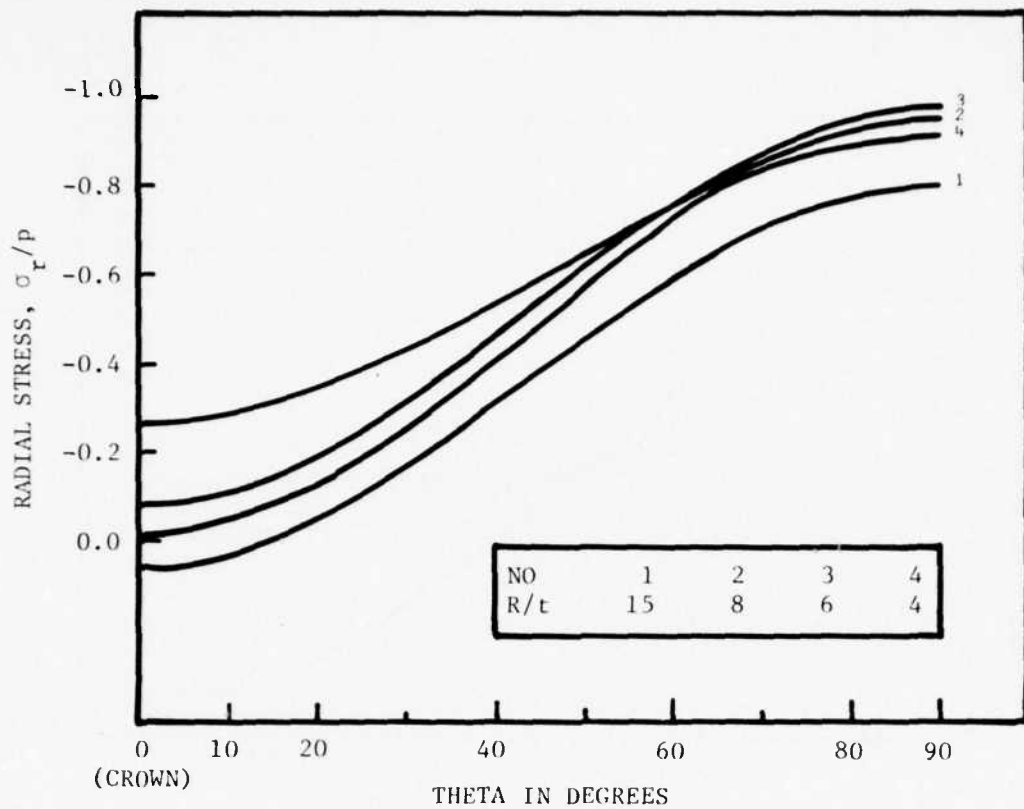


Figure 5a. Nondimensional SSI Stresses, NS Case C
 $(\alpha = 0.096, k = 0, \nu = 1/4)$

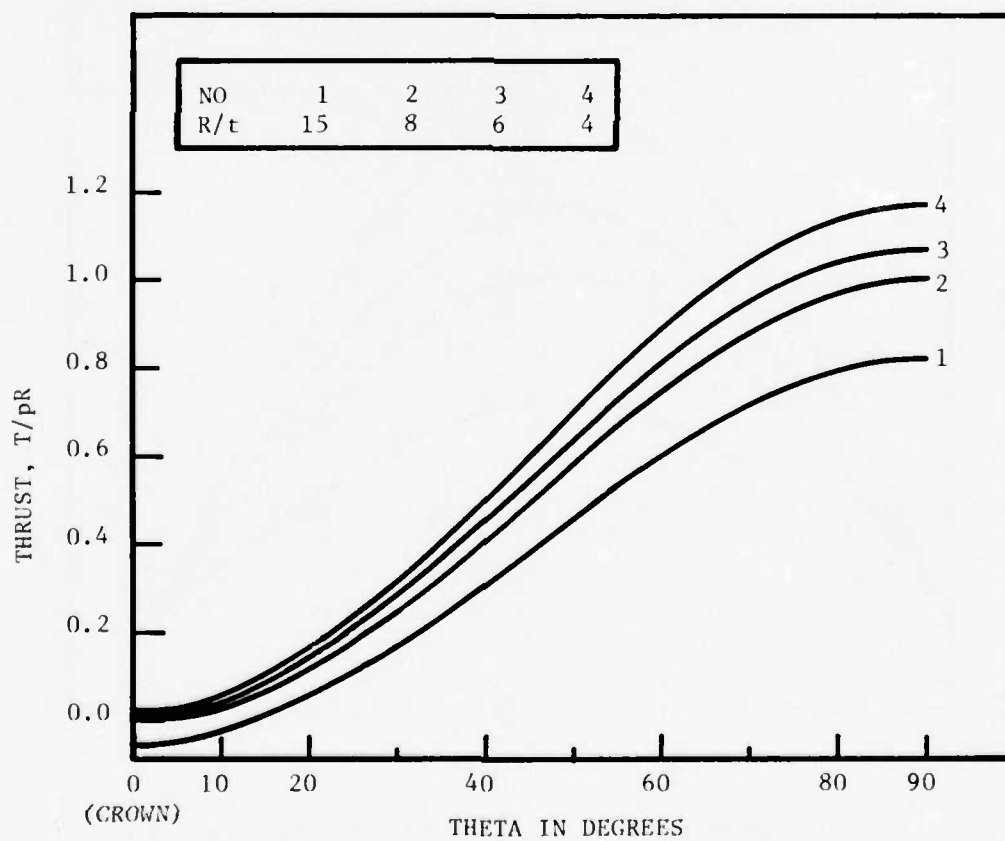
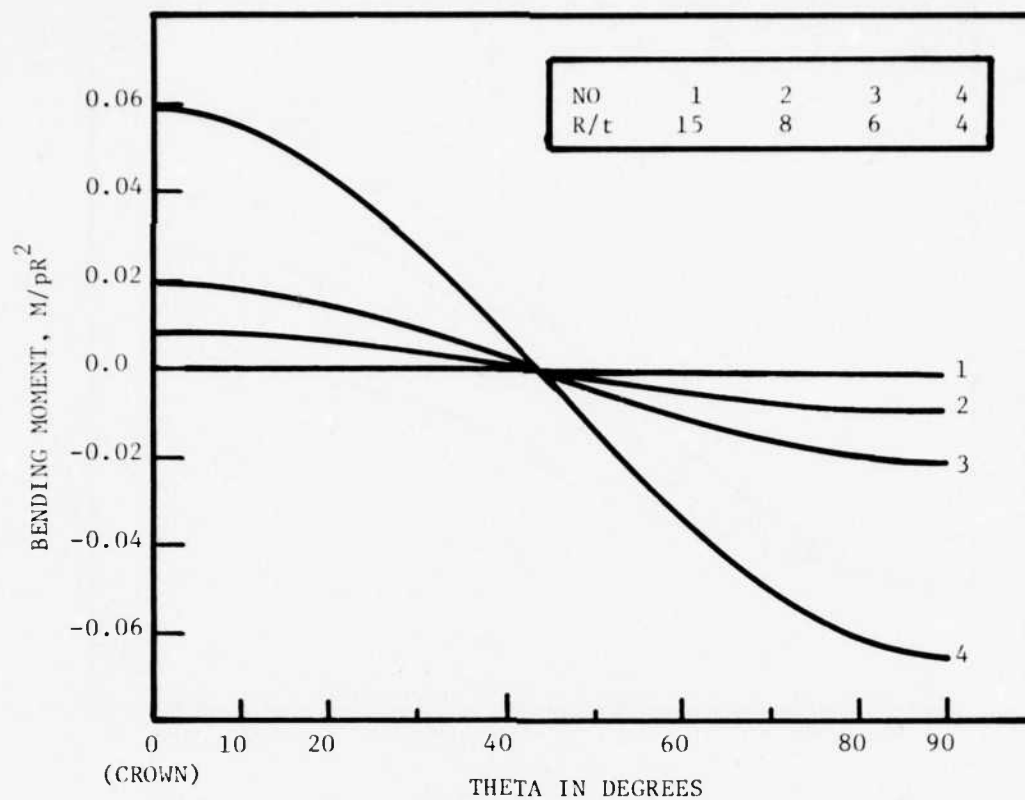


Figure 5b. Nondimensional Cylinder Internal Forces, NS Case C

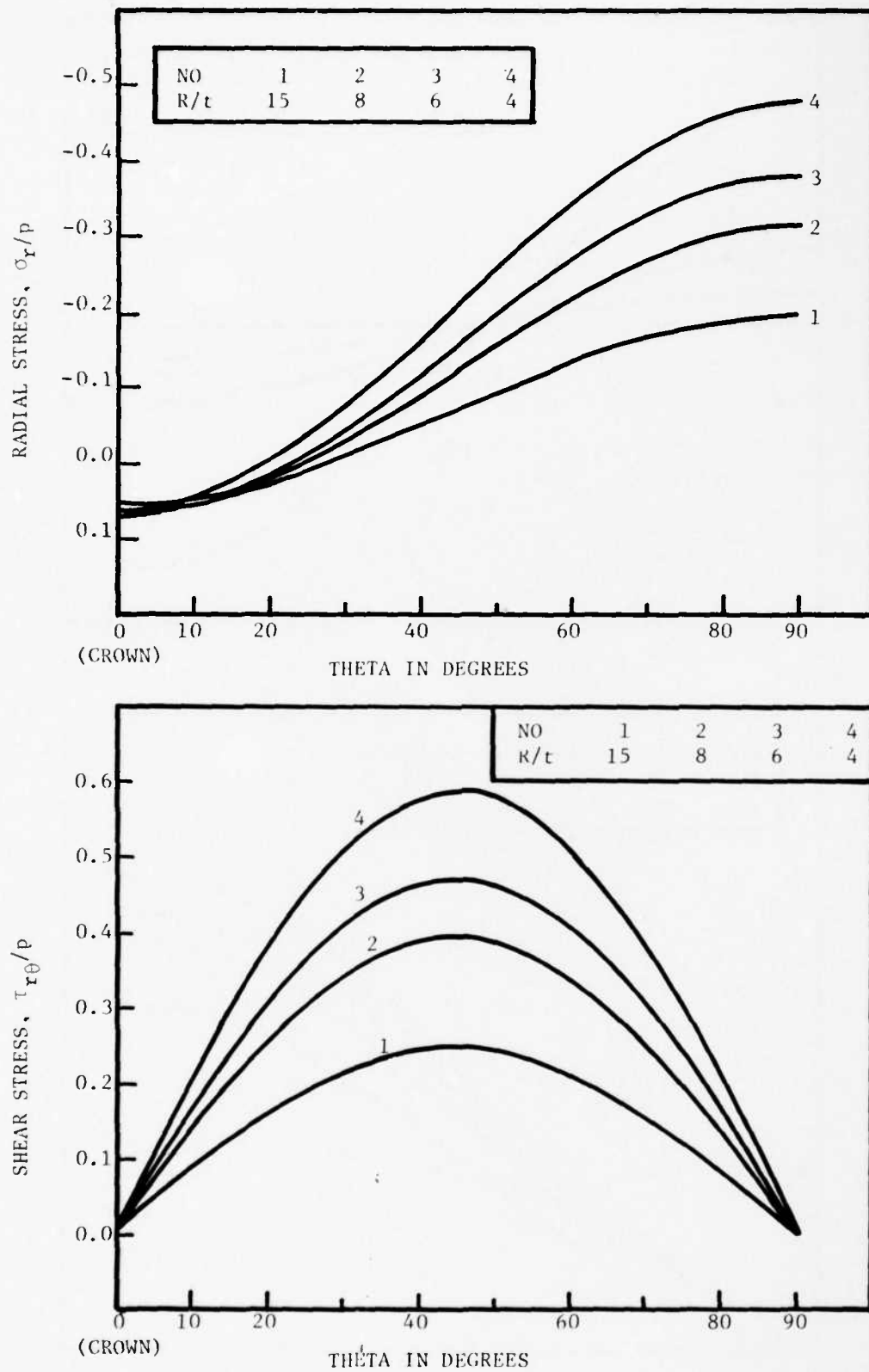


Figure 6a. Nondimensional SSI Stresses, NS Case D
 $(\alpha = 0.96, k = 0, \nu = 1/4)$

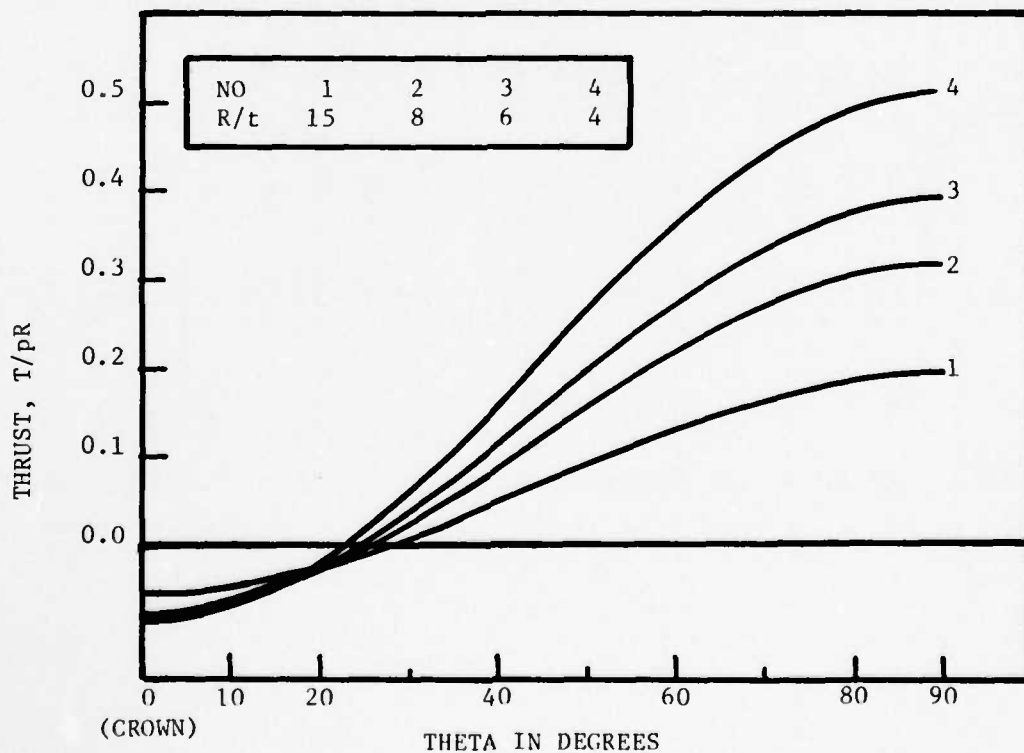
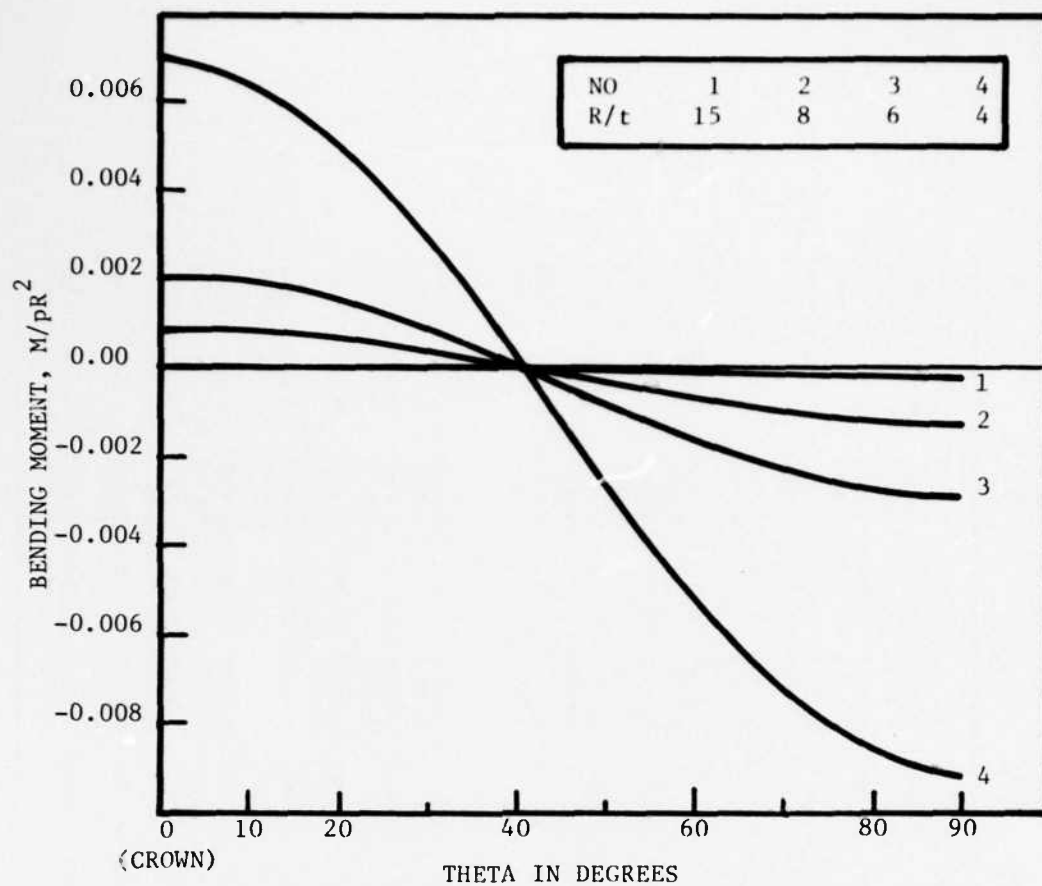


Figure 6b. Nondimensional Cylinder Internal Forces, NS Case D

Table I
NONDIMENSIONAL SSI AND CYLINDER FORCE AND DISPLACEMENT COMPONENTS

Case	R/t	Interface	$\bar{\sigma}_{r0}$	$\bar{\sigma}_{r2}$	$\bar{\sigma}_{\theta 0}$	$\bar{\sigma}_{\theta 2}$	\bar{T}_{r02}	\bar{M}_0	\bar{M}_2	\bar{T}_0	\bar{T}_2	$\bar{\psi}_0$	$\bar{\psi}_2$
Material Parameters Cases A and B													
A	4	NS	-0.9750	-0.1994	-0.3583	-0.0563	0.5951	-0.00508	0.16566	0.9751	-0.4633	0.0374	0.4071
		FS		-0.5838		0.7495	0		0.19462		-0.1947		0.4783
	6	NS	-0.9630	0.0638	-0.3703	0.0387	0.6792	-0.00223	0.09192	0.9631	-0.4316	0.0555	0.7626
		FS		-0.3322		1.0011	0		0.11075		-0.1108		0.9186
	8	NS	-0.9513	0.2151	-0.3820	0.0965	0.7260	-0.00124	0.04929	0.9513	-0.4123	0.0731	0.9690
B		FS		-0.1806		1.1527	0		0.06022		-0.0603		1.1839
	15	NS	-0.9124	0.3530	-0.4209	0.1663	0.7600	-0.00034	0.00901	0.9124	-0.3890	0.1314	1.1677
		FS		-0.0334		1.3000	0		0.01113		-0.0111		1.4416
	4	NS	-0.7312	-0.2991	-0.2687	-0.0845	0.8927	-0.00381	0.24849	0.7313	-0.6948	0.0280	0.6107
		FS		-0.8758		1.1242	0		0.29192		-0.2919		0.7174
C	6	NS	-0.7223	0.0957	-0.2777	0.0580	1.0189	-0.00167	0.13791	0.7223	-0.6474	0.0416	1.1439
		FS		-0.4984		1.5016	0		0.16612		-0.1661		1.3779
	8	NS	-0.7135	0.3227	-0.2865	0.1447	1.0890	-0.00093	0.07393	0.7135	-0.6184	0.0548	1.4535
		FS		-0.2710		1.7290	0		0.09032		-0.0903		1.7758
	15	NS	-0.6843	0.5295	-0.3157	0.2494	1.1400	-0.00026	0.01352	0.6843	-0.5835	0.0985	1.7515
		FS		-0.0501		1.9499	0		0.01669		-0.0167		2.1624
Material Parameters Cases C and D													
C	4	NS	-0.5973	0.3224	-0.4029	0.2816	1.0204	-0.00311	0.06261	0.5972	-0.5729	0.2293	1.5387
		FS		-0.2263		1.7737	0		0.07544		-0.0755		1.8540
	6	NS	-0.5419	0.4456	-0.4581	0.4092	1.0182	-0.00126	0.02119	0.5419	-0.5303	0.3121	1.7570
		FS		-0.0765		1.9235	0		0.02552		-0.0255		2.1161
	8	NS	-0.4960	0.4654	-0.5040	0.4920	0.9867	-0.00065	0.00932	0.4960	-0.5027	0.3810	1.8311
D		FS		-0.0334		1.9666	0		0.01115		-0.0112		2.1915
	15	NS	-0.3827	0.4285	-0.6173	0.6969	0.8658	-0.00014	0.00148	0.3827	-0.4344	0.5510	1.9176
		FS		-0.0052		1.9948	0		0.00173		-0.0018		2.2409
	4	NS	-0.2107	0.2698	-0.7893	1.0936	0.5881	-0.00110	0.00809	0.2107	-0.3022	0.8090	1.9870
		FS		-0.0269		1.9731	0		0.00897		-0.0090		2.2029
E	6	NS	-0.1550	0.2286	-0.8450	1.2845	0.4720	-0.00036	0.00248	0.1550	-0.2385	0.8926	2.0600
		FS		-0.0081		1.9919	0		0.00270		-0.0027		2.2359
	8	NS	-0.1226	0.1934	-0.8775	1.4069	0.3933	-0.00016	0.00107	0.1226	-0.1978	0.9412	2.0969
		FS		-0.0034		1.9966	0		0.00114		-0.0012		2.2440
	15	NS	-0.0708	0.1235	-0.9293	1.6277	0.2479	-0.000027	0.000167	0.0708	-0.1242	1.0189	2.1562
		FS		-0.0005		1.9995	0		0.000174		-0.0002		2.2491

Note: The mode 0 component for the FS interface condition is the same value as for the NS condition.

4. DEPTH OF BURIAL ANALYSIS

This portion of the static analysis investigations again considers an elastic, horizontally oriented cylinder embedded in a homogeneous elastic soil media. The influence of depth of burial of the cylinder was studied by performing static finite element analyses for ratios of depth of burial to cylinder radius (h/R) values of 0.5, 1.0, 2.0 and 4.0. The SAP4 computer code (Ref. 54) was employed for all of these investigations. The following soil media and structural parameters were used for each of the four depth of burial finite element investigations:

Soil Parameters: $E = 25 \text{ ksi (172.4 MPa)}$
 $\nu = 0.25$

Cylinder Parameters: $E_c = 3000 \text{ ksi (20,700 MPa)}$
 $\nu_c = 0.2$
 $R/t = 15, 8, 6, 4$

The ground surface is subject to a uniform pressure loading (p) as indicated in figure 1. Since the postulated problem is symmetric about a vertical plane through the axis of the cylinder, only half of the system needs to be modeled. A plane strain analysis has been employed for the soil media for each of the SAP4 numerical solutions. The results of the infinite media analyses illustrated in figure 2 imply that for a static analysis the influence of the cylindrical inclusion is essentially negligible for points greater than 1.5 times the cylinder diameter. This conclusion is based on the observation that the state of stress for points 1.5 diameters from the cylinder is essentially the same as the free field state of stress. Therefore, the finite element mesh boundaries (vertical "lateral" and horizontal "lower") were located at two diameters from the edge of the cylinder. The boundary conditions imposed on the vertical and lower horizontal finite element mesh perimeters were such that the nodes were free to translate parallel to the boundary but were restrained from all motion normal to the boundary and were also not permitted to rotate. These conditions simulate a roller bearing surface at the boundaries. The remaining grid points, including the upper ground surface nodes, were unrestrained.

A considerable effort was made to keep the aspect ratio of each element close to 1 for each of the finite element meshes used. The resulting grid works are shown in figures 7 through 10 for the four depth of burial h/R values of 0.5, 1.0, 2.0 and 4.0, respectively. As previously indicated, two-dimension plane strain elements were used to model the soil media (type 4 elements - SAP4).

Twenty-five equally spaced node points were used to simulate the half-model of the soil-structure interface. Thus, each pair of adjacent nodes is located 7.5 deg apart at the soil-structure interface. The tunnel liner was modeled by interconnecting 24 beam "line" elements (type 2 elements - SAP4) to these 25 node points. Therefore, the finite element mesh simulates the NS condition at the structure media interface.

Each of the four depth-of-burial meshes (figures 7 through 10) was used to obtain numerical solutions for the four cylinder stiffnesses ($R/t = 15, 8, 6, 4$); thus, solutions were obtained for a total of 16 cases. The cylinder stiffness (R/t) was simulated by specifying appropriate moments of inertia and cross-sectional areas for the beam elements. The number of nodes and media elements used for each of the finite element meshes is indicated below.

<u>h/R</u>	<u>Nodes</u>	<u>Elements</u>
0.5	173	159
1.0	186	177
2.0	190	188
4.0	202	198

The results from the 16 SAP4 numerical solutions are summarized in table II and figure 11. Also included on these displays are the infinite media or infinite depth of burial analytical solutions described in section I for the appropriate material parameters, i.e., case A with NS at the soil-structure interface.

An examination of figure 11 indicates that for a depth of burial of two diameters, the soil stresses are essentially the same as the infinite media soil stresses along the crown and springline rays for all of the liner stiffness considered.

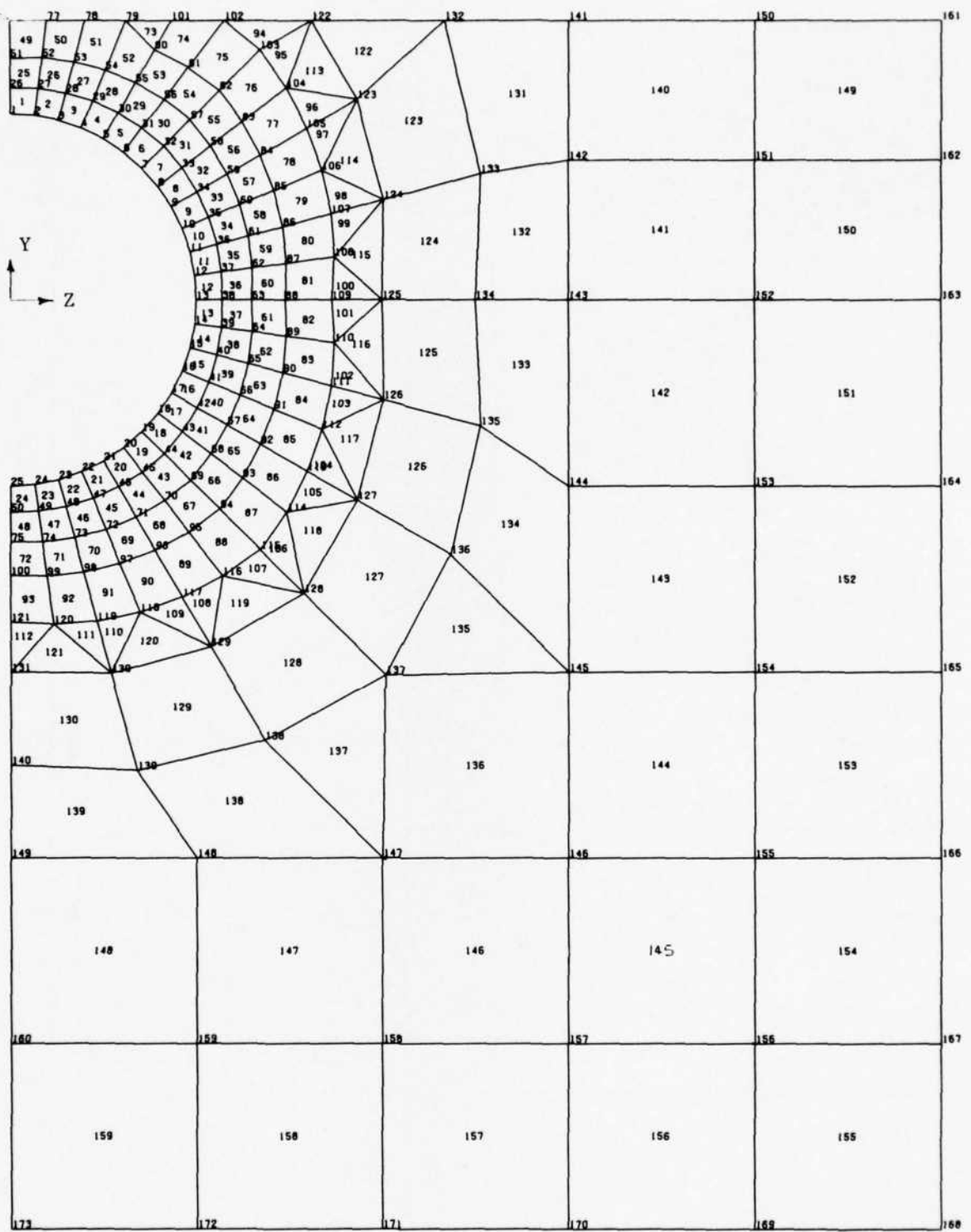


Figure 7. Finite Element Mesh for SAP4 Static Analysis, $h/R = 0.5$

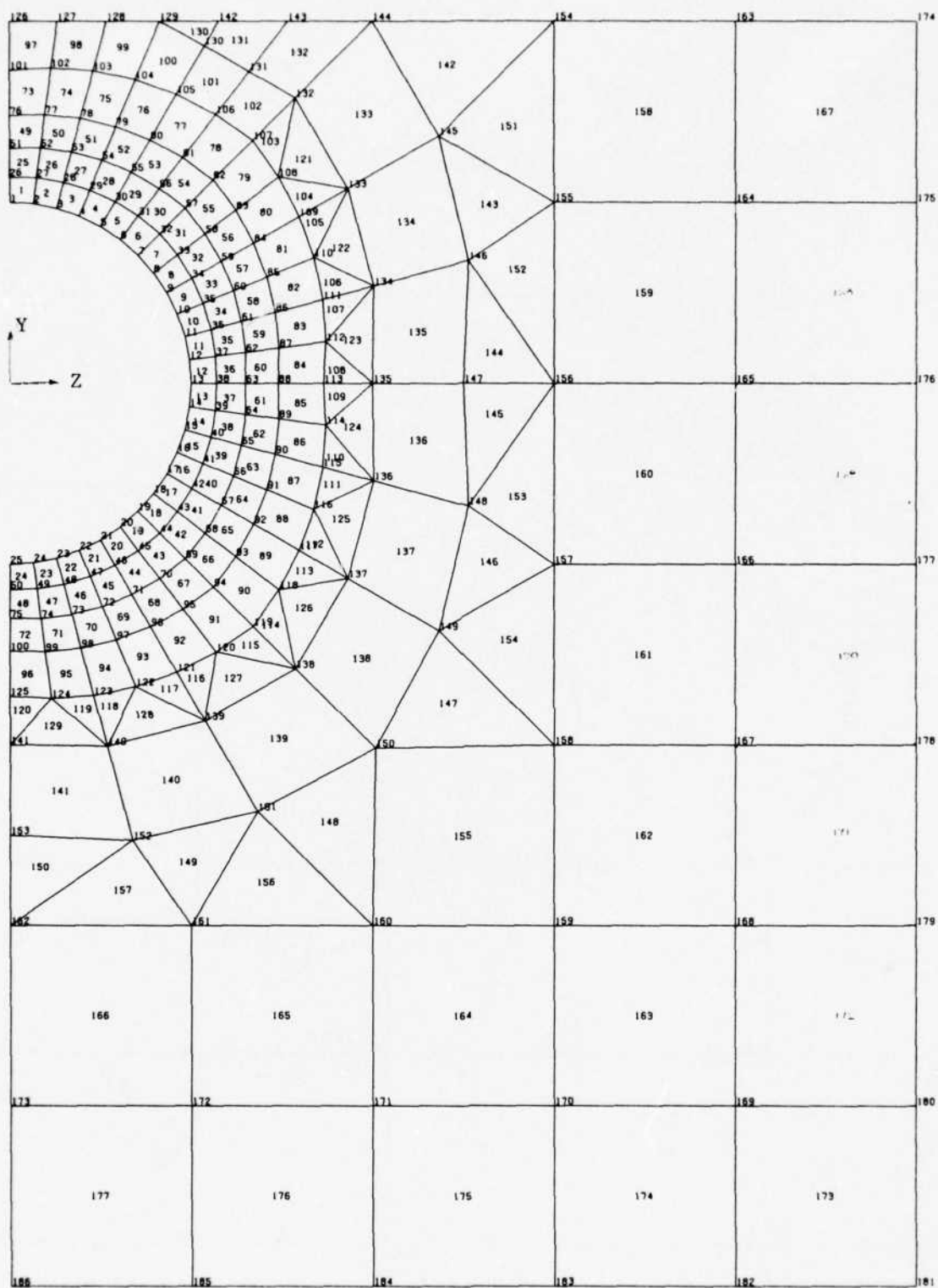


Figure 3. Finite Element Mesh for SAP4 Static Analysis, $h/R = 1.0$

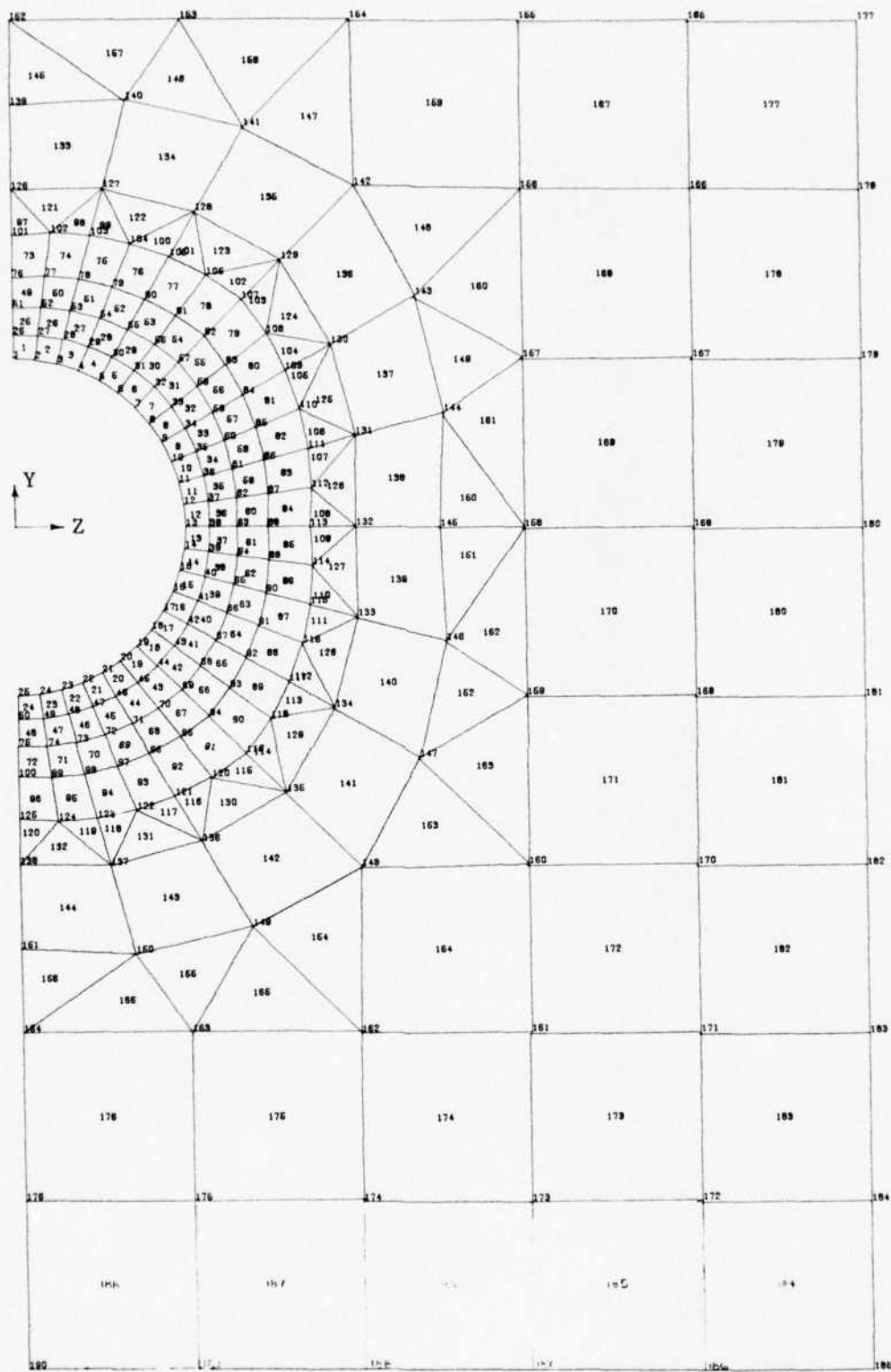


Figure 9. Finite Element Mesh for SAP4 Static Analysis, $h/R = 2.0$

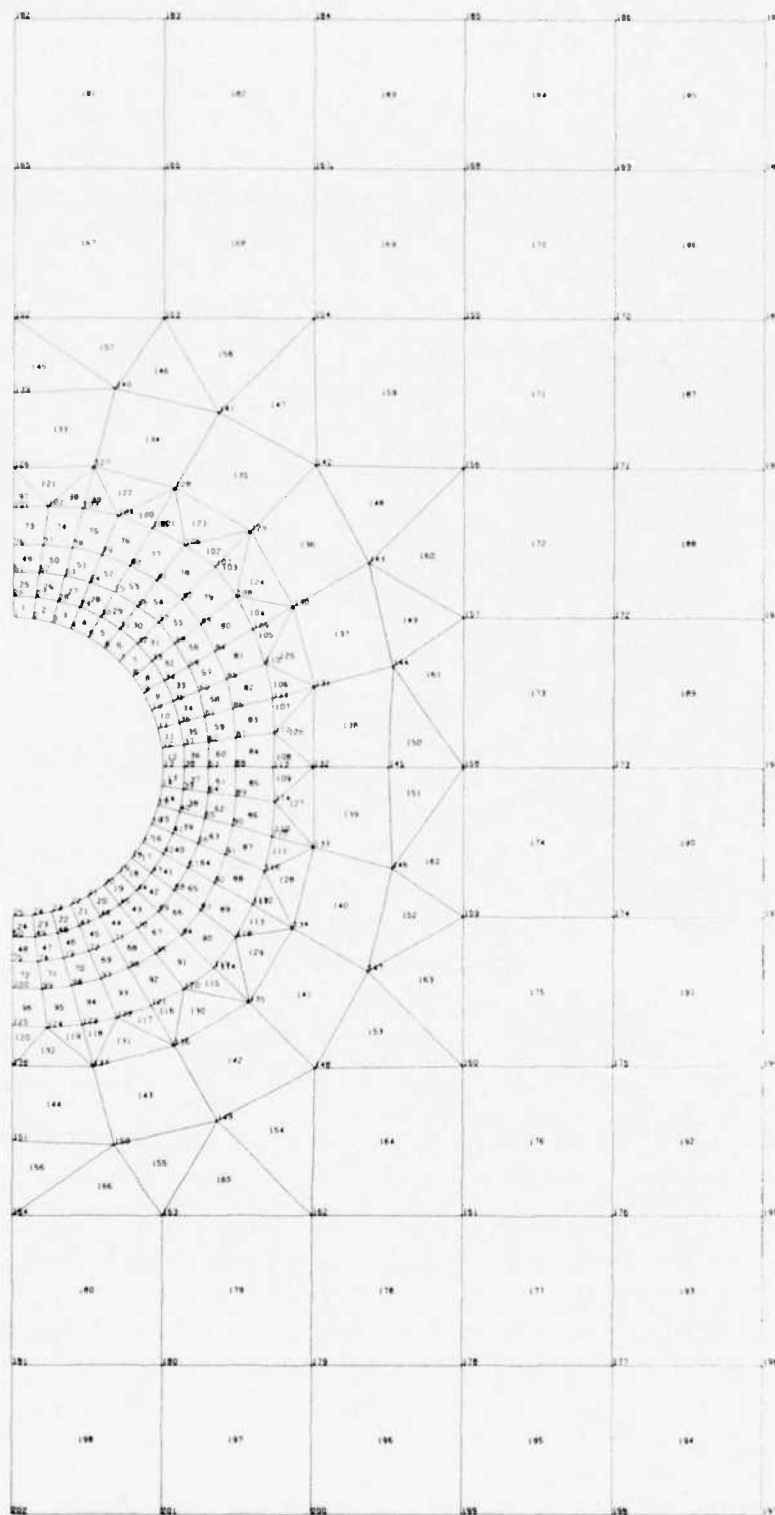


Figure 10. Finite Element Mesh for SAP4 Static Analysis, $h/R = 4.0$

Table II
CYLINDER NONDIMENSIONAL THRUST AND MOMENT
FOR VARIOUS DEPTHS OF BURIAL - SAP4 RESULTS ($R/t = 15, 8, 6, 4$)

h/R	R/t	θ	Thrust			Moment		
			0°	90°	180°	0°	90	180°
0.5	15		0.514	1.292	0.536	0.01195	-0.00801	0.00812
	8		0.504	1.314	0.556	0.05020	-0.04420	0.04430
	6		0.477	1.315	0.549	0.08430	-0.08190	0.08270
	4		0.428	1.312	0.531	0.13600	-0.14270	0.14600
1.0	15		0.540	1.295	0.549	0.00928	-0.00816	0.00812
	8		0.545	1.331	0.566	0.04610	-0.04450	0.04450
	6		0.527	1.341	0.556	0.08290	-0.08300	0.08360
	4		0.490	1.350	0.531	0.14320	-0.14790	0.15020
2.0	15		0.554	1.290	0.554	0.00838	-0.00820	0.00812
	8		0.567	1.340	0.569	0.04520	-0.04500	0.04490
	6		0.552	1.370	0.556	0.08460	-0.08500	0.08520
	4		0.519	1.390	0.526	0.15300	-0.15500	0.15600
4.0	15		0.555	1.290	0.556	0.00816	-0.00814	0.00808
	8		0.569	1.350	0.569	0.04520	-0.04510	0.04500
	6		0.555	1.376	0.555	0.08600	-0.08600	0.08600
	4		0.521	1.413	0.517	0.15890	-0.15930	0.15990
∞ (case A)	15		0.523	1.301	0.523	0.00867	-0.00935	0.00867
	8		0.539	1.364	0.539	0.04810	-0.05050	0.04810
	6		0.532	1.395	0.532	0.08970	-0.09420	0.08970
	4		0.512	1.438	0.512	0.16060	-0.17070	0.16060

The curves also show that the state of stress in the soil immediately adjacent to the structure, i.e., the SSI stresses, at the crown is essentially unaffected by the depth of burial for the flexible liner case ($R/t = 15$). As the structural stiffness decreases, the SSI stresses at the crown are somewhat but not drastically reduced. There is a moderately pronounced depth of burial effect on the state of soil stress for points that are slightly away from the crown.

The soil stresses along the springline ray ($\theta = 90$ deg) are not drastically affected by the depth of burial. In fact, it can be argued that the springline ray soil stress differences between the infinite media and the SAP4 results can be attributed to the inherent difference in the solution technique, i.e., continuous versus discrete.

SOIL: $E = 25 \text{ ksi (172.4 MPa)}$
 $\nu = 0.25$

LINER: $E_c = 3000 \text{ ksi (20,690 MPa)}$
 $\nu_c = 0.2$

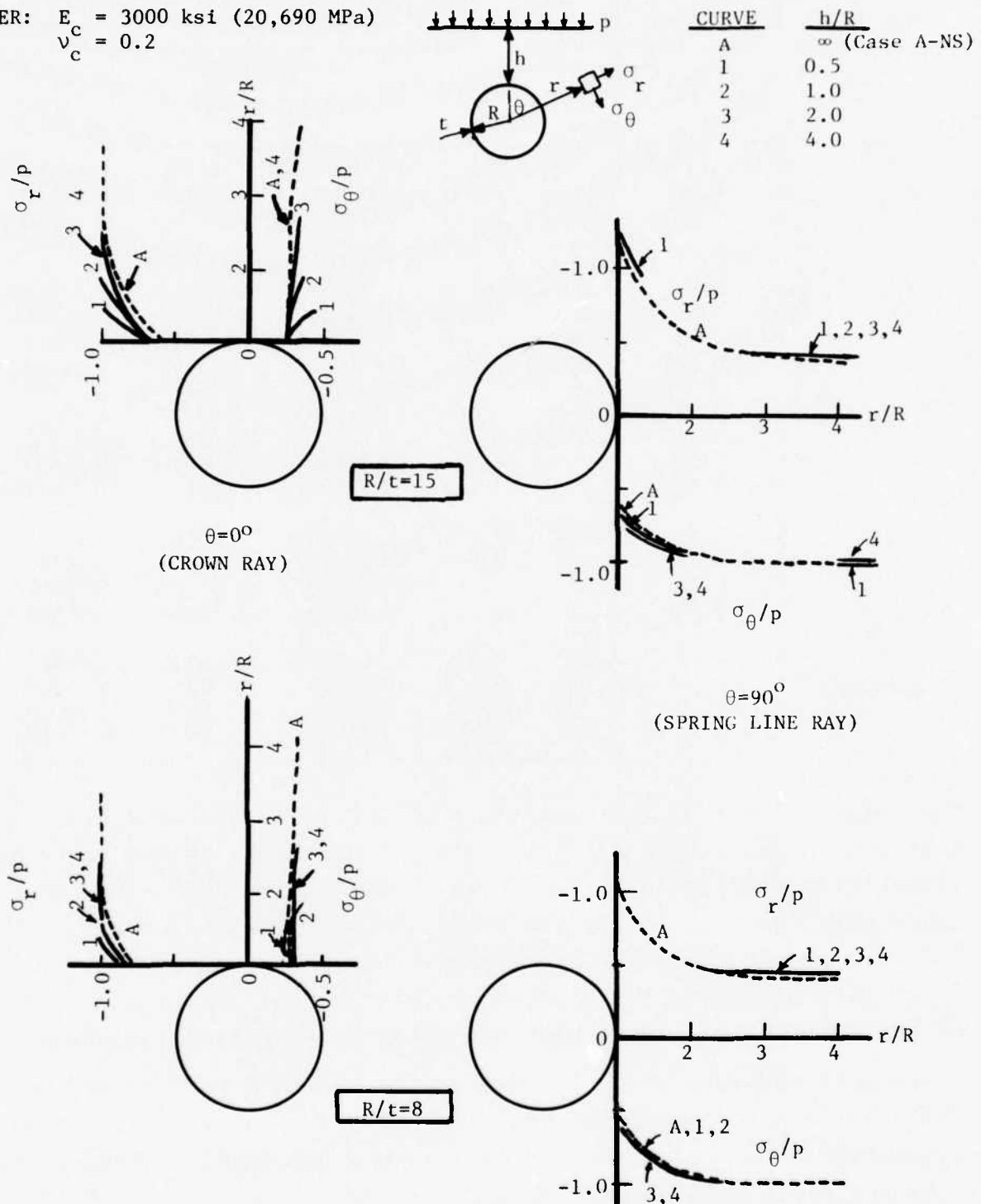


Figure 11a. Nondimensional Soil Stress Variation for Various Depths of Burial ($R/t = 15, 8$)

SOIL: $E = 25 \text{ ksi (172.4 MPa)}$
 $\nu = 0.25$

LINER: $E_c = 3000 \text{ ksi (20,690 MPa)}$
 $\nu_c = 0.2$

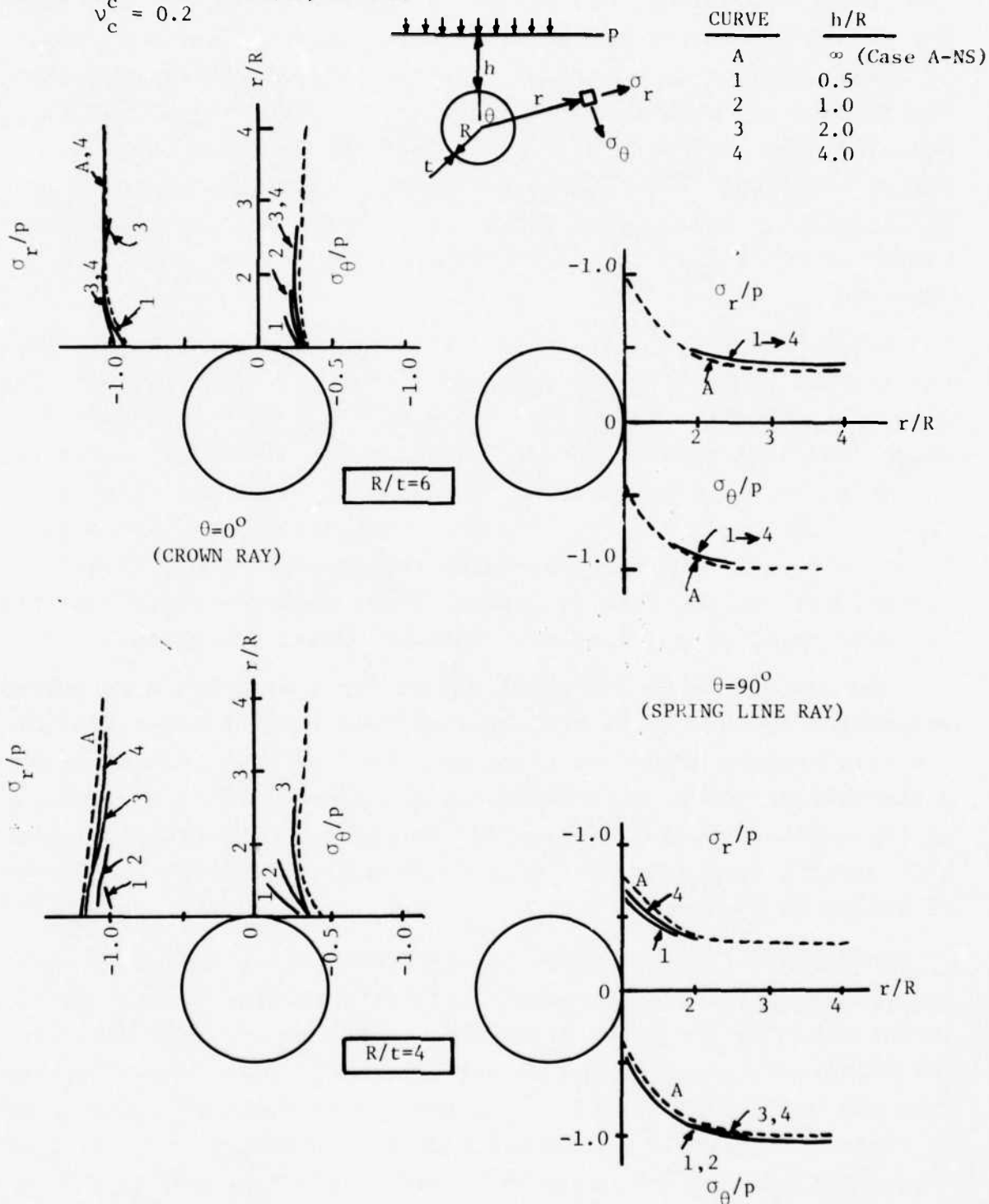


Figure 11b. Nondimensional Soil Stress Variation for Various Depths of Burial ($R/t = 6, 4$)

Table II gives the nondimensional thrust and bending moment at the crown, springline, and invert locations ($\theta = 0, 90, 180$ deg) for the 16 SAP4 depth of burial solutions and the infinite depth of burial analytical solution (case A). These results show that the thrusts and moments for a depth of burial of two diameters are generally well within 10 percent of the infinite depth of burial results. The largest difference, 13 percent, occurs for the springline moment, and these differences can again be essentially attributed to the different solution schemes that were employed.

Using the SAP4 results only, it is observed that the cylinder thrusts are reduced as the depth of burial is reduced for all except the springline thrust for the most flexible cylinder ($R/t = 15$) which increases very slightly. As the depth of burial decreases, the crown moment increases for the flexible liner and decreases for the stiffer liner. For the more flexible liners, the depth of burial has very little influence on the springline and invert moment; but for the stiffer liners, these moments slightly decrease (as much as 12 percent) as the depth of burial decreases.

The overall depth of burial effect for static loads on buried structures appears to be the negating influence or moderation of the soil arching phenomena. For example, the soil arching around a flexible structure is reduced and hence the loading is increased as the depth of burial decreases. Conversely, the action of the soil arching onto a stiff structure is also reduced as the depth of burial is reduced.

For depths of burial equal to one tunnel liner radius or more, the primary SSI loads are essentially derived from modes 0 and 2 as evidenced by the Table II results. This is apparent since the crown and invert moment and thrust are nearly equal which implies that the uniform and ovaling load components dominate. For a depth of burial of one-half the tunnel radius, additional (higher) modes of the SSI loading are required to accurately determine the loading; however, modes 0 and 2 will still produce quite credible results even for this depth of burial case for all but the most flexible liner.

The mode 0 and 2 SSI stresses can be approximated in the following manner by using the liner force resultants given in table II. First the mode 0 and 2 thrust and moment modes are calculated from the crown, springline, and invert values in the table ($\theta = 0, 90, 180$) as

$$\bar{T}_0 = (\bar{T}_{CR} + \bar{T}_{INV})/4 + \bar{T}_{SPR}/2$$

$$\bar{T}_2 = \bar{T}_0 - \bar{T}_{SPR}$$

$$\bar{M}_0 = (\bar{M}_{CR} + \bar{M}_{INV})/4 + \bar{M}_{SPR}/2$$

$$\bar{M}_2 = \bar{M}_0 - \bar{M}_{SPR}$$

Neglecting the \bar{M}_0 solution, the desired SSI modal stresses ($\bar{\sigma}_{r0}, \bar{\sigma}_{r2}, \bar{\tau}_{r\theta 2}$) can be obtained by application of equations (11e) through (11g).

SECTION III

DYNAMIC ANALYSES

The dynamic airblast loading finite element investigations and the related processing of the numerical results undertaken during this project are described in this section. The fundamental purpose of these dynamic solutions was to see if the important aspects of the SSI loads, i.e., radial and shear stresses, could be satisfactorily characterized by a few time varying amplitudes of the modal components of the SSI loads. This concept was postulated as a logical extension of the technique discussed in the static analyses in section II, where it was shown that modes 0 and 2 generally provide an accurate definition of the SSI loads. For the static analyses, both the tunnel liner and the soil media were idealized as elastic materials and the results are proportional to the loading. Since the dynamic analyses employ a nonlinear soil material, the solutions are sensitive to the magnitude of the loading and therefore both high and low values of peak airblast overpressure have been included in these analyses. These dynamic investigations use the same range of tunnel liner radius to thickness ratios and depths of burial that were used in the static analyses.

A plane strain solution procedure has been used; in general, the soil medium has been modeled as a nonlinear material and the buried cylinder liner was representative of a linear elastic concrete material with a 13.12 ft (4.0 m) inside diameter (see figure 12). The dynamic loading is assumed to originate from a nuclear weapon airblast overpressure. The passage of the airblast shock front over the ground surface has not been included in these investigations, and the airblast loading is applied uniformly to the entire ground surface. Referring to figure 12 the airblast loading is represented by a time varying pressure acting uniformly over the ground surface. Table III presents the time duration of an equivalent triangular pulse of intense airblast overpressures for a reasonable range of weapon yields, 0.125,

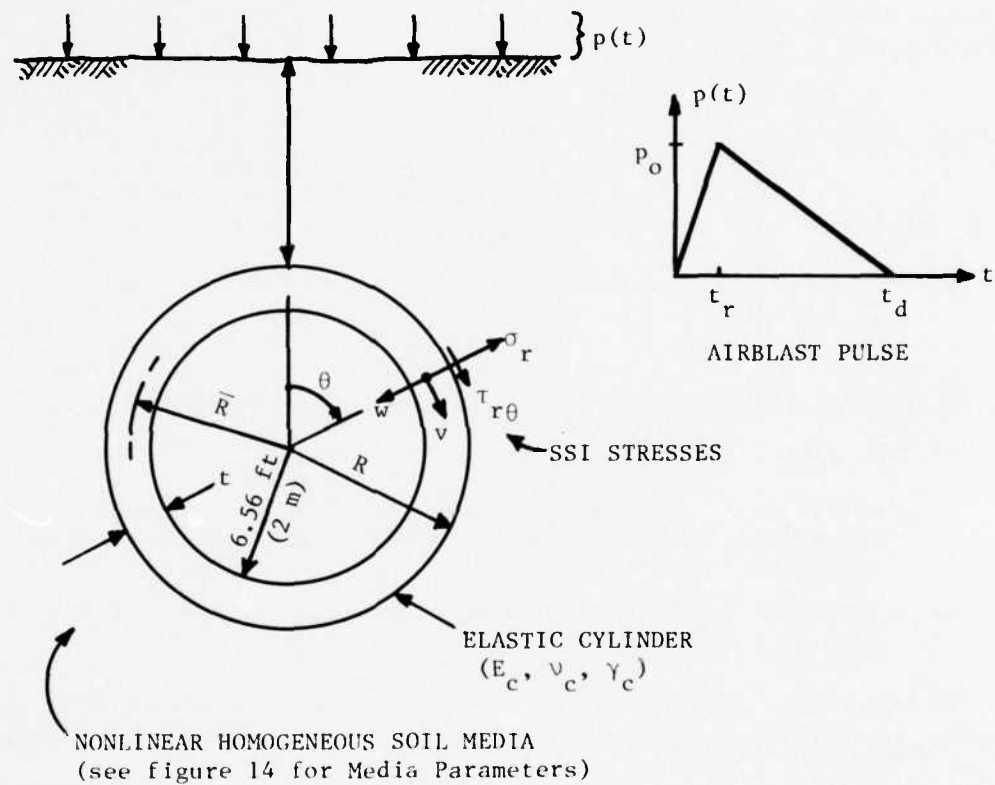


Figure 12. Dynamic Analysis Parameters.

1.0, and 8.0 MT (0.53×10^9 , 4.2×10^9 , and 33.6×10^9 MJ) and peak overpressures, p_o , of 500, 1000, and 1500 psi (3.448, 6.895, and 10.343 MPa).

Table III
APPROXIMATE EQUIVALENT TRIANGULAR PULSE AIRBLAST
OVERPRESSURE DURATION (msec)

Overpressure, p_o psi (MPa)		Weapon Yield, MT (MJ)		
		0.125 (0.525×10^9)	1.0 (4.2×10^9)	8.0 (33.6×10^9)
500 (3.448)	t_{00}	10	20	40
	t_{50}	25	50	100
1000 (6.895)	t_{00}	8	15	30
	t_{50}	15	30	60
1500 (10.343)	t_{00}	5	10	20
	t_{50}	10	20	40

The duration parameters were derived from reference 49 for two triangular idealizations:

- t_{00} , derived by using the slope of the triangular pulse as equal to the initial decay slope of the actual pressure time curve.
- t_{50} , derived by assuming that the triangular pulse passes through the actual curve at $0.5 p_o$.

The primary objective of these dynamic solutions was to obtain SSI loads acting on the structure and internal liner forces for a reasonable variation of the significant soil and structure parameters.

1. RUN MATRIX OF DYNAMIC CASES

A desirable matrix of solution parameters that might be selected consistent with the static investigations could conceivably include three or four variations for each fundamental parameter. For example, consider a run matrix that includes these five parameters:

- Structural Stiffness (elastic concrete)
 $R/t = 15, 8, 6, 4$
- Depth of Burial
 $h/R = 0.5, 1.0, 2.0, 4.0$
- Peak Airblast Overpressure
 $p_o = 500, 1000, 1500 \text{ psi (3.45, 6.90, 10.34 MPa)}$
- Airblast Loading Duration
 $t_d = 0.015, 0.030, 0.060 \text{ sec}$
- Soil Media (see figure 13)
 Sand, Cemented Sand, Clay.

Even this rather restrictive set of parameters would result in $4 \times 4 \times 3 \times 3 \times 3 = 432$ cases if all combinations were taken. Obviously this number of cases would have resulted in an effort that was well beyond the scope of work for this research project. To study the effects of the above parameter ranges on the dynamic response of the tunnel liner, a series of cases were made up using the extreme values of the above nonsoil parameters:

$R/t = 15 \text{ and } 4$
 $h/4 = 0.5 \text{ and } 4.0$
 $p_o = 500 \text{ and } 1500 \text{ psi (3.45 and 10.34 MPa)}$
 $t_d = 0.015 \text{ and } 0.060 \text{ sec.}$

Parameters associated with two soil media (sand and cemented sand) were also used to define the dynamic run matrix. All combinations of these parameters result in $2 \times 2 \times 2 \times 2 \times 2 = 32$ cases. Four additional cases were also defined which involve elastic soil media and nonlinear structure parameters. The resulting matrix of solution cases defining each of the 36 dynamic finite element solutions is given in table IV.

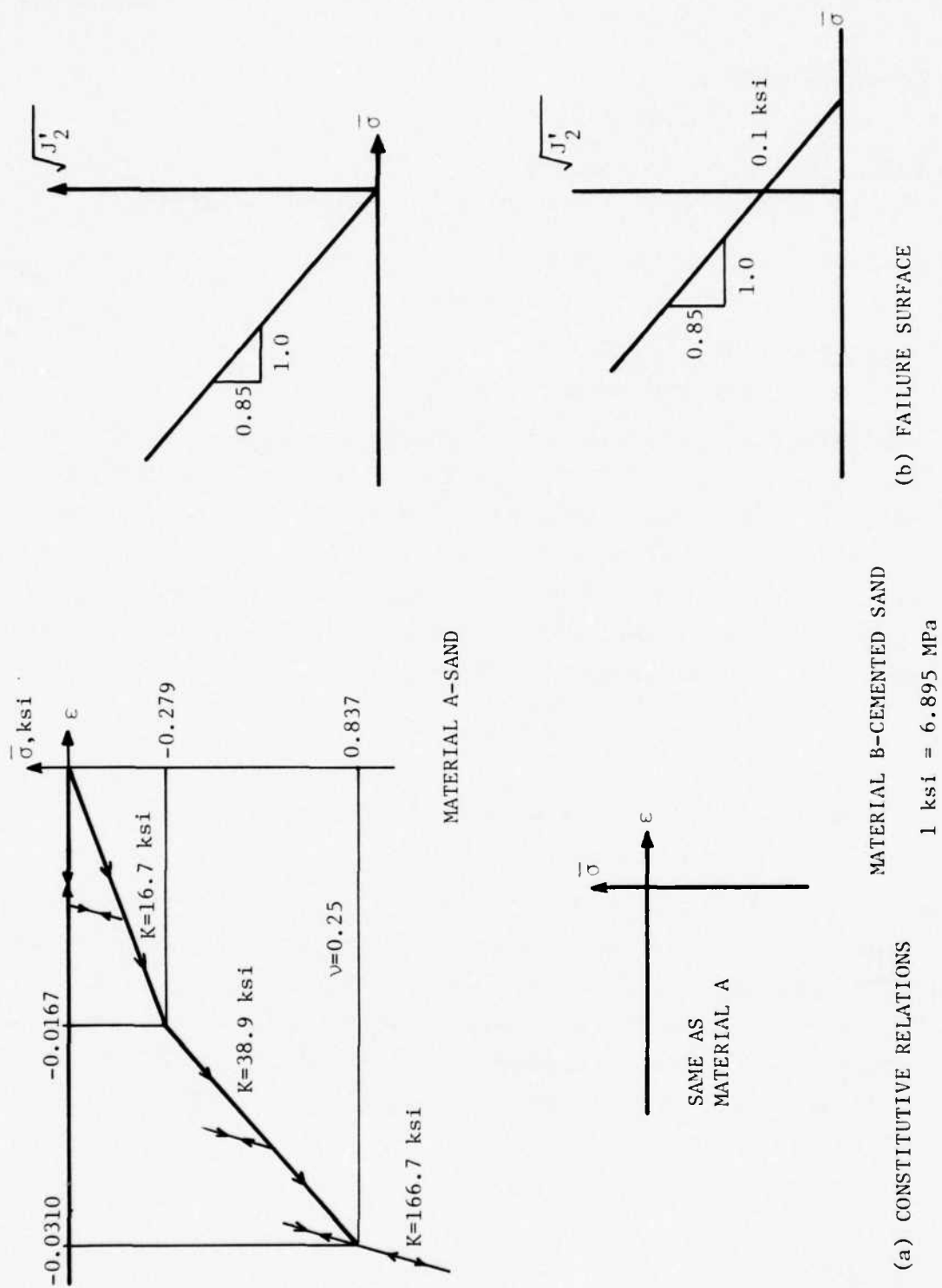


Figure 13. Nonlinear ROCKMT3 Soil Media Properties

Table IV
RUN MATRIX FOR (SAMSON) DYNAMIC SOLUTIONS

Case	R/t	h/R	p _o psi	t _d msec	Soil ^a	Case	R/t	h/R	p _o psi	t _d msec	Soil ^a
1	4	0.5	500	15	A	21	4	4	500	15	B
2	4	0.5	1500			22	4	4	1500		
3	4	0.5	500	60		23	4	4	500	60	
4	4	0.5	1500			24	4	4	1500		
5	4	0.5	500	15	B	25	15	4	500	15	A
6	4	0.5	1500			26	15	4	1500		
7	4	0.5	500	60		27	15	4	500	60	
8	4	0.5	1500			28	15	4	1500		
9	15	0.5	500	15	A	29	15	4	500	15	B
10	15	0.5	1500			30	15	4	1500		
11	15	0.5	500	60		31	15	4	500	60	
12	15	0.5	1500			32	15	4	1500		
13	15	0.5	500	15	B	33 ^c	15	0.5	1500	15	Elastic ^b
14	15	0.5	1500			34 ^c	15	0.5	1500	15	B
15	15	0.5	500	60		35	4	0.5	500	15	Elastic ^b
16	15	0.5	1500			36 ^c	4	0.5	500	15	B
17	4	4	500	15	A						
18	4	4	1500								
19	4	4	500	60							
20	4	4	1500								

^aSoil A - Sand; Soil B - Cemented Sand

^bElastic Soil; E = 25 ksi, $\nu = 0.25$

^cNonlinear Liner, 1 percent Steel R/C

Note: Cases 33, 34 same as 14 except as indicated.

Cases 35, 36 same as 5 except as indicated.

1 psi = 6.895 kPa

2. DYNAMIC FINITE ELEMENT SOLUTION ANALYSIS

A modified version of the SAMSON computer code (Ref. 48) was used to obtain solutions to the 36 cases defined in table IV. This computer code is a finite element code for the two-dimensional dynamic stress analysis of plane and axisymmetric media. It is based on small strain theory and is particularly suited for handling problems with nonlinear material properties and a large number of degrees of freedom. Although it was designed especially for the investigation of SSI problems, it can be used for more general applications.

For nonlinear problems a direct method of solution is employed without explicit formulation of a stiffness matrix. This method has several advantages for large-scale nonlinear transient problems. By avoiding construction of the stiffness matrix, considerable computer storage is saved, and the solution of much larger problems is permitted. Moreover, it is also computationally more efficient than other commonly used solution methods in nonlinear analysis. For linear elastic problems, the normal stiffness matrix method of solution can be optionally used. The following features of the SAMSON code were used to obtain the solutions to the 36 dynamic cases.

a. Automatic Generation of Mesh Data

The SAMSON code has a mesh generation capability which allows the user to skip node and element cards in the data deck. The code fills in missing node cards by assuming uniform spacing between the nodes for which data are provided. Missing element cards are generated by assuming that the missing node numbers may be derived from the node numbers of the previous element.

b. Pressure and Force Loadings

Arbitrary time variations in pressure or forces can be specified at nodes. The forces represented by pressures at nodes are computed assuming a linear variation in pressure between nodes along a user-defined surface.

c. Materials

Two types of material constitutive models were used in the analysis, elastic and nonlinear. The elastic model incorporates a linear elastic material which was used to model the concrete cylindrical material for the majority of the cases.

The important parameters that define the elastic cylinder are:

$$E_c = 3000 \text{ ksi (20,700 MPa)}$$

$$\nu_c = 0.2$$

$$\gamma_c = 150 \text{ pcf (2.403 Mg/m}^3\text{), density}$$

The nonlinear soil medium was modeled by using the soil/rock material model (ROCKMT3) described in reference 55. Input to this material model includes the density, loading and unloading bulk moduli and Poisson's ratios, and a failure surface description. The bulk moduli are specified by using a piecewise linear variation to approximate the mean normal stress ($\bar{\sigma}$) and the volumetric strain (ϵ) as shown in figure 13a. Tension stress cutoffs can also be included in the material response. The yield or failure surface is defined by a piecewise linear approximation of the $\sqrt{J_2'}$ versus $\bar{\sigma}$ curve as indicated in figure 13b. Note that only a very simple "single" linear variation was used to approximate the yield surface for the soil models of this investigation. The variables used in the ROCKMT3 material model are defined as:

$$\bar{\sigma} = (\sigma_1 + \sigma_2 + \sigma_3)/3 \quad (12a)$$

$$\epsilon = \epsilon_1 + \epsilon_2 + \epsilon_3 \quad (12b)$$

$$J_2' = \frac{1}{2} (S_1^2 + S_2^2 + S_3^2) \quad (12c)$$

where σ_i and ϵ_i are principal components of stress and strain

$$S_i = \sigma_i - \bar{\sigma}, \text{ deviatoric stresses} \quad (12d)$$

The slope of each piecewise linear material response characteristic curve ($\Delta\bar{\sigma}/\Delta\epsilon$) is the bulk modulus (K) of the material for each state of loading or unloading. Figure 14 gives dynamic uniaxial test results (Ref. 56) that have been used to define simplified

ROCKMT3 stress-strain characteristics for both of the sand material models (A and B) used in the dynamic finite element analyses. It has been tacitly assumed that the unloading/reloading path is parallel to the highest or last slope of the curve, i.e., for $\sigma_1 < -1.5$ ksi (-10.34 MPa). The confined compression moduli (M) for each of the three linear rates used in the approximation are given on the uniaxial data curve. Poisson's ratio for both sand materials (A and B) have been taken as $\nu = 0.25$. Thus an elastic biaxiality ratio of lateral to axial stress is $k = \nu/(1-\nu) = 1/3$. The uniaxial approximation data of figure 14 were used to obtain the figure 13a curves. For example, the $(\bar{\sigma}, \epsilon)$ point at the end of the first linear portion is obtained by application of equation (12a) and (12b) where

$$\begin{aligned}\sigma_1 &= -0.5 \\ \sigma_2 &= \sigma_3 = k\sigma_1 = -0.5/3 \\ \epsilon_1 &= -0.0167 \\ \epsilon_2 &= \epsilon_3 = 0\end{aligned}$$

There results

$$\begin{aligned}\bar{\sigma} &= (1+2k)\sigma_1/3 \\ &= -0.279\end{aligned}\tag{13a}$$

$$\begin{aligned}\epsilon &= \epsilon_1 \\ &= -0.0167\end{aligned}\tag{13b}$$

Thus the volumetric strains at the break points on the piecewise linear $\bar{\sigma}$ versus ϵ curve are the same as the axial strains (ϵ_1) for the uniaxial approximation. The bulk modulus (K) is computed from the modulus of confined compression (M) from equations (13a,13b).

There results

$$\begin{aligned}K &= M(1+2k)/3 \\ &= \frac{5}{9} M\end{aligned}\tag{13c}$$

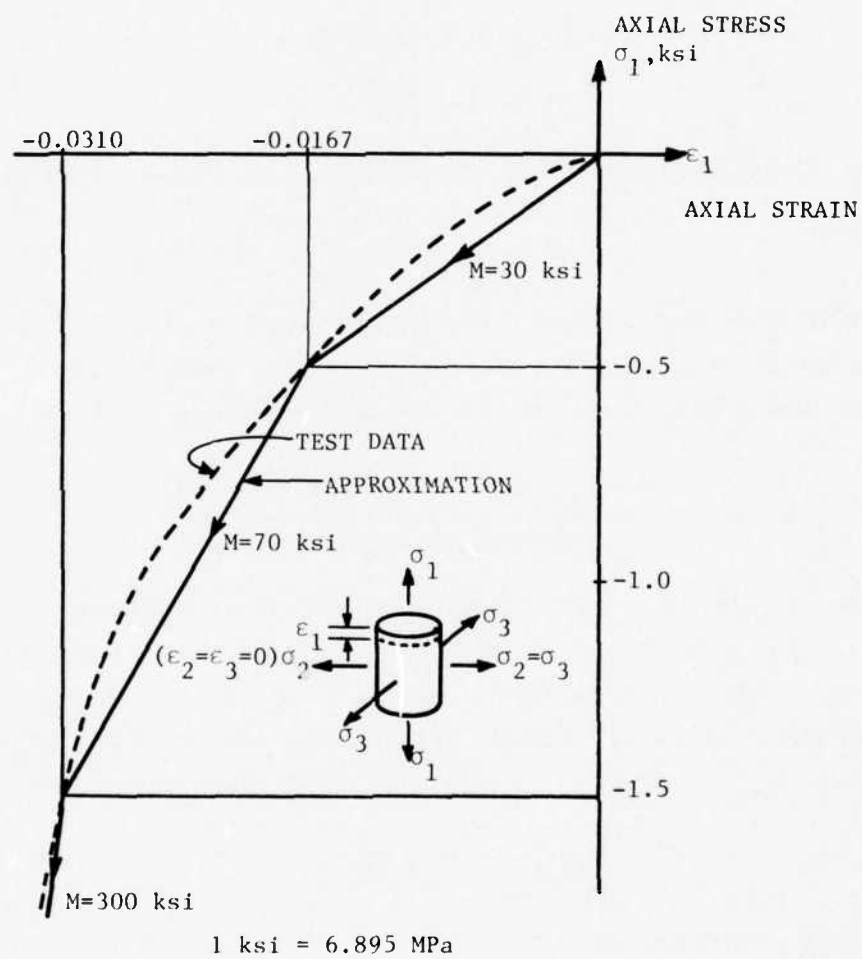


Figure 14. Dynamic Uniaxial Data - Dense Dry Sand

Referring to figure 15, the relationship between the $\sqrt{J_2'}$ versus $\bar{\sigma}$ failure surface and the angle of internal friction (ϕ) and cohesion (c) of the material is now determined. Consider a triaxial shear test state of stress (figure 15a) where the axial pressure is p_1 and the hydrostatic lateral pressures are $p_2 = p_3$ where $p_i = -\sigma_i$. The stress state on any plane from the vertical plane (θ) is

$$p = p_1 \cos^2 \theta + p_3 \sin^2 \theta \quad (14a)$$

$$\begin{aligned} \tau &= (p_1 - p_3) \cos \theta \sin \theta \\ &= 0.5 (p_1 - p_3) \sin 2\theta \end{aligned} \quad (14b)$$

The Coulomb-Mohr law for shear failure (figure 15c) can be written as

$$\tau = c + p \tan \phi \quad (14c)$$

where c and ϕ are determined from the envelope of the Mohr diagram circles drawn from the triaxial shear tests. Substituting equations (14a) and (14b) into (14c) and rearranging terms yields

$$p_1 = \frac{c + p_3 (\sin \theta \cos \theta + \sin^2 \theta \tan \phi)}{\sin \theta \cos \theta - \cos^2 \theta \tan \phi} \quad (15a)$$

The critical plane (θ_{cr}) is found when p_1 is a minimum to cause failure; and p_1 is a minimum when the denominator of equation (15a) is a maximum. This occurs when the rate of change of the denominator with respect to θ is zero. Performing the indicated operation on the denominator results in the well known solution of

$$\theta_{cr} = \frac{\phi}{2} + 45^\circ \quad (15b)$$

From elementary trigonometry

$$\begin{aligned} \tan \phi &= \cot(90 - \phi) \\ &= -\cot(90 + \phi) \\ &= -\cot 2\theta_{cr} \end{aligned} \quad (15c)$$

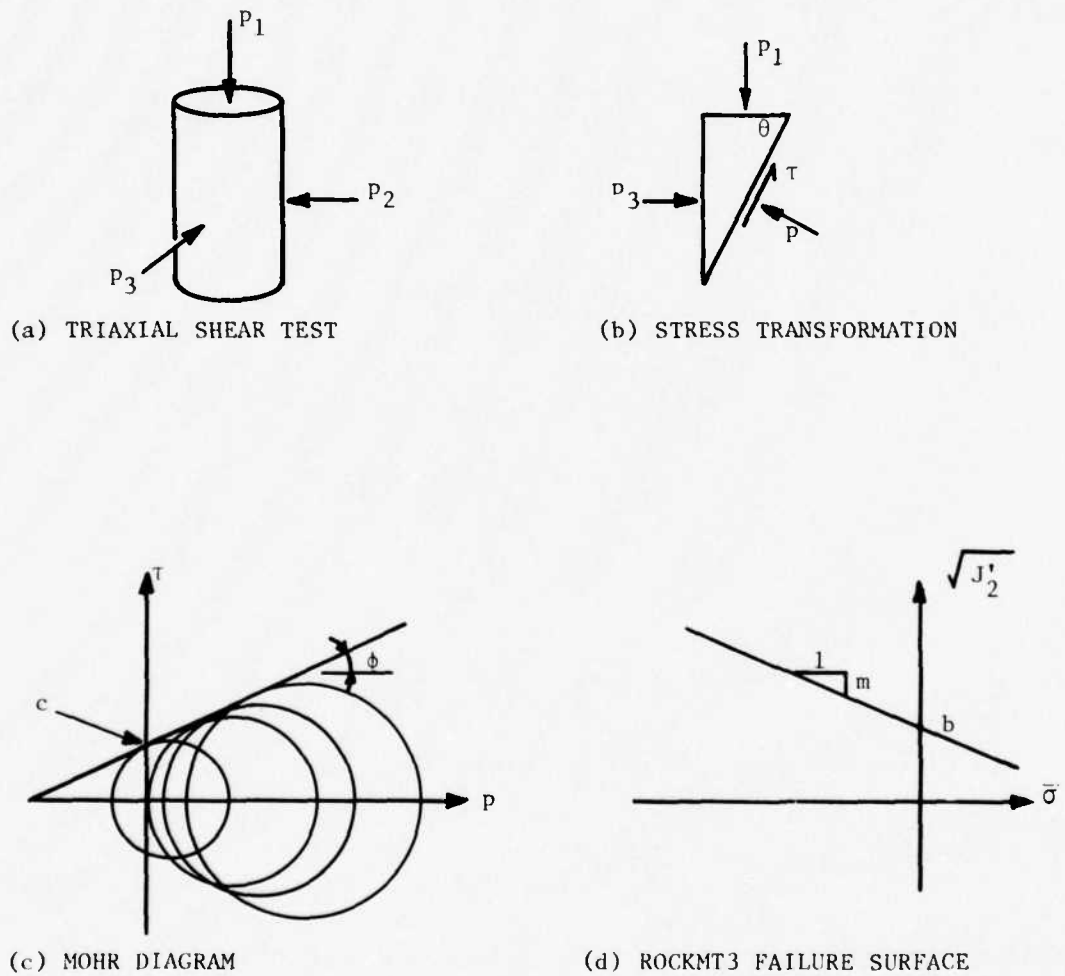


Figure 15. Coulomb-Mohr Shear Strength Parameters Compared with ROCKMT3 Parameters

Using equation (15b) for θ in equation (15a) and also employing equation (15c) and multiplying the numerator and denominator of the equation (15a) by $2 \tan \theta_{cr}$, it can be shown, by using the trigonometric identity $\cot 2\theta = (1 - \tan^2 \theta) / (2 \tan \theta)$, that

$$p_1 = 2c \tan(\frac{\phi}{2} + 45) + p_3 \tan^2(\frac{\phi}{2} + 45) \quad (15d)$$

For triaxial tests, the principal stresses are the axial ($\sigma_1 = -p_1$) and the hydrostatic lateral stress ($\sigma_2 = \sigma_3 = -p_2 = -p_3$); therefore,

$$\bar{\sigma} = -\frac{1}{3} (p_1 + 2p_3) \quad (16a)$$

$$\begin{aligned} S_1 &= \sigma_1 - \bar{\sigma} \\ &= \frac{2}{3} (\sigma_1 - \sigma_3) \end{aligned}$$

$$\begin{aligned} S_2 &= S_3 = \sigma_3 - \bar{\sigma} \\ &= -\frac{1}{3} (\sigma_1 - \sigma_3) \\ &= -\frac{1}{2} S_1 \end{aligned}$$

$$\begin{aligned} J_2' &= \frac{1}{2} (S_1^2 + 2S_2^2) \\ &= \frac{1}{3} (\sigma_1 - \sigma_3)^2 \end{aligned}$$

$$\sqrt{J_2'} = (p_1 - p_3) / \sqrt{3} \quad (16b)$$

Substituting equation (15d) into (16a) and defining

$$t = \tan(\frac{\phi}{2} + 45) \quad (16c)$$

yields the following expression for the lateral pressure,

$$p_3 = -(3\bar{\sigma} + 2ct) / (2 + t^2) \quad (16d)$$

Solving for p_1 from equation (16a) and then using this result and equation (16d) in (16b) gives

$$\sqrt{J'_2} = \sqrt{3} \left(\frac{1-t^2}{2+t^2} \right) \bar{\sigma} + 2\sqrt{3} \left(\frac{t}{2+t^2} \right) c \quad (17a)$$

Referring to figure 15d it is observed that equation (17a) is of the form $y = mx + b$ where b is the intercept of the straight line with the $\sqrt{J'_2}$ axis and m is the slope of the line. From equation (17a)

$$m = \sqrt{3} \left(\frac{1-t^2}{2+t^2} \right) \quad (17b)$$

$$b = 2\sqrt{3} \left(\frac{t}{2+t^2} \right) c \quad (17c)$$

For both of the sand materials considered (figure 13b), the slope of the failure surface is $m = -0.85$. Using this value in equation (17b) and solving for t and then using equation (16c) to calculate the conventional angle of internal friction (ϕ) yields

$$\phi = 36.234^\circ, \text{ soil materials A and B}$$

Since $b = 0$ for the sand material (A), the cohesion (c) is zero by equation (17c). However $b = 0.1$ ksi (0.6895 MPa) for the cemented sand material (B) and this results in a cohesion magnitude of

$$c = 0.0862 \text{ ksi (0.5943 MPa), soil material B}$$

$$c = 0, \text{ soil material A}$$

A soil density of $\gamma = 109.6$ pcf (1.756 Mg/m^3) was used for both materials.

The nonlinear reinforced concrete cylinder used for cases 34 and 36 was modeled by also using the ROCKMT3 material model. A fiber reinforced concrete material with 1 percent steel (Ref. 57) has been selected for this liner idealization. Figure 16 gives the material characteristics for this model.

d. Damping

The SAMSON Code provides an option for incorporating both linear damping, proportional to the strain rate in an element, and nonlinear damping, proportional to the square of the strain rate. Both

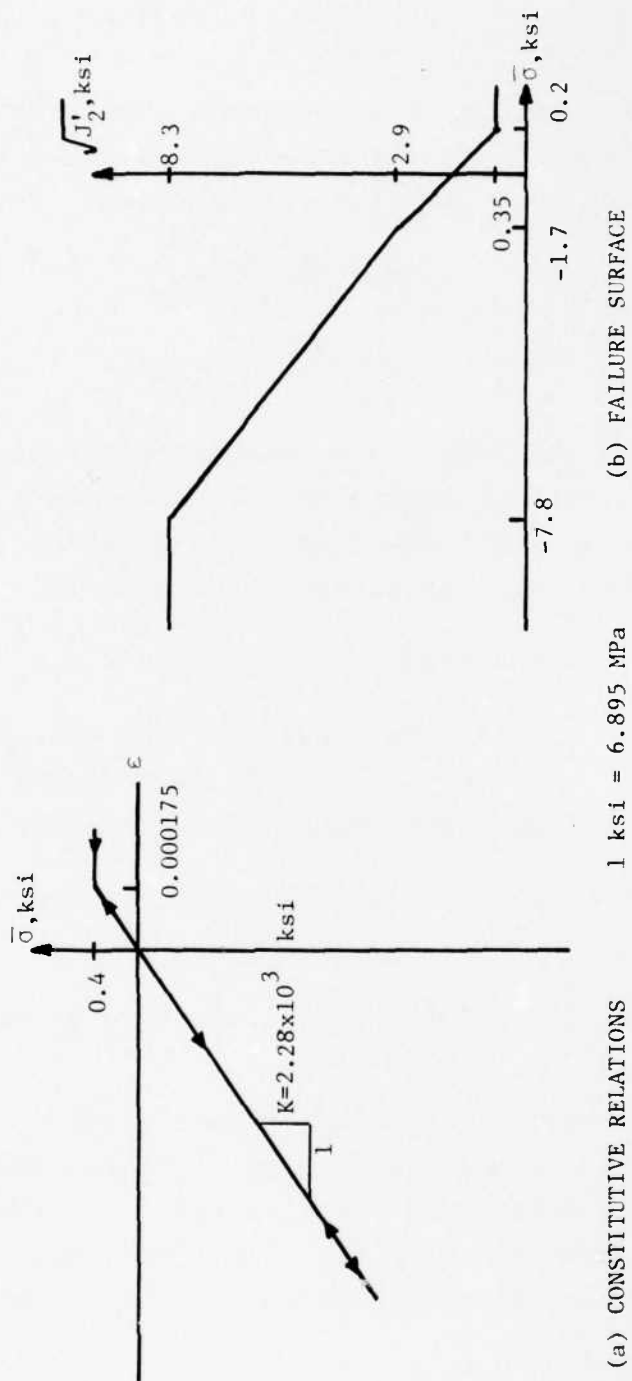


Figure 16. Nonlinear R/C Liner (1% Steel) ROCKMT3 Parameters

types of damping consist of a hydrostatic component and a deviatoric component which may be applied separately or in combination. The following damping parameters have been found to yield good results for buried structure dynamic analyses by AFWL personnel.

(1) Linear Coefficients

$$b_1 = 0.04, \text{ hydrostatic}$$

$$b_2 = 0.02, \text{ deviatoric}$$

(2) Nonlinear Coefficients

$$b_3 = b_4 = 2.0, \text{ hydrostatic and deviatoric}$$

Coefficients b_1 and b_2 are approximately the fractions of critical damping.

e. Finite Element Model

The finite element models of the soil media for the two depths of burial considered ($h/R = 0.5$ and 4.0) are shown in figures 17 and 18. These meshes are very similar to the static analysis meshes (figures 7 and 10) except more refinement of the gridwork has been used in certain portions and the entire mesh is composed of triangular and rectangular elements. The latter is required since the SAMSON code does not have a general quadrilateral finite element capability. The added mesh refinement was incorporated, especially between the ground surface and the tunnel liner, so that the airblast induced stress wave traversing through the soil would not be unduly modified by abrupt element size discontinuities.

The left and right boundaries of each mesh are free to move vertically, and the lower boundary is free to move horizontally. The lower boundary is sufficiently removed from the cylindrical liner so that reflected waves from this boundary do not reach the structure in the time of interest for the short duration airblast loads (0.015 sec). For the long duration loads (0.060 sec) additional elements were added to the lower portion of the mesh to extend the lower boundary by two outside tunnel liner diameters or by $4.0 R$.

Mesh 4DS (liner not shown)

354 Nodes
608 Elements

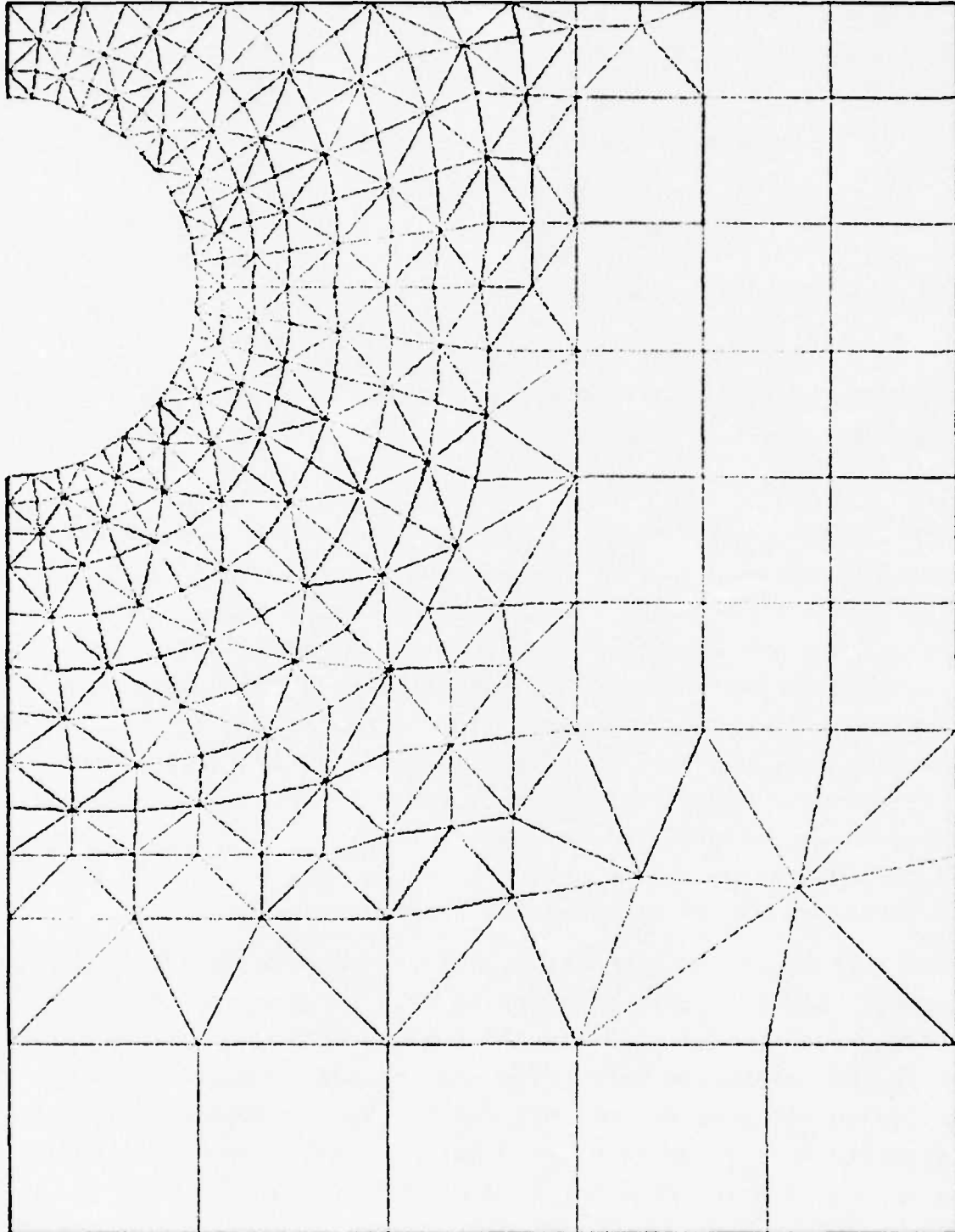


Figure 17. Finite Element Mesh of Soil
for SAMSON Dynamic Analysis ($h/R = 0.5$)

Mesh 5DS (liner not shown) 510 Nodes
799 Elements

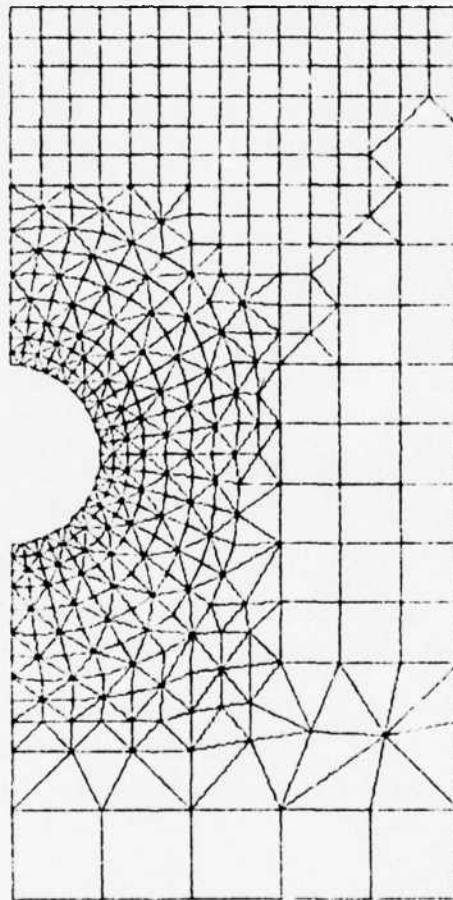


Figure 18. Finite Element Mesh of Soil
for SAMSON Dynamic Analysis ($h/R = 4.0$)

Triangular finite elements have also been used to model each of the tunnel liners. The outer nodes of the liner mesh were attached to the soil mesh so that no relative motion was permitted at the soil-structure interface. In an effort to comprehensively model both the membrane and the bending deformations of the tunnel, the liner thickness was subdivided by four layers of equal thickness. The circumference was subdivided by rays at 7.5 deg increments, which yields 24 equal divisions for the 180 deg half-model of the liner. This results in $4 \times 24 = 96$ cells requiring two triangular elements per cell for a total of $2 \times 96 = 192$ elements to model each tunnel liner. Figure 19 shows the resulting finite element mesh for the most flexible liner ($R/t = 15$) and a portion of the soil media mesh. Each of the 24 circumferential liner subdivisions has been numbered as indicated on this figure for future reference in the numerical solutions. The finite element mesh for the stiff tunnel liner ($R/t = 4$) is defined in the same way as the flexible liner (i.e., four subdivisions through the thickness and 24 circumferential segments requiring 192 triangular elements) with the obvious difference that the node points are further apart, through the thickness, to model the increased liner thickness.

As previously noted, an inside radius of the tunnel liner of 6.56 ft (2 m) was maintained for all of the SAMSON numerical solutions. This was implemented by providing basic mesh node point data so that the radius to the soil-structure interface was 1.0 and then applying an appropriate scale factor to the coordinates, within the SAMSON code, so that the inside radius of the liner was 6.56 ft (2 m).

f. SAMSON Modifications

The output element stresses in the computer code are related to the vertical (z) horizontal (x) coordinate system. The SSI stresses and the tunnel liner internal force resultants are the desired solution results. To facilitate this, program modifications were made such that the element stresses are referred to the radial (r) and circumferential (θ) coordinates for the elements of interest, i.e., the 192 tunnel liner elements and the 48 triangular soil elements in

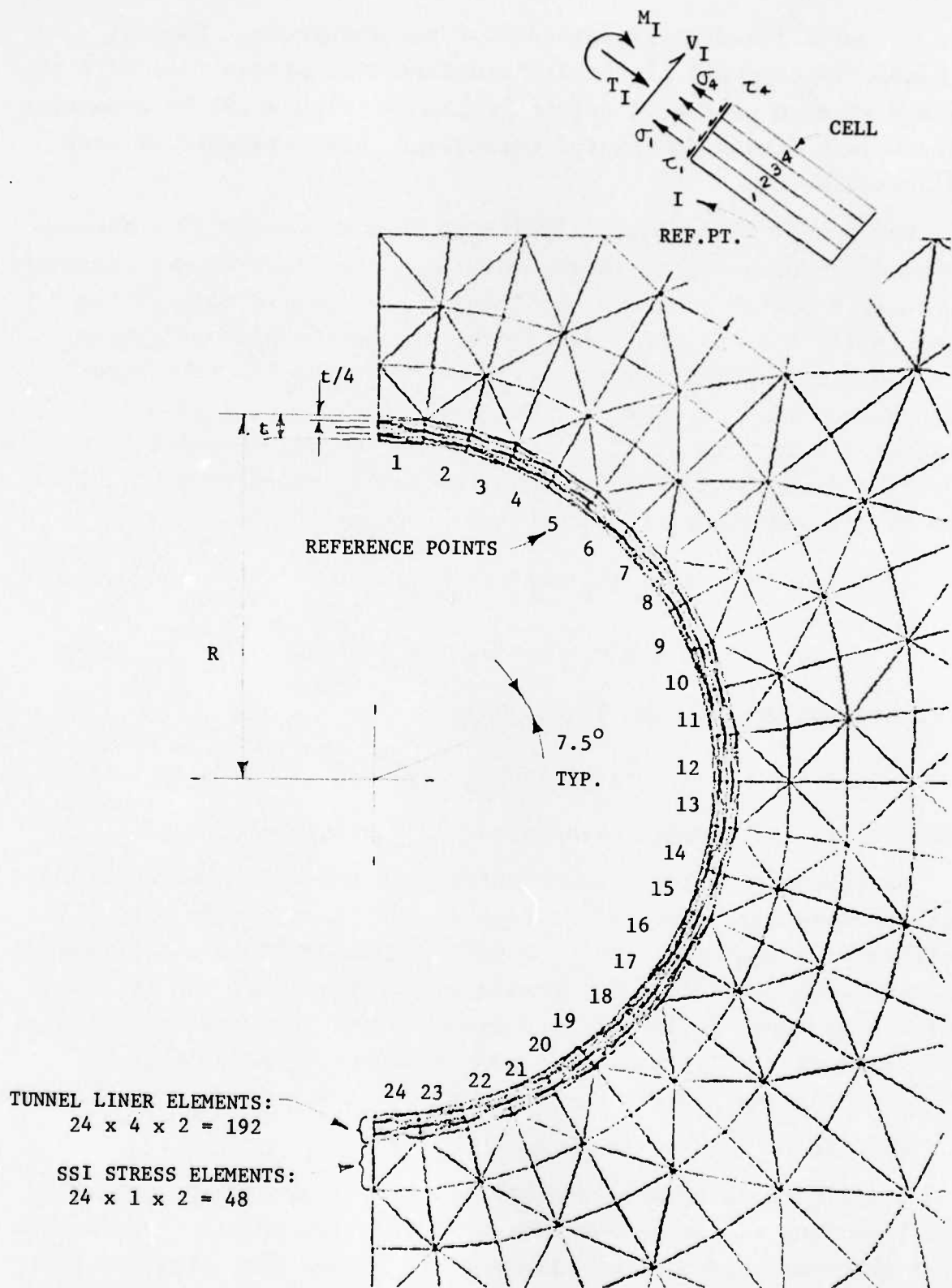


Figure 19. Tunnel Liner Mesh for SAMSON Dynamic Analysis ($R/t = 15$)

the 24 cells immediately adjacent to the structure. The SSI stresses ($\sigma_r, \tau_{r\theta}$) and also the circumferential stress (σ_θ) were obtained at each of the 24 reference points (figure 19) by computing the average stress in the two triangular soil elements at each reference point.

The tunnel liner force resultants (M,T,V) at the 24 reference points were computed by first converting the liner element stresses to the r, θ system and then obtaining the stress in each of the four cells, through the liner thickness, as the average stress of the two triangular elements in the cell. Referring to figure 19 denote the hoop stress, σ_θ , for each of the four cells at a given reference point, I, as $\sigma_1, \sigma_2, \sigma_3, \sigma_4$ where the subscripts 1 through 4 correspond to the inner through outer cells, respectively. Then the thrust and moment at the reference point can be computed as

$$T = -(\sigma_1 + \sigma_2 + \sigma_3 + \sigma_4) t/4 \quad (18a)$$

$$M = (3\sigma_1 + \sigma_2 - \sigma_3 - 3\sigma_4) t^2/32 \quad (18b)$$

In a similar manner, the liner shear is

$$V = -(\tau_1 + \tau_2 + \tau_3 + \tau_4) t/4 \quad (18c)$$

where τ_i is the average shear stress ($\tau_{r\theta}$) in the i th cell.

Nondimensional liner force resultants and also nondimensional SSI stresses were computed at each of the 24 reference points at uniform time increments (Δt_{out}) during the SAMSON solution. These results were written on a magnetic tape for each of the 36 cases for use as input to the postprocessor codes. For the more flexible liner ($R/t = 15$) cases the results were stored on tape at $\Delta t_{out} = 0.1$ msec and for the liner with $R/t = 4$, $\Delta t_{out} = 0.075$ msec.

3. RESULTS OF DYNAMIC (SAMSON) SOLUTIONS

A postprocessing code was written to facilitate the processing and reporting of the SAMSON numerical solution results. Both tabular printout and plotted time history curves were obtained for all 36 cases. All of the results are nondimensional, and any

future reference to the liner internal forces and SSI stresses refers to the nondimensional values unless otherwise stated.

Nondimensional Liner Force Resultants

Thrust, $T/p_o R \rightarrow T$

Moment, $M/p_o R^2 \rightarrow M$

Shear, $V/p_o R \rightarrow V$

Nondimensional SSI Stresses

Radial, $\sigma_r/p_o \rightarrow \text{STR-R}$

Circumferential, $\sigma_\theta/p_o \rightarrow \text{STR-T}$

Shear, $\tau_{r\theta}/p_o \rightarrow \text{TAU-RT}$

The majority of the tabulated and plotted results for the 36 cases defined in table IV are presented in volume II of this report. The results are grouped for each case, and the tables are presented first followed by the GOULD plotted curves. Each table and graph in volume II contains information to identify the data and the case number.

The results for case 5 are presented at this point to illustrate the kind of information that has been obtained for all cases.

a. Peak Response Results

The minimum and maximum values of the nondimensional liner internal force resultants and the SSI nondimensional stresses that occurred at each of the 24 reference points during the complete solution history are presented in table V. Reference points 1, 12, and 24 are denoted as the crown, springline and invert points; however, they actually refer to the center of the segment that is closest to the $\theta = 0, 90, \text{ and } 180$ deg points.

Figures 20a through 20f give curves of the maximum and minimum results of table V. In these figures, the abscissa title Liner-Pt. is the same as the 24 reference points (see figure 19) around the tunnel liner.

b. Modal History Results

As previously discussed, the structural system and the loading environment for the cases considered in this project are symmetric about a vertical plane through the longitudinal axis of the

Table V
MINIMUM AND MAXIMUM NONDIMENSIONAL LINER
FORCE RESULTANTS (T,M,V) AND SSI STRESSES ($\sigma_r, \sigma_\theta, \tau_{r\theta}$) CASE 5

MIN, VALULS

		T	M	V	STR-R	STR-T	TAU-RT
CR	1	-.040613	-.0143650	-.063124	-1.774550	-.606920	-.097641
	2	-.026475	-.0134288	-.138412	-1.640147	-.550174	-.093637
	3	-.018911	-.0114872	-.231459	-1.448520	-.532477	-.118864
	4	-.038226	-.0104900	-.287636	-1.315900	-.420579	-.211325
	5	-.040031	-.0090779	-.319110	-1.042376	-.427643	-.110643
	6	-.044756	-.0194173	-.354016	-.980272	-.380161	-.133454
	7	-.061458	-.0350598	-.336338	-.664439	-.371048	-.025705
	8	-.060277	-.0489208	-.333302	-.546171	-.341634	-.049141
	9	-.056465	-.0615459	-.319199	-.534161	-.271294	-.086594
	10	-.049060	-.0712308	-.290147	-.477970	-.256816	-.118566
	11	-.046686	-.0785453	-.268366	-.407752	-.278492	-.173515
SPR	12	-.044009	-.0844685	-.232850	-.539892	-.267731	-.254487
	13	-.041699	-.0887611	-.152208	-.390217	-.105323	-.258710
	14	-.040014	-.0959391	-.038785	-.439549	-.242540	-.316320
	15	-.050987	-.0934658	-.046446	-.472596	-.224526	-.287552
	16	-.060280	-.0839811	-.067939	-.488064	-.303547	-.306009
	17	-.027408	-.0647784	-.072204	-.489176	-.148677	-.308321
	18	-.015671	-.0387692	-.056636	-.461635	-.258053	-.314812
	19	-.018515	-.0070030	-.054868	-.503693	-.209061	-.326951
	20	0.000000	-.0051808	-.103205	-.450255	-.183309	-.344719
	21	-.082415	-.0085961	-.091643	-.515492	-.170401	-.217094
	22	-.153452	-.0124597	-.119027	-.564544	-.208227	-.173006
	23	-.216547	-.0197450	-.084208	-.631070	-.239533	-.177946
INV	24	-.249184	-.0237359	-.044605	-.653144	-.255843	-.039630

MAX, VALULS

		T	M	V	STR-R	STR-T	TAU-RT
CR	1	.604221	.0598346	.036298	.009330	.057991	.096014
	2	.625507	.0563811	.053802	.083039	.050160	.240796
	3	.689656	.0533775	.065637	0.000000	.103460	.384267
	4	.737775	.0451568	.051813	.056673	.069951	.275098
	5	.809896	.0386171	.068426	.001746	.036241	.349676
	6	.880002	.0277277	.062460	.009462	.027919	.279468
	7	.918283	.0131877	.067314	.058662	.033140	.343141
	8	.939720	.0072914	.061531	0.000000	.024771	.188969
	9	.925684	.0092612	.063631	0.000000	.030786	.323413
	10	.888232	.0113297	.047134	.028240	0.000000	.185413
	11	.829997	.0141341	.154342	0.000000	0.000000	.061694
SPR	12	.756888	.0157613	.195038	.085960	0.000000	.068750
	13	.672518	.0165160	.228144	.065613	.013636	.000000
	14	.601492	.0160766	.255018	.054756	0.000000	.000000
	15	.585564	.0138029	.267119	.051871	.039590	0.000000
	16	.538580	.0095912	.296232	.030859	.065279	.158177
	17	.514104	.0097481	.327757	0.000000	.053388	.082567
	18	.443471	.0170358	.402193	.053870	.026589	.217629
	19	.346488	.0242057	.439213	0.000000	.059688	.196760
	20	.262098	.0344694	.423137	.006090	.045999	.103762
	21	.240801	.0548387	.389176	.026557	.100455	.088967
	22	.235163	.0802028	.288690	.037808	.165643	.057986
	23	.230308	.0969140	.203941	.023198	.171096	.000000
INV	24	.230069	.1056470	.078171	0.000000	.195450	.041969

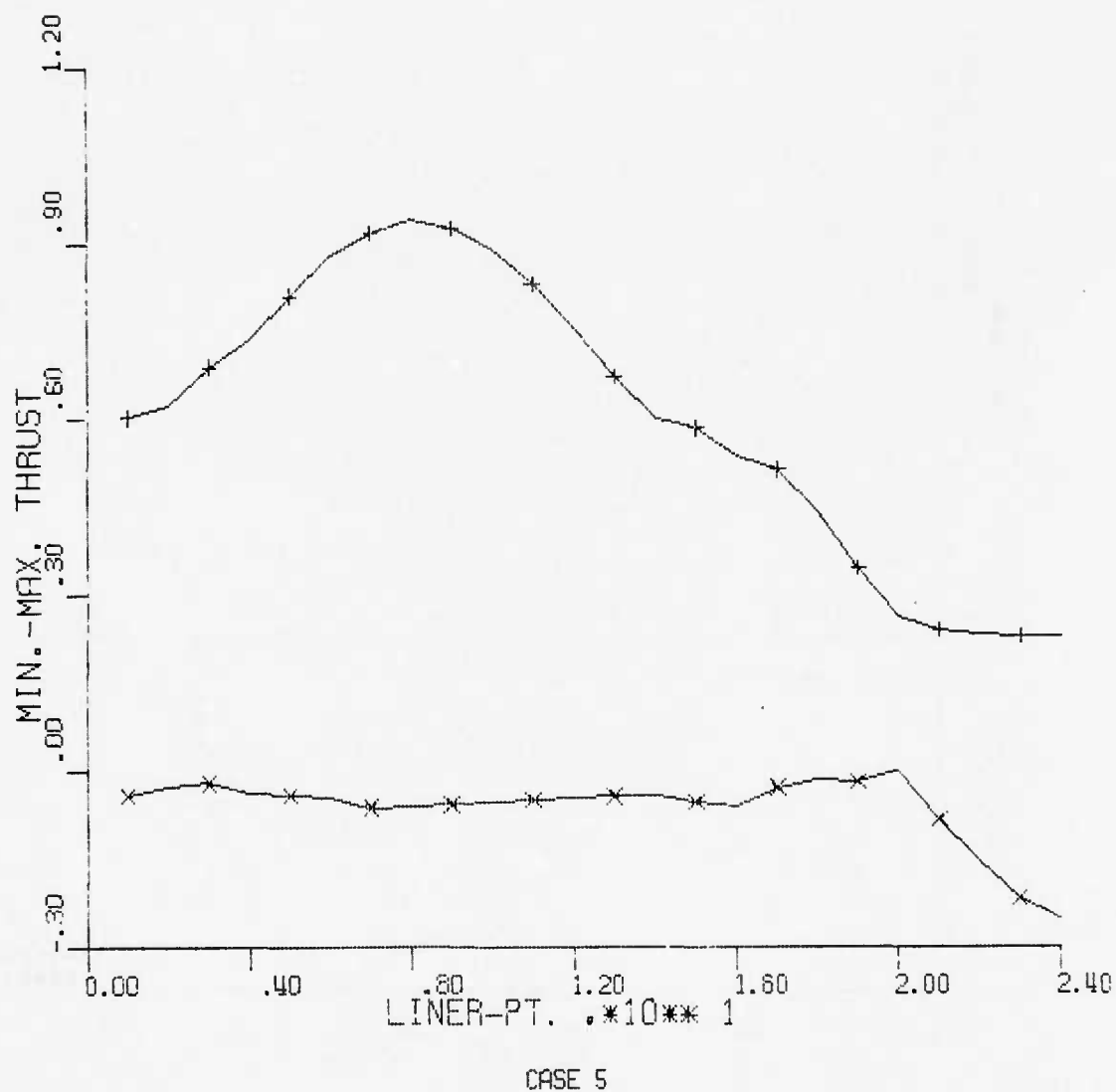
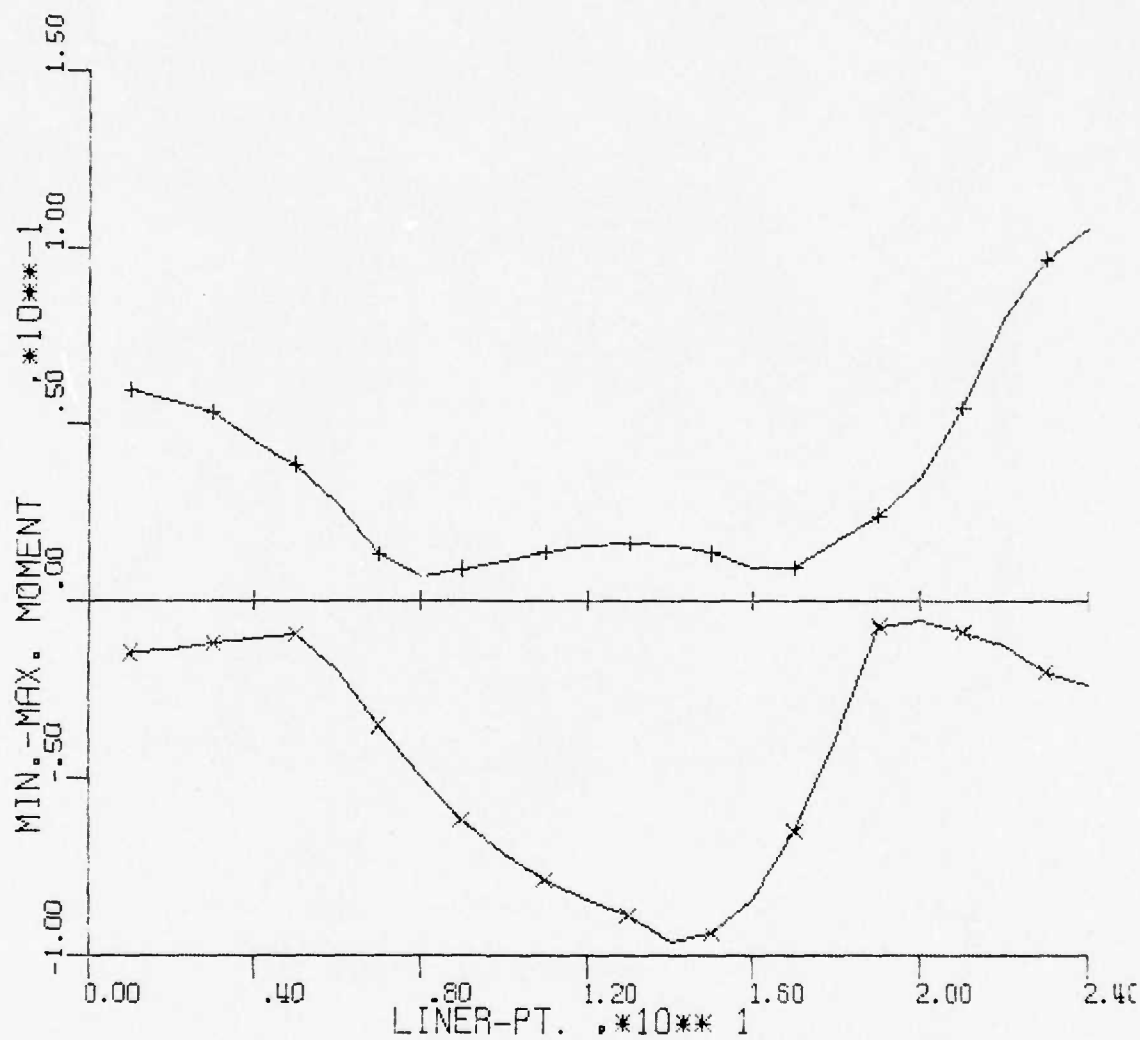
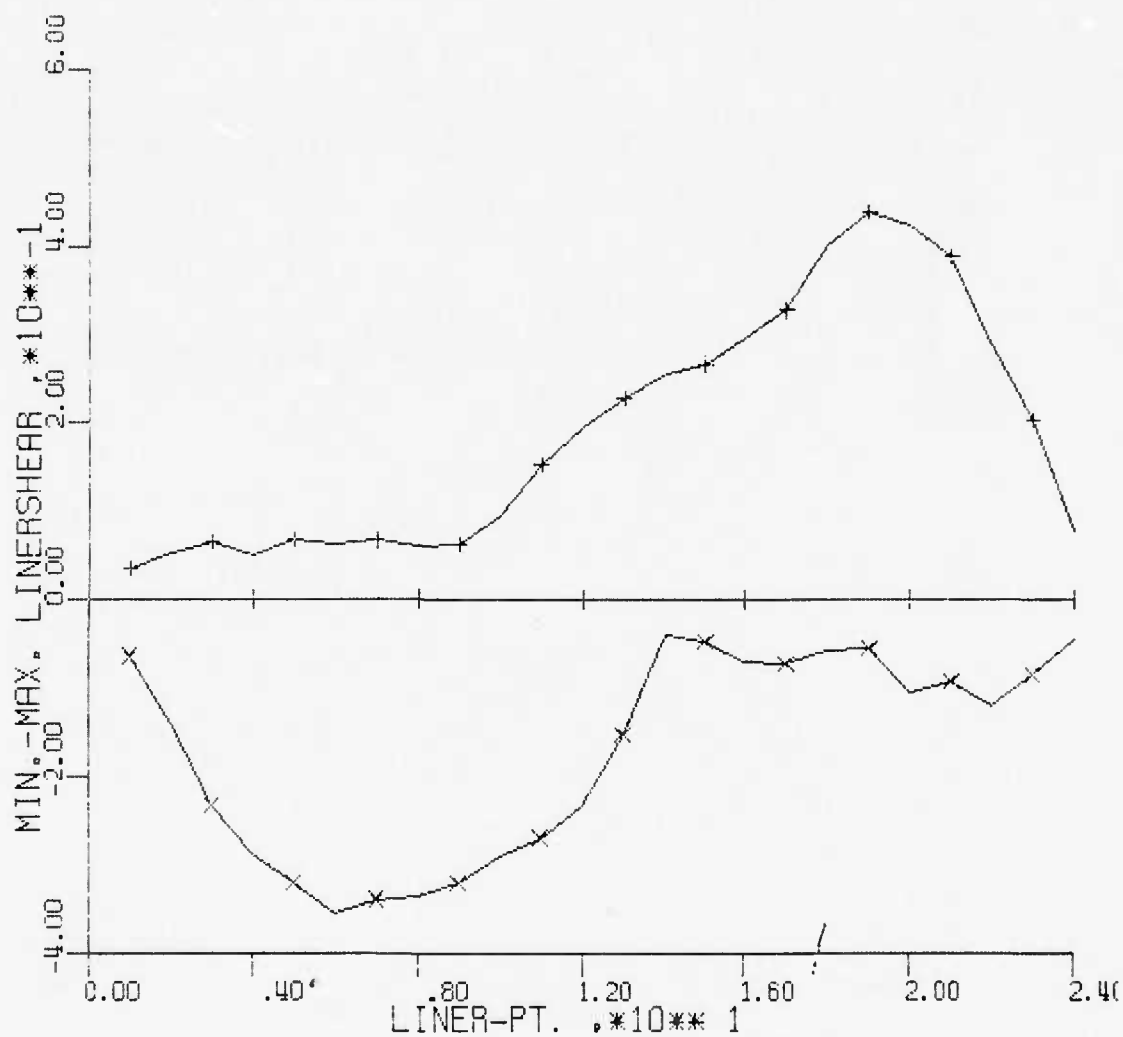


Figure 20a. Minimum and Maximum Nondimensional Thrust Variation around Liner, Case 5



CASE 5
 Figure 20b. Minimum and Maximum Nondimensional Moment
 Variation around Liner, Case 5



CASE 5

Figure 20c. Minimum and Maximum Nondimensional Shear Variation around Liner, Case 5

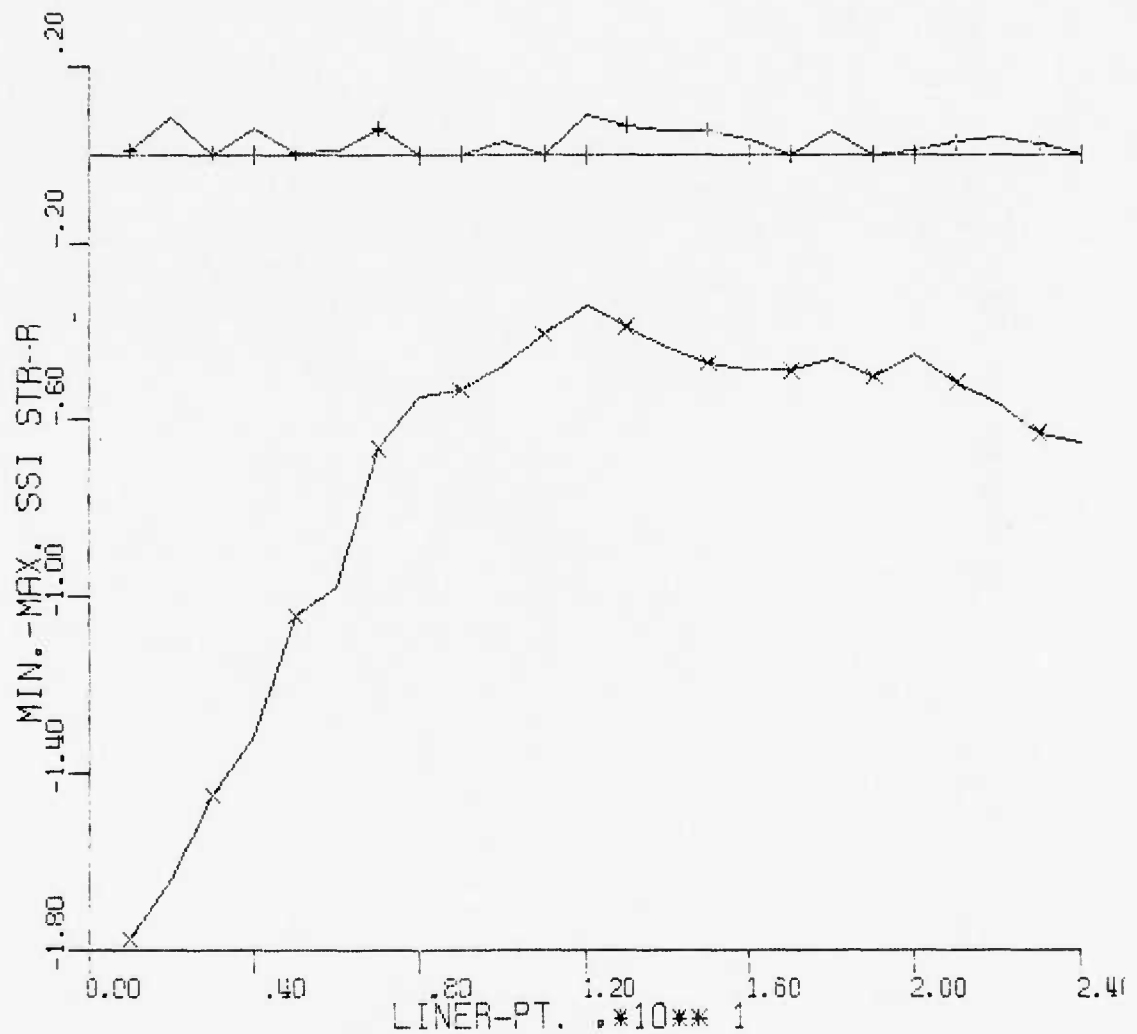
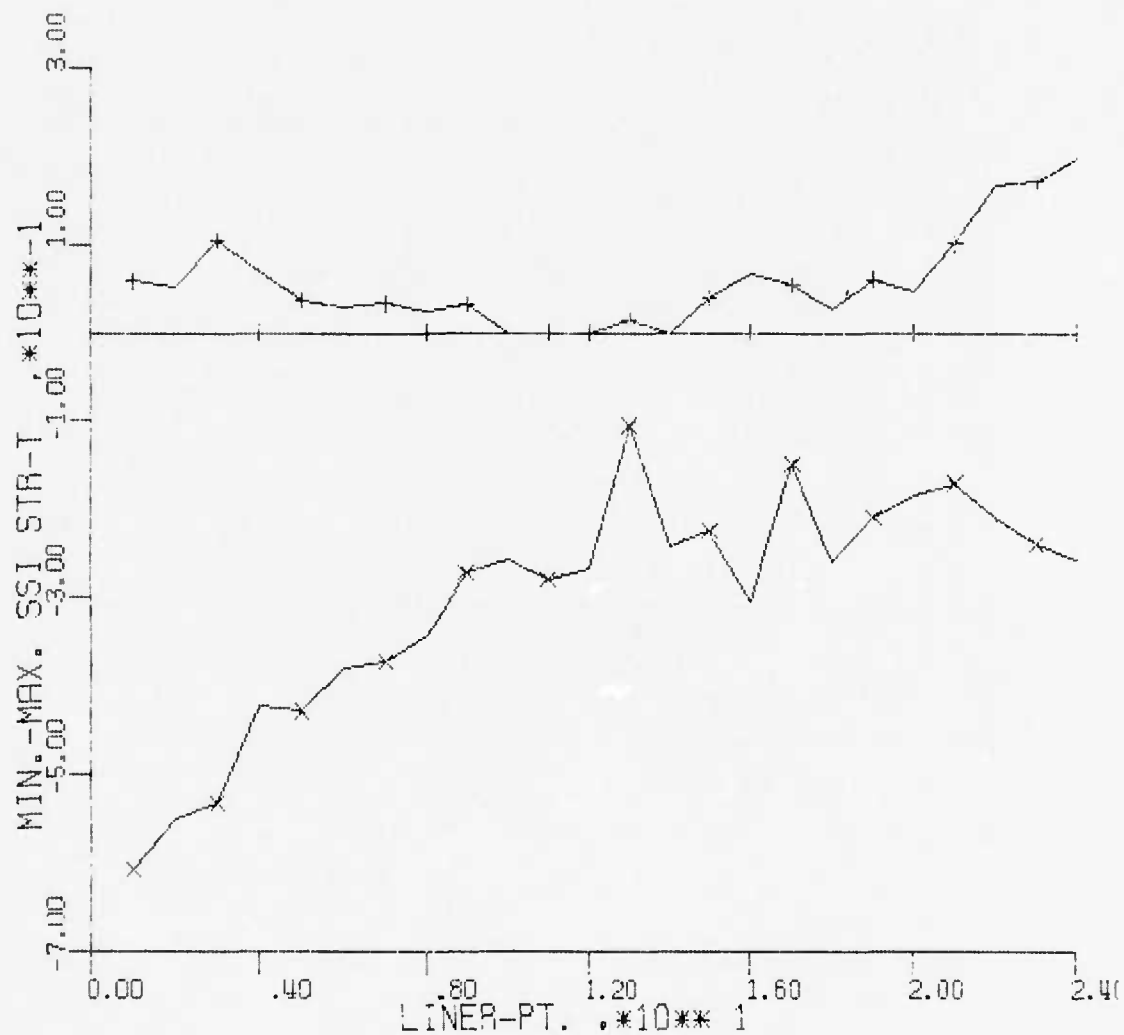
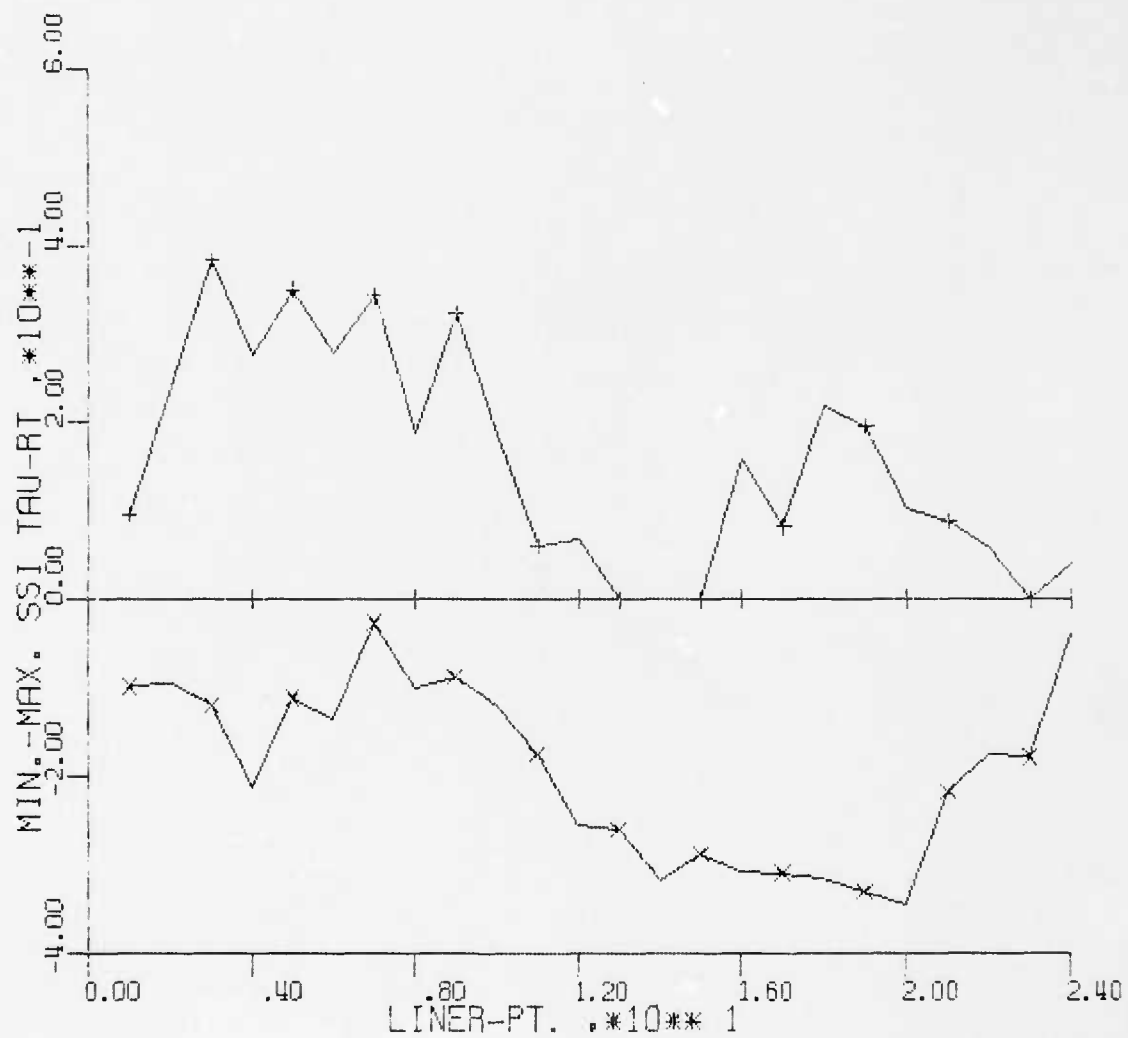


Figure 20d. Minimum and Maximum SSI Nondimensional Radial Stress Variation around Liner, Case 5



CASE 5

Figure 20e. Minimum and Maximum SSI Nondimensional Circumferential Stress Variation around Liner, Case 5



CASE 5

Figure 20f. Minimum and Maximum SSI Nondimensional Shear Stress Variation around Liner, Case 5

tunnel. Therefore, the radial and circumferential motions of the structure are symmetric and antisymmetric, respectively, with respect to the plane of symmetry. The liner thrust and moment and the SSI radial and circumferential stresses are symmetric, and the liner shear and SSI shear stresses are antisymmetric. Therefore, each response variable of interest can be represented by an appropriate Fourier sine or cosine series. Referring to figure 21 these responses can be represented as follows.

(1) Symmetric Response (S)

$$s(t, \theta) = \frac{S_0(t)}{2} + \sum_{n=1}^{\infty} S_n(t) \cos n\theta \quad (19a)$$

where $S_n \equiv S_n(t)$ are the time dependent modal amplitude histories. Variables that can be represented in this manner are the liner thrust and moment and the soil media radial and circumferential stresses at the SSI interface. The modal amplitudes (S_n) are evaluated by multiplying equation (19a) by $\cos n\theta$ and integrating from $\theta = 0$ to π , and results in

$$\begin{aligned} \int_0^{\pi} S(t, \theta) \cos n\theta \, d\theta &= S_n \int_0^{\pi} \cos^2 n\theta \, d\theta \quad n > 0 \\ &= \frac{\pi}{2} S_n \end{aligned}$$

Therefore

$$S_n = \frac{2}{\pi} \int_0^{\pi} S(t, \theta) \cos n\theta \, d\theta \quad (19b)$$

At any time step t in the solution, the variable $S(t, \theta)$ is known at the 24 discrete reference points around the tunnel liner. Denoting these magnitudes at the 24 reference points (θ_i) as $S(t, \theta_i)$, the right-hand side of equation (19b) can be numerically integrated, and the modal amplitude is

$$S_n = \frac{2}{\pi} \Delta\theta \sum_{i=1}^{24} S(t, \theta_i) \cos n\theta_i, \quad n > 0 \quad (19c)$$

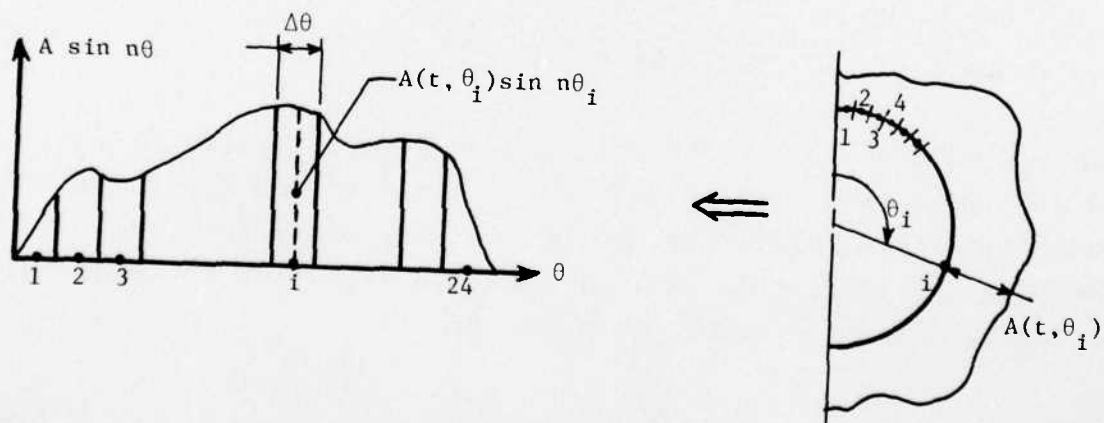
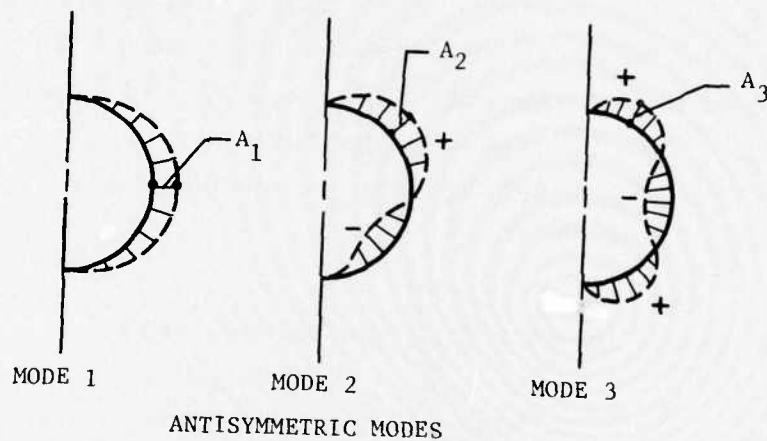
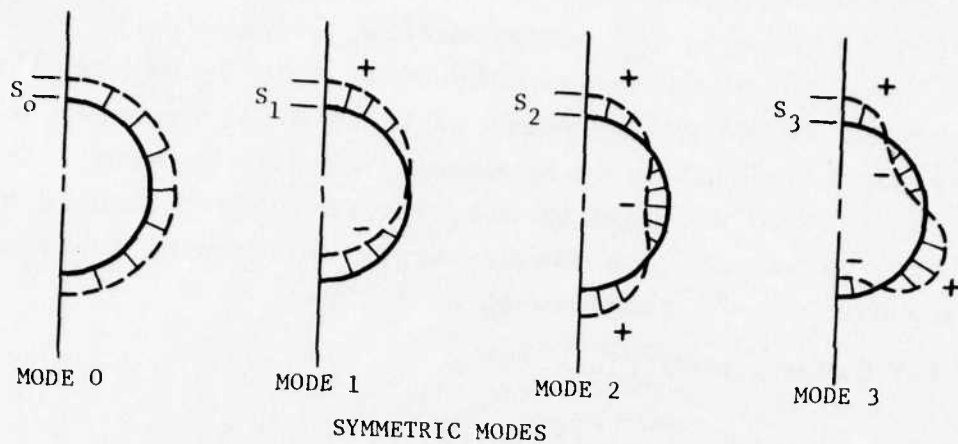


Figure 21. Notation for Modal Amplitudes from Dynamic (SAMSON) Results

The zero mode amplitude is given by

$$S_0 = \frac{2}{\pi} \Delta\theta \sum_{i=1}^{24} S(t, \theta_i) \quad (19d)$$

(2) Antisymmetric Response (A)

$$A(t, \theta) = \sum_{n=1}^{\infty} A_n(t) \sin n\theta \quad (20a)$$

where $A_n \equiv A_n(t)$ are the time dependent modal amplitude histories. Variables that can be represented in this manner are the liner shear force and the soil media shear stresses at the SSI interfaces. The modal amplitudes (A_n) are evaluated by multiplying equation (20a) by $\sin n\theta$ and integrating from $\theta = 0$ to π , and results in

$$A_n = \frac{2}{\pi} \int_0^{\pi} A(t, \theta) \sin n\theta \, d\theta \quad (20b)$$

Following the numerical integration solution process used in the symmetric response analysis, the modal amplitude is obtained from

$$A_n = \frac{2}{\pi} \Delta\theta \sum_{i=1}^{24} A(t, \theta_i) \sin n\theta_i, \quad n > 0 \quad (20c)$$

The above techniques, equations (19c) and (20c), were used to convert the dynamic results obtained from the SAMSON code to modal amplitude histories.

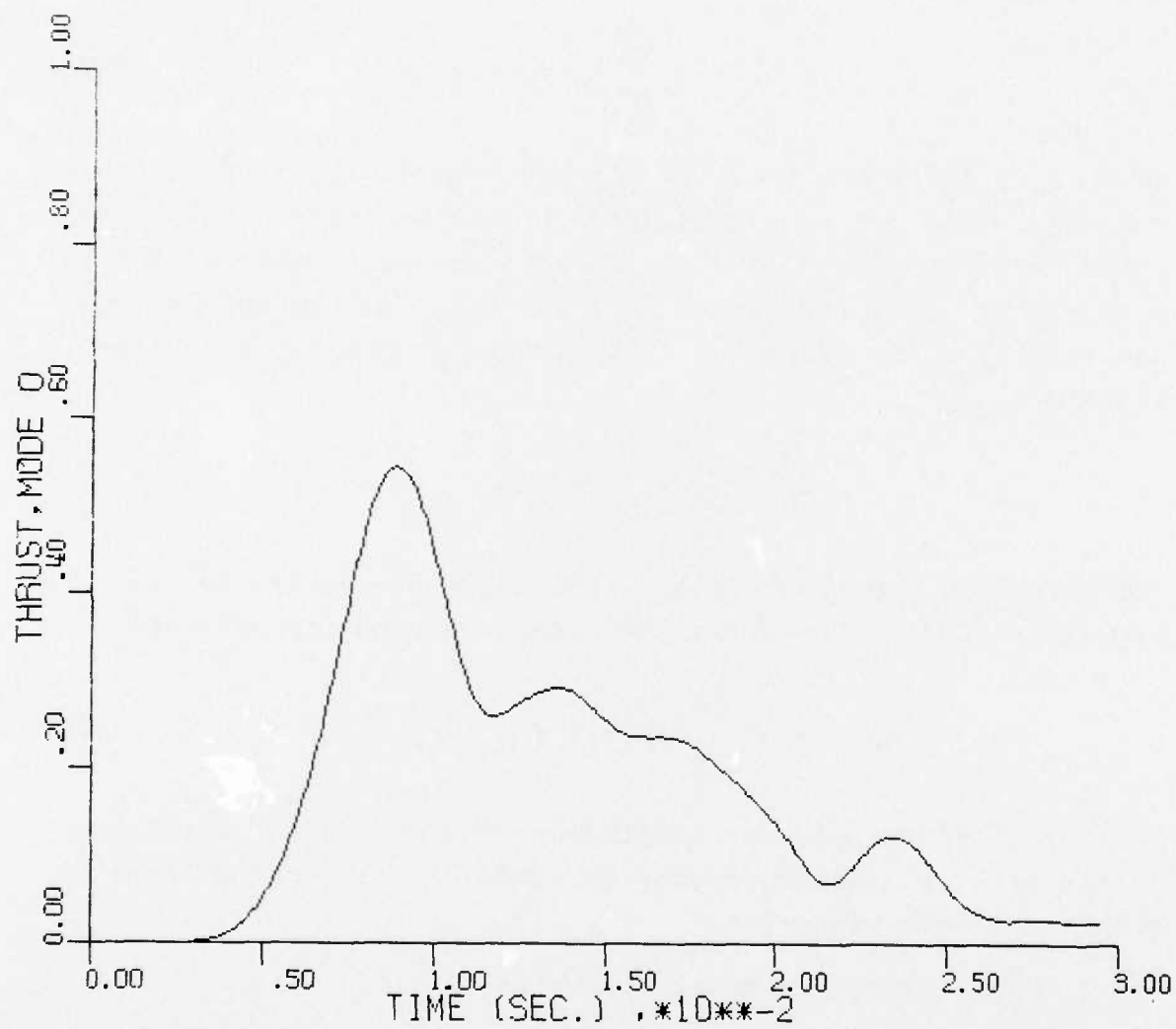
(3) Symmetric Modal Histories

Modal histories were computed for modes 0 through 6 for the following symmetric response variables. The modal history curves for each mode are given in the indicated figures.

Nondimensional Liner Thrust, figure 22 $(S_n \leftarrow T_n/p_o R)$

Nondimensional Liner Moment, figure 23 $(S_n \leftarrow M_n/p_o R^2)$

Nondimensional SSI Radial Stress, figure 24 $(S_n \leftarrow \sigma_{rn}/p_o)$



CASE 5

Figure 22a. Nondimensional Thrust History, Mode 0, Case 5

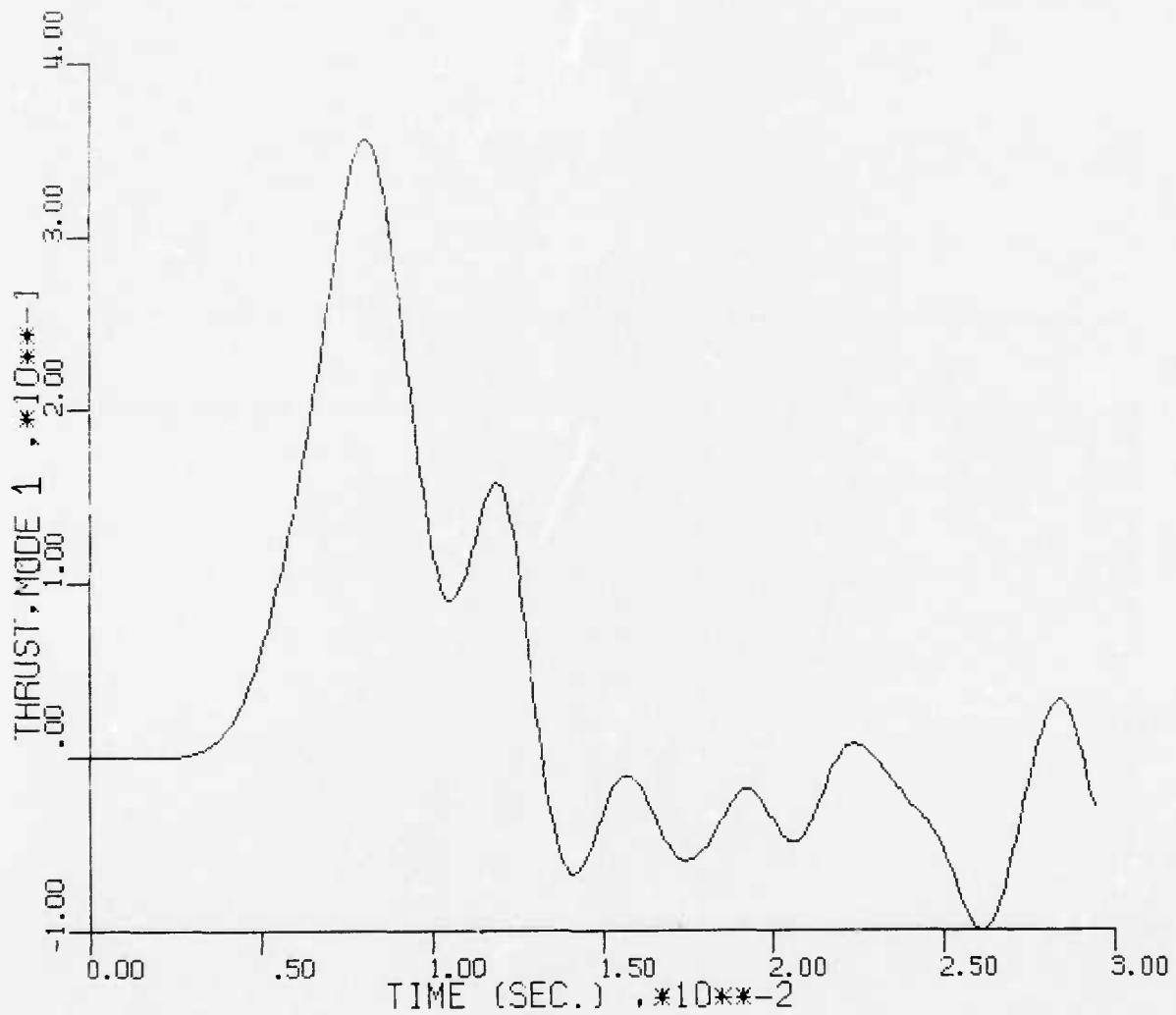
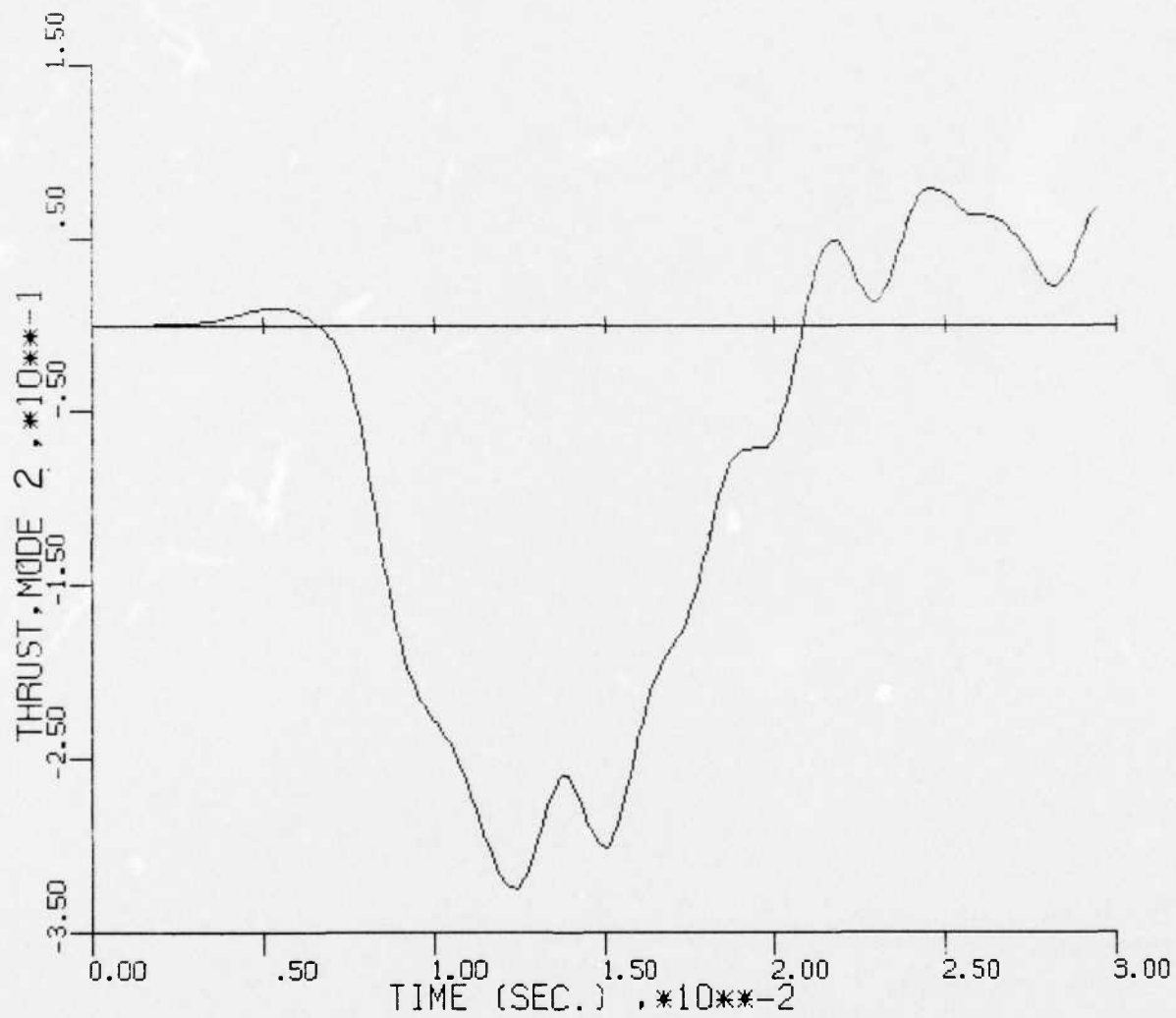
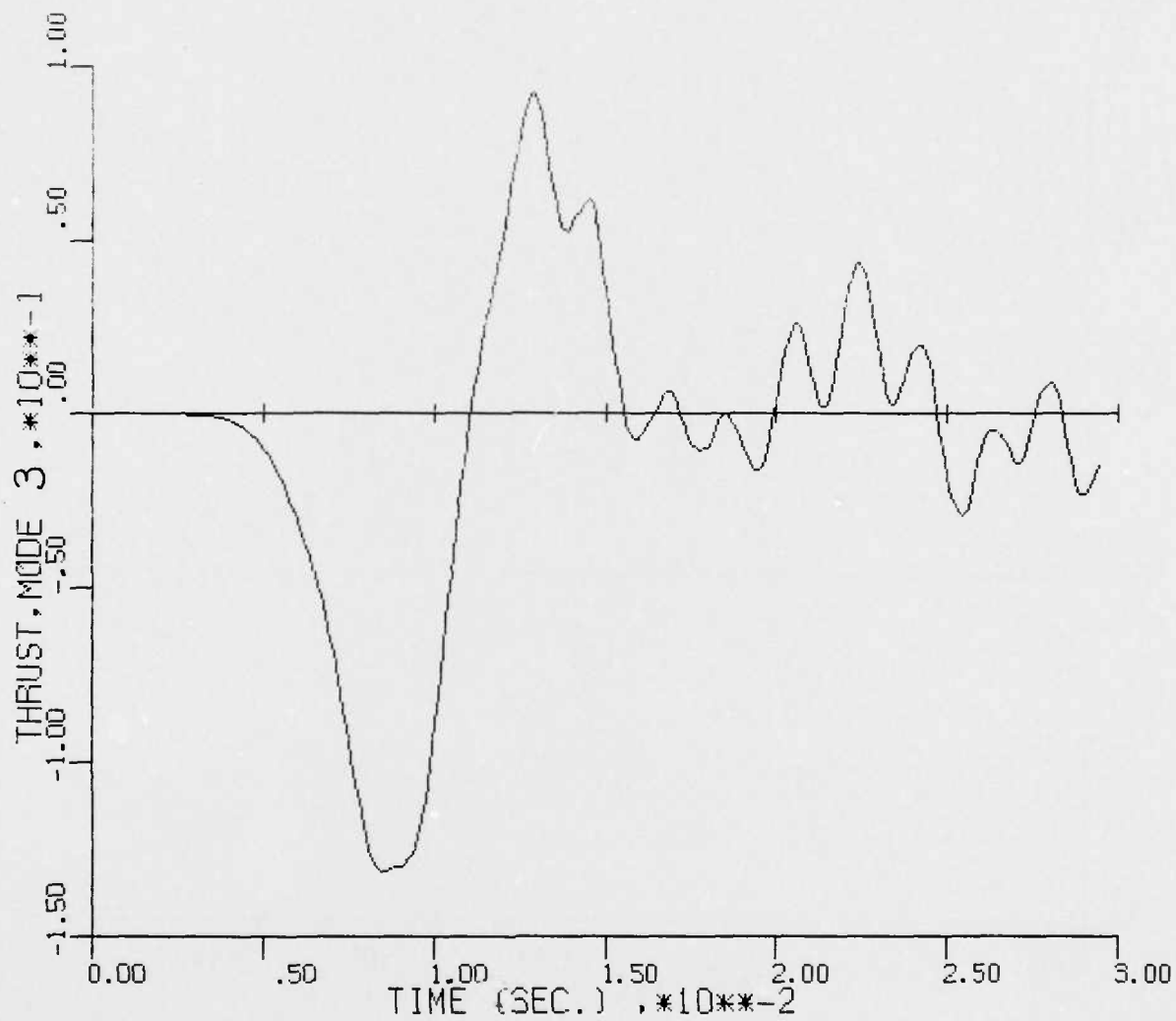


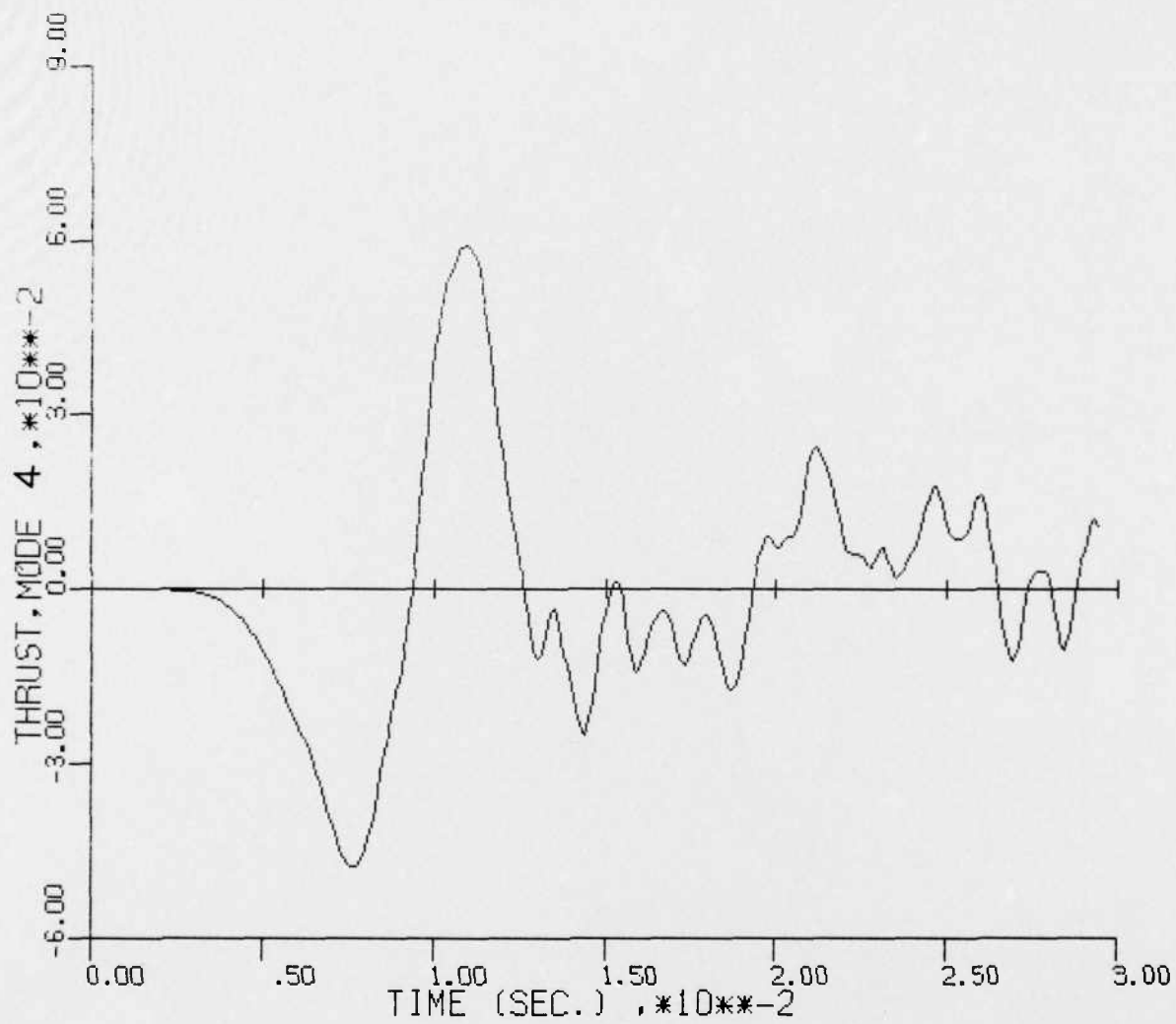
Figure 22b. Nondimensional Thrust History, Mode 1, Case 5



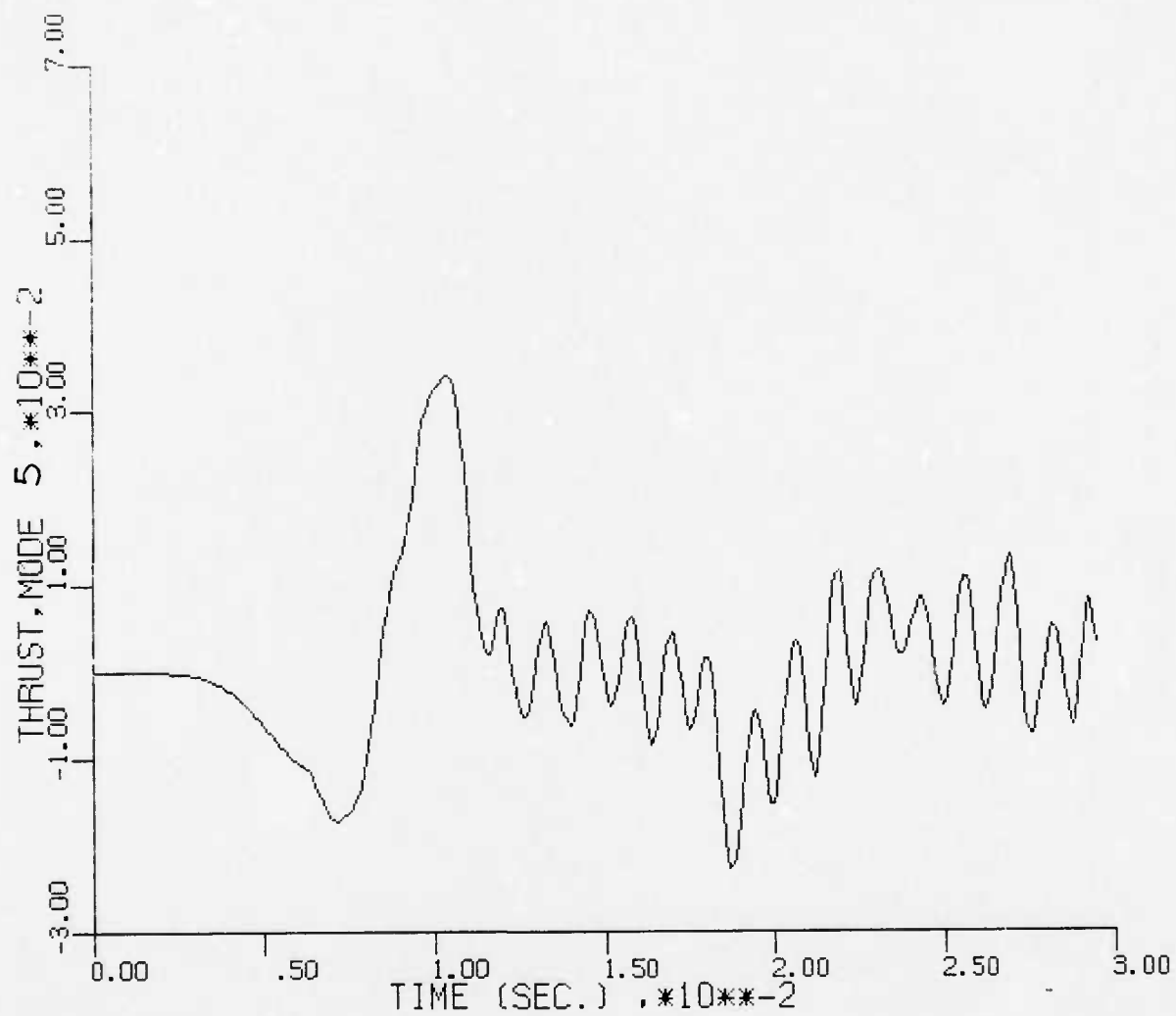
CASE 5
Figure 22c. Nondimensional Thrust History, Mode 2, Case 5



CASE 5
Figure 22d. Nondimensional Thrust History, Mode 3, Case 5

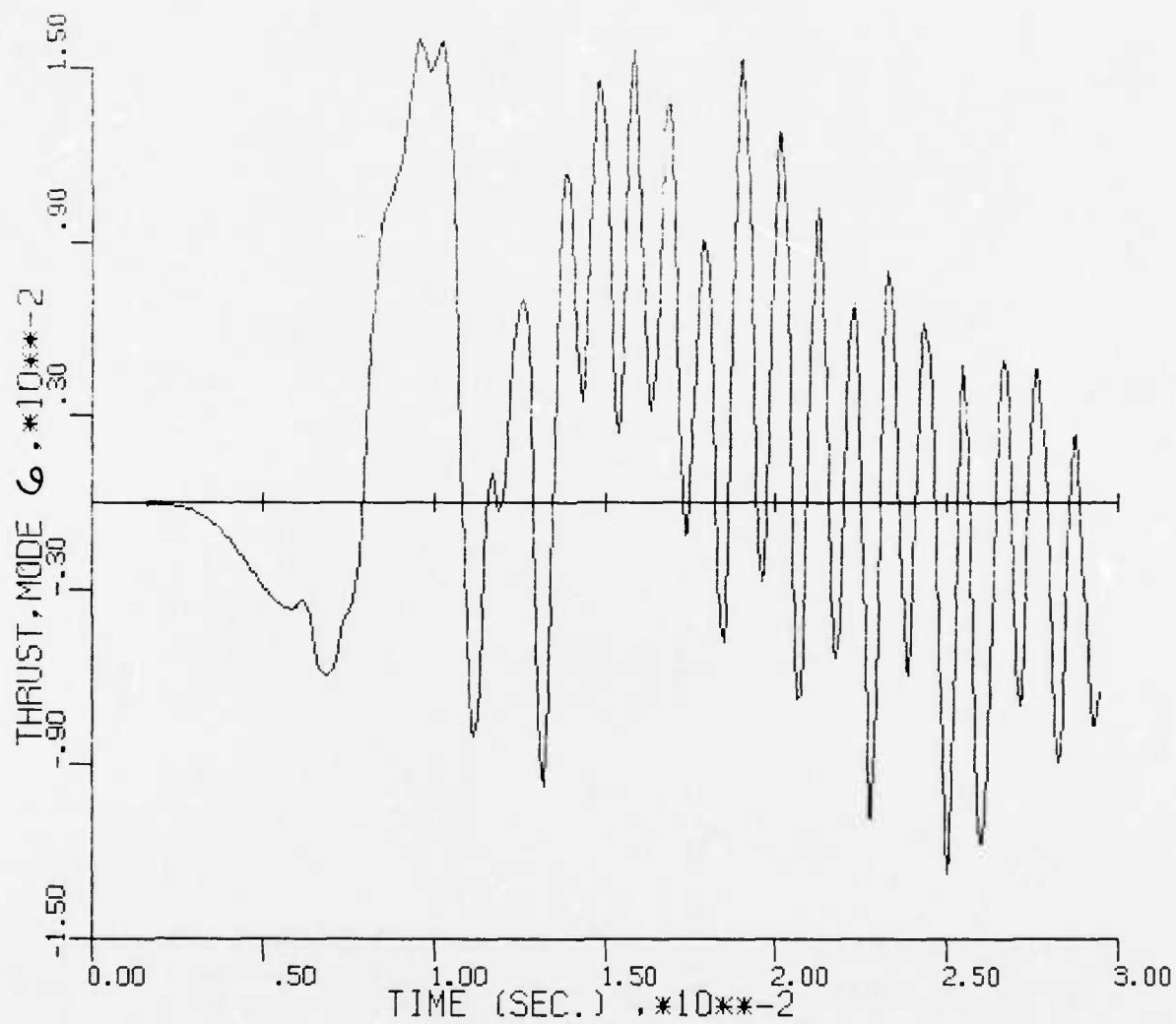


CASE 5
Figure 22e. Nondimensional Thrust History, Mode 4, Case 5



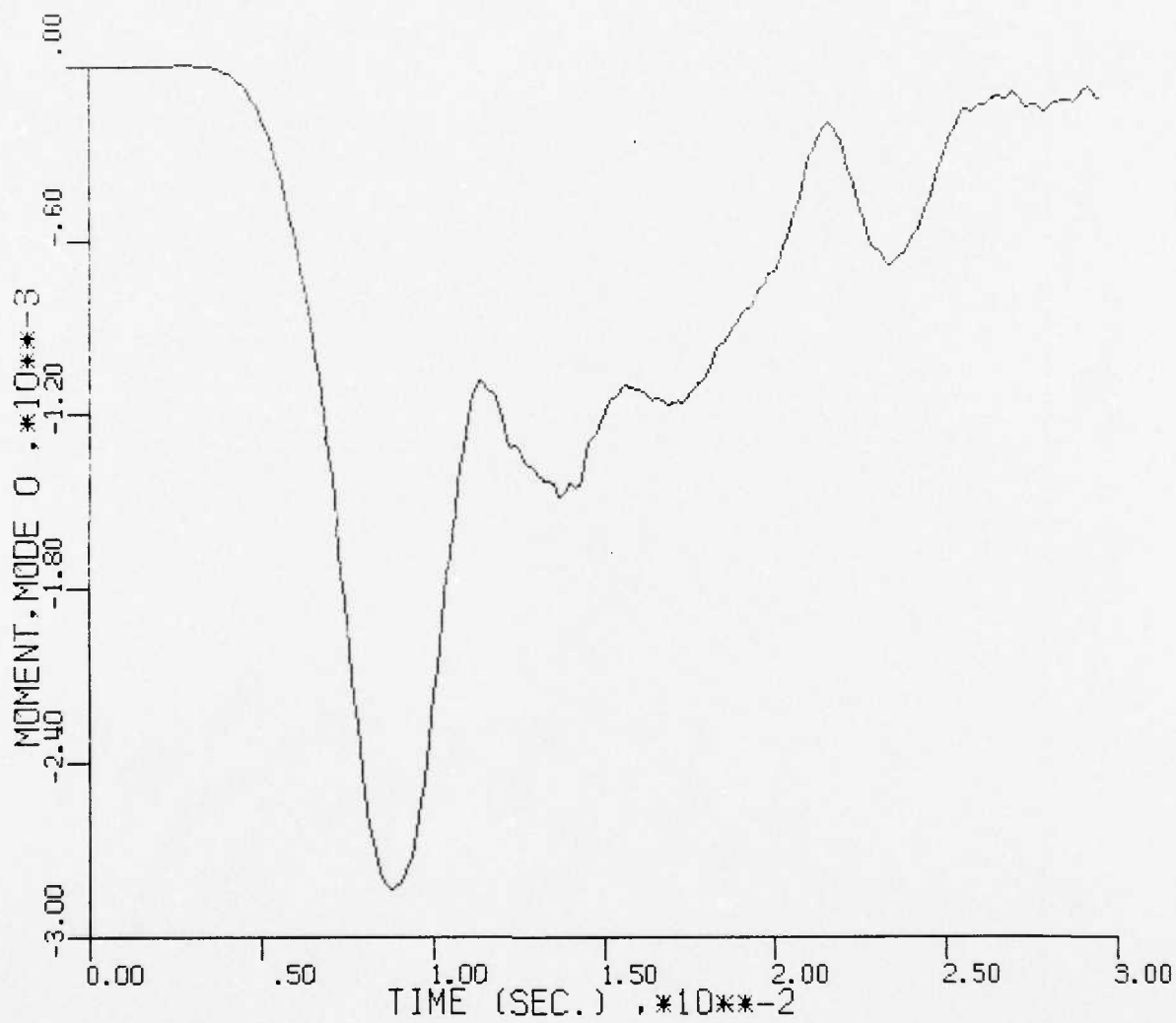
CASE 5

Figure 22f. Nondimensional Thrust History, Mode 5, Case 5

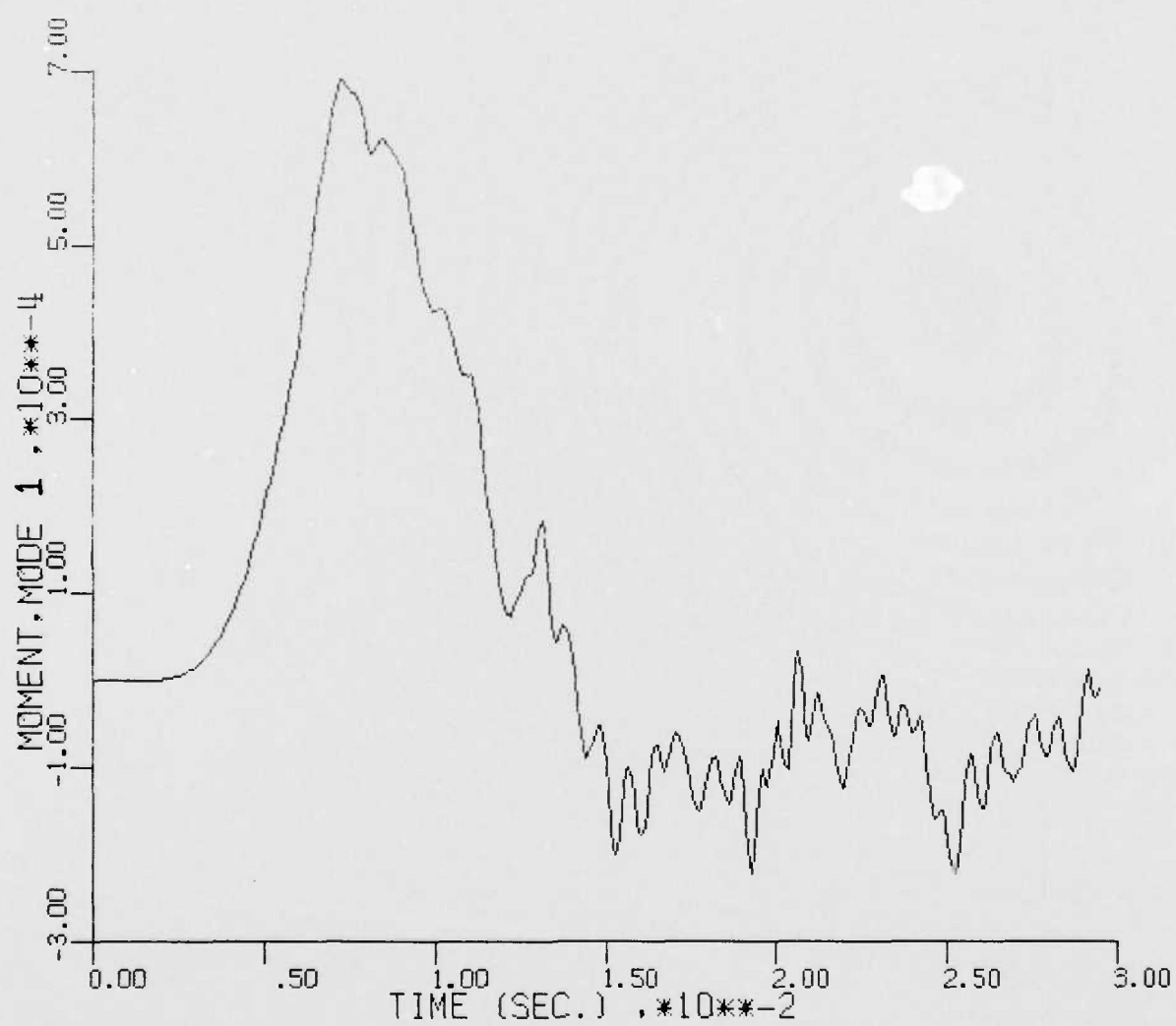


CASE 5

Figure 22g. Nondimensional Thrust History, Mode 6, Case 5

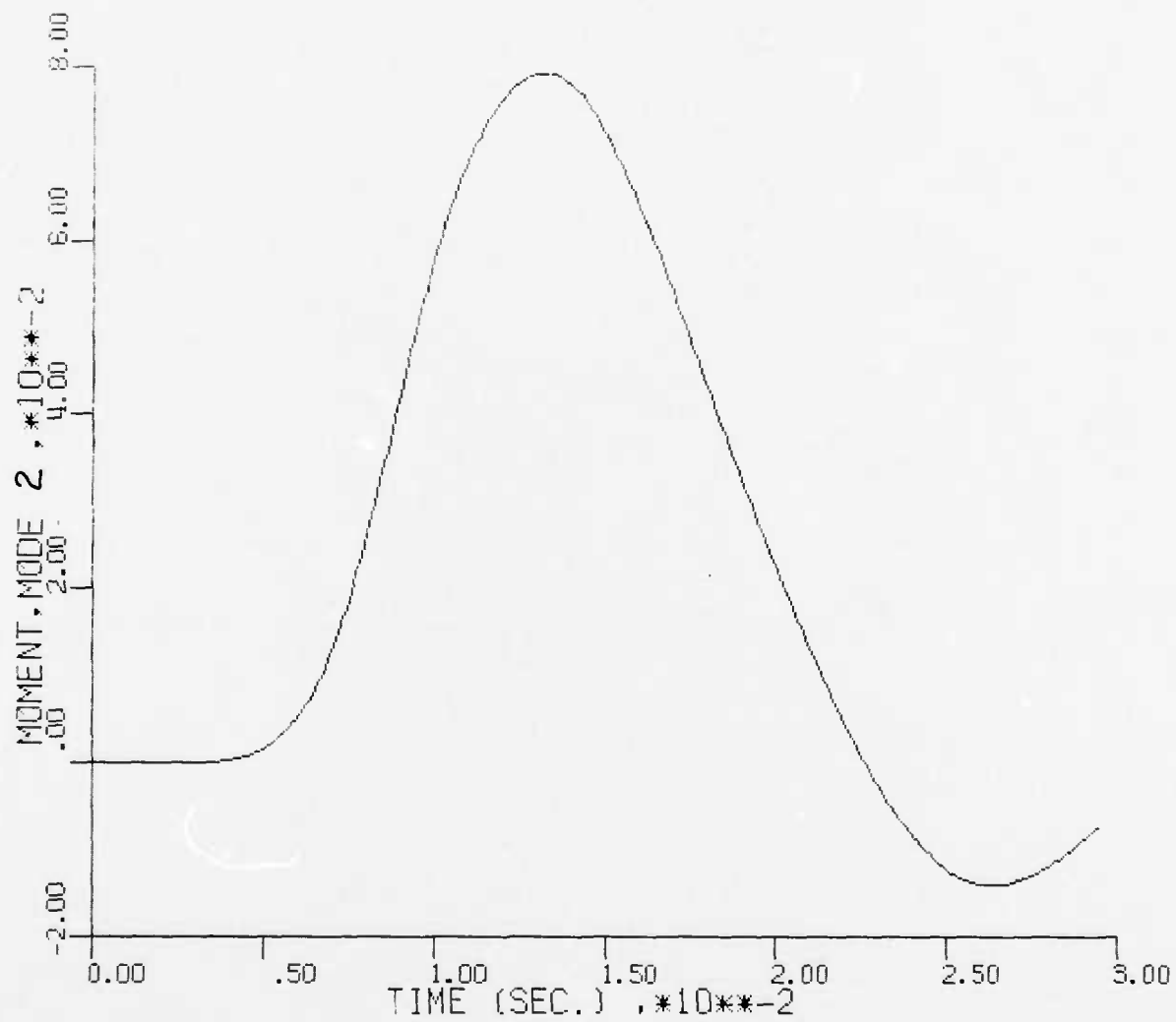


CASE 5
Figure 23a. Nondimensional Moment History, Mode 0, Case 5



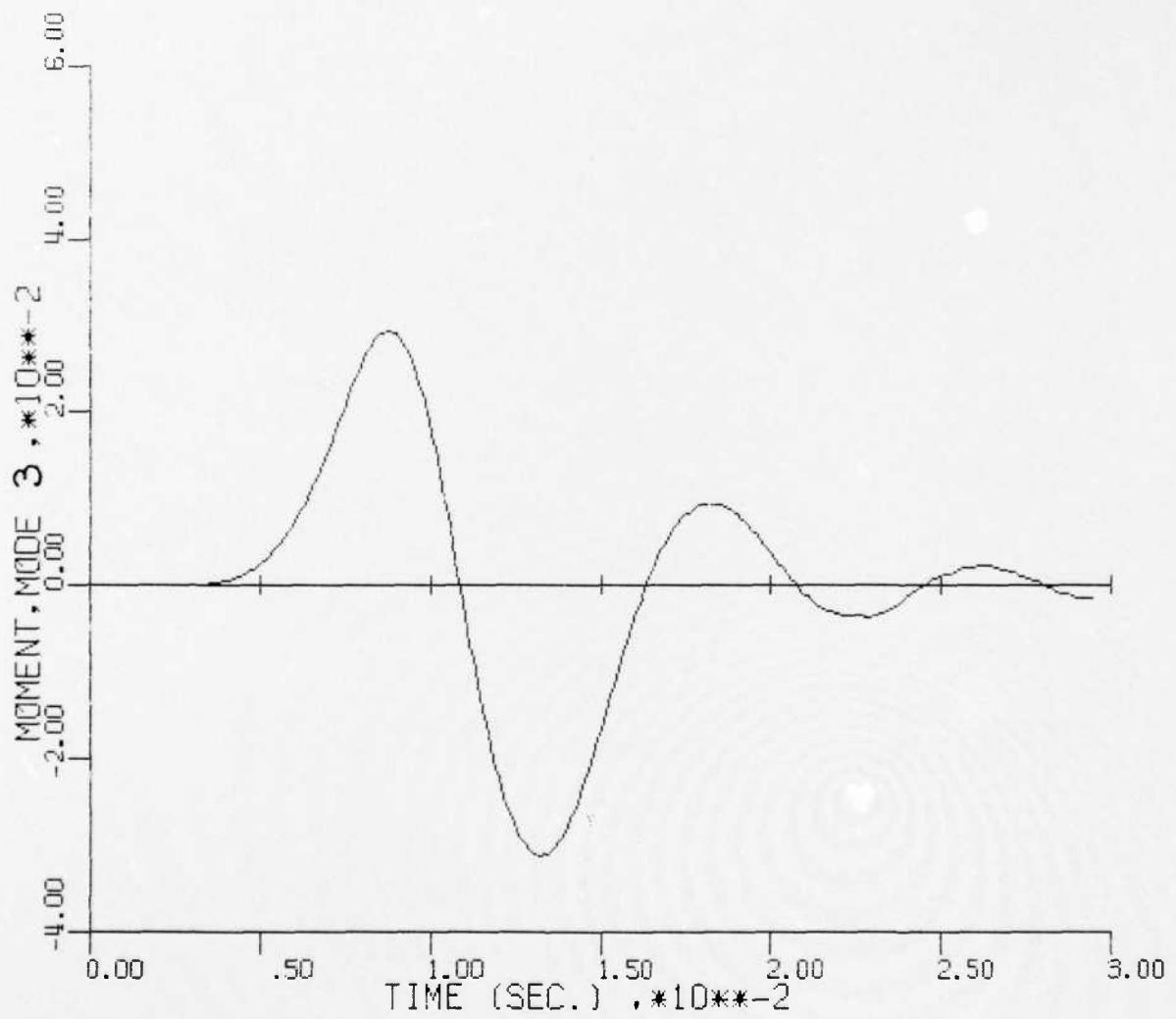
CASE 5

Figure 23b. Nondimensional Moment History, Mode 1, Case 5



CASE 5

Figure 23c. Nondimensional Moment History, Mode 2, Case 5



CASE 5

Figure 23d. Nondimensional Moment History, Mode 3, Case 5

AD-A061 464

IIT RESEARCH INST CHICAGO ILL

F/G 18/3

THEORETICAL INVESTIGATION OF LOADS ON BURIED STRUCTURES. VOLUME--ETC(U)

AUG 78 R R ROBINSON

F29601-76-C-0124

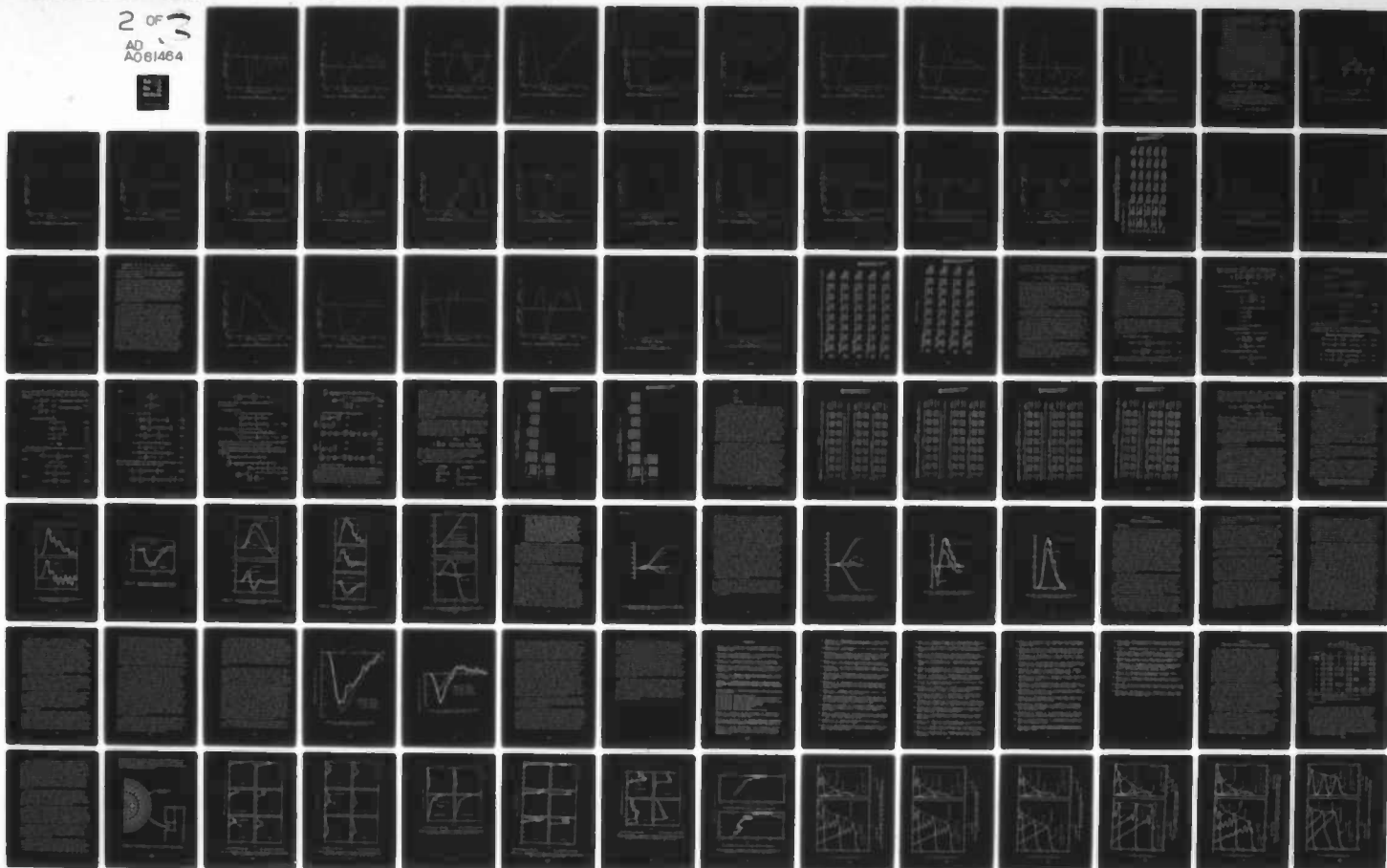
UNCLASSIFIED

IITRI-J6378-VOL-1

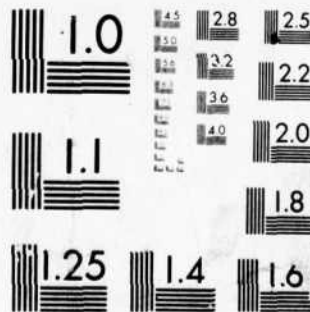
AFWL-TR-78-6-VOL-1

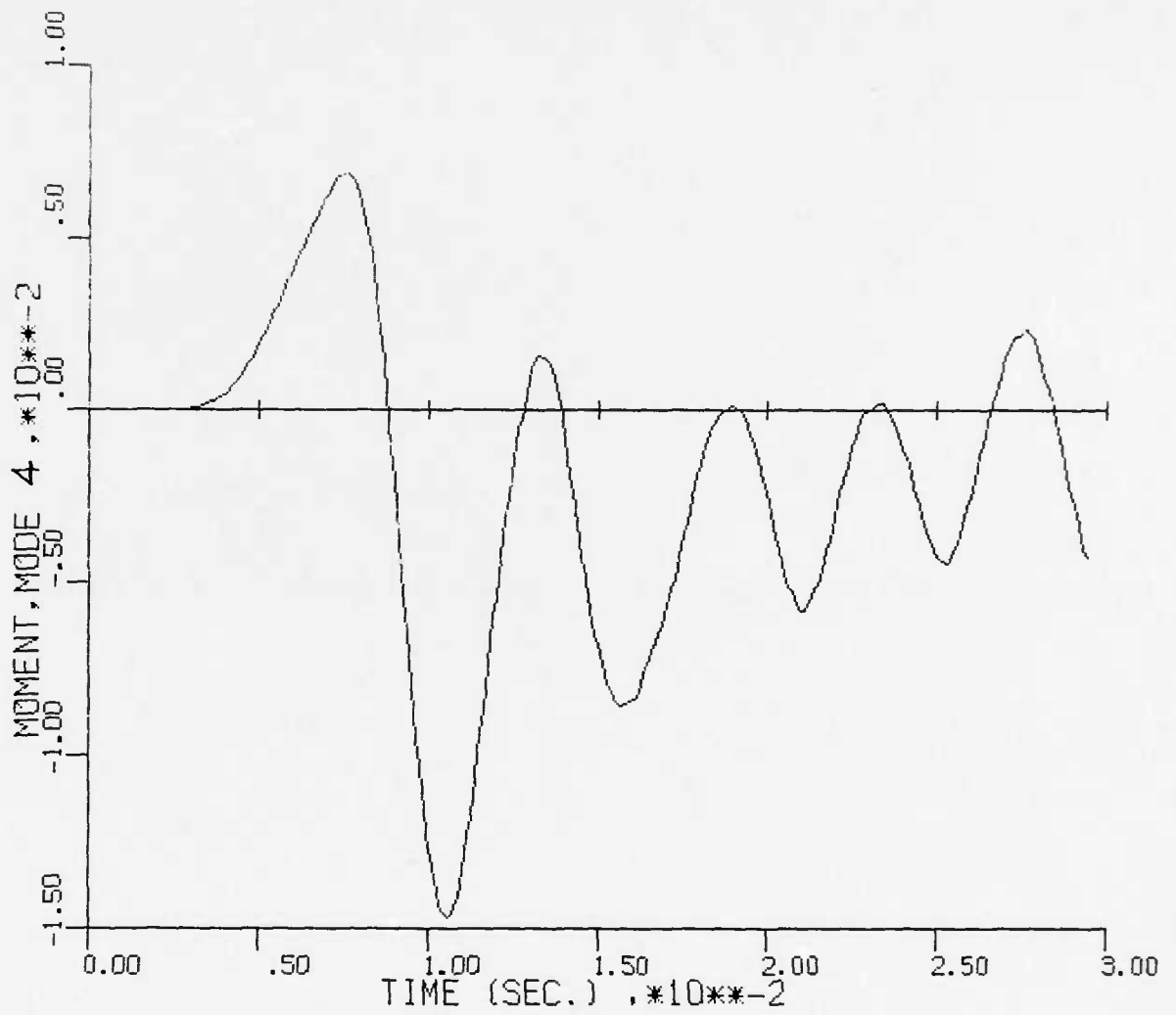
NL

2 OF 5
AD
A061464



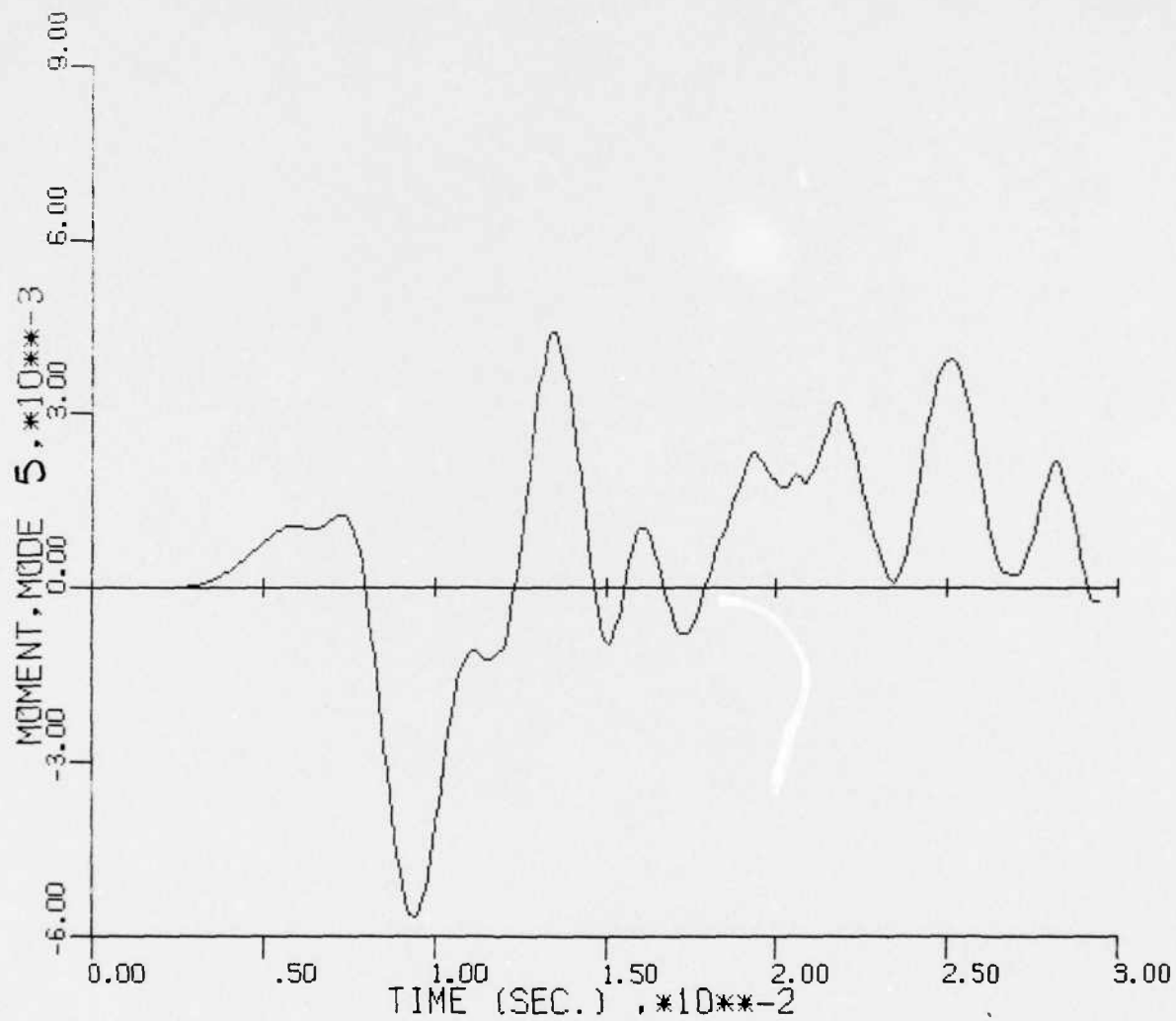
06/46



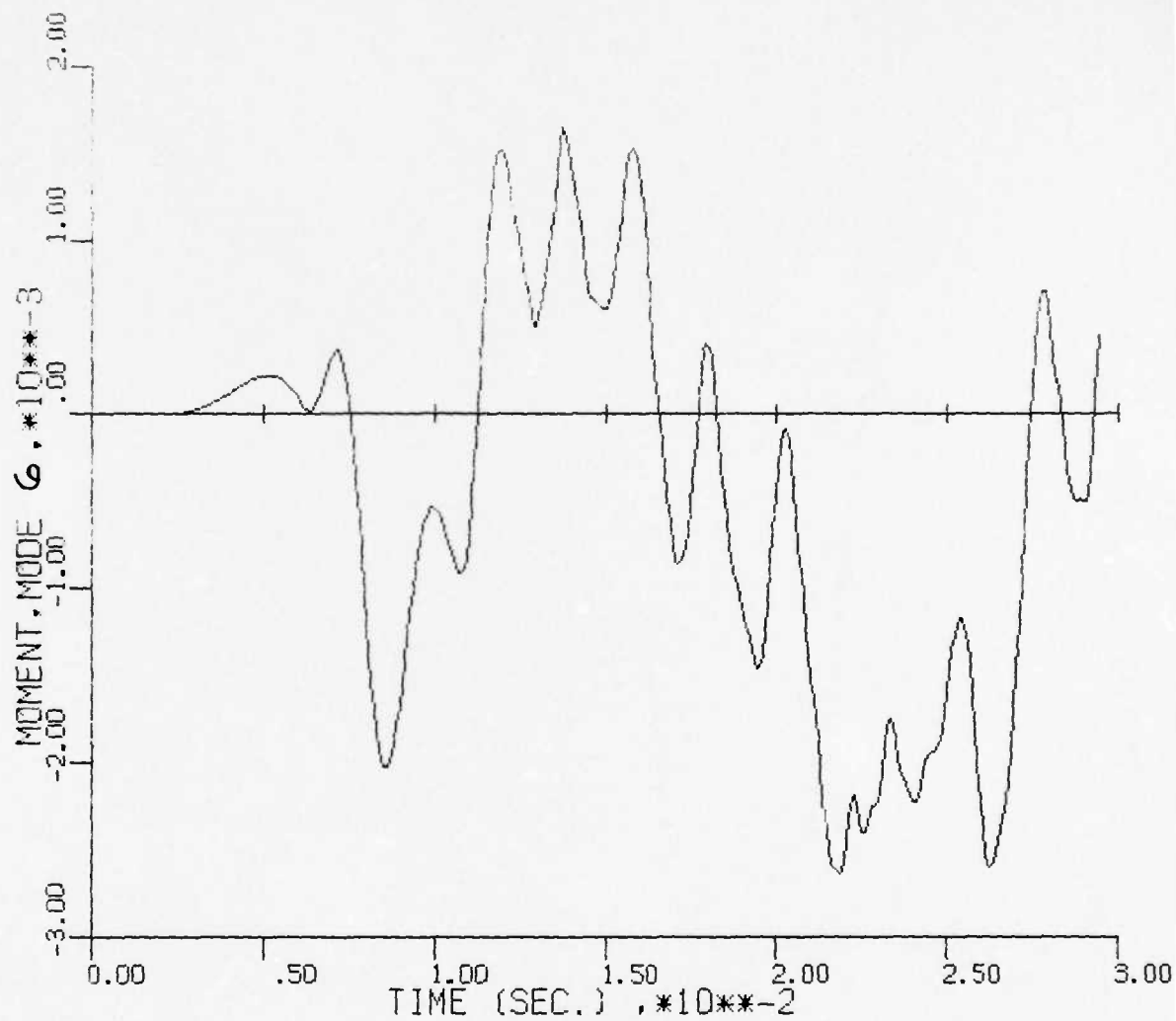


CASE 5

Figure 23e. Nondimensional Moment History, Mode 4, Case 5

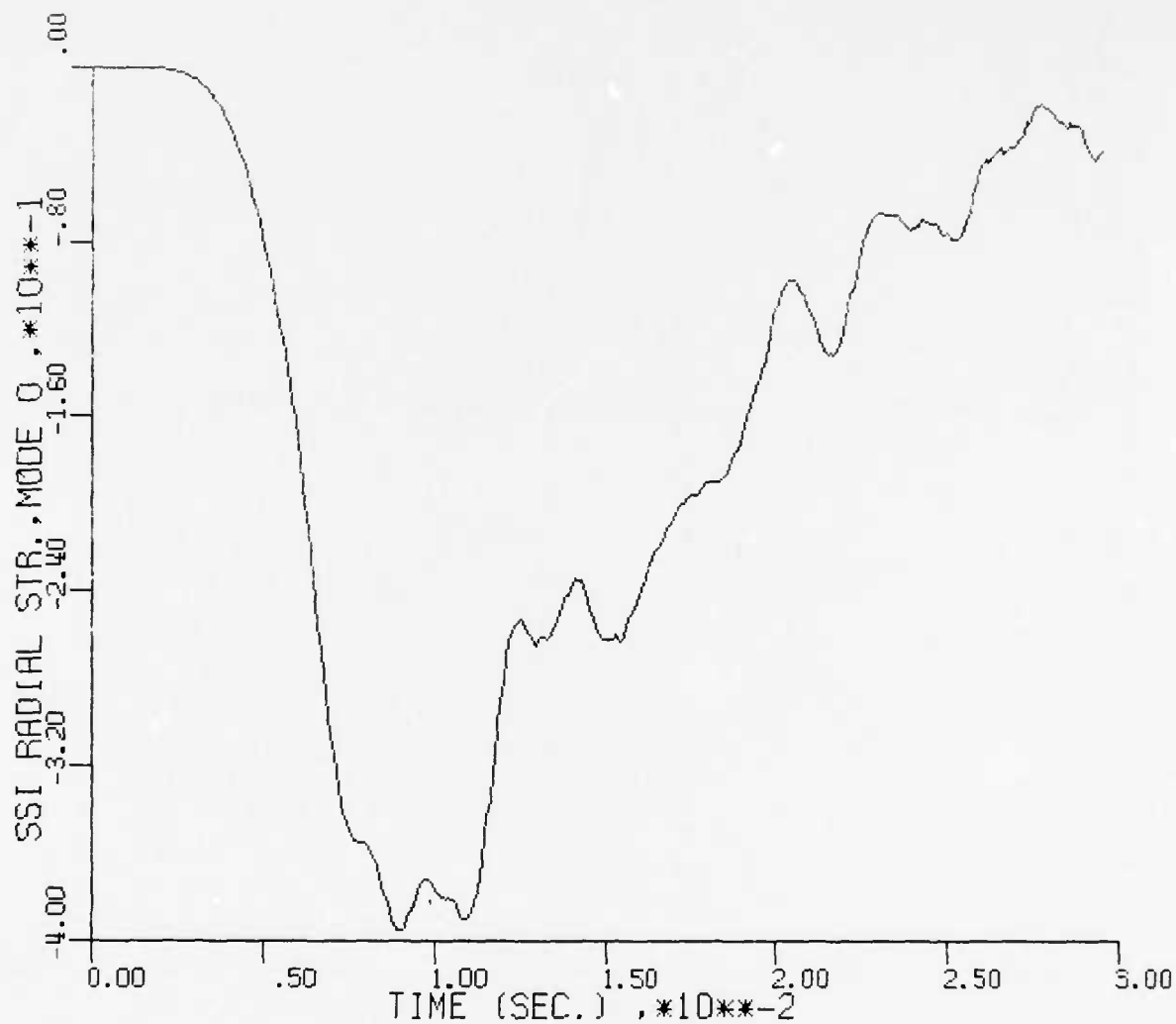


CASE 5
Figure 23f. Nondimensional Moment History, Mode 5, Case 5



CASE 5

Figure 23g. Nondimensional Moment History, Mode 6, Case 5



CASE 5
Figure 24a. Nondimensional SSI Radial Stress, Mode 0, Case 5

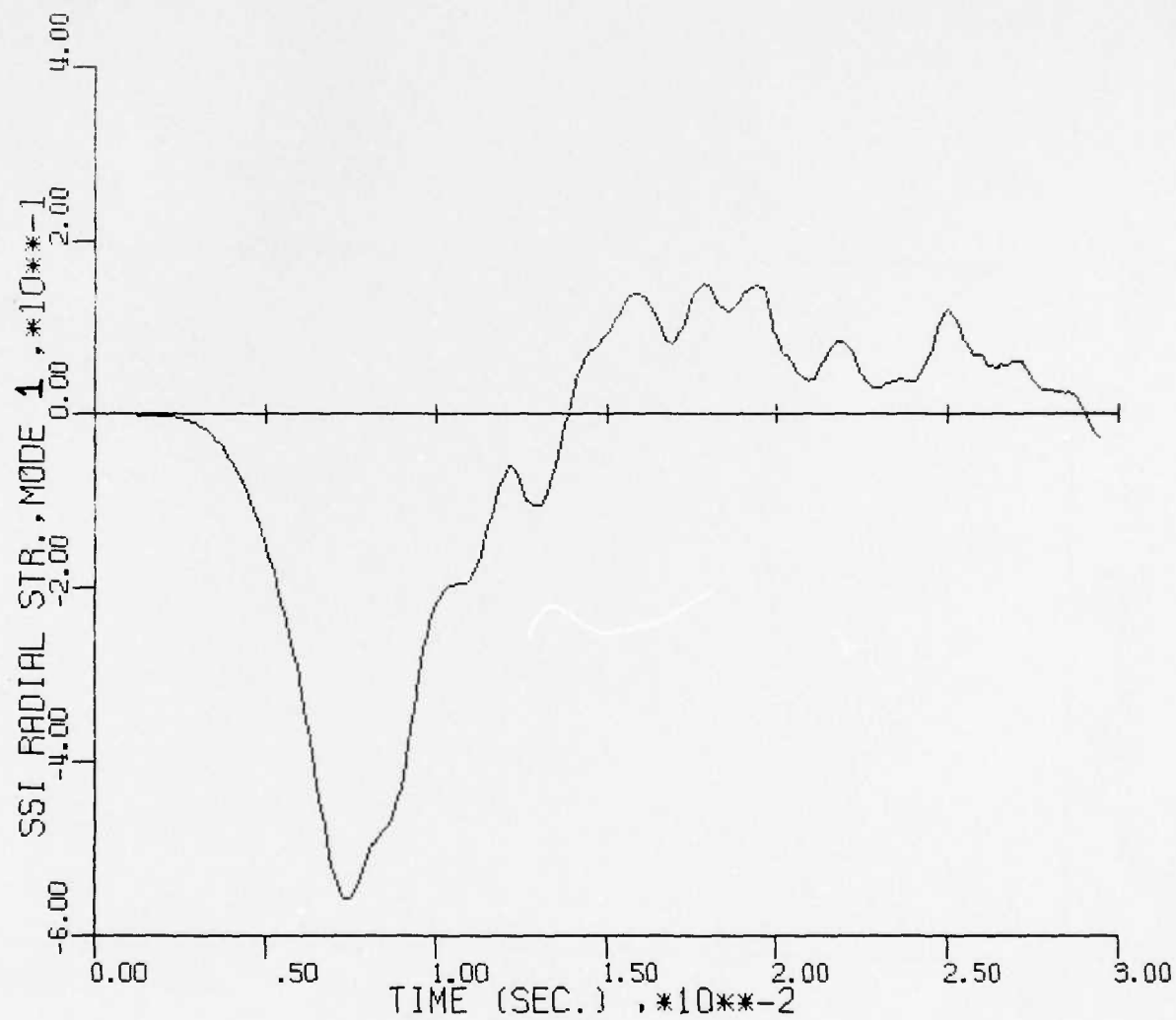
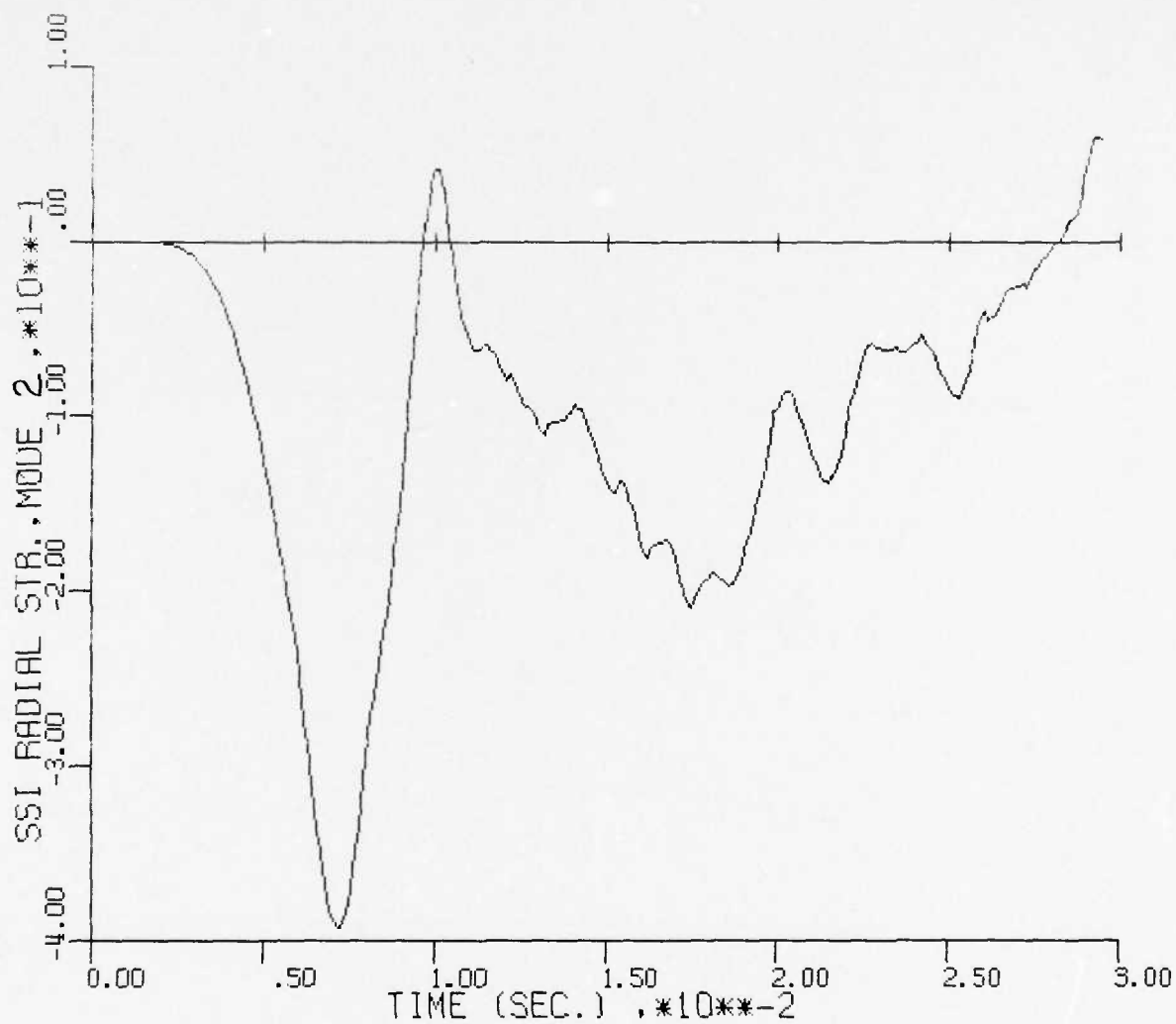


Figure 24b. Nondimensional SSI Radial Stress, Mode 1, Case 5



CASE 5

Figure 24c. Nondimensional SSI Radial Stress, Mode 2, Case 5

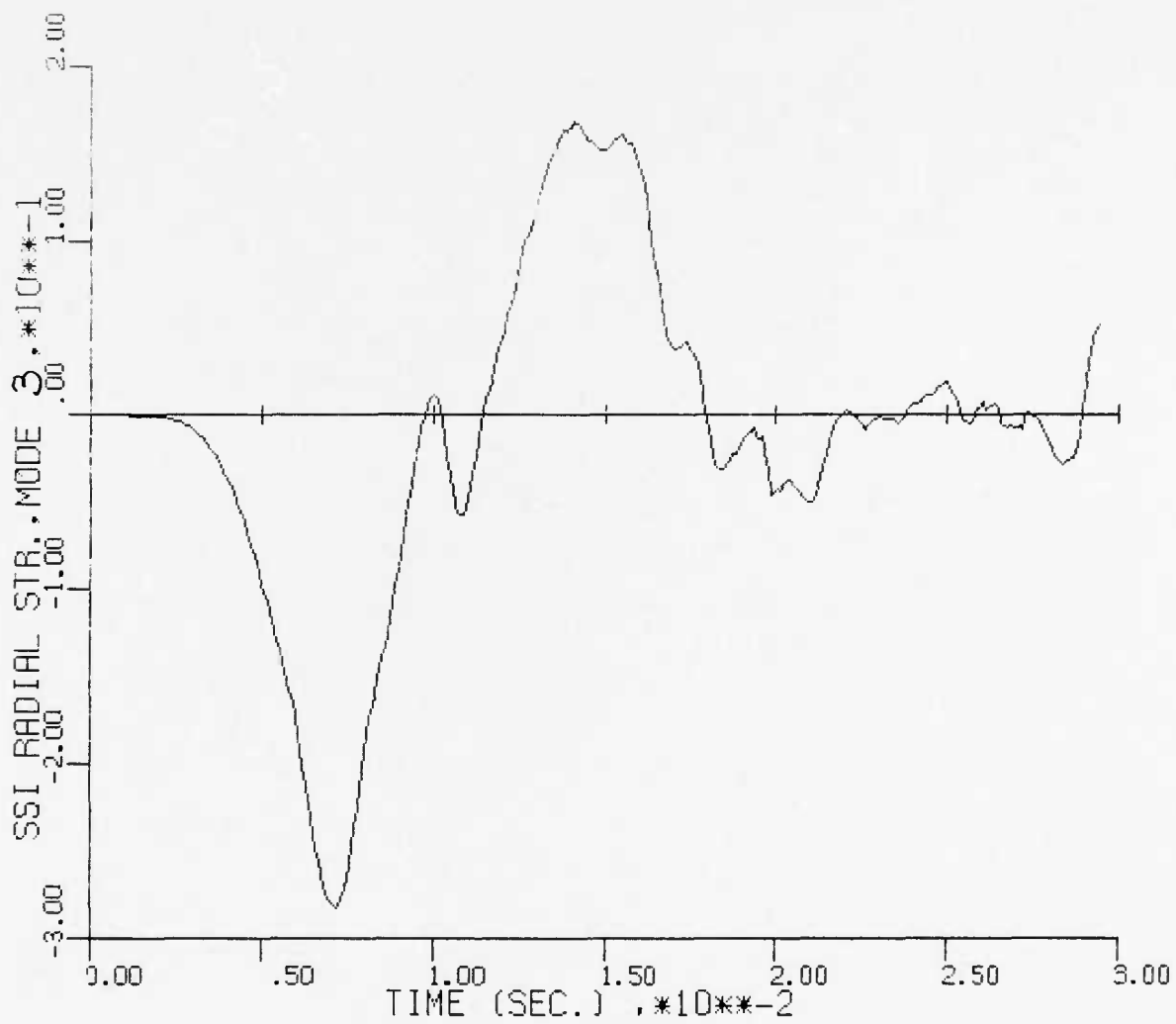
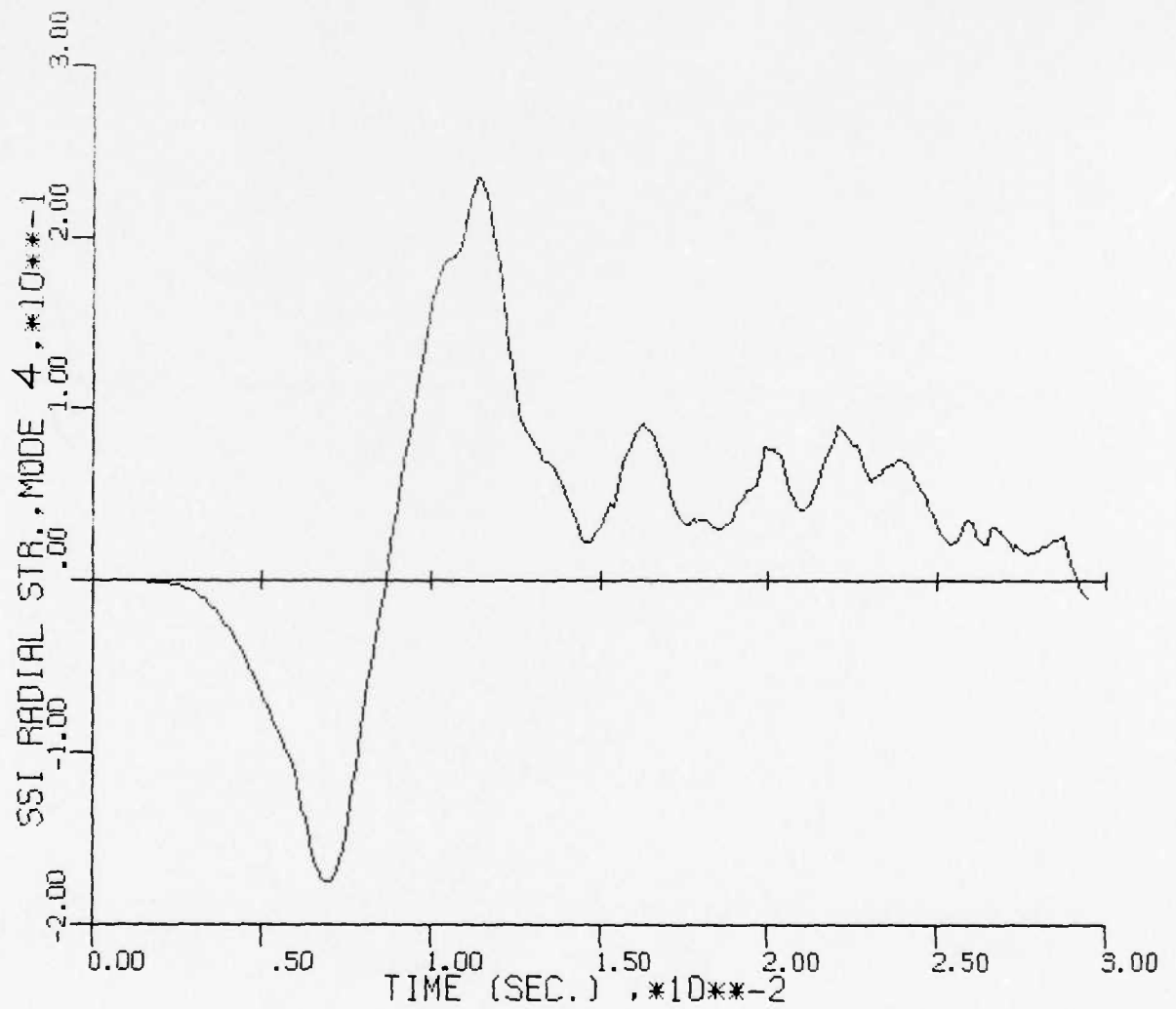
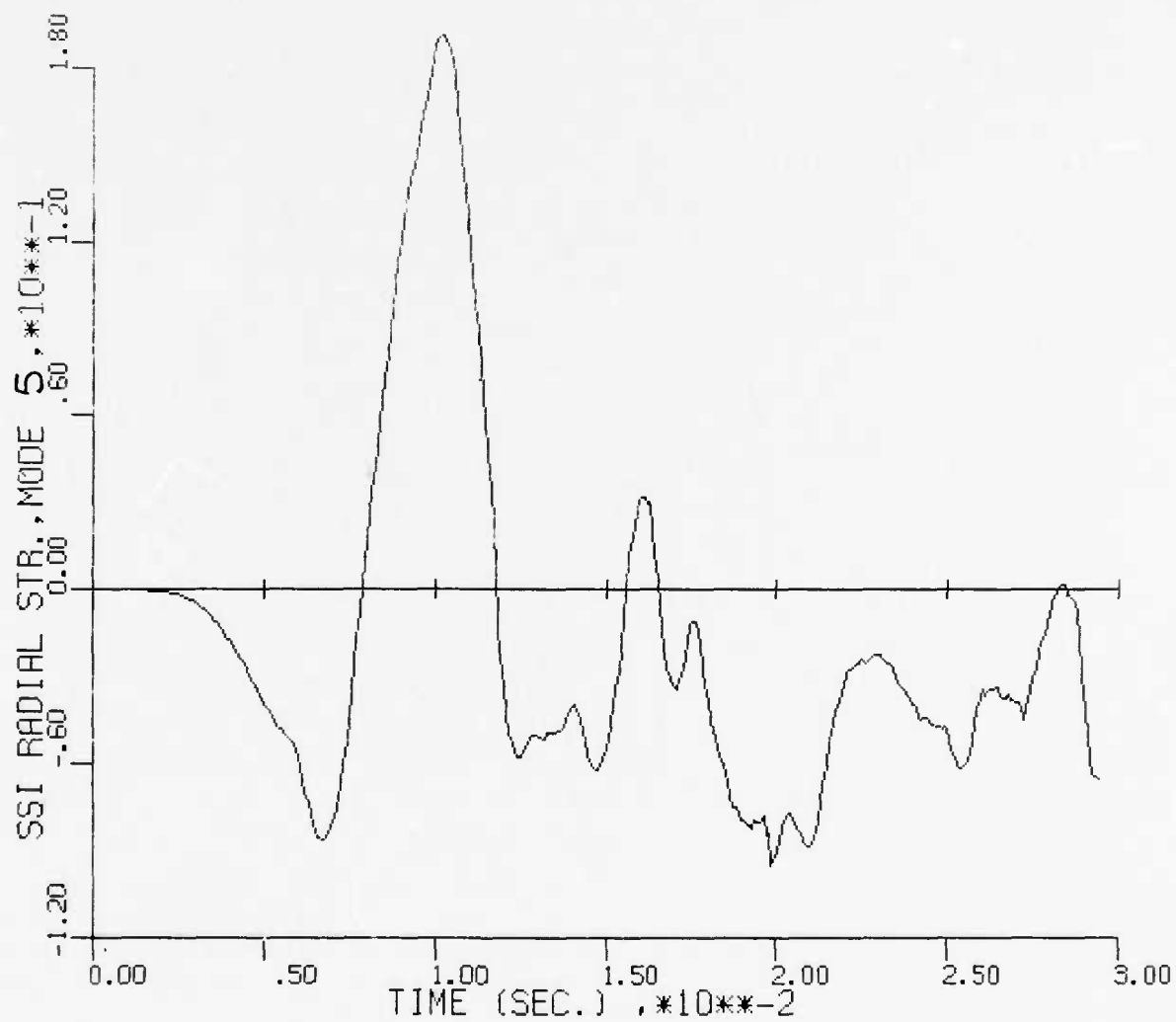


Figure 24d. Nondimensional SSI Radial Stress, Mode 3, Case 5



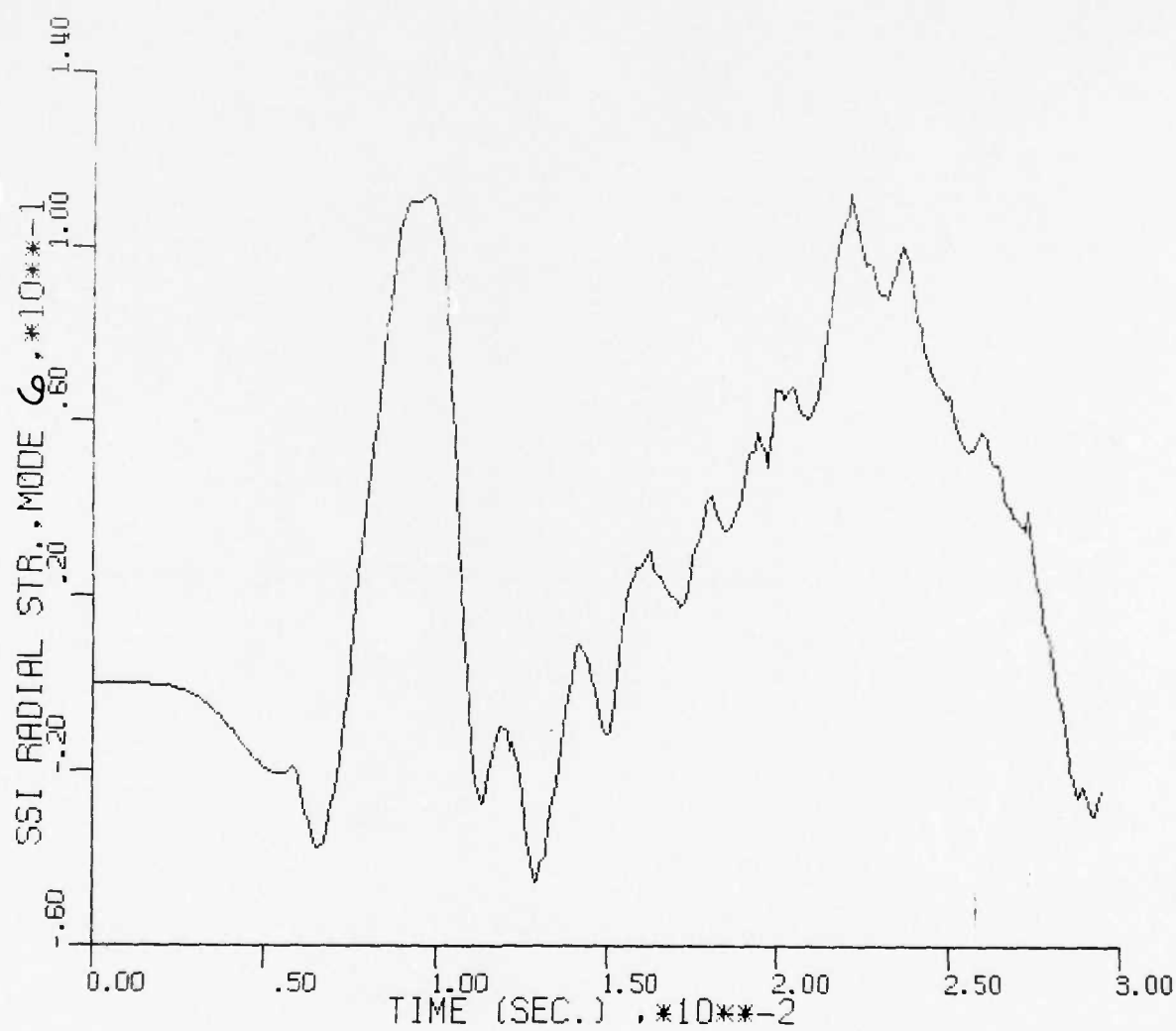
CASE 5

Figure 24e. Nondimensional SSI Radial Stress, Mode 4, Case 5



CASE 5

Figure 24f. Nondimensional SSI Radial Stress, Mode 5, Case 5



CASE 5

Figure 24g. Nondimensional SSI Radial Stress, Mode 6, Case 5

(4) Antisymmetric Modal Histories

Since the zero mode does not exist for the antisymmetric modes, the modal histories were computed for modes 1 through 6 for the following variables.

Nondimensional Liner Shear, figure 25 ($A_n \leftarrow V_n/p_o R$)

Nondimensional SSI Shear Stress, figure 26 ($A_n \leftarrow \tau_{rn}/p_o$)

Modal amplitude histories for the circumferential soil stresses were not determined since these stresses do not act as loads on the liner structure and are only of academic interest.

Table VI gives the minimum and maximum values of the modal amplitude that occur during the time history for each mode. Since these peaks do not occur at the same time for all modes, the maximum and minimum values of response at a particular point (θ_i) cannot be obtained by simply summing the angular modification of the peak values, i.e., $\sum S_n \cos n\theta_i$ or $\sum A_n \sin n\theta_i$. Even if the peaks do occur at the same time, the maximum value of θ_i is in general not obtained from the sum of the maximum modal amplitudes since the $\sin n\theta_i$ or $\cos n\theta_i$ will change the effect from maximum at the crown ($\theta = 0$) to minimum (or negative) at θ_i depending on the sign of the appropriate trigonometric function. For example, if all peak amplitudes (minimum and maximum) occurred at the same time for a symmetric variable, the maximum value of the variable at say $\theta = 90$ deg would be obtained (for the modes 0 through 6) as

$$\text{Max. } S(\theta = 90) = \sum_{n=0,2,4,6}^6 \text{Max. } S_n + \sum_{n=1,3,5}^5 \text{Min. } S_n$$

c. Crown, Springline, Invert Results

Time history plots of the liner nondimensional moment and thrust and the nondimensional SSI radial stress computed during the dynamic SAMSON analysis are presented for three reference points on the liner. The reference points and figures containing the history plots are:

Crown - Ref. Pt. 1, $\theta_1 = 3.75$ deg, figure 27

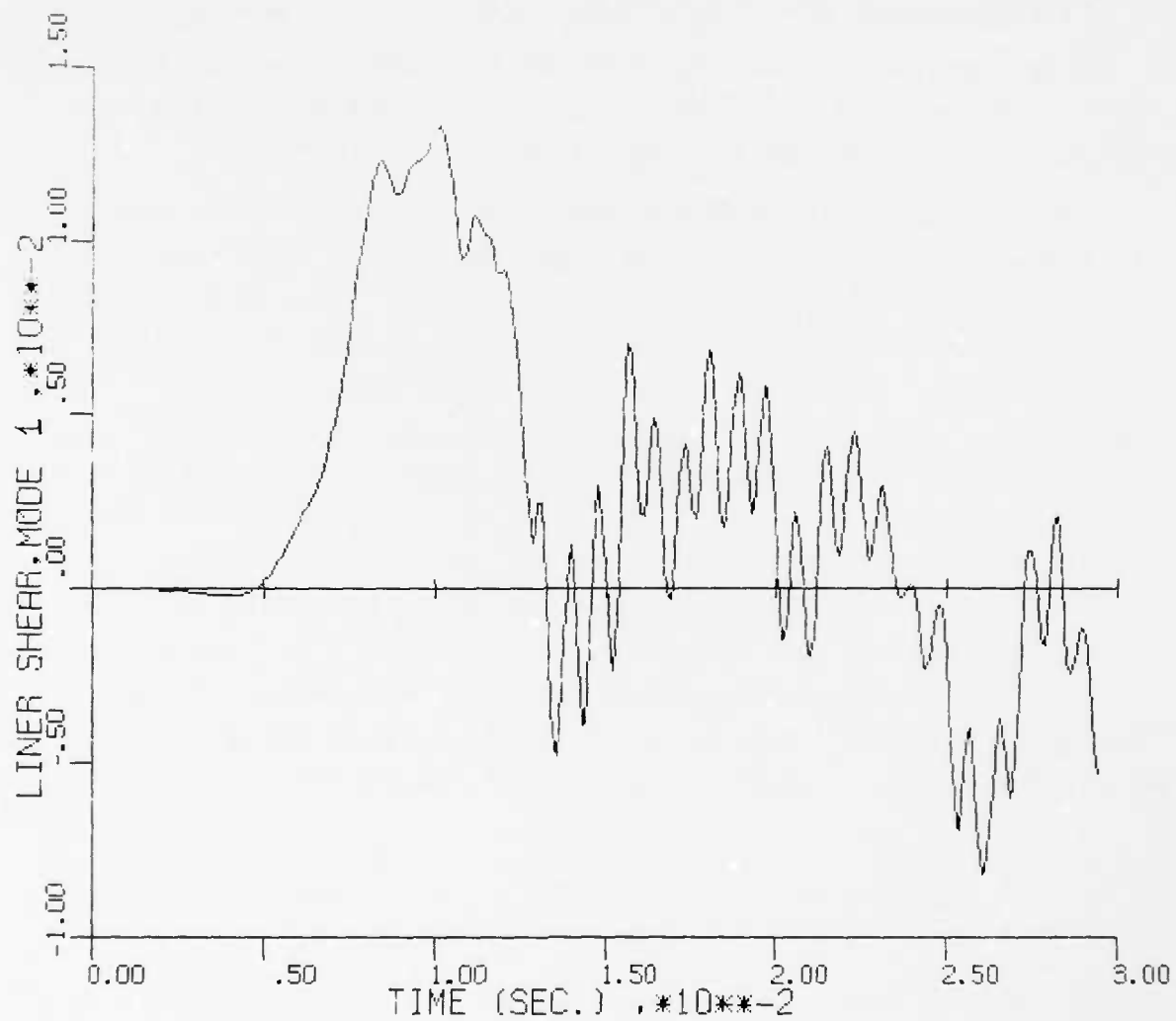


Figure 25a. Nondimensional Liner Shear, Mode 1, Case 5

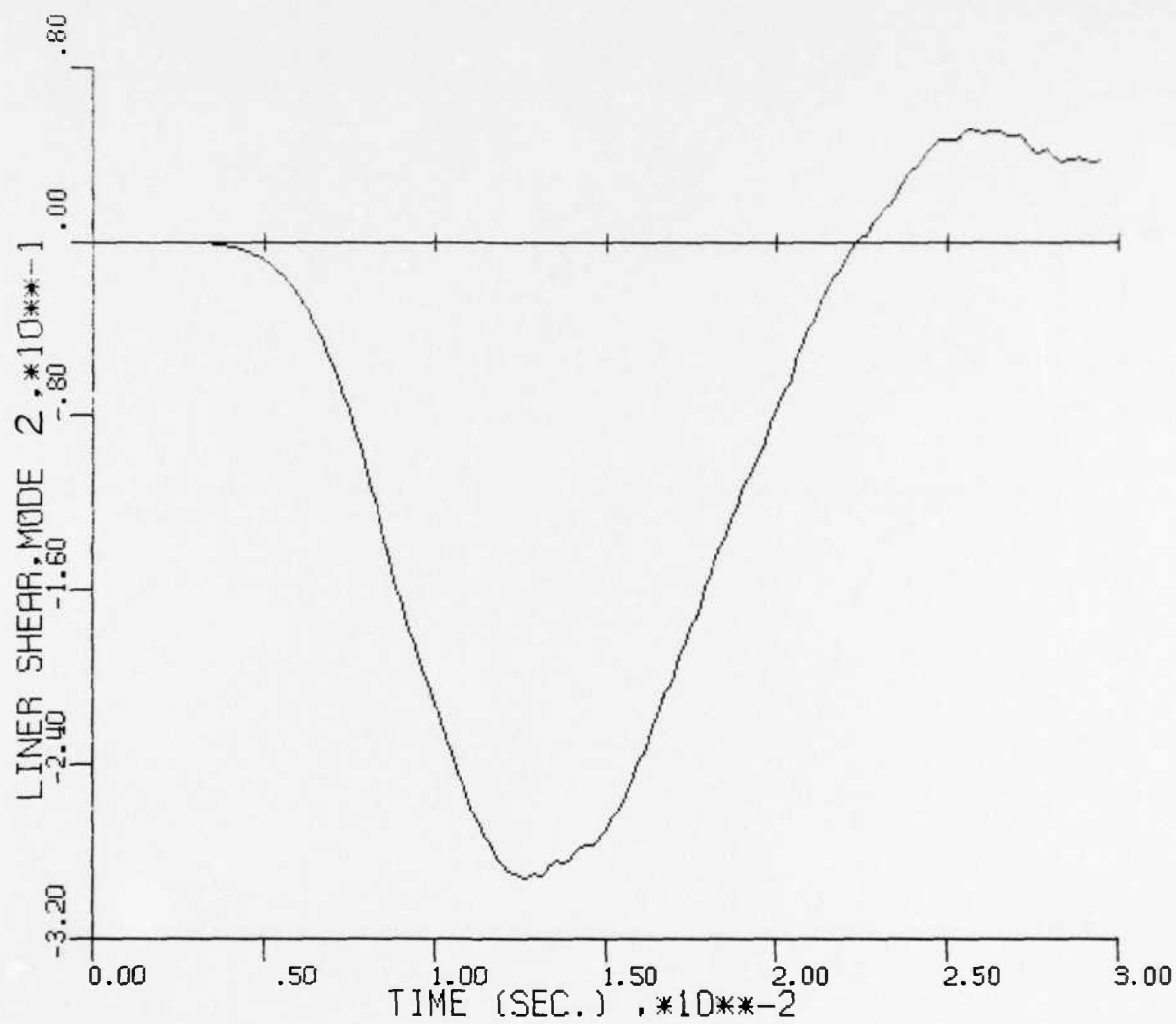


Figure 25b. Nondimensional Liner Shear, Mode 2, Case 5

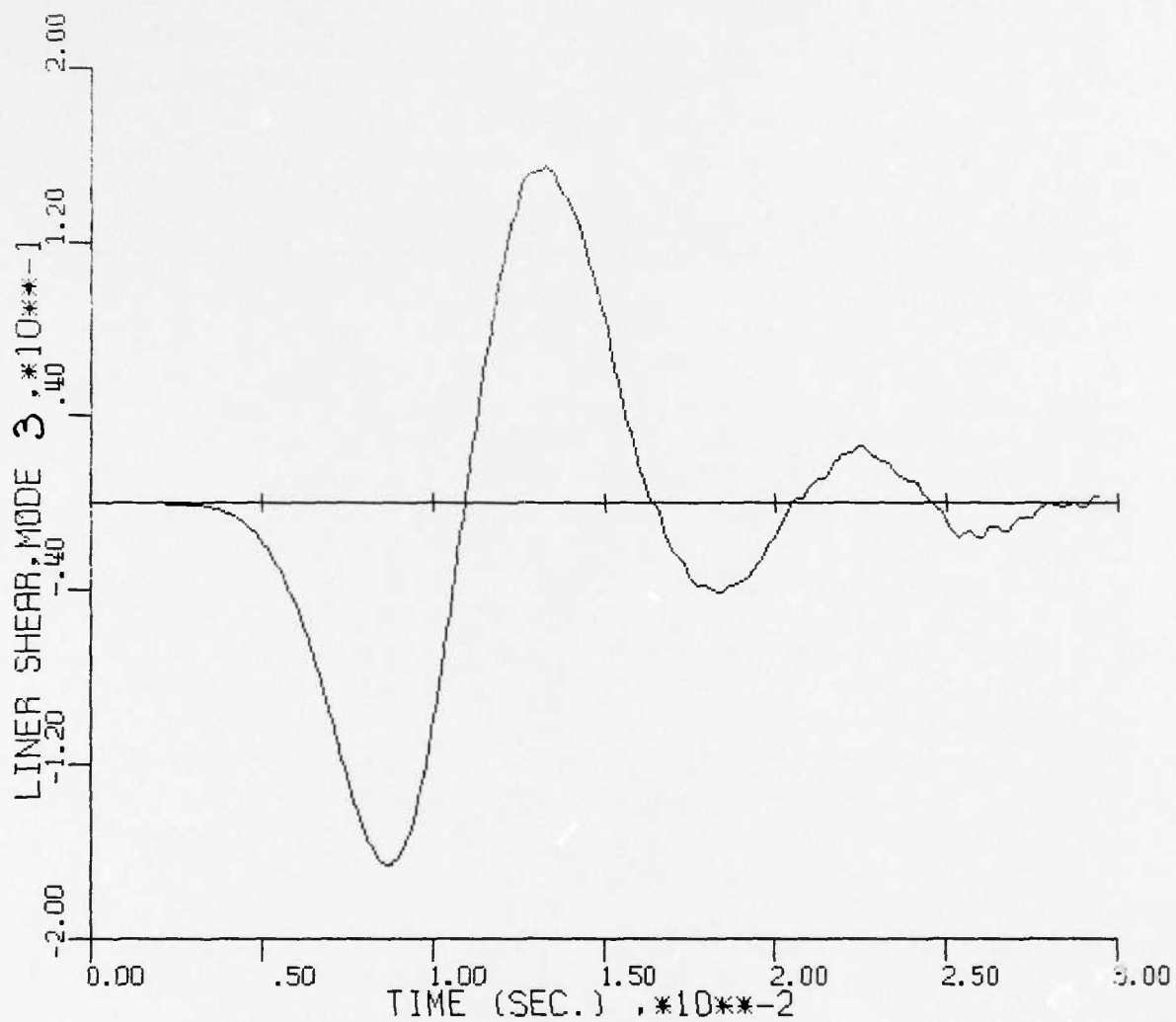


Figure 25c. Nondimensional Liner Shear, Mode 3, Case 5

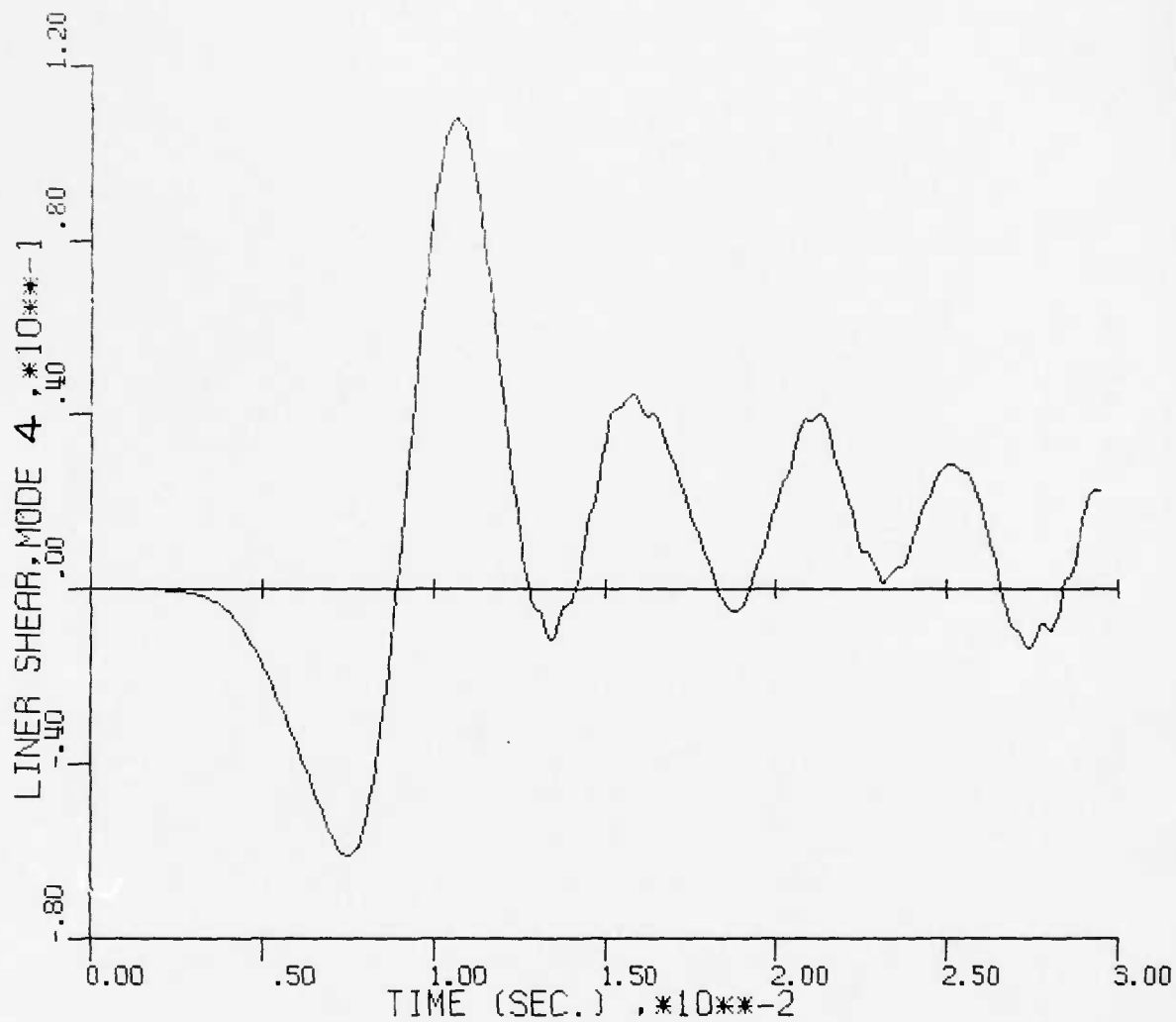


Figure 25d. Nondimensional Liner Shear, Mode 4, Case 5

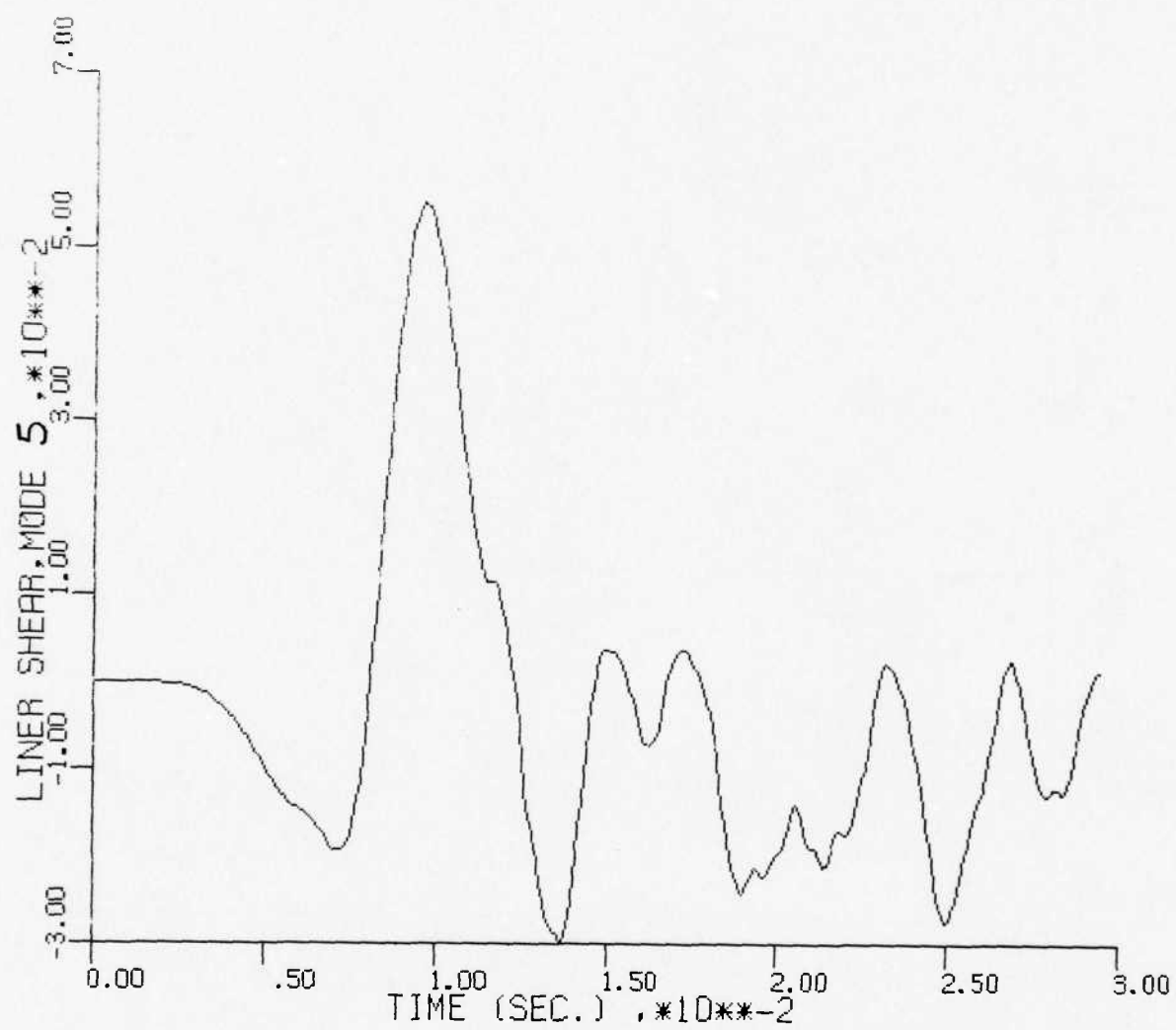


Figure 25e. Nondimensional Liner Shear, Mode 5, Case 5

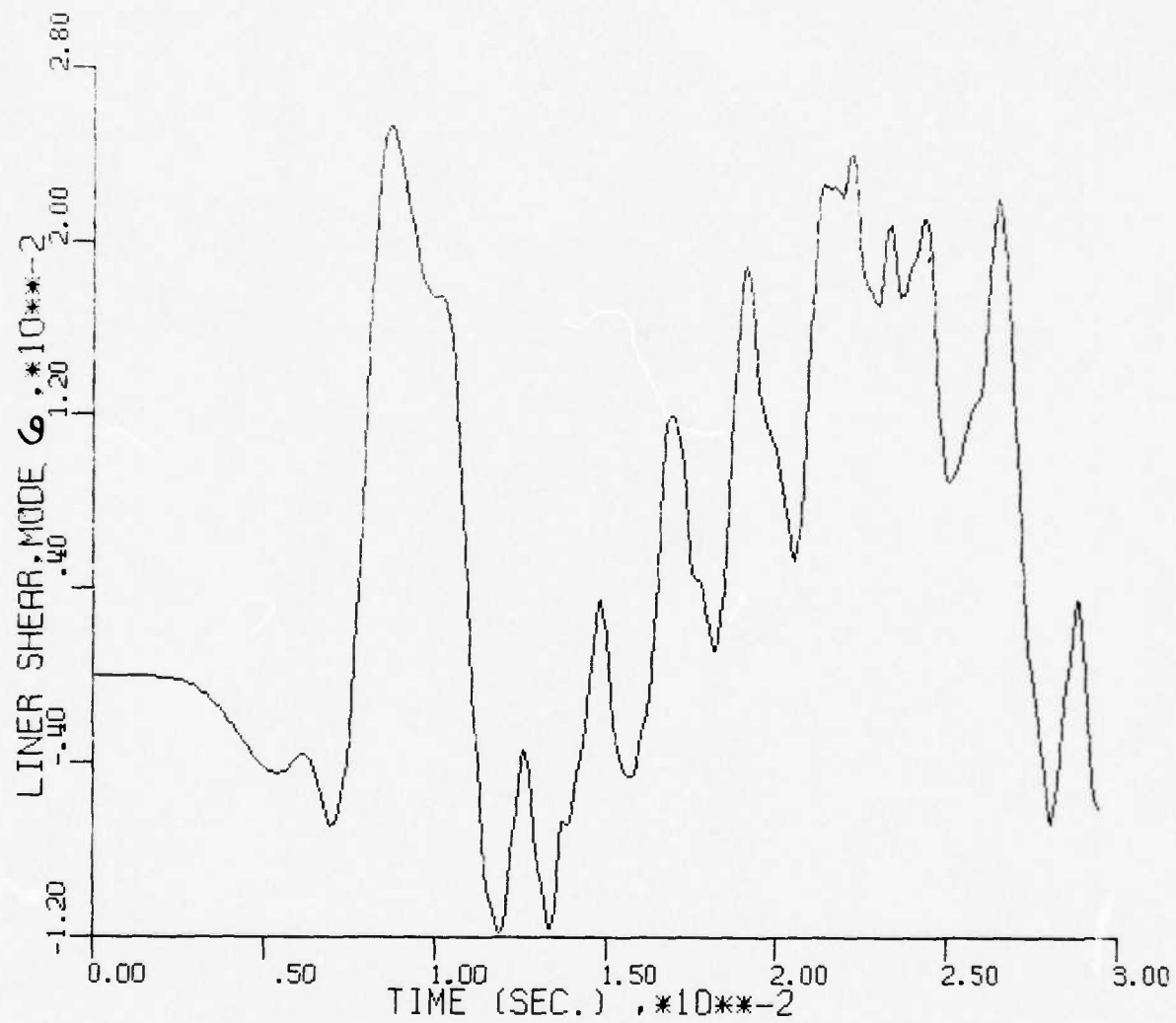


Figure 25f. Nondimensional Liner Shear, Mode 6, Case 5

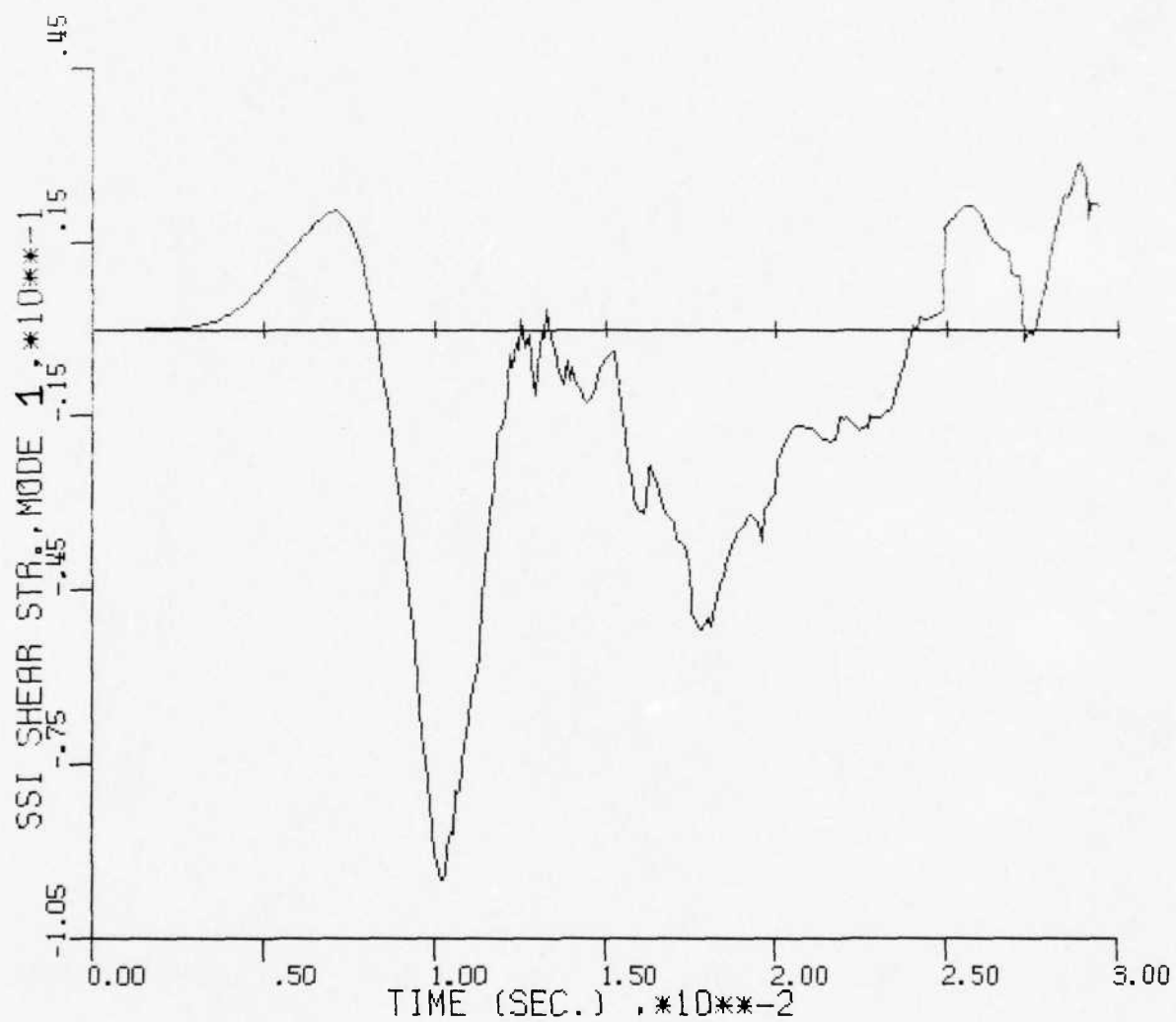
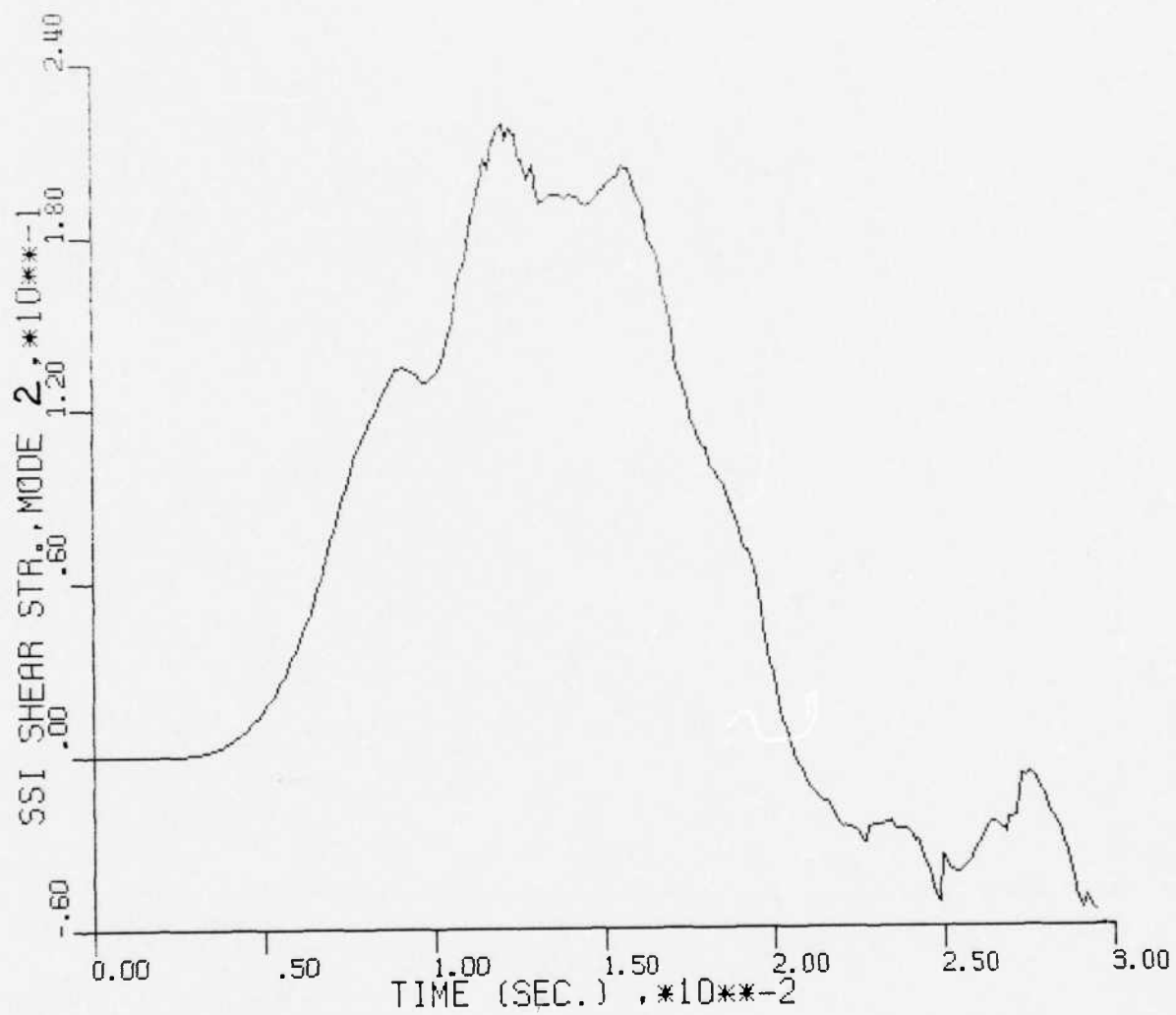
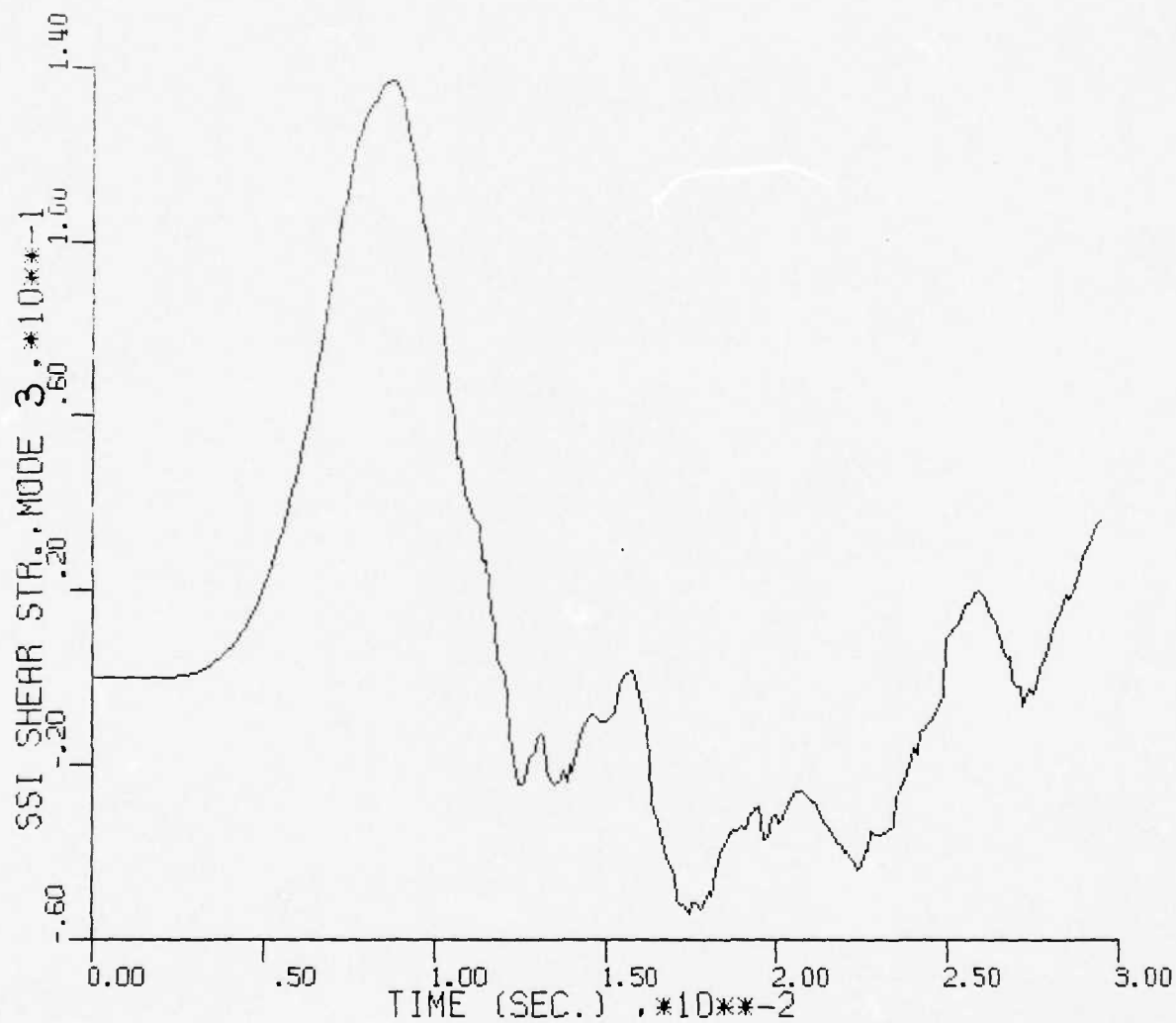


Figure 26a. Nondimensional SSI Shear Stress, Mode 1, Case 5

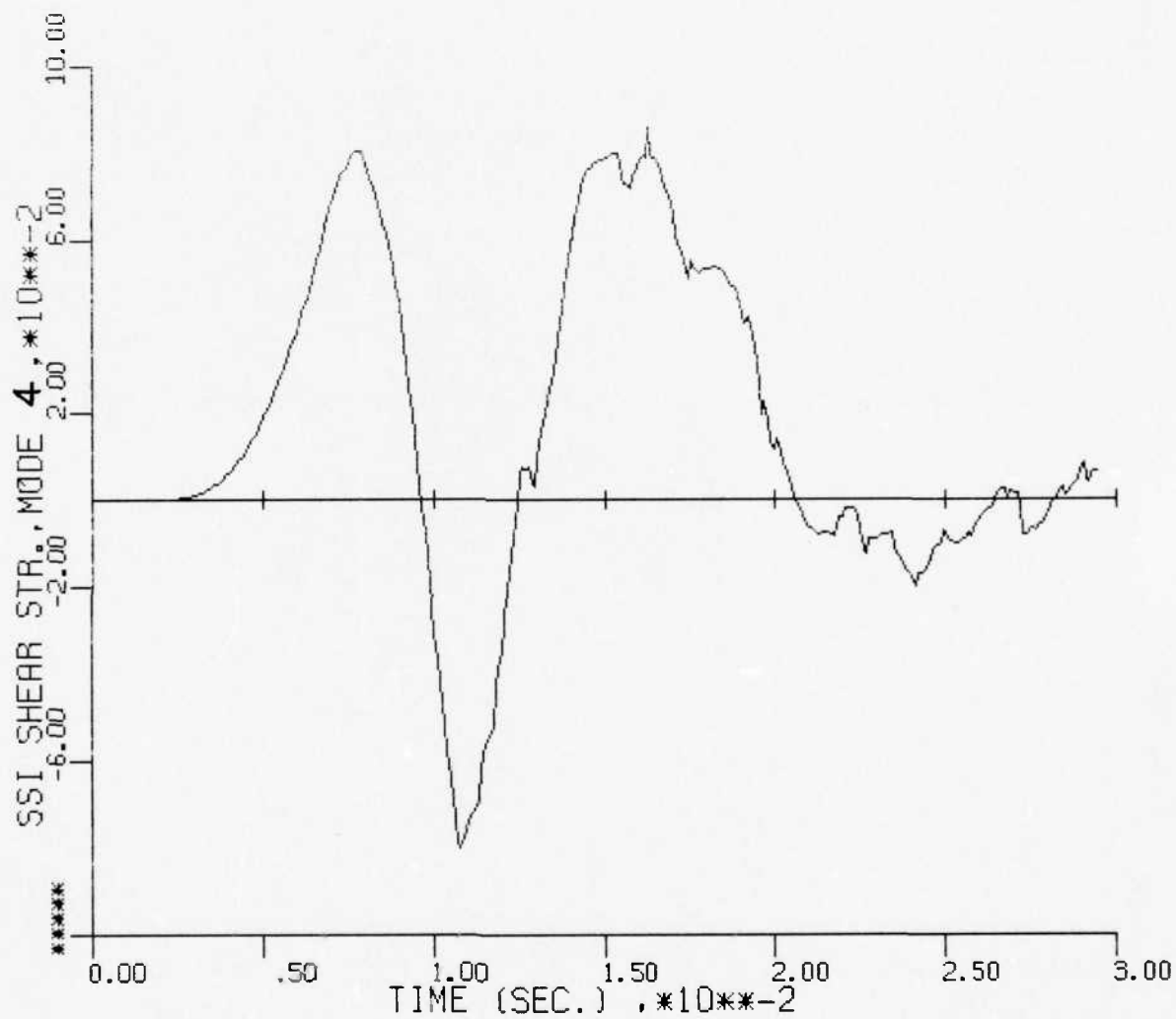


CASE 5
Figure 26b. Nondimensional SSI Shear Stress, Mode 2, Case 5

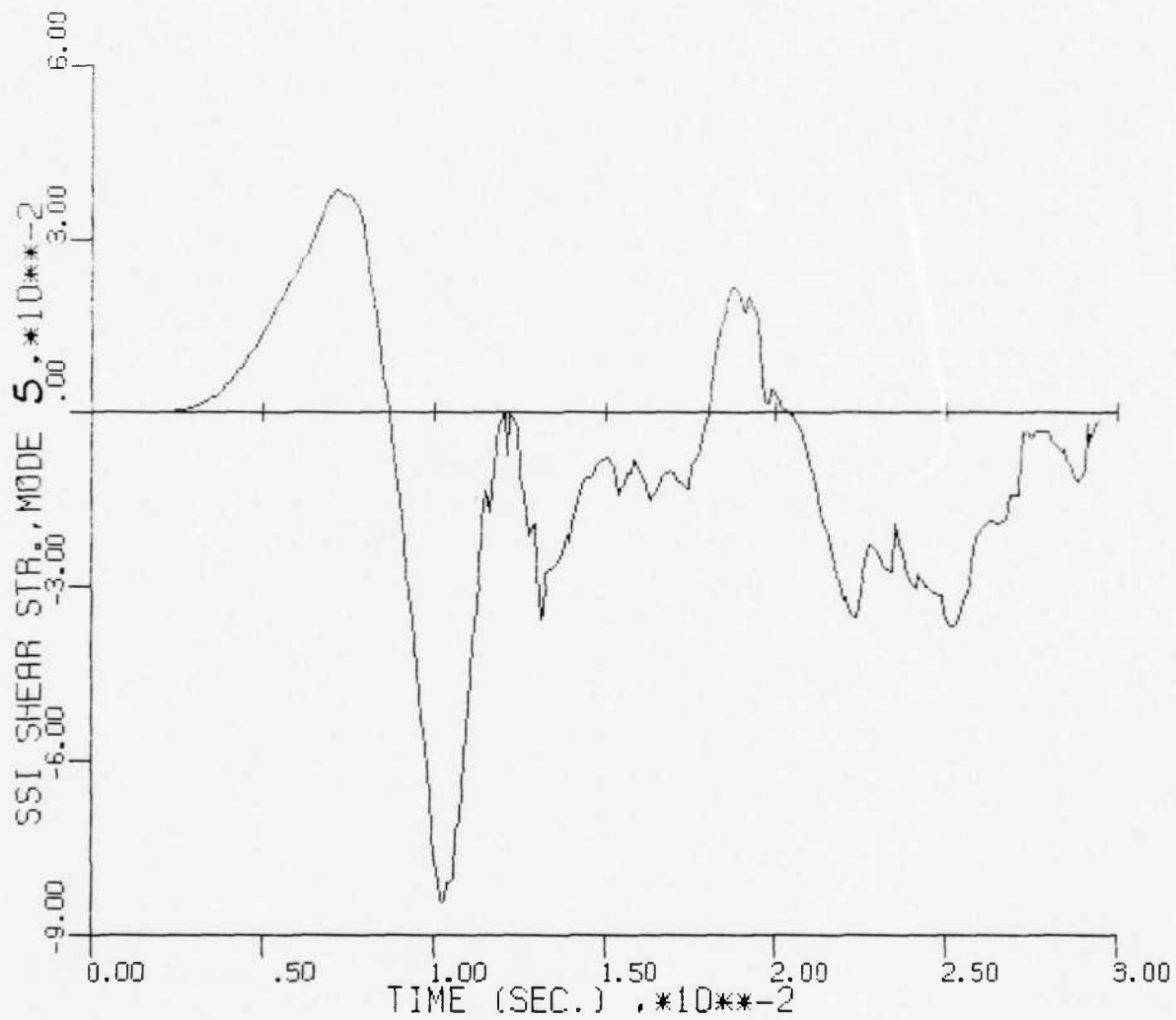


CASE 5

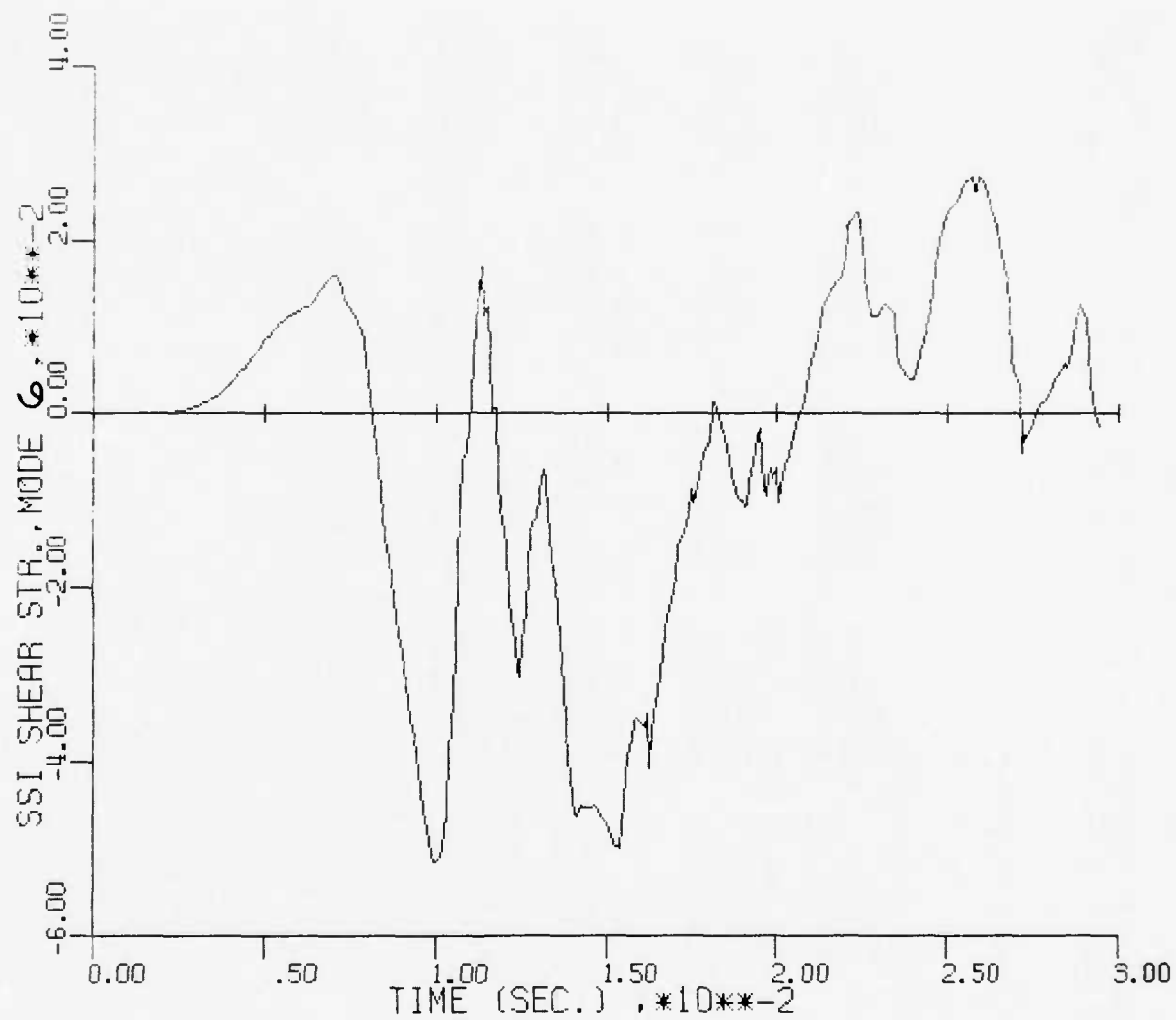
Figure 26c. Nondimensional SSI Shear Stress, Mode 3, Case 5



CASE 5
Figure 26d. Nondimensional SSI Shear Stress, Mode 4, Case 5



CASE 5
Figure 26e. Nondimensional SSI Shear Stress, Mode 5, Case 5



CASE 5

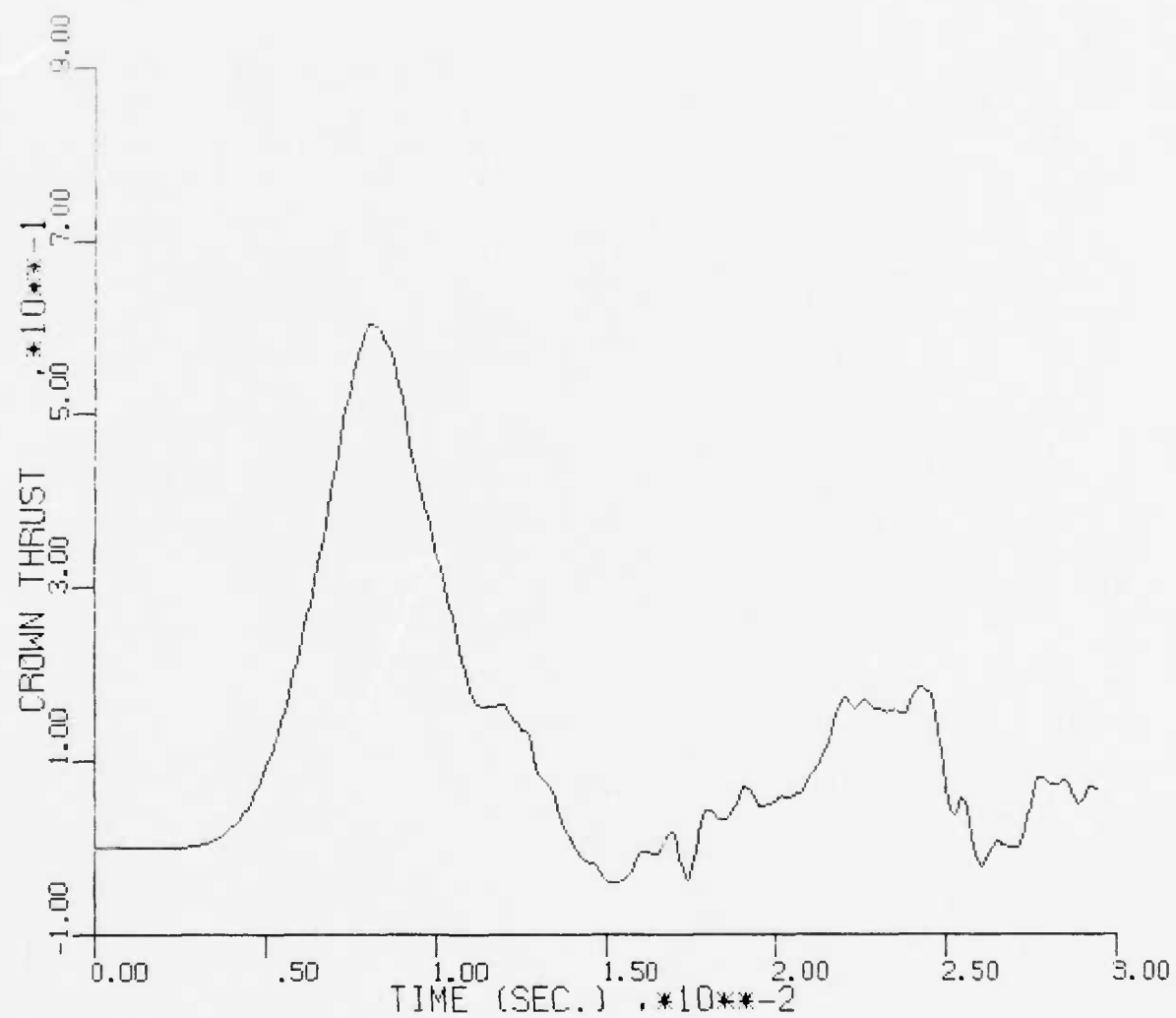
Figure 26f. Nondimensional SSI Shear Stress, Mode 6, Case 5

Table VI

MINIMUM AND MAXIMUM FOURIER MODAL AMPLITUDES OF NONDIMENSIONAL
LINER FORCE RESULTANTS (T,M,V) AND SSI STRESSES ($\sigma_r, \tau_{r\theta}$) CASE 5

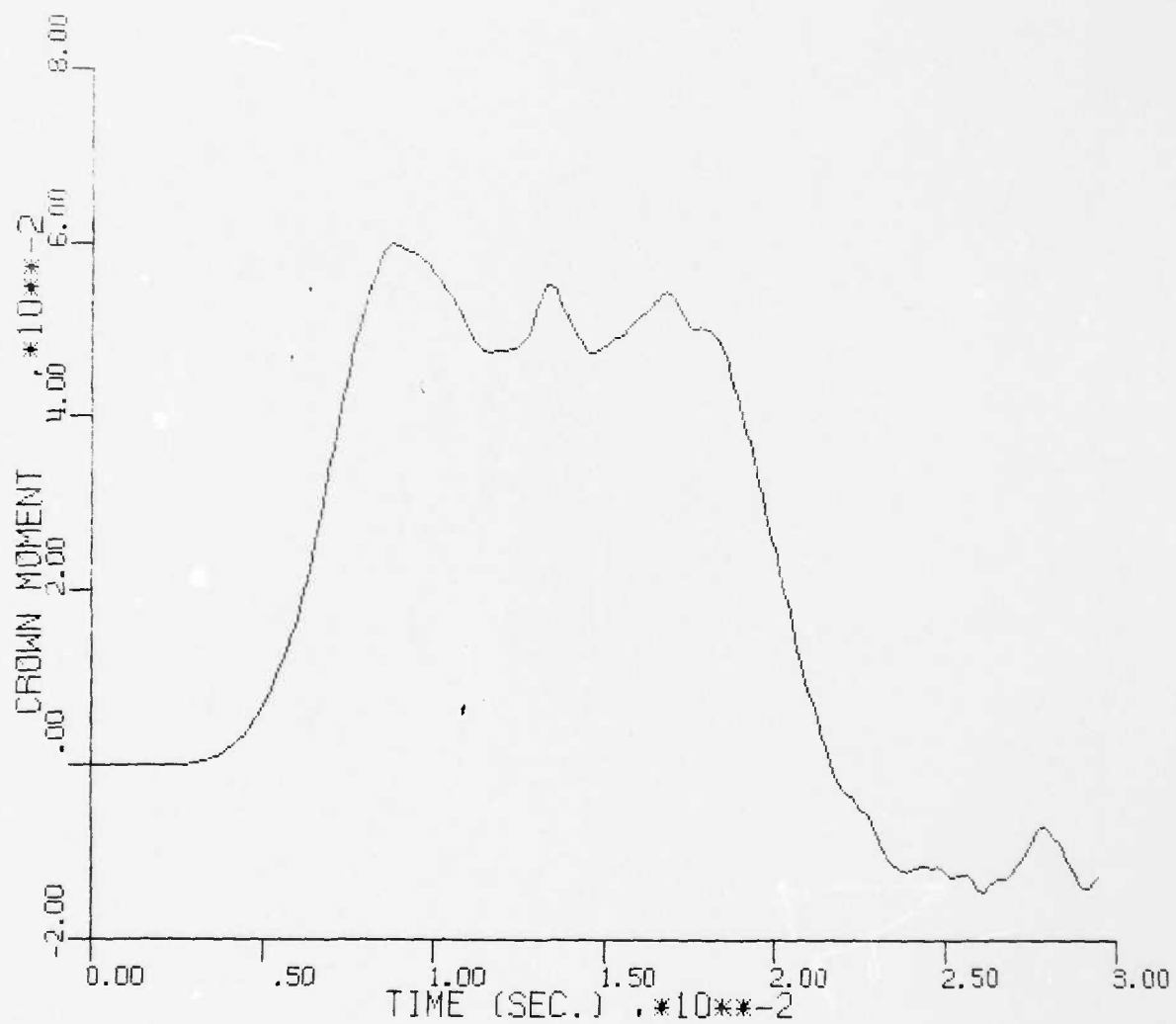
MIN-MAX MODAL AMPLITUDES -- CASE 5

LINER THRUST PLAK MODAL AMPLITUDES						
MODE 0	MODE 1	MODE 2	MODE 3	MODE 4	MODE 5	MODE 6
MIN 0.	-0.99870E-01	-0.32451E+00	0.13107E+00	-0.47704E+01	-0.22575E+01	-0.12733E-01
MAX 0.	0.54571E+00	0.35616E+00	0.92144E-01	0.59044E+01	0.34225E+01	0.15921E-01
LINER MOMENT PLAK MODAL AMPLITUDES						
MODE 0	MODE 1	MODE 2	MODE 3	MODE 4	MODE 5	MODE 6
MIN 0.	-0.22254E-03	-0.14049E-01	-0.31163E-01	-0.14669E+01	-0.56616E-02	-0.26290E-02
MAX 0.	0.68974E-03	0.79299E-01	0.29376E-01	0.68877E+02	0.44147E-02	0.16462E-02
LINER SHEAR PLAK MODAL AMPLITUDES						
MODE 0	MODE 1	MODE 2	MODE 3	MODE 4	MODE 5	MODE 6
MIN 0.	-0.81824E-02	-0.29144E+00	-0.16602E+00	-0.61002E+01	-0.29858E-01	-0.11799E-01
MAX 0.	0.13286E-01	0.51669E-01	0.15413E+00	0.10795E+00	0.55037E-01	0.25311E-01
SSI RADIAL STR. PEAK MODAL AMPLITUDES						
MODE 0	MODE 1	MODE 2	MODE 3	MODE 4	MODE 5	MODE 6
MIN 0.	-0.39531E+00	-0.55680E+00	-0.28193E+00	-0.17491E+00	-0.95009E-01	-0.45482E-01
MAX 0.	0.15183E+00	0.60007E-01	0.16823E+00	0.23482E+00	0.19138E+00	0.11230E+00
SSI SHLAR STR. PEAK MODAL AMPLITUDES						
MODE 0	MODE 1	MODE 2	MODE 3	MODE 4	MODE 5	MODE 6
MIN 0.	-0.94025E-01	-0.54265E-01	-0.53758E-01	-0.80020E-01	-0.84241E-01	-0.51539E-01
MAX 0.	0.28562E-01	0.21894E+00	0.13690E+00	0.85899E-01	0.38453E-01	0.27510E-01



CASE 5

Figure 27a. Nondimensional Crown Thrust History, Case 5



CASE 5
Figure 27b. Nondimensional Crown Moment History, Case 5

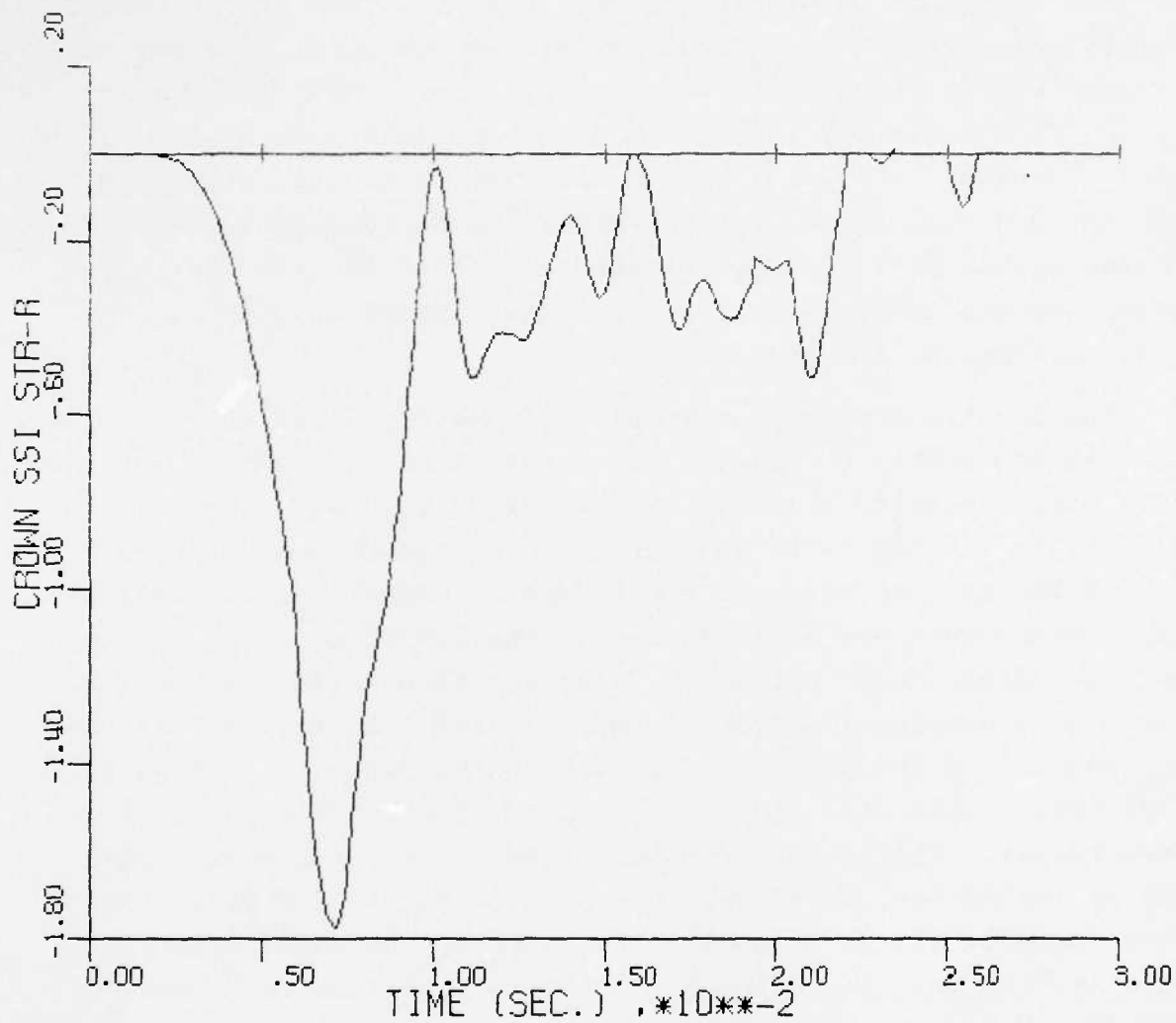


Figure 27c. Nondimensional Crown SSI Radial Stress History, Case 5

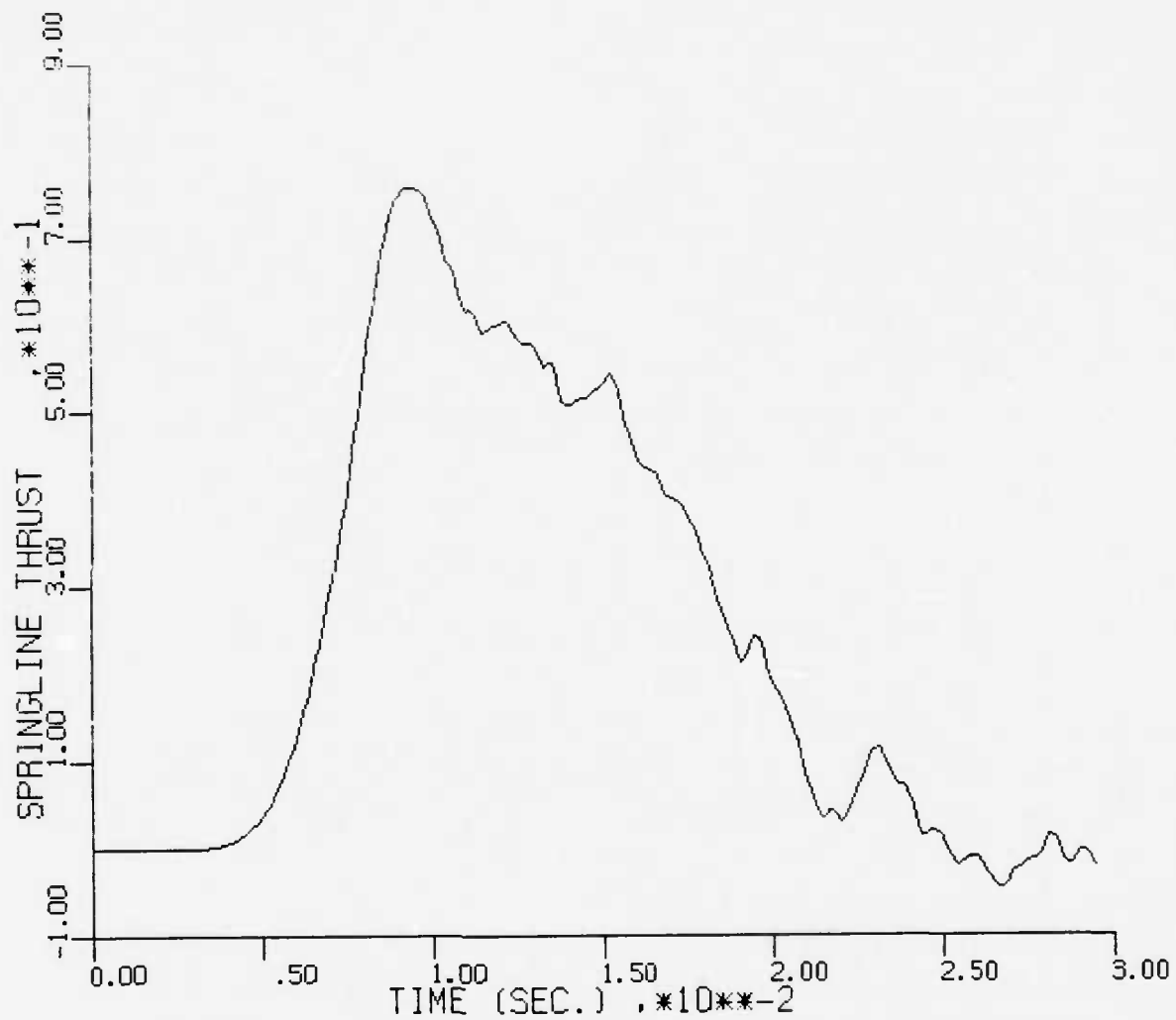
Springline - Ref. Pt. 12, $\theta_{12} = 86.25$ deg, figure 28

Invert - Ref. Pt. 24, $\theta_{24} = 176.25$ deg, figure 29

Hereafter, any allusion to the crown, springline, and invert points will actually correspond to the above identified reference points unless otherwise indicated.

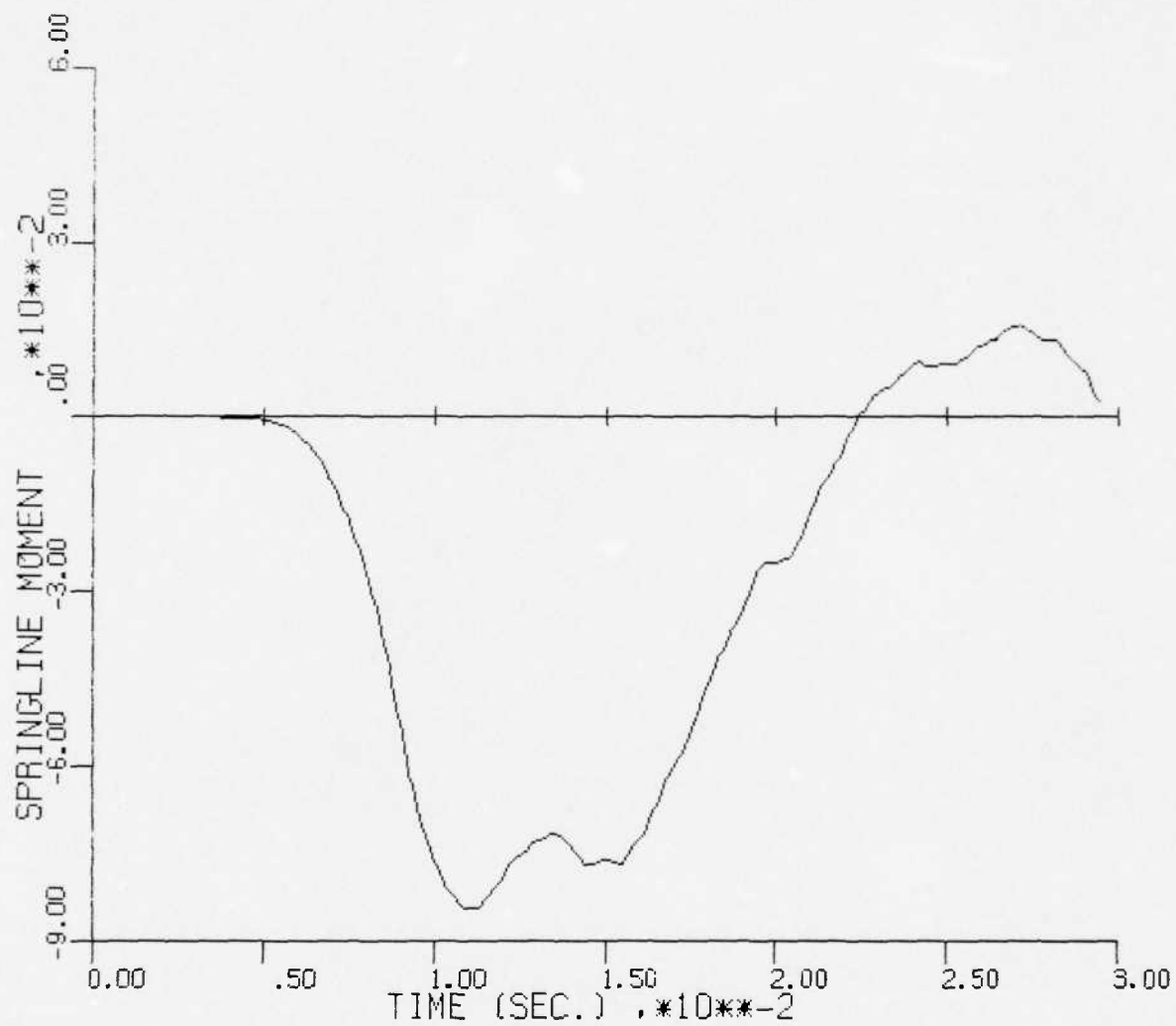
The final bit of processing that was performed on the SAMSON results was directed at indicating which modes contribute the most (or are the most important) when trying to approximate the elementary SAMSON history results by an appropriate combination of the modal histories. Table VII gives the results of this investigation, and a discussion of the parameters given therein follows. Processing was performed on the nondimensional liner moment and thrust, and the SSI radial stress at three reference points, i.e., crown, springline and invert.

The results presented in table VII are described by discussing the Crown Thrust results. First consider the last row of the crown thrust results which is labeled MAX. The last column in this row is labeled INPUT VARIABLE with a magnitude of 0.60422. This is the maximum value of the reference point 1 nondimensional liner thrust that was obtained during the SAMSON solution and is the same value given in table V, also see figure 27a. If only the mode 0 nondimensional thrust history is used (see figure 22a) that was obtained by the process described in the derivation of equation (19d), the result is a single mode (mode 0) approximation to the crown thrust. The maximum nondimensional thrust for this single mode approximation, which for this case is simply the mode 0 max given in table VI, is 0.54571. The ratio of the modal history approximation maximum to the SAMSON history maximum is $0.54571 / 0.60422 = 0.903163$ which is the value given in the Mode 0 column of table VII. The remaining columns for the MAX row are similarly determined except the approximation to the thrust is determined by including the modes 0-n as indicated by the column headings.



CASE 5

Figure 28a. Nondimensional Springline Thrust History, Case 5



CASE 5

Figure 28b. Nondimensional Springline Moment History, Case 5

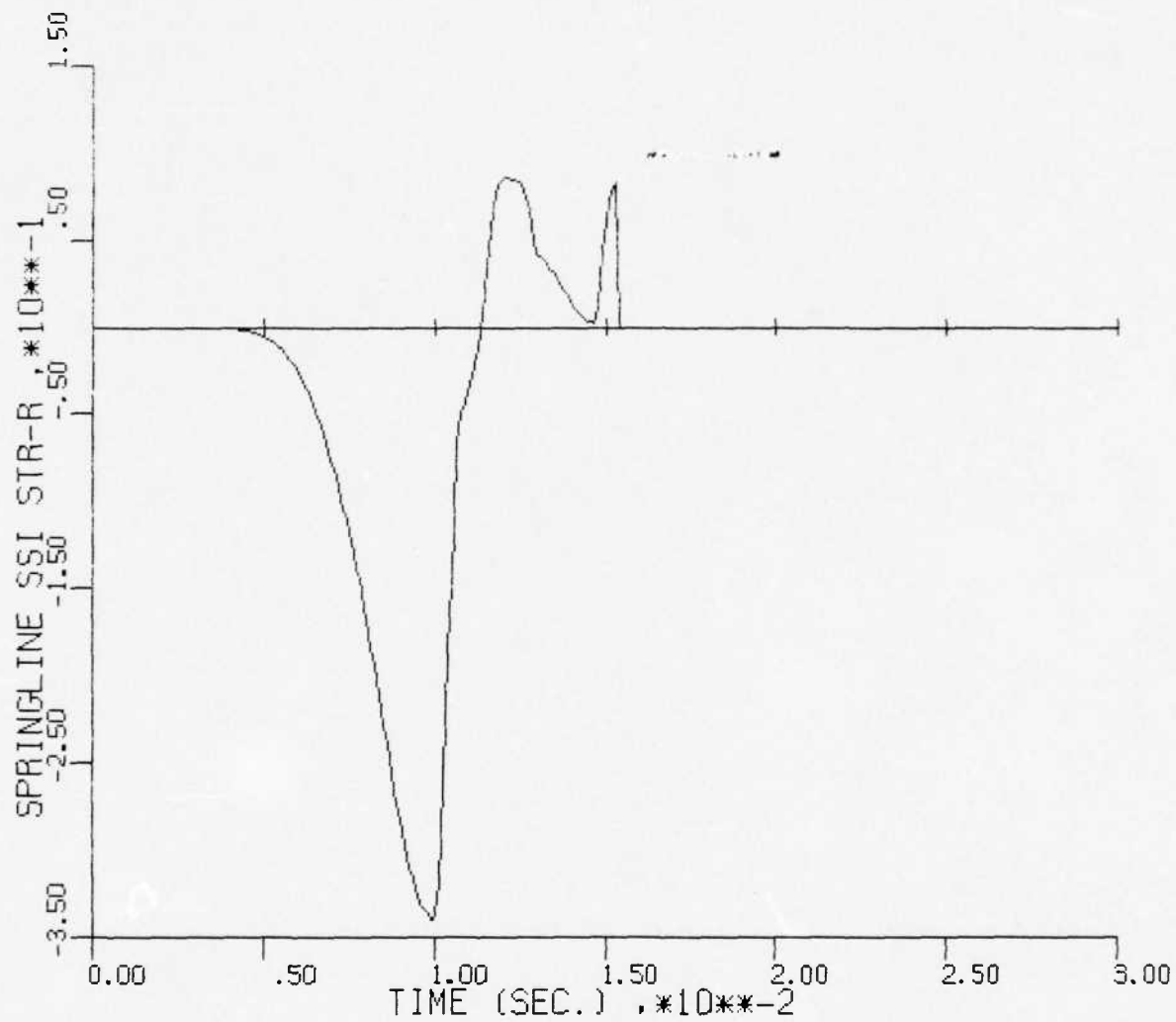
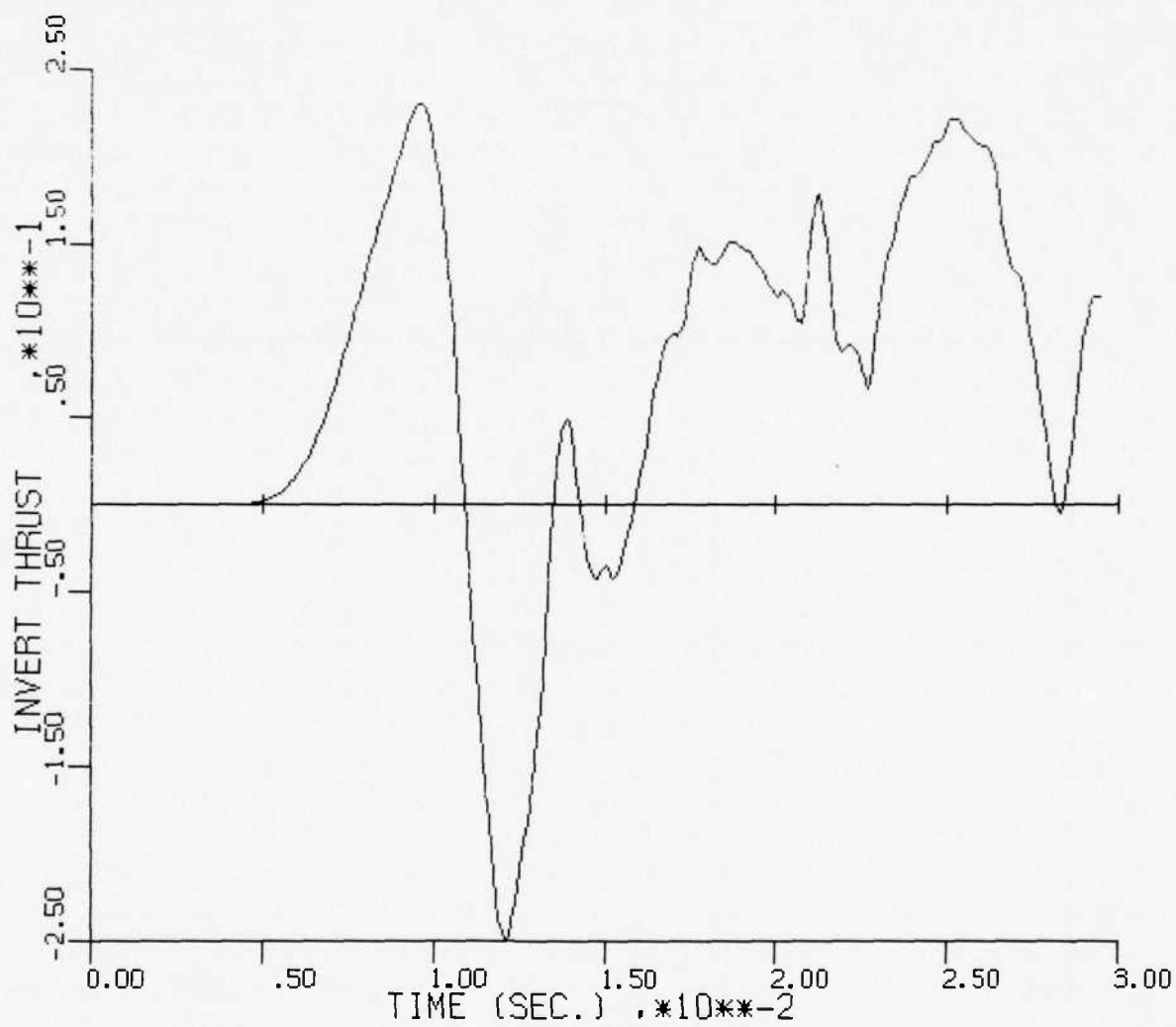
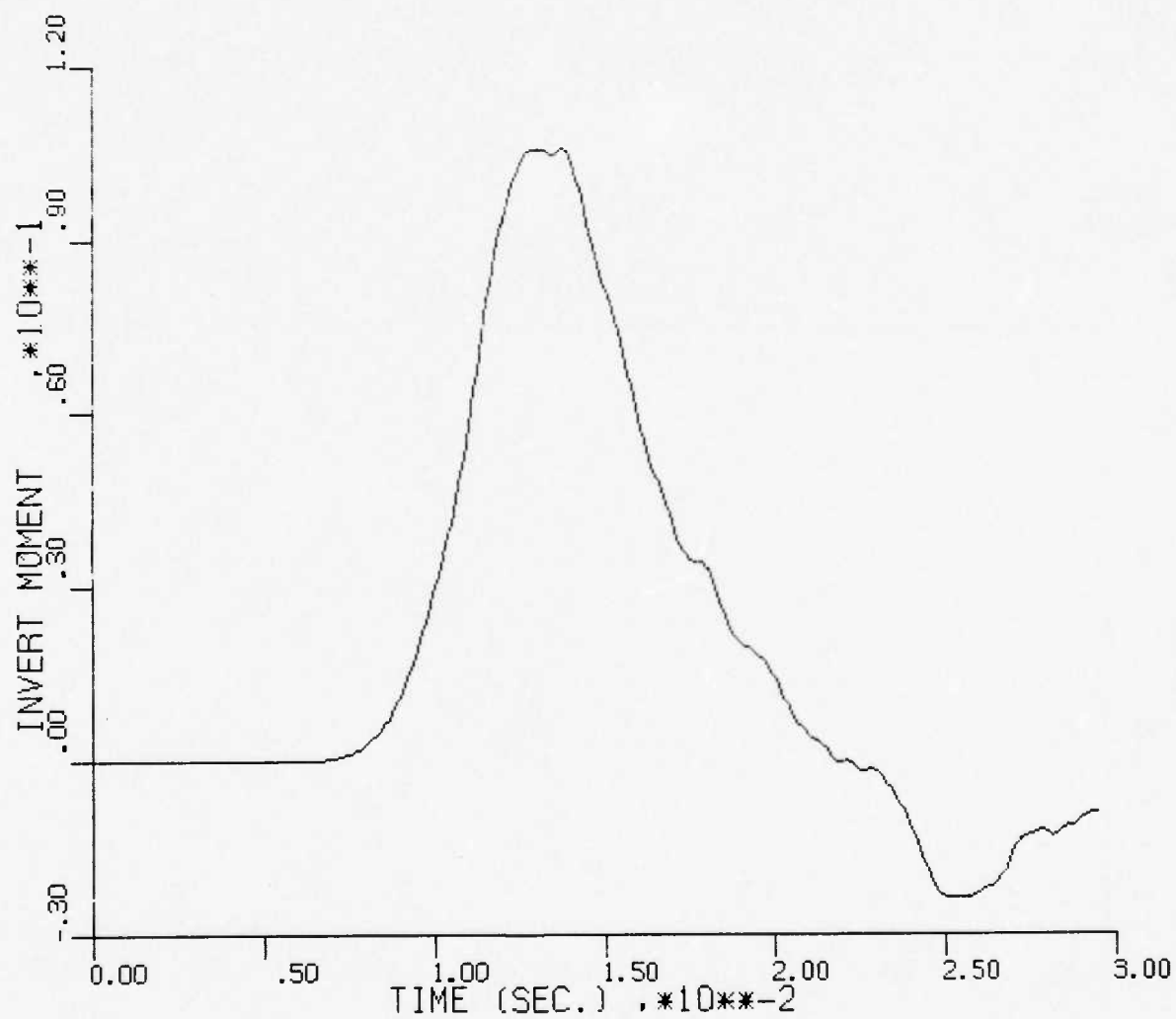


Figure 28c. Nondimensional Springline Radial Stress History, Case 5



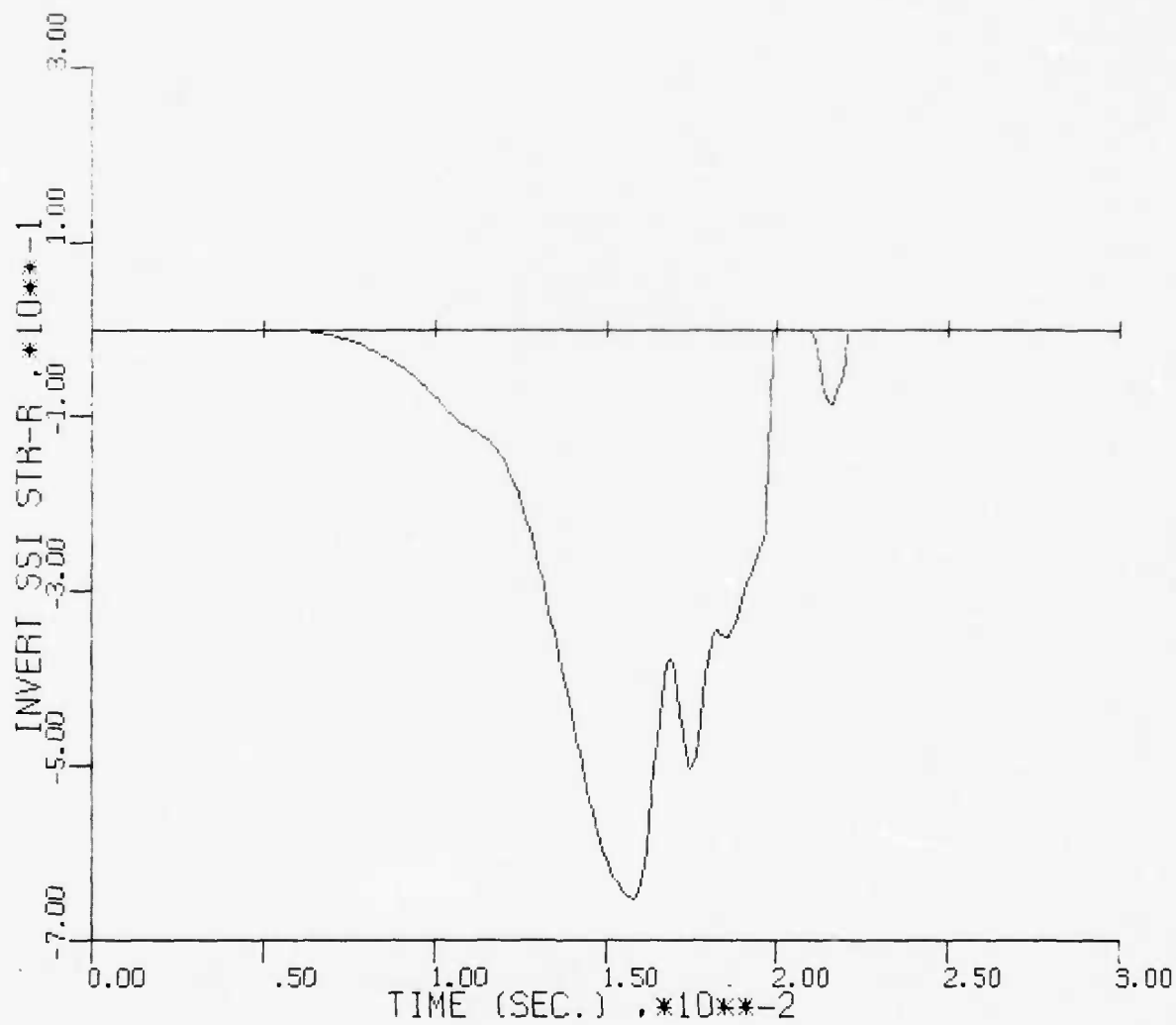
CASE 5

Figure 29a. Nondimensional Invert Thrust History, Case 5



CASE 5

Figure 29b. Nondimensional Invert Moment History, Case 5



CASE 5
Figure 29c. Nondimensional Invert SSI Radial Stress History, Case 5

Table VII
COMPARISON OF MODAL HISTORY APPROXIMATION WITH SAMSON SOLUTION HISTORY (INPUT VARIABLE)

CROWN THRUST									
MODE	U	MODLS	U-1	MODLS	U-2	MODLS	U-3	MODLS	U-6
SRSS	.010588	.017835	.001133	.004820	.002098	.001297	.002818	.00091	.00091
MIN.	0.00000	1.082130	1.893801	1.159131	1.194221	1.226813	1.114163	.40613E+01	.40613E+01
MAX.	.903163	1.438191	1.262856	1.062403	.992212	.980750	.990866	.60422E+00	.60422E+00
CROWN MOMENT									
MODE	U	MODLS	U-1	MODLS	U-2	MODLS	U-3	MODLS	U-6
SRSS	.018507	.018493	.007767	.005591	.000440	.000713	.000091	.17305E+02	.17305E+02
MIN.	.197289	.155585	.988511	.848803	1.121216	.917821	1.037172	.14365E+01	.14365E+01
MAX.	.000031	.000911	1.292321	1.236923	1.110394	1.050505	1.004635	.59835E+01	.59835E+01
CROWN SSI STR-H									
MODE	U	MODLS	U-1	MODLS	U-2	MODLS	U-3	MODLS	U-6
SRSS	.003632	.006022	.000520	.004278	.003410	.002453	.004583	.26820E+01	.26820E+01
MIN.	.22764	.509889	.722592	.875529	.966076	1.001471	1.009098	.17746E+01	.17746E+01
MAX.	0.00000	4.075761	1.238126	4.833084	4.206972	1.040335	5.069456	.93302E+02	.93302E+02
SPRINGLINE THRUST									
MODE	U	MODLS	U-1	MODLS	U-2	MODLS	U-3	MODLS	U-6
SRSS	.006307	.006040	.003364	.002951	.001418	.001265	.000409	.17885E+01	.17885E+01
MIN.	0.00000	0.00000	.958304	.892363	.970208	.867325	.987704	.44009E+01	.44009E+01
MAX.	.720992	.746363	.985659	1.018998	1.011984	1.021105	1.002908	.75689E+00	.75689E+00
SPRINGLINE MOMENT									
MODE	U	MODLS	U-1	MODLS	U-2	MODLS	U-3	MODLS	U-6
SRSS	.003344	.003344	.005321	.005671	.000798	.000723	.000221	.21420E+02	.21420E+02
MIN.	.033552	.033085	.907571	.875928	.979048	.963879	.974507	.84469E+01	.84469E+01
MAX.	.000118	.000174	.874971	.845449	.928965	.954764	1.011517	.15761E+01	.15761E+01

TABLE VII (Concluded)

SPRINGLINE SSI STR-R									

MODE 0	MODLS 0-1	MODLS 0-2	MODLS 0-3	MODLS 0-4	MODLS 0-5	MODLS 0-6	INPUT		
SRSS	.022284	.023245	.057002	.062858	.068184	.067328	VARIABLE		
MIN.	1.163033	1.246053	1.271363	1.277055	.827071	.961935	.43713E-02		
MAX.	0.000000	0.000000	.583489	1.149771	.924200	.186806	-.33989E+00		

INVERT THRUST									

MODE 0	MODLS 0-1	MODLS 0-2	MODLS 0-3	MODLS 0-4	MODLS 0-5	MODLS 0-6	INPUT		
SRSS	.038451	.026654	.000531	.006532	.010962	.007182	VARIABLE		
MIN.	0.000000	.013311	.838042	1.044924	.981852	.986559	.61863E-02		
MAX.	2.371944	1.547691	.902889	1.021160	1.067470	1.016406	-.24918E+00		

INVERT MOMENT									

MODE 0	MODLS 0-1	MODLS 0-2	MODLS 0-3	MODLS 0-4	MODLS 0-5	MODLS 0-6	INPUT		
SRSS	.010951	.010963	.002001	.003819	.001221	.000473	VARIABLE		
MIN.	.119400	.144760	.588161	.688509	.804964	.982261	.20711E-02		
MAX.	.000018	.000192	.729828	1.018165	1.032535	1.003637	-.23736E-01		

INVERT SSI STR-R									

MODE 0	MODLS 0-1	MODLS 0-2	MODLS 0-3	MODLS 0-4	MODLS 0-5	MODLS 0-6	INPUT		
SRSS	.008547	.002924	.010024	.001267	.003310	.005476	VARIABLE		
MIN.	.605234	.593468	.837545	1.058382	.963938	.943716	.11397E-01		
MAX.	0.000000	.216240	.044896	.105293	.024927	.027122	-.65314E+00		

For example, if modes 0 through 5 are used to determine the approximation to the crown thrust (denoted by $T_{0,5}$) the maximum crown thrust derived from these modes would be obtained from

$$\text{Max } T_{0,5} = \text{Max} \left\{ \sum_{n=0}^5 T_n(t_i) \cos n\theta_1 \right\}, i=1,L$$

where $T_n(t_i)$ is the discrete value of the mode n nondimensional thrust at the i th time step and there are a total of L time steps. This maximum divided by the SAMSON max (0.60422) would give the value given in the Mode 0-5 column, which is 0.98075. If the SAMSON peak value, given in the INPUT VARIABLE column, is zero (0) then the peak value obtained from the modal history approximation is not normalized since this would result in division by zero. For this situation, the normalized peak value of the modal history approximation is used in the table. The invert SSI radial maximum stress is an example of this situation.

In an exactly parallel manner, the values given in the row labeled MIN are computed except these results are obtained by dealing with the minimum values of the SAMSON and modal histories.

The first row, labeled SRSS, gives the results from performing square root of sum of squares (SRSS) processing on the data. The last column gives the SRSS of the nondimensional crown thrust. The other columns are determined by computing the SRSS of the difference between the modal history approximation (for the number of modes indicated in the column heading) and the SAMSON response history. The desired result here is a ratio of 0.0, which indicates that there is no difference between the approximate modal history curve and the SAMSON time history curve.

Obviously the desired result of the MODAL HISTORY/INPUT VALUE ratios is 1.0 for the MIN and MAX rows and 0.0 for the SRSS row. A crown thrust history based on modes 0 through 3 gives a reasonably good approximation to the most important peak values of the response and an acceptable SRSS ratio. Additional modes do not significantly change the peak values or the SRSS ratio.

Some of the ratios show some seemingly disparaging results such as the crown SSI radial stress MAX row. The inclusion of modes 0 through 6 for the approximation to this variable does not yield the desired result of approximately 1.0. However, an examination of figure 27c reveals the fact that the maximum radial stress (tension) is so small that even an error of an order of magnitude is not significant.

4. ANALYSIS OF CYLINDRICAL SHELL TO SSI LOADING

This analysis follows closely that presented in reference 9. It presents the response analysis of an elastic cylindrical shell to a transverse shock wave. For this research investigation the shock wave can be represented by the SSI radial and shear stresses such as those computed in the dynamic SAMSON solutions. The effect of viscous damping of the cylinder has been added for this analysis. The dynamic modal response analysis is employed for the solution, and both extensional and inextensional effects are considered. The extensional effects are frequently neglected for analyses of this type; however, they are important during the early time engulfment process.

The basic objective of this analysis was to see if the SSI modal loads computed from the dynamic SAMSON solutions, when applied to a cylinder in vacuo, would produce the same modal internal force resultants (moment and thrust) that were computed from the SAMSON results. The theoretical aspects of the modal analysis are summarized in the following.

a. Displacements (see figure 12)

$$w(\theta, t) = \bar{q}_0(t) + \sum_{n=1}^{\infty} \left[q_n(t) + \bar{q}_n(t) \right] \cos n\theta \quad (21)$$

$$v(\theta, t) = \sum_{n=1}^{\infty} \left[\frac{q_n(t)}{d_n} - d_n \bar{q}_n(t) \right] \sin n\theta \quad (22)$$

where the bar notation ($\bar{}$) denotes the extensional effects and the comparable unbarred variable the inextensional effects. Thus, q_n and

\bar{q}_n are the time varying inextensional and extensional modal amplitudes, respectively. Define $N_1 = n^2 - 1$, $C = t^2 / (12\bar{R}^2)$ then

$$d_n = \frac{N_1}{2n} - \frac{N_1^2}{2n} C + \frac{1}{2} \left[\left(\frac{n^2+1}{n} \right)^2 - \frac{2N_1^3}{n^2} C + \frac{N_1^4}{n^2} C^2 \right]^{1/2} \quad (23a)$$

$$\bar{d}_n = -1/d_n \quad (23b)$$

Note that $d_0 = 0$ and $d_1 = 1$.

b. Exact Circular Frequencies

$$\omega_n^2 = a - \sqrt{a^2 - b} \quad n \geq 1 \quad (24)$$

$$\bar{\omega}_n^2 = a + \sqrt{a^2 - b} \quad n \geq 0 \quad (25)$$

where

$$a = 0.5 e(n^2+1) + 0.5 f N_1^2$$

$$b = e f n^2 N_1^2$$

$$e = \bar{E}_c / (\rho \bar{R}^2)$$

$$f = eC$$

$$\rho = \gamma/g, \text{ mass density}$$

c. Approximate Frequencies

If $n \leq 5$ and $A\bar{R}^2 \gg 1$ or $12 (\bar{R}/t)^2 \gg 1$

$$\omega_n^2 = \frac{\bar{E}_c I}{\rho t \bar{R}} \frac{N_1^2 n^2}{(n^2+1)} = \frac{f(1-n^2)^2 n^2}{n^2+1}$$

$$\bar{\omega}_n^2 = \frac{\bar{E}_c A}{\rho t \bar{R}} (n^2+1) = e(n^2+1)$$

d. Radial and Tangential Shear Loads

$$\sigma_r(\theta, t) = \sum_{n=0}^{\infty} \sigma_{rn}(t) \cos n\theta \quad (26)$$

$$\tau_{r\theta}(\theta, t) = \sum_{n=1}^{\infty} \tau_{r\theta n}(t) \sin n\theta \quad (27)$$

e. Equations of Motion

$$\ddot{q}_n + 2 \zeta_n \omega_n \dot{q}_n + \omega_n^2 q_n = - \frac{\sigma_{rn}(t) - \frac{1}{d_n} \tau_{r\theta n}(t)}{m_n} \quad n \geq 1 \quad (28)$$

$$\ddot{\bar{q}}_n + 2 \zeta_n \bar{\omega}_n \dot{\bar{q}}_n + \bar{\omega}_n^2 \bar{q}_n = - \frac{\sigma_{rn}(t) - \frac{1}{\bar{d}_n} \tau_{r\theta n}(t)}{\bar{m}_n} \quad n \geq 0 \quad (29)$$

where

$$m_n = \rho t (1 + \frac{1}{d_n^2}) \quad (30a)$$

$$\bar{m}_n = \rho t (1 + \bar{d}_n^2) \quad (30b)$$

$$(\dot{}) = \frac{d()}{dt}$$

ζ_n = Fraction of critical damping

Note that $1/\bar{d}_n = 0$ for $n=0$.

To get the solution for the separate effects of the radial (R) and tangential (T) shear loads the following equations are presented.

Equations of Motion for Radial Loads

$$\ddot{q}_n^R + 2 \zeta_n \omega_n \dot{q}_n^R + \omega_n^2 q_n^R = - \sigma_{rn}(t)/m_n, \quad n \geq 1 \quad (31a)$$

$$\ddot{\bar{q}}_n^R + 2 \zeta_n \bar{\omega}_n \dot{\bar{q}}_n^R + \bar{\omega}_n^2 \bar{q}_n^R = - \sigma_{rn}(t)/\bar{m}_n, \quad n \geq 0 \quad (31b)$$

Equations of Motion for Shear Loads

$$\ddot{q}_n^T + 2 \zeta_n \omega_n \dot{q}_n^T + \omega_n^2 q_n^T = \tau_{r\theta n}(t)/d_n/m_n, \quad n \geq 1 \quad (31c)$$

$$\ddot{\bar{q}}_n^T + 2 \zeta_n \bar{\omega}_n \dot{\bar{q}}_n^T + \bar{\omega}_n^2 \bar{q}_n^T = \tau_{r\theta n}(t)/\bar{d}_n/\bar{m}_n, \quad n \geq 1 \quad (31d)$$

Note that for equation (31d) the $n=0$ mode does not exist since $\tau_{r\theta n} = 0$ and $1/\bar{d}_n = 0$ for the zero mode. The complete solution is obviously

$$q_n = q_n^R + q_n^T \quad n \geq 1 \quad \text{Inextensional solution} \quad (32a)$$

$$\bar{q}_n = \begin{cases} \bar{q}_n^R & n = 0 \\ \bar{q}_n^R + \bar{q}_n^T & n \geq 1 \end{cases} \quad \text{Extensional solution} \quad (32b)$$

$$(32c)$$

f. Cylinder Force Resultants

$$M = \frac{-K}{R^2} (w + w'') \quad (33a)$$

$$T = \frac{D}{R} (w - v') - \frac{M}{R} \quad (33b)$$

where

$$K = \bar{E}_c I = \bar{E}_c t^3/12 \quad (33c)$$

$$D = A\bar{E}_c = \bar{E}_c t \quad (33d)$$

$$(\)' = \frac{d(\)}{d\theta}$$

The radial and tangential displacements, equations (21) and (22), can also be written as

$$w(\theta, t) = w_0(t) + \sum_{n=1}^{\infty} w_n(t) \cos n\theta \quad (34a)$$

where

$$w_0(t) = \bar{q}_0(t) \quad (34b)$$

$$w_n(t) = q_n(t) + \bar{q}_n(t) \quad (34c)$$

$$v(\theta, t) = \sum_{n=1}^{\infty} v_n(t) \sin n\theta \quad (35a)$$

where

$$v_n(t) = \frac{q_n(t)}{d_n} - d_n \bar{q}_n(t) \quad (35b)$$

Thus,

$$w + w'' = w_0 + \sum_{n=1}^{\infty} (1-n^2) w_n \cos n\theta \quad (36)$$

$$w - v' = w_0 + \sum_{n=1}^{\infty} (w_n - nv_n) \cos n\theta \quad (37)$$

From equations (33a) and (36)

$$M = \frac{-K}{R^2} \left\{ w_0 + \sum_{n=1}^{\infty} (1-n^2) w_n \cos n\theta \right\} \quad (38a)$$

$$= -\frac{K}{R^2} \left\{ \bar{q}_0 + \sum_{n=1}^{\infty} (1-n^2) (q_n + \bar{q}_n) \cos n\theta \right\} \quad (38b)$$

or

$$M = \bar{M}_0 + \sum_{n=1}^{\infty} \bar{M}_n \cos n\theta + \sum_{n=1}^{\infty} M_n \cos n\theta \quad (38c)$$

where

\bar{M}_n = Moments from extensional effects

$$\bar{M}_n = -\frac{K}{R^2} (1-n^2) \bar{q}_n \quad n \geq 0 \quad (38d)$$

M_n = Moments from inextensional effects

$$M_n = -\frac{K}{R^2} (1-n^2) q_n \quad n \geq 1 \quad (38e)$$

Note that both components of the moment are zero for mode 1 since $1-n^2=0$. From equations (37) and (33b) obtain

$$T = \frac{D}{R} \left[w_0 + \sum_{n=1}^{\infty} (w_n - nv_n) \cos n\theta \right] - M/R \quad (39a)$$

$$= \frac{D}{R} \left[\bar{q}_0 + \sum_{n=1}^{\infty} \left(q_n + \bar{q}_n - \frac{nq_n}{d_n} + nd_n \bar{q}_n \right) \cos n\theta \right] - M/R \quad (39b)$$

or

$$T = \bar{T}_0 + \sum_{n=1}^{\infty} \bar{T}_n \cos n\theta + \sum_{n=1}^{\infty} T_n \cos n\theta - M/R \quad (39c)$$

The last term (M/R) is usually neglected; however, it is retained in this analysis.

In equation (39c)

$$\begin{aligned} \bar{T}_n &= \text{Thrusts from extensional effects} \\ &= \frac{D}{R} \bar{q}_n (1 + n d_n) + \frac{K}{R^3} (1 - n^2) \bar{q}_n \\ &= \frac{D}{R} \bar{q}_n (1 - n/\bar{d}_n) + \frac{K}{R^3} (1 - n^2) \bar{q}_n \quad n \geq 0 \end{aligned} \quad (39d)$$

Note that $1 - n/\bar{d}_n = 1$ and 2 for $n=0$ and 1 .

$$\begin{aligned} T_n &= \text{Thrusts from inextensional effects} \\ &= \frac{D}{R} q_n (1 - n/d_n) + \frac{K}{R^3} (1 - n^2) q_n \quad n \geq 2 \end{aligned} \quad (39e)$$

Also note that $d_n = n$ for $n=1$ thrust $T_1 = 0$ and this has been used to define the applicable range of n for equation (39e).

The nondimensional equations of internal liner forces for the separate effects of radial and tangential SSI loads can be written as follows.

g. Nondimensional Moment Modal Amplitudes

$$\begin{aligned} \frac{M_n^R}{p_0 R^2} &= \text{Nondimensional modal amplitude for SSI } \sigma_r \text{ load only} \\ &= - \frac{K}{R^2 R^2} (1 - n^2) \begin{cases} \bar{q}_n^R / p_0, & n=0 \text{ since } q_n^R = 0 \text{ for } n=0 & (40a) \\ 0, & n=1 \text{ since } 1 - n^2 = 0 \text{ for } n=1 & (40b) \\ \left(\frac{q_n^R}{p_0} + \frac{\bar{q}_n^R}{p_0} \right) & n \geq 2 & (40c) \end{cases} \end{aligned}$$

$$\frac{M_n^T}{p_o R^2} = \text{Nondimensional modal amplitude for SSI } \tau_{r\theta} \text{ load only}$$

$$= -\frac{K}{R^2 \bar{R}^2} (1-n^2) \begin{cases} 0, & n < 2 \quad \text{since } \tau_{r\theta n} = 0 \text{ for } n=0 \\ & \text{and } 1-n^2=0 \text{ for } n=1 \end{cases} \quad (40d)$$

$$\begin{cases} \frac{q_n^T}{p_o} + \frac{\bar{q}_n^T}{p_o} & n \geq 2 \end{cases} \quad (40e)$$

h. Nondimensional Thrust Modal Amplitudes

$$\frac{T_n^R}{p_o R} = \begin{cases} \left[\frac{D}{R\bar{R}} + \frac{K}{R^2 \bar{R}^2} (1-n^2) \right] \frac{\bar{q}_n^R}{p_o} & n=0 \end{cases} \quad (41a)$$

$$\frac{T_n^R}{p_o R} = \begin{cases} \frac{D}{R\bar{R}} \left(1 - \frac{n}{\bar{d}_n} \right) \frac{\bar{q}_n^R}{p_o} & n=1 \end{cases} \quad (41b)$$

$$\frac{T_n^R}{p_o R} = \begin{cases} \left[\frac{D}{R\bar{R}} \left(1 - \frac{n}{\bar{d}_n} \right) + \frac{K}{R^2 \bar{R}^2} (1-n^2) \right] \frac{\bar{q}_n^R}{p_o} + \left[\frac{D}{R\bar{R}} \left(1 - \frac{n}{\bar{d}_n} \right) + \frac{K}{R^2 \bar{R}^2} (1-n^2) \right] \frac{q_n^R}{p_o} & n \geq 2 \end{cases} \quad (41c)$$

$$\frac{T_n^T}{p_o R} = \begin{cases} 0 & n=0 \end{cases} \quad (41d)$$

$$\frac{T_n^T}{p_o R} = \begin{cases} \frac{D}{R\bar{R}} \left(1 - \frac{n}{\bar{d}_n} \right) \frac{\bar{q}_n^T}{p_o} & n=1 \end{cases} \quad (41e)$$

$$\frac{T_n^T}{p_o R} = \begin{cases} \left[\frac{D}{R\bar{R}} \left(1 - \frac{n}{\bar{d}_n} \right) + \frac{K}{R^2 \bar{R}^2} (1-n^2) \right] \frac{\bar{q}_n^T}{p_o} + \left[\frac{D}{R\bar{R}} \left(1 - \frac{n}{\bar{d}_n} \right) + \frac{K}{R^2 \bar{R}^2} (1-n^2) \right] \frac{q_n^T}{p_o} & n \geq 2 \end{cases} \quad (41f)$$

i. Application of Method

The above analysis has been applied to two of the SAMSON solutions, cases 5 and 13. A computer code was written which used the SSI radial and shear stress modal loads that were computed from the SAMSON solution (see section III for derivation of these modal histories). These modal loads were used in the equations of motion, equations (31a), (31b), (31c) and (31d), which were solved

numerically by a Runge-Kutta technique for the extensional and in-extensional modal displacement histories for all modes up to $n=7$. These results were then used to compute the nondimensional modal thrust and moment variations, equations (40) and (41). Finally, the liner forces computed by this process, which are referred to as the analytical liner forces, are compared to those computed from SAMSON results. These latter liner forces are referred to as the SAMSON liner forces. The analytical modal thrusts compared fairly well with the SAMSON modal thrust for both cases 5 and 13. The modal moments did not compare very well for some of the modes, especially mode 2.

The details of the method employed to make the comparisons and to measure the influence of the separate effects of the radial and shear SSI stresses are now discussed. Tables VIII and IX give the vibrational characteristics of modes 0 through 6 for the two cylinders for cases 5 and 13 ($R/t = 4$ and 15). The outer radius and the liner thickness used for these cases are

	<u>Case 5</u>	<u>Case 13</u>
R/t	4	15
R, inch (m)	104.99 (2.667)	84.37 (2.143)
t, inch (m)	26.25 (0.667)	5.63 (0.143)

These values are consistent with the 2.0 m inside tunnel radius that has been used in this project. In the tables for the $n=1$ mode, a very small value for the inextensional frequency (0.1×10^{-8}) has been used instead of 0.0.

The column headings for tables VIII and IX denote the following:

<u>Heading</u>	<u>Parameter</u>
OMEGA-SQ.	ω_n^2
OMEGA-BAR-SQ	$\bar{\omega}_n^2$
FREQ.	$f_n = \omega_n / 2\pi$, frequency (Hz)
FREQ.-BAR	\bar{f}_n
T	$T_n = 1/f_n$, period (sec)

Table VIII
MODAL VIBRATION PARAMETERS (R/t = 4) CASE 5

N	OMEGA-SQ.	OMEGA-BAR-SQ.	FREQ.	FREQ.-BAR	T	T-BAR	D
0	0.	.105810E+07		.204939E+03		.487949E-02	.100000E+0
1		.329378E+07	.100000E-08	.286847E+13	.100000E+10	.346200E-02	.197556E+0
2	.004912E+05	.025482E+07	.451538E+02	.457271E+03	.221465E-01	.216089E-02	.286993E+0
3	.642611E+06	.165435E+08	.127583E+03	.647343E+03	.783801E-02	.154478E-02	.364181E+0
4	.235959E+07	.281591E+08	.244477E+03	.844558E+03	.409036E-02	.118405E-02	.425129E+0
5	.616519E+07	.431092E+08	.395174E+03	.104497E+04	.253050E-02	.956963E-03	.465865E+0
6	.132544E+08	.614091E+08	.579429E+03	.124720E+04	.172584E-02	.801795E-03	

GENERALIZED MASSES

N	MASS	MASS-BAR
0		.590285E-02
1	.118057E-01	.118057E-01
2	.741530E-02	.289408E-01
3	.661952E-02	.545218E-01
4	.634792E-02	.841911E-01
5	.622945E-02	.112586E+00
6	.617483E-02	.134012E+00

Table IX
MODAL VIBRATION PARAMETERS (R/t = 15) CASE 13

N	OMEGA-SQ.	OMEGA-BAR-SQ.	FREQ.	FREQ.-BAR	T	T-BAR	D
0	0.	.209041E+07		.230110E+03		.434571E-02	
1		.417916E+07	.100000E+08	.325360E+03	.100000E+10	.307352E-02	.100000E+01
2	.596820E+04	.104494E+08	.122954E+02	.514477E+03	.813314E-01	.194372E-02	.199857E+01
3	.477403E+05	.204011E+08	.347746E+02	.727620E+03	.287566E-01	.137431E-02	.299238E+01
4	.175506E+06	.355339E+08	.666755E+02	.948728E+03	.149980E-01	.105400E-02	.397900E+01
5	.459002E+06	.543476E+08	.107827E+03	.117330E+04	.927412E-02	.852291E-03	.495607E+01
6	.987765E+06	.773423E+08	.158178E+03	.139968E+04	.632198E-02	.714449E-03	.592122E+01

GENERALIZED MASSES

N	MASS	MASS-BAR
0		.126535E-02
1	.253069E-02	.253069E-02
2	.158213E-02	.631951E-02
3	.140666E-02	.125957E-01
4	.134527E-02	.212989E-01
5	.131686E-02	.323455E-01
6	.130144E-02	.456294E-01

T-BAR	ϵ_n
D	d_n
MASS	m_n
MASS-BAR	\bar{m}_n

In an effort to efficiently assess the effect of each SSI modal load component on the response of the cylinder, maximum and minimum analytical values of the moment and thrust at the crown, springline and invert were computed and compared with the corresponding peak values obtained from the SAMSON time history results. These comparisons are given in tables X through XIII and are similar to those in table VII. The modal forces (thrusts and moments) used for table VII were computed directly from the SAMSON tunnel liner force histories whereas tables X through XIII were computed from the response of the cylinder in vacuo to the SSI (SAMSON) modal loads for tables IX through XII. Furthermore, the time of occurrences of the peak moment and thrust for both the analytical and the SAMSON results are given in tables X through XIII to compare this important aspect of the problem.

The comparisons given in these tables are described by discussing the "Crown Thrust" results. First consider the two rows labeled MAX-2 and T-MAX-2. The last column, Exact Response, gives the maximum value of the nondimensional crown thrust (0.60422) and the time of occurrence (0.0081 sec) from the SAMSON solution for reference point 1. Knowing the analytical modal thrust amplitude histories (T_n^R , T_n^T) for the separate effects of the radial and shear SSI loads, the crown ($\theta_1 = 3.75$ deg) thrust history is calculated for a mode by mode addition of these modal amplitude histories. The maximum value of the crown thrust was computed for each addition of a mode to the analytical history, and then this maximum thrust is normalized by dividing by the SAMSON maximum value. These are the normalized values that are presented in the MAX-1 and MAX-2 rows for the columns labeled MODE=0 through 6. As indicated in the table, the -2 row includes the response from both the radial and the shear SSI modal loads for modes 0 through N where N

TABLE X
COMPARISON OF PEAK THRUSTS FROM ANALYTICAL MODES WITH SAMSON RESULTS, CASE 5

CASE 5	UNPLT THRUST (3.75-DEGREES)	COMPUTED MODAL RESPONSE/EXACT RESPONSE	EXACT RESPONSE				
*****	*****	*****	*****				
CURRENT MODE=0	1	2	3				
MIN-1	.735571	1.030707	2.771802	3.680330	3.972331	4.150067	4.137526
-2	.735571	2.108251	3.453066	3.792949	4.147185	4.222664	4.124051
T-MIN-1	.0291750	.0294000	.0294000	.0195750	.0195000	.0195750	.0195750
-2	.0291750	.0294000	.0195750	.0195750	.0195000	.0195750	.0195750
MAX-1	.769413	1.307061	1.259050	1.133297	1.028575	.987907	.979178
-2	.769413	1.206257	1.215058	1.058604	.994001	.976648	.976754
T-MAX-1	.0087750	.0082500	.0081000	.0079500	.0078750	.0079500	.0079500
-2	.0087750	.0082500	.0081000	.0079500	.0078750	.0079500	.0079500

RESPONSE CALC. FROM BOTH RADIAL AND SHEAR MODAL LOADS FOR MODES 0 THRU CURRENT MODE
RESAVE AS 2 EXCEPT RESPONSE FOR SHEAR MODAL LOADS FOR CURRENT MODE IS NOT INCL.

NOTE IF MIN.(OR MAX.) EXACT RESPONSE IS .01. 1.1-6 . MODAL MIN.(OR MAX.) HAS NOT BEEN NORMALIZED

CASE 5	SPRINGING THRUST (86.25-DEGREES)							
	*****		COMPUTED MODAL RESPONSE/EXACT RESPONSE		*****		EXACT RESPONSE	
CURRENT MODE=0	1	2	3	4	5	6		
MIN-1	.078010	.343132	2.654722	2.439069	2.410862	2.410529		
-2	.078010	2.644000	2.635008	2.457575	2.413189	2.429085		
T-MIN-1	.0291750	.0290250	.0292500	.0292500	.0293250	.0294000		
-2	.0291750	.0292500	.0292500	.0293250	.0293250	.0294000		.0267000
MAX-1	.037770	.740164	.837289	.850941	.839827	.838749		
-2	.037770	.419532	.850867	.836467	.842491	.831431		.75689E+00
T-MAX-1	.0087750	.0090000	.0090000	.0091500	.0093000	.0093000		
-2	.0087750	.0090000	.0090000	.0093000	.0093750	.0092250		.0093750

CASE 5	INVERT THRUST (176.25-DEGREES)							
CURRENT MODE=0	1	2	3	4	5	6	EXACT RESPONSE	
MIN-1	.119086	.162553	.205222	.563062	.631112	.700501	.694453	
-2	.119086	.214970	.406765	.631764	.699950	.704131	.694453	
T-MIN-1	.0291750	.0284500	.0285000	.0146250	.0145500	.0145500	.0145500	
-2	.0291750	.0284500	.0147000	.0145500	.0145500	.0144750	.0145500	
MAX-1	.0490156	1.065169	1.039044	1.167103	1.187205	1.180449	1.168377	
-2	.0490156	1.716446	1.197191	1.202837	1.184456	1.163568	1.153004	
T-MAX-1	.0087750	.0160500	.0160500	.0264750	.0264000	.0264000	.0264000	
-2	.0087750	.01605750	.0264000	.0264000	.0264750	.0264000	.0264000	

THIS PAGE IS BEST QUALITY PRACTICABLE
FROM COPY FURNISHED TO DDG

TABLE XI

COMPARISON OF PEAK MOMENTS FROM ANALYTICAL MODES WITH SAMSON RESULTS, CASE 5

CASE 5	INVERT	MOMENT	(176.25-DEGREES)	MODAL RESPONSE/EXACT RESPONSE	EXACT RESPONSE
CURRENT MODES	1	2	3	4	5
MAX-1	.198400	.004194	2.063915	3.014002	3.080383
-2	.198400	2.4400332	2.740140	5.025001	3.126964
1-MIN-1	.0087750	.0256500	.0282250	.0293250	.0291750
-2	.0087750	.0294000	.0294000	.0293250	.0291750
MAX-1	.002925	1.401173	1.701743	1.673761	1.662746
-2	.002925	1.915063	1.823870	1.690964	1.660367
1-MAX-1	.0291750	.0128250	.0098250	.0093000	.0177750
-2	.0291750	.0141000	.0099000	.0092250	.0178500

2-RESPONSE CALC. FROM JOINT RADIAL AND SHEAR MODAL LOADS FOR MODES 0 THRU CURRENT MODE
1-SEMI AS 2 EXCEPT RESPONSE FOR SP-LAR MODAL LOADS FOR CURRENT MODE IS NOT INCL.

NOTE: IF "IN. (OR MAX.) EXACT RESPONSE IS .LT. 1.E-6, MODAL MIN. (OR MAX.) HAS NOT BEEN NORMALIZED

CASE 5	SPRINGLINE	MOMENT	(176.25-DEGREES)	MODAL RESPONSE/EXACT RESPONSE	EXACT RESPONSE
CURRENT MODES	1	2	3	4	5
MAX-1	.033826	1.079830	1.318473	1.345006	1.390529
-2	.033826	1.388446	1.303231	1.370780	1.411076
1-MIN-1	.0087750	.0126750	.0144000	.0115500	.0114000
-2	.0087750	.0139500	.0143250	.0115500	.0114000
MAX-1	.011219	.040211	2.008374	2.458634	2.432934
-2	.011219	2.700733	2.071692	2.449413	2.438458
1-MAX-1	.0291750	.0253500	.0294000	.0294000	.0277500
-2	.0291750	.0294000	.0294000	.0294000	.0277500

CASE 5	INVERT	MOMENT	(176.25-DEGREES)	MODAL RESPONSE/EXACT RESPONSE	EXACT RESPONSE
CURRENT MODES	1	2	3	4	5
MAX-1	.120375	.041879	1.954289	2.029432	2.007072
-2	.120375	1.779199	1.876447	2.036738	1.986484
1-MIN-1	.0087750	.0256500	.0294000	.0291750	.0294000
-2	.0087750	.0294000	.0294000	.0291750	.0294000
MAX-1	.001674	.827724	1.366525	1.434727	1.475564
-2	.001674	1.080021	1.443169	1.452847	1.476374
1-MAX-1	.0291750	.0128250	.0135000	.0138000	.0137250
-2	.0291750	.0141000	.0134500	.0138000	.0137250

TABLE XII
COMPARISON OF PEAK THRUSTS FROM ANALYTICAL MODES WITH SAMSON RESULTS, CASE 13

CASE 13									
KNOWN THRUST (3.75-DEGREES)									
CURRENT MODE=0	1	2	3	4	5	6	EXACT RESPONSE		
MIN-1	0.000000	.145272	.246355	1.754876	1.461474	1.458943	1.559557		
-2	0.000000	.041508	1.634501	1.141658	1.540735	1.462912	1.611638		
1-MIN-1	0.000000	.029400	.025500	.021900	.021900	.025500	.025500		
-2	0.000000	.025500	.021900	.021800	.021800	.025500	.025600		
MAX-1	1.160224	1.305860	1.374701	1.110652	.984537	.930827	.940077		
-2	1.160224	1.428136	1.121645	.996449	.940812	.932037	.943643		
1-MAX-1	.010400	.009500	.009400	.009200	.006400	.006400	.009200		
-2	.010400	.009300	.009300	.006500	.006400	.009200	.009200		
2=RESPONSE CALC. FROM BOTH RADIAL AND SHEAR MODAL LOADS FOR MODES 0 THRU CURRENT MODE									
1=SAME AS 2 EXCEPT RESPONSE FOR SHEAR MODAL LOADS FOR CURRENT MODE IS NOT INCL.									
NOTE IF MIN.(OR MAX.) EXACT RESPONSE IS .LT. 1.E-6, MODAL MIN.(OR MAX.) HAS NOT BEEN NORMALIZED									
CASE 13									
SPRINGLINE THRUST (80.25-DEGREES)									
CURRENT MODE=0	1	2	3	4	5	6	EXACT RESPONSE		
MIN-1	0.000000	.000000	-.000021	0.000000	0.000000	0.000000	0.000000		
-2	0.000000	0.000000	-.000001	-.000004	-.000000	-.000001	0.000000		
1-MIN-1	0.000000	0.000000	.002000	0.001800	0.000000	0.000000	.001700		
-2	0.000000	0.000000	.001400	.001700	.001400	.001500	0.000000		
MAX-1	.047402	.049005	.702623	.280341	.885610	.899245	.903013		
-2	.047402	.051058	.877616	.894192	.896384	.899080	.911722		
1-MAX-1	.010400	.010300	.010700	.011000	.011000	.011000	.011000		
-2	.010400	.010300	.011000	.011000	.011000	.011000	.011000		
CASE 13									
INVERT THRUST (170.25-DEGREES)									
CURRENT MODE=0	1	2	3	4	5	6	EXACT RESPONSE		
MIN-1	0.000000	.437312	0.000000	.070798	.967031	1.523459	1.626478		
-2	0.000000	.306124	0.000000	.509837	1.143424	1.770072	1.762186		
1-MIN-1	0.000000	.004500	0.000000	.003800	.021000	.021000	.020900		
-2	0.000000	.004300	0.000000	.021000	.021200	.021000	.020900		
MAX-1	1.917168	1.856217	1.745306	1.162782	1.364885	1.346749	1.337795		
-2	1.917168	1.847366	1.145508	1.577789	1.368698	1.331508	1.317563		
1-MAX-1	.010400	.010700	.013800	.014000	.014000	.010300	.010300		
-2	.010400	.013700	.010500	.016400	.010400	.010300	.010300		

CASE XIII

COMPARISON OF PEAK MOMENTS FROM ANALYTICAL MODES WITH SAMSON RESULTS, CASE 13

CASE 13	CURRENT	MOMENT	COMPUTED	EXACT	RESPONSE	EXACT	RESPONSE
	MODE=0	1	2	3	4	5	6
MIN-1	0.000187	0.000187	0.000187	0.000000	0.000000	0.003607	0.005560
-2	0.000187	0.000187	0.000000	0.000000	0.000000	0.004399	0.005727
1-MIN-1	0.0104000	0.0104000	0.0294000	0.000000	0.000000	0.0294000	0.0293000
-2	0.0104000	0.0104000	0.0000000	0.0000000	0.0000000	0.0294000	0.0293000
MAX-1	0.0000000	0.0000000	1.223987	5.0846983	0.978518	0.059298	7.106124
-2	0.0000000	0.0000000	9.260762	7.546937	7.304921	7.020528	7.150267
1-MAX-1	0.0000000	0.0000000	0.0118000	0.0212000	0.0205000	0.0161000	0.0244000
-2	0.0000000	0.0000000	0.0294000	0.0167000	0.0213000	0.0163000	0.0245000

2=RESPONSE CALC. FROM BOTH RADIAL AND SHEAR MODAL LOADS FOR MODES 0 THRU CURRENT MODE
1=SAME AS 2 EXCEPT RESPONSE FOR SPHER MODAL LOADS FOR CURRENT MODE IS NOT INCL.

CASE 13	CURRENT	MOMENT	COMPUTED	EXACT	RESPONSE	EXACT	RESPONSE
	MODE=0	1	2	3	4	5	6
MIN-1	0.03917	0.03917	1.038000	0.746661	7.080619	8.190234	7.976443
-2	0.03917	0.03917	7.278411	0.184001	7.866848	8.247001	7.941169
1-MIN-1	0.0104000	0.0104000	0.0118000	0.0294000	0.0294000	0.0294000	0.0294000
-2	0.0104000	0.0104000	0.0294000	0.0294000	0.0294000	0.0294000	0.0294000
MAX-1	0.0000000	0.0000000	89.616972	9.000000	4.573890	11.646137	18.560838
-2	0.0000000	0.0000000	0.000000	0.000000	7.301655	12.412398	18.839846
1-MAX-1	0.0000000	0.0000000	0.0294000	0.0000000	0.062000	0.066000	0.078000
-2	0.0000000	0.0000000	0.0000000	0.0000000	0.066000	0.066000	0.079000

CASE 13	CURRENT	MOMENT	COMPUTED	EXACT	RESPONSE	EXACT	RESPONSE
	MODE=0	1	2	3	4	5	6
MIN-1	0.000187	0.000187	0.009768	0.001299	0.008289	0.014764	0.020720
-2	0.000187	0.000187	0.000000	0.003610	0.009632	0.015777	0.020953
1-MIN-1	0.0104000	0.0104000	0.0294000	0.075000	0.148000	0.155000	0.155000
-2	0.0104000	0.0104000	0.0000000	0.0128000	0.151000	0.156000	0.156000
MAX-1	0.0000000	0.0000000	0.031529	9.644965	11.145795	11.679973	11.579772
-2	0.0000000	0.0000000	7.052501	12.368063	11.317717	11.842144	11.545565
1-MAX-1	0.0000000	0.0000000	0.0118000	0.0294000	0.0282000	0.0294000	0.0294000
-2	0.0000000	0.0000000	0.0294000	0.0294000	0.0259000	0.0294000	0.0294000

denotes the column label mode number. The -1 row does not include the SSI shear load effects for the current mode N. For example, using modes 0 through 5 to obtain the results given in the MODE 5 column, the MAX-1 result is obtained from

$$\text{Max } \bar{T}_{0,5}^1 = \text{Max} \left\{ \sum_{n=0}^4 \left[\bar{T}_n^R(t_i) + \bar{T}_n^T(t_i) \right] \cos n \theta_1 + \bar{T}_5^R(t_i) \cos 5 \theta_1 \right\}, \quad i=1, L$$

where the ($\bar{}$) notation indicates the nondimensional magnitude, n is the mode number, i is the discrete time step, and there are L time steps. This maximum divided by the SAMSON maximum (0.60422) would give the result 0.987907. The T-MAX-1 and -2 rows give the time that the respective analytical maximums occur.

In a similar manner, the first four rows (labeled MIN-1, MIN-2, T-MIN-1, and T-MIN-2) are obtained except the minimum values of the modal histories are computed and compared with the SAMSON solution minimum nondimensional crown thrust (-0.040613) and time of occurrence (0.015225 sec).

j. Discussion of Results

It was anticipated that the cylinder moment and thrust modal results obtained from this analysis would be close to those obtained from the SAMSON results; however, an examination will show that the comparison is fair for the thrusts and relatively poor for the moments for case 5. The moment comparison is especially bad for case 13. Just as with the table VII results, the desired ratio of the peak maximum and minimum analytical response to the corresponding SAMSON peak is 1.0. In general, the minimum thrust ratios are not very close to 1.0; however, since these ratios are the tension thrust which are relatively small except at the invert for case 5, large errors are not significant. That is, a large error in a small magnitude number still gives a small magnitude number. It also appears that large errors exist for the time of occurrence of some of the analytically determined peaks compared with the SAMSON times; however, these actually represent only minor errors.

For example, the case 5 maximum invert thrust for the SAMSON solution occurs at $t=0.0096$ sec, whereas the maximum occurs at approximately 0.026 sec when modes 0 through 2 (or more) are included in the analytical determination of the invert thrust. However, an examination of figure 29a shows that a second large compression thrust occurs at approximately 0.025 sec which is almost equal to that at $t=0.0096$ sec, and this explains this seemingly large discrepancy.

Even though the comparisons of the analytical results with the SAMSON solution are not as good as anticipated, it appears that the SSI modal loads 0 through 2 are the primary contributors to the cylinder thrust, and mode 2 is the significant loading causing cylinder moments. As previously indicated, the desired result was to have the analytically determined modal thrust and moment histories essentially the same as the SAMSON results. A comparison of these modal histories for case 5 for the thrust modes 0, 1, and 2 and the moment modes 2 and 3 is given in figures 30 and 31. The thrust modes compared fairly well; however, relatively large differences exist for the moment modes even though the general time variations of the curves are similar, i.e., the analytical moment magnitudes are approximately 50 percent higher than the SAMSON magnitudes.

The thrust and moment modal comparisons for case 13 are shown in figures 32 and 33. Just as with case 5, the thrust modes compare fairly well; but the important mode 2 moment comparison is very poor, and this is the major error which creates the large moment ratios in table XIII.

A separate analysis of the poor comparison of the analytical moments with the SAMSON results was undertaken to try and resolve this problem. This study was not completed, due to fiscal restraints on this research project; however, the following observations are made. For several reasons it is suggested that the SAMSON determined cylinder thrusts and moments are more reliable (or accurate) than the SSI stresses. Two of these reasons are:

- (1) The tunnel liner is modeled in considerable detail (four element layers through the thickness) compared to the soil mesh immediately adjacent to the cylinder.

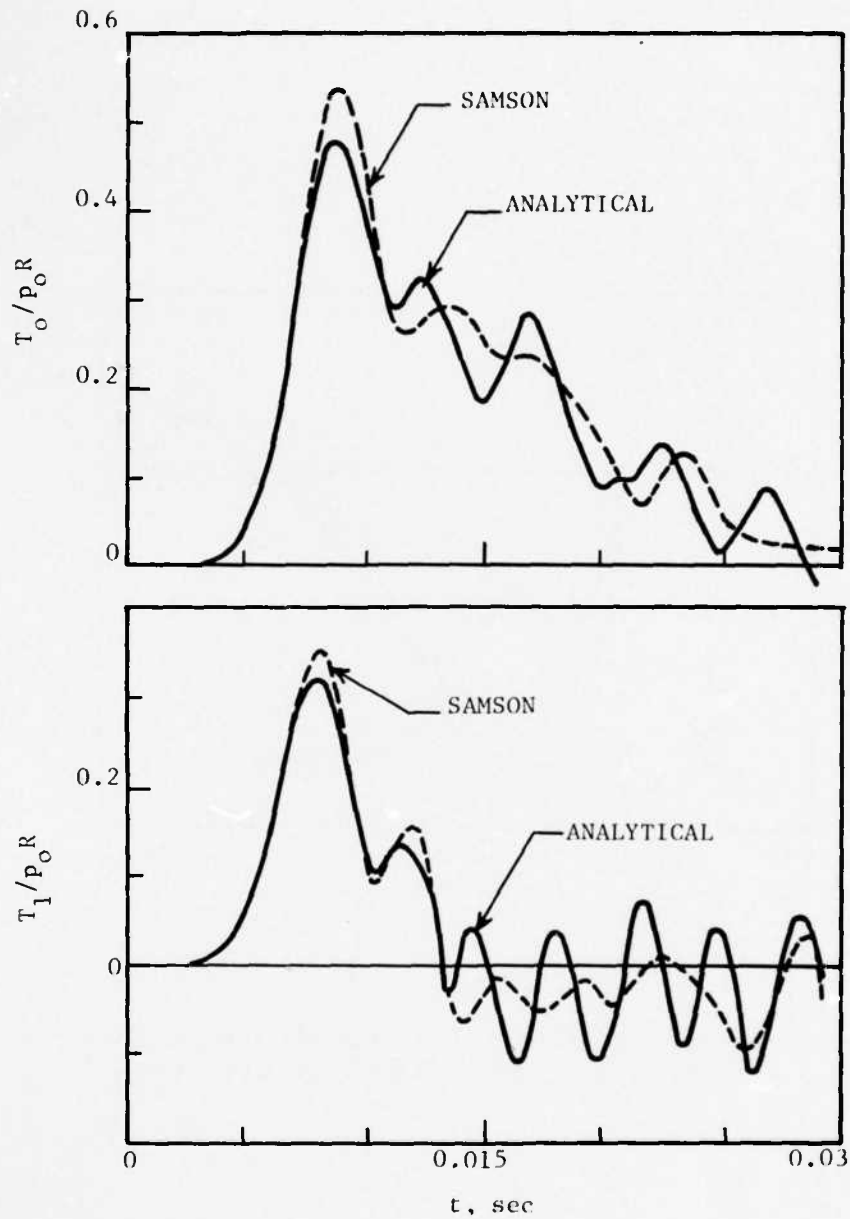


Figure 30a. Comparison of Analytical Thrust Mode Variation with SAMSON Result, Case 5

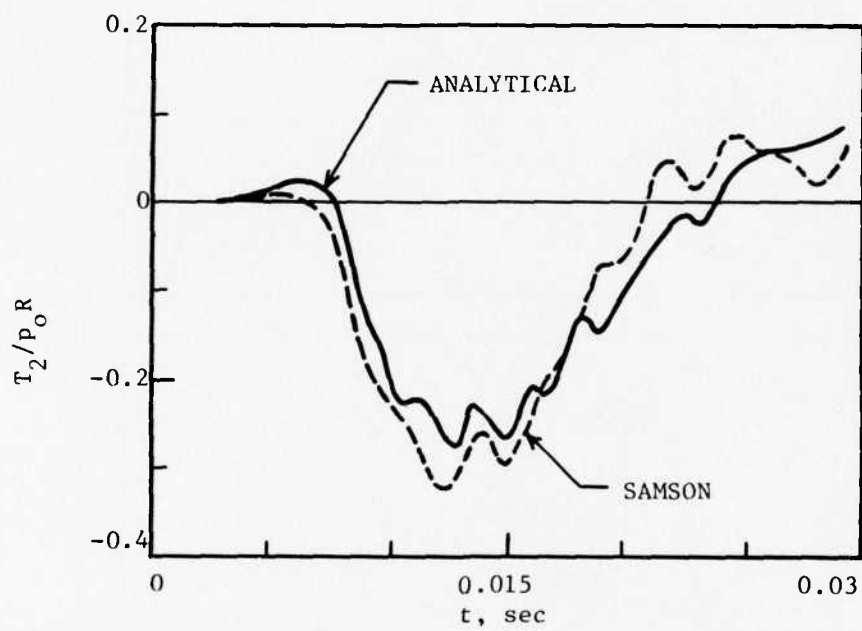


Figure 30b. Comparison of Analytical Thrust Mode Variation with SAMSON Result, Case 5

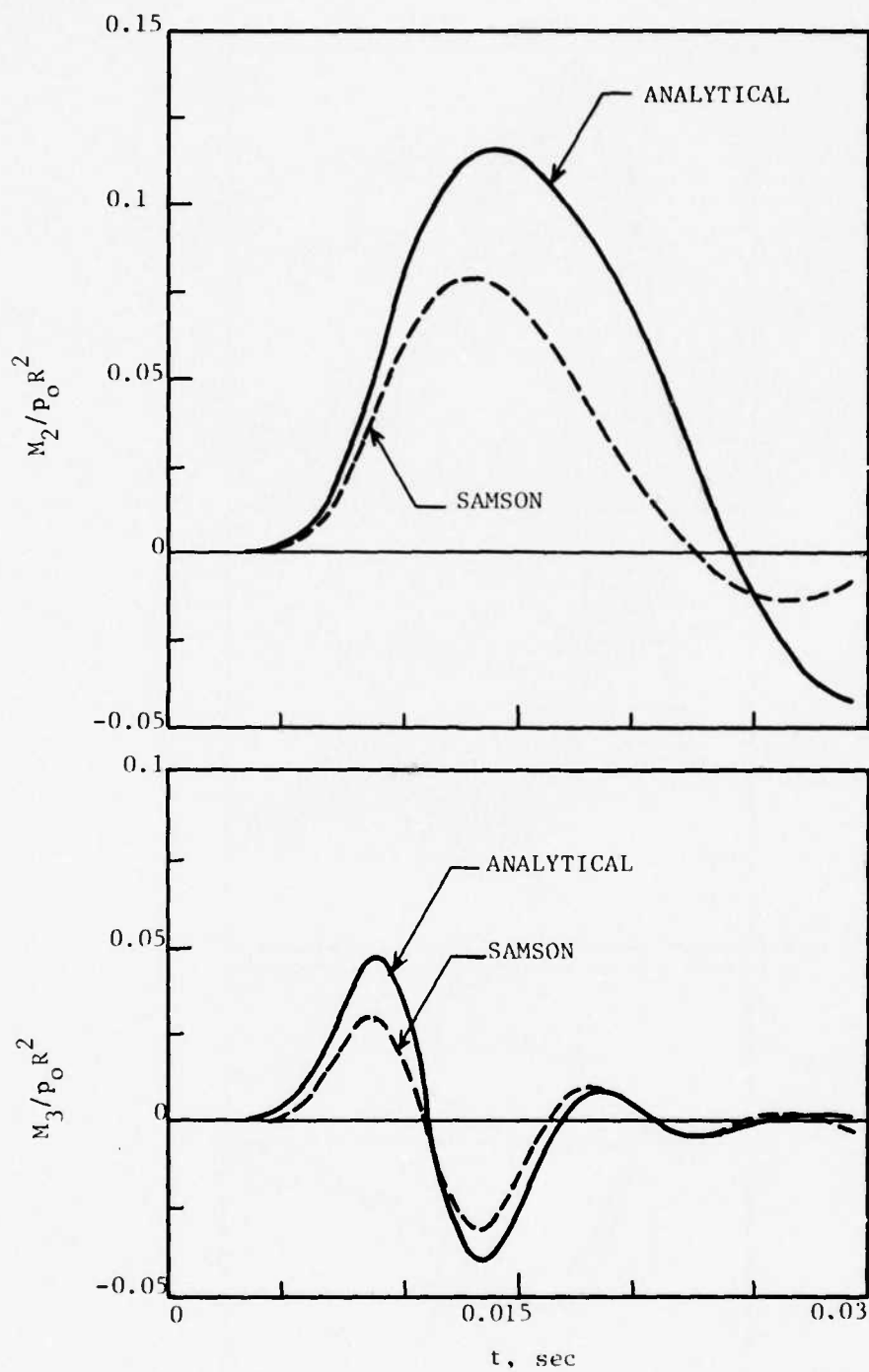


Figure 31. Comparison of Analytical Moment Mode Variation with SAMSON Result, Case 5

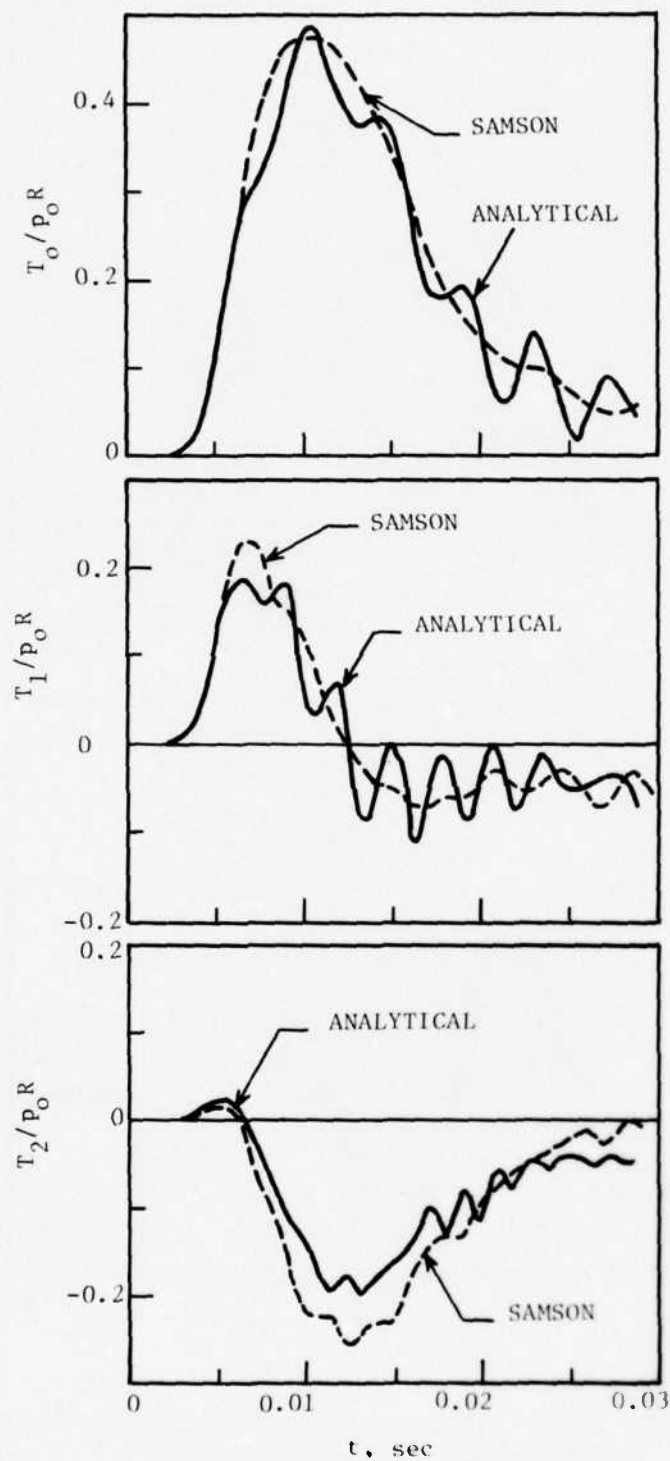


Figure 32. Comparison of Analytical Thrust Mode Variation with SAMSON Result, Case 13

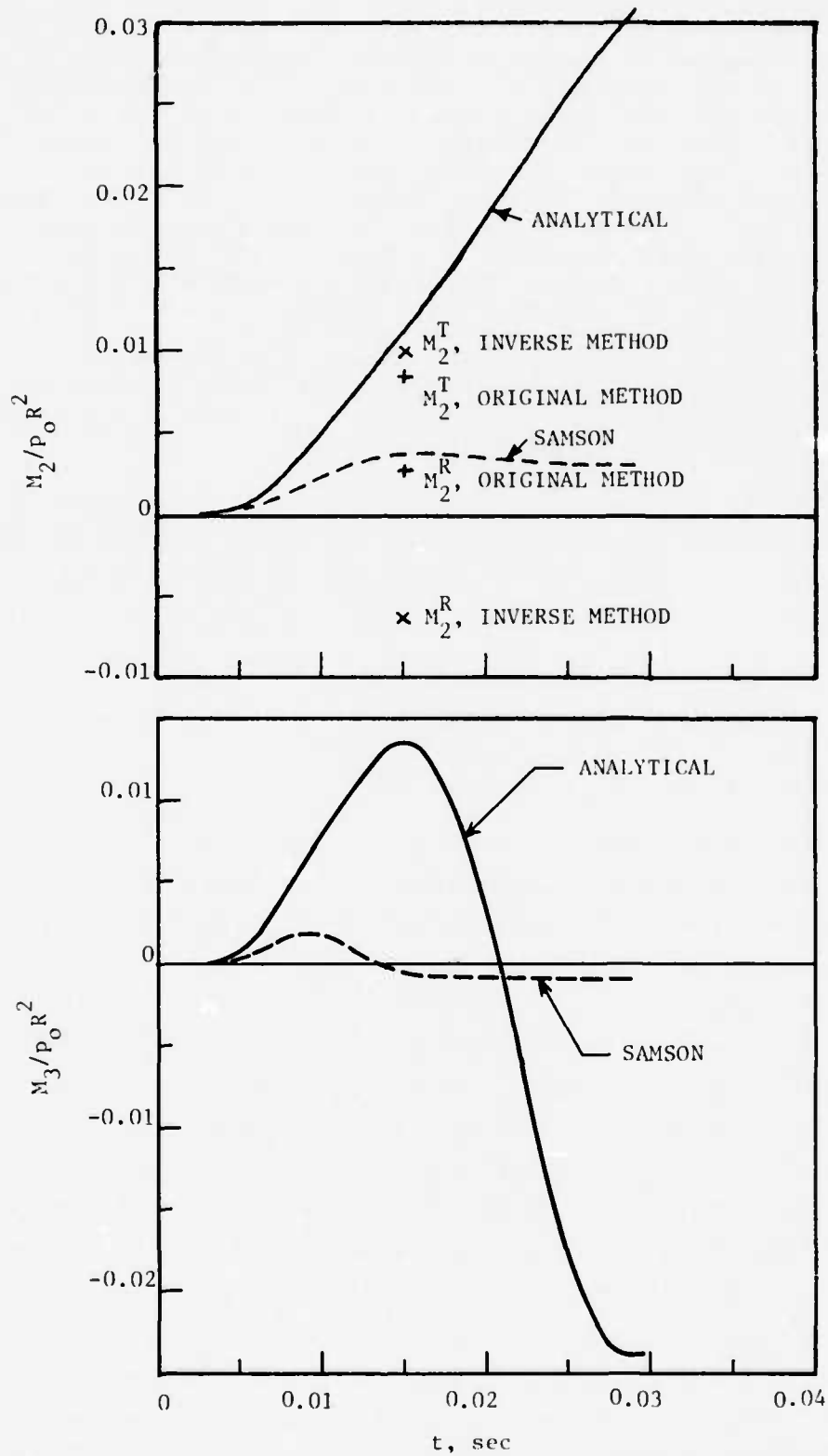


Figure 33. Comparison of Analytical Moment Mode Variation with SAMSON Result, Case 13

- (2) The stresses in the soil elements immediately adjacent to the cylinder are not truly the SSI stresses because the soil mass dynamic effects were not eliminated. That is, the discrete mass at the SSI nodes contain contributions from both the soil and the cylinder elements that are attached to the nodes. For the flexible liner (case 13) the soil elements are the major contributor to the mass at the SSI node points. The stresses in the soil elements immediately surrounding the structure are properly used to find the loads applied to the SSI interface nodes. However, it is clear that the dynamic force effects of the soil mass, e.g., inertial loads, must be removed to obtain the true SSI stresses. Appendix C gives a further discussion of this concept.

Accepting the premise that the SAMSON thrusts and moments are essentially correct, it is possible to solve for the SSI modal stresses from the internal liner force resultant nodal histories. This is done by first solving for the modal deformation histories (q_n and \bar{q}_n) using equations (40) and (41). Then, by application of numerical differentiation, the time derivatives of q_n and \bar{q}_n can be obtained and equations (31a) through (31c) will yield the modal histories of the SSI stresses.

The above inverse method was used for cases 5 and 13; and even though the results are preliminary, they imply that the mode 2 radial and shear stresses should be higher, i.e., more positive. A major effect occurs on the case 13 moments when the higher mode 2 radial stresses computed from the inverse process are used. These revised radial stresses reduce the M_2^R amplitudes (make them more negative) which, when coupled with the mode 2 moments M_2^T from the SSI shear stresses, yield essentially the same total mode 2 moment variation that was obtained from the SAMSON results. This is illustrated in figure 33 by showing the magnitudes of M_2^T , M_2^R at $t = 0.015$ sec as computed from the inverse process (denoted by "inverse method"). Also shown on this figure are the M_2^T , M_2^R magnitudes at $t = 0.015$ sec which were computed from the SAMSON mode 2 SSI radial and shear stresses (denoted by ORIGINAL METHOD). The combination of these two moments yields a point on the "analytical" curve. Figure 34 shows the time history of

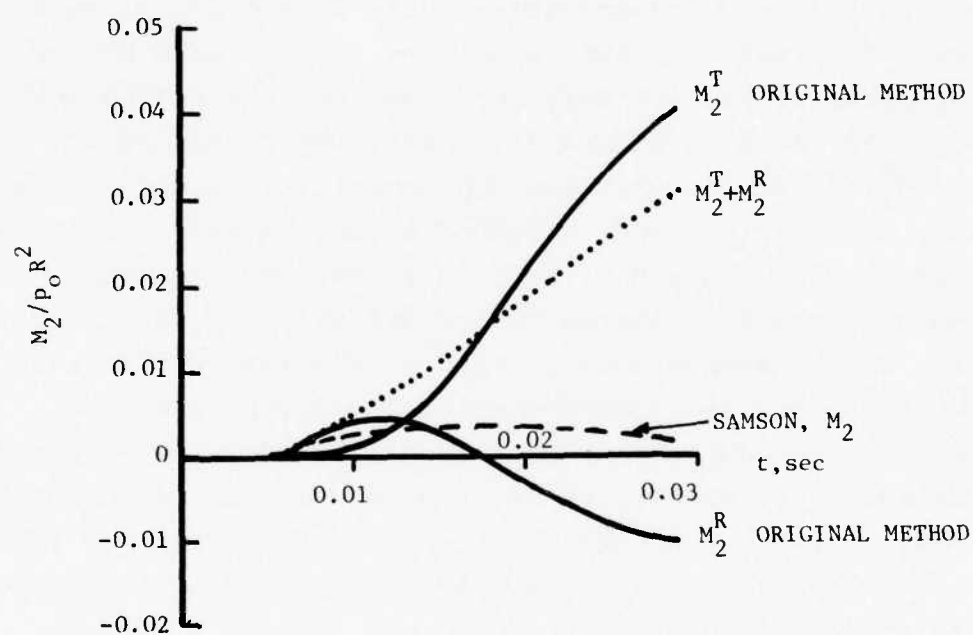


Figure 34. Nondimensional Mode 2 Moment Variation Computed from SAMSON Mode 2 SSI Shear and Radian Stress, Case 13.

the M_2^T and M_2^R curves as computed from the SAMSON mode 2 SSI radial and shear stresses. Combining these two curves results in the dotted curve which is the same as the curve denoted "analytical" in figure 33. Figure 35 shows the nondimensional mode 2 moment variation that was computed from the SSI shear and radial stresses that were derived by using the inverse method. That is, the M_2^T and M_2^R curves in figure 35 are based on the SSI mode 2 stress histories calculated from the SAMSON mode 2 moment and thrust histories as discussed above. These mode 2 SSI stress histories are shown in figure 36 and for comparison, the SAMSON SSI stresses are also given. As previously indicated, the SSI stresses determined from the inverse method are more positive than the SAMSON mode 2 stresses as indicated in figure 36. Referring to figure 35, combining the M_2^T and M_2^R (inverse method) moment variations yields essentially the original mode 2 SAMSON moment variation which is the desired result. In a similar manner, the mode 2 thrust variation computed from the inverse method SSI stresses (figure 36) is the same as the SAMSON mode 2 thrust. Similar results were obtained for the other modes when the inverse method was used. This indicates that the computer coding associated with the original analytical method is correct since this same coding was used to compute modal moments and thrusts from modal SSI shear and radial stresses after replacing the SAMSON SSI modal stresses with those determined from the inverse method.

In summary, it is concluded that for the results available from this investigation, the SSI stresses should be computed by the inverse method. That is, the modal SSI stress variation should be calculated from the SAMSON modal thrust and moment histories. However, further research studies should be undertaken to verify this conclusion.

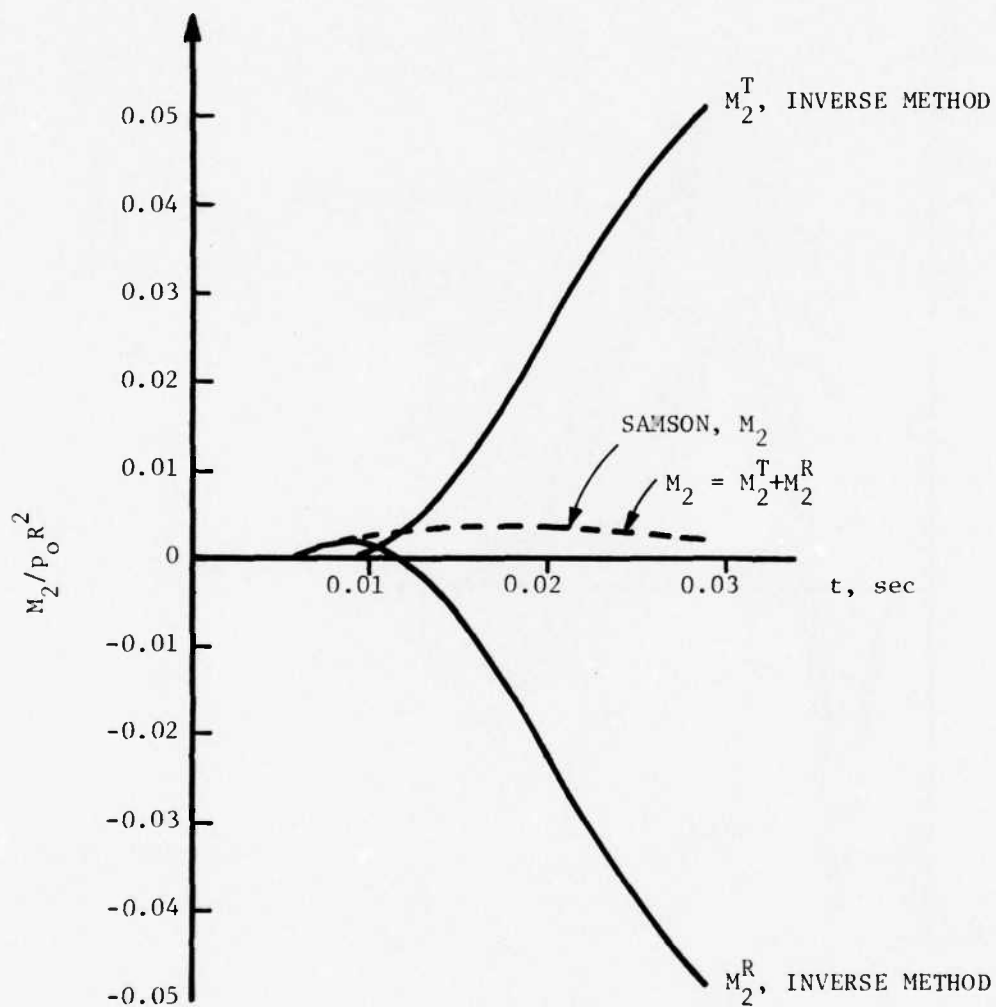


Figure 35. Nondimensional Mode 2 Moment Variation
Computed from Mode 2 SSI Shear and Radial
Stresses Derived by Inverse Method, Case 13

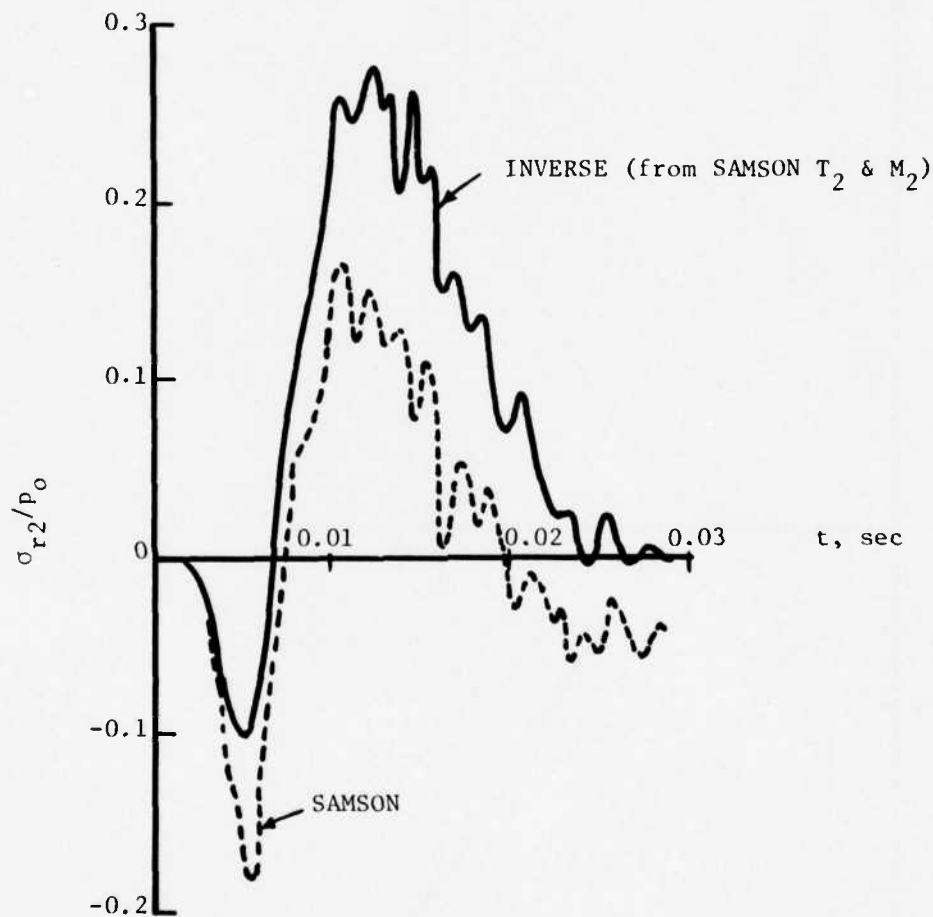


Figure 36a. Nondimensional Mode 2 SSI Radial Stress Variation from Inverse Method, Case 13

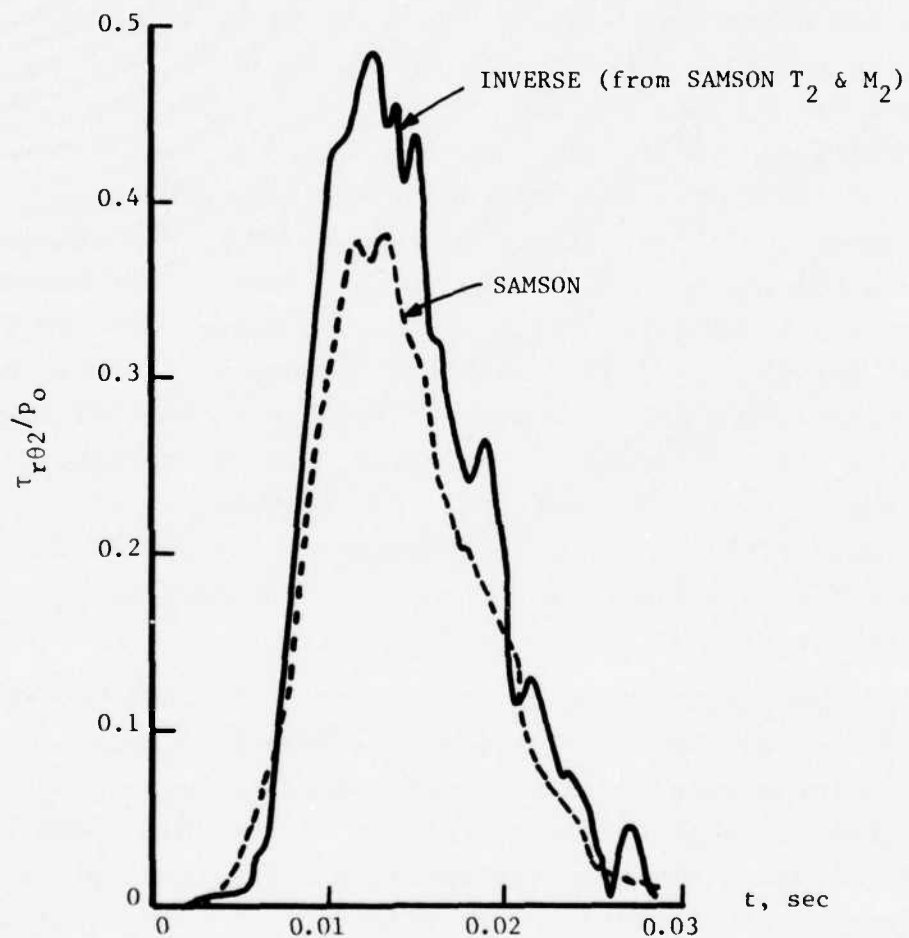


Figure 36b. Nondimensional Mode 2 SSI Shear Stress Variation from Inverse Method, Case 13

SECTION IV

CONCLUSIONS AND RECOMMENDATIONS

1. CONCLUSIONS

The overall objective of the research investigations described in this report was to develop a simplified method for computing loads on buried structures. The results discussed in Section III indicated that the soil structure interaction (SSI) loads, as determined from the dynamic loading finite element analyses, may not be a sufficiently reliable data base upon which to base a new or more comprehensive simplified loading technique. Even though reliable SSI loads are not available some meaningful conclusions can be drawn from the results of the study. The conclusions associated with the dynamic loading results are based on the assumption that the detailed results, such as modal time history variations, may be subject to question; but the overall effects on the SSI loads and the tunnel liner internal forces, from varying the independent parameters should be fairly reliable. For example, if the peak thrust goes down with an increase in structure flexibility, the trend is essentially correct even though the precise reduction may be subject to question.

The major conclusion drawn from the project is that the concept of using a few of the SSI modal loads to arrive at a simplified method of loading appears to have a great deal of merit. In fact, it appears that it is generally sufficient to use only modes 0 through 2 to obtain a sufficiently detailed definition of the loading to satisfactorily compute the internal tunnel liner forces. In some cases, it may be necessary to include mode 3 to accurately obtain the bending moments around the tunnel liner.

Some of the conclusions that can be drawn from the static and dynamic investigations undertaken during this project are presented. In this discussion, the terms "flexible" and "stiff" refer to the tunnel liner with radius to thickness ratios of 15 and 4, respectively. Also, "shallow" and "deep" refer to depths of overburden above the tunnel crown of 0.25 and 2.0 tunnel diameters, respectively.

(1) For static ground surface loads, the SSI radial and shear stress loads acting on a buried cylinder are not very sensitive to the depth of burial.

(2) For dynamic airblast ground surface loads, the SSI loads on a buried cylinder are significantly reduced as the depth of burial increases. This is due primarily to the attenuation with depth of the peak free field stress for the nonlinear soil material models (sand and cemented sand) considered in this study. This attenuation with depth is due to the hardening stress-strain law employed. Also, a short duration airblast load ($t_d = 0.015$ sec) results in considerably more peak stress attenuation than the long duration loading ($t_d = 0.06$ sec) considered in this study.

(3) An increased failure strength of the soil (i.e., cemented sand versus cohesionless sand) does not essentially modify the SSI loads on a buried cylinder for dynamic airblast loads.

(4) For static ground surface loads, the buried cylinder crown and invert thrusts are approximately the same, and the springline thrust is two or three times larger than the crown and invert thrust. For a shallow depth of burial, the invert thrust is slightly higher (maximum of 24 percent for the stiff tunnel) than the crown thrust. As the depth of burial increases, the crown thrusts increase until they are essentially equal to the invert thrusts. This occurs at approximately one diameter of overburden for the flexible tunnel and two diameters for the stiff tunnel.

(5) For dynamic airblast loads, the crown thrust is 30 to 120 percent higher than the invert peak thrust for the stiff tunnel; however, for the flexible tunnel, the crown thrust is more nearly equal to the peak invert thrust. For the shallow buried stiff tunnel, the springline peak thrust is slightly higher (10 to 30 percent) than the crown thrust; otherwise, the springline thrust ranges between 50 and 150 percent higher than the crown thrust. The peak thrusts throughout the tunnel liner are considerably reduced with depth as the duration of loading is reduced for both the stiff and the flexible tunnels.

(6) For static ground surface loads, the crown moment is somewhat larger (47 percent higher) than the peak invert moment for the most flexible shallow buried tunnel; however, the crown moment is nearly the same (7 percent lower) for the stiffest shallow buried tunnel liner. As the depth of burial increases, the crown and invert moments approach equal magnitudes. This result occurs at a depth of burial of one tunnel diameter. The invert and springline moments are essentially of equal and opposite magnitudes for all depths of burial and tunnel liner flexibilities considered.

(7) For dynamic airblast loads, the largest bending moments occurred at the invert for all cases considered. This rather surprising result corresponds to the limited experimental results available at this time (Ref. 58,59,60). The largest nondimensional moments for the dynamic load cases were always smaller than the static solution case for the corresponding R/t ratio; however, the invert peak moments approached the static results for the shallow buried stiff tunnel liner cases. For the shallow buried stiff tunnel, the peak dynamic invert moment is 60 to 100 percent higher than the crown moment. For all other depth of burial and tunnel stiffness combinations considered in this study, the peak invert moment was 20 to 50 percent higher than the crown peak value except for the deep buried, flexible liner subjected to the high overpressure long duration loading. For this case the invert peak bending moment was 80 percent higher than the crown value. In most cases, the invert peak bending moments were only 5 to 20 percent higher than the springline magnitudes (but of opposite sign). In some of the stiff tunnel cases, the magnitude was 40 to 50 percent higher. For the shallow buried stiff tunnel cases subjected to short duration airblast loading, moment reversal occurred throughout the liner. The maximum reversal (38 percent) occurred for the crown bending moment when the large overpressure short duration loading was used. That is, the largest negative moment (causing tension in the outer fibers of the tunnel liner) was 38 percent of the largest positive moment at the crown. The smallest reversal (16 percent) for the stiff shallow buried cases, occurred for this airblast load case also.

(8) For dynamic airblast loading, an increase in the peak overpressure has a relatively small effect on the peak nondimensional moments and thrusts in the tunnel liner. The largest effect on thrusts is an increase in the invert compressive nondimensional thrusts of approximately 100 percent when the peak overpressure is tripled for the shallow-buried stiff tunnel with the short duration loading. All other changes in the peak nondimensional thrust with an increase in overpressure are relatively small except for the deep-buried stiff cylinder subjected to the long duration loading where the nondimensional crown and invert thrusts increase by approximately 50 percent. The largest effect on bending moments is a reduction in the peak nondimensional moment by approximately 40 percent when the peak overpressure is tripled for the shallow buried flexible tunnel liner.

(9) A fourfold increase in the duration of the airblast dynamic loading (from 15 to 60 msec) has the effect of increasing the peak thrusts and moments by from 10 to 90 percent for the shallow buried tunnels. For the deep buried tunnels, the increased duration of loading causes large increases in both the thrusts and the moments which generally range from 150 to 350 percent.

(10) Increasing the structural flexibility causes a reduction in the crown and invert nondimensional thrusts for the shallow buried dynamic load cases; however, an opposite effect is observed for comparable static load cases. The nondimensional bending moments are drastically reduced for both the static and dynamic load cases as the tunnel liner flexibility is increased.

2. RECOMMENDATIONS

This research project produced a great number of numerical results (36 cases) from dynamic finite element solutions which modeled buried cylinders subjected to ground shock effects of airblast loading. The SSI loads on the cylinder were derived from the stresses in the soil elements immediately adjacent to the cylinder. These SSI loads were then used in a modal analysis to compute the response of a cylinder in vacuo, and the internal forces (moments)

and thrust) computed from the modal analysis were compared with those determined from the finite element solution. In general, the thrust compared fairly well, but the moments compared poorly for some cases. This implies that either the SSI stresses or the cylinder forces determined from the finite element solution are in error. At this point, it is believed that the SSI stresses are in error and the cylinder forces are essentially correct. If this is true, then the finite element determined cylinder forces can be used to calculate the SSI stresses, and the overall objective of determining a simplified method for defining loads on buried structures can be completed by using the results from the 36 cases.

Briefly stated, the simplified loading method involves the determination of the important modes of the SSI loads and an analysis of how these modal histories change with the important parameters such as (1) structural stiffness, (2) depth of burial, (3) soil type, and (4) airblast waveform peak overpressure and duration of loading. It appears that modes 0 through 2 provide the most significant loads on the structure; however, before any simplified loading method can be determined from these SSI modes, it is essential to have confidence in the SSI modal histories. Several factors have been identified which make the finite element determined SSI loads suspect such as (1) the damping stresses are not included in the finite element stresses, (2) the soil mass of the elements adjacent to the structure is included with the SSI nodes and (3) a more refined mesh may be required to accurately determine the SSI loads from a finite element dynamic analysis. In summary, it is recommended that this research study be continued and completed since the technique of defining a simplified loading procedure by using a few modal loads appears to have great merit. Specific recommendations are:

(1) Reliable SSI radial and shear stress modal loadings should be determined from the results available from this project. Consequently, when these modal load histories are applied to the cylindrical tunnel liner structure in vacuo, the internal forces computed from a dynamic model will compare favorably with those obtained from the finite element (SAMSON) solution.

(2) Once the SSI modal loadings are unquestionably known to be without error, the simplified method of determining dynamic loads on buried structures should be formalized. This effort will require the determination of the number of SSI modal loads required and the time history details (amplitude and duration characteristics) of each mode as a function of the structural characteristics, soil media, depth of burial, and airblast waveform. The time details of each mode can be simply characterized by triangular, piecewise linear or simple sinusoidal or parabolic waveforms without introducing significant errors to the calculation of internal tunnel liner forces.

For example, figures 37a and 37b show the mode 0 and 1 nondimensional SSI radial stress variations for cases 5 and 13. These cases are identical except case 5 employs a stiff tunnel lining ($R/t=5$) and case 13 a flexible lining ($R/t=15$). The other important parameters are: peak overpressure, $p_o=500$ psi (3.45 MPa); airblast duration, $t_d=0.015$ sec; depth of burial, $h=0.5$ R. From the figures, it is seen that the mode 0 radial stress can be simplified by a triangular waveform and mode 1 by three linear approximations giving a large amplitude negative triangle followed by a smaller amplitude positive phase triangle. The mode 0 triangular approximation is nearly the same for both cases; however, the peak stress for the more flexible liner (case 13) is slightly higher (15 percent) and occurs slightly later. Note that the initial slope and load duration of the mode 0 simplified waveform is the same for these two cases. For the mode 1 approximation, the initial (negative) peak stress is (65 percent) higher for the stiff tunnel (case 5) than the flexible liner; however, the positive phase peak amplitude can be approximated by the same magnitude. It is also observed that the overall load duration and the first and last (third) slopes of the mode 1 approximation are the same for both cases.

Similar simplified SSI stress waveforms can be determined for higher radial stress modes and the SSI shear stress modes as required. It has been indicated that modes higher than mode 2 will

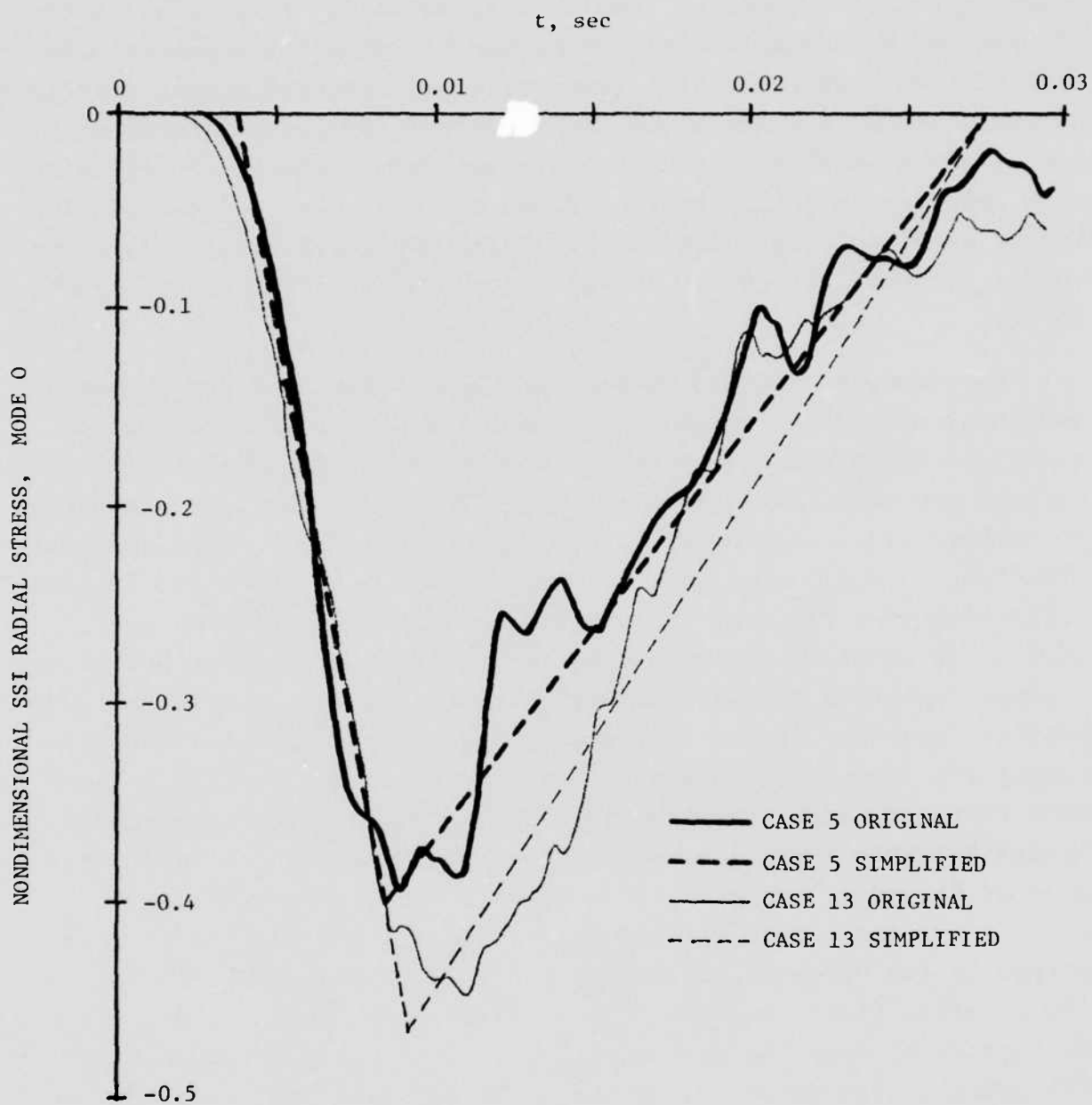


Figure 37a. Approximations to Mode 0 SSI Radial Stress Variation, Cases 5 and 13

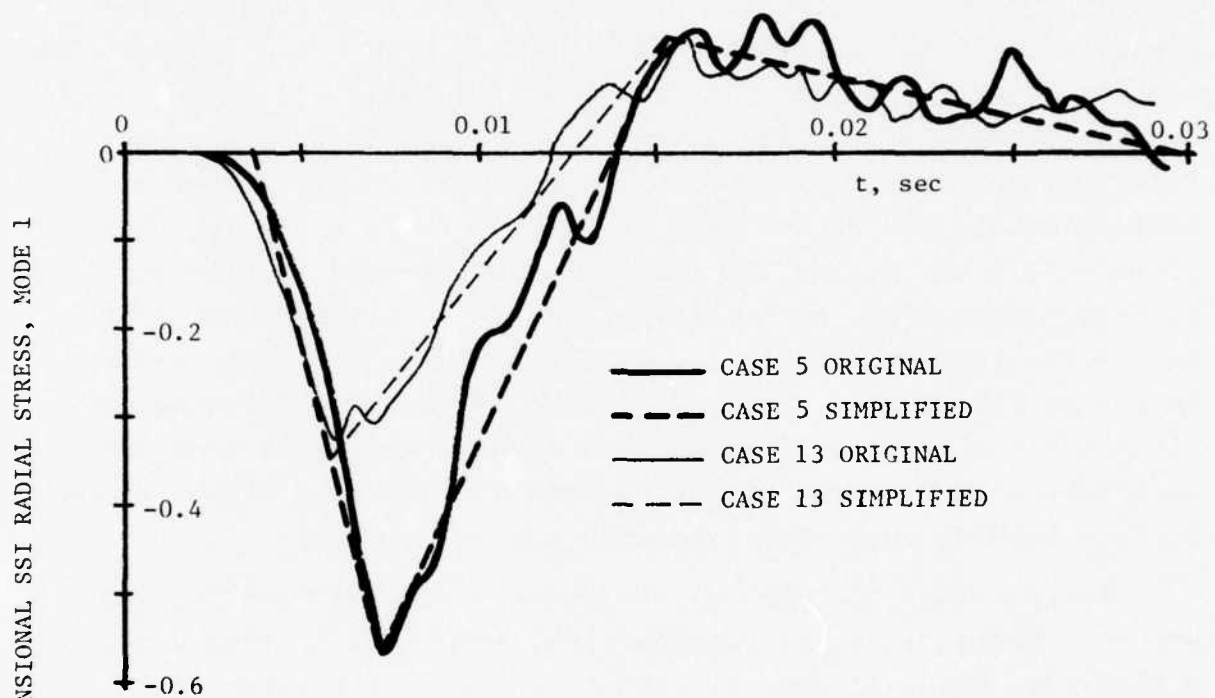


Figure 37b. Approximations to Mode 1 SSI Radial Stress Variation, Cases 5 and 13

generally not be required to accurately determine the buried structure loads. When the simplified SSI loads are characterized (as a function of the structure, soil, depth of burial and airblast loading parameters) the reliability of these buried structure load approximations should be judged by computing the response of the cylinder in vacuo to these loads and comparing the results with those obtained from the original unsimplified modal load histories.

(3) The results of the dynamic finite element solutions considered in this investigation employed two different nonlinear granular type soil materials with a rather high yield surface. The results from the solutions using these two materials do not vary drastically, and this implies that the loads on a buried tunnel liner are not very dependent on the material type. However a limited number of results were obtained during the project using an elastic soil media, and the tunnel liner response is significantly different than with the nonlinear media. This implies that the soil media characteristics are important in determining the loads on buried structures. This, of course, is not a surprising conclusion since it is well known that structures buried in a competent material, such as rock, will withstand considerably higher ground surface loading than when buried in a poor material.

In an effort to quantify the relationship between SSI loading and soil media, it is recommended that solutions be obtained using a clay-like material and also two other materials which would simulate very good and poor materials.

(4) It was observed that for certain of the dynamic solutions, significant tension thrusts occur in the lower portion of the buried cylinder liner for a portion of the dynamic solution. In some cases these tension thrusts exceed the peak compression thrust that occurs in the same portion of the liner during the solution. It appears that sizeable tension thrusts, which can greatly exceed the tensile capacity of a reinforced tunnel liner, occur for shallow buried stiff cylinders loaded by short duration ground shock waveforms.

The soil characteristics are also an important aspect of this phenomenon, since for the stiff tunnel, only minor tension thrusts occur when the soil is considered to be elastic. Alternatively, large invert tension thrusts appeared for the flexible structure when elastic soil was used instead of the nonlinear soil media.

The tensile thrusts have initially been attributed to the soil-structure interaction shear stresses that occur over the lower portion of the cylinder during the early phases of the loading. That is, the initial motion of the cylinder is downward in response to the compression wave impinging on the upper portion of the cylinder. This motion creates SSI shear stresses over the lower portion of the cylinder that resist the downward motion, and these shear stresses induce sizeable tensile waves in the invert portion of the liner.

Sizeable tension thrust in a buried cylinder has not been previously reported by other analytical or experimental studies incorporating realistic soil media material laws. For this reason, it is recommended that this phenomenon be investigated in more detail so that the mechanics of the loading are understood and it will be known what parameters (loading waveforms, structure stiffness, soil parameters, etc.) can create these potentially devastating structural loads.

REFERENCES

1. Welch, R. E., "A Review of the Inclusion Dynamics Aspect of Hardened Ground Facilities," Shock and Vibration Digest, 3(9), (September 1971).
2. Scavuzzo, R. J. and Raftopoulos, D., "Literature Review of Structure Foundation Interaction," Univ. Toledo Tech. Report 1, AEC Contract AT-(40-1)-3822 (October 1968).
3. Werner, S. D., "Analysis of Dynamic Response of SAFEGUARD Structures," Shock and Vibration Bull. 41(3) (October 1970).
4. Chiapetta, R. L. and Costantino, C. J., "A Bibliography on the Response of Earth Media and Buried Structures to Ground Shock Loading," IITRI Report M6177, Waterways Experiment Station (June 1967).
5. Allgood, J. R., Summary of Soil-Structure Interaction, Technical Report R771, AD748581, Naval Civil Engineering Laboratory Port Hueneme, Calif. (July 1972).
6. Isenberg, J., A Review of Current Analytic and Field Testing Programs: Status of Research In Structure - Medium Interaction, DNA 3976F, Weidlinger Associates, Menlo Park, Calif. (December 1975).
7. Corps of Engineers - Design of Structures to Resist the Effects of Atomic Weapons
 EM 1110-345-413 Weapons Effects Data
 EM 1110-345-414 Strength of Materials and Structural Elements
 EM 1110-345-415 Principles of Dynamic Analysis and Design
 EM 1110-345-416 Structural Elements Subjected to Dynamic Loads
 EM 1110-345-417 Single-Story Frame Buildings
 EM 1110-345-418 Multi-Story Frame Buildings
 EM 1110-345-419 Shear Wall Structures
 EM 1110-345-420 Arches and Domes
 EM 1110-345-421 Buried and Semiburied Structures
8. Baron, M. L.; Bleich, H. H. and Weidlinger, P., "Theoretical Studies on Ground Shock Phenomena," SR-19, The MITRE Corporation, Bedford, Mass. (October 1960).
9. Baron, M. L. and Bleich, H. H., Further Studies of the Response of a Cylindrical Shell to a Transverse Shock Wave, Technical Report 10, Columbia University, New York, N.Y. (December 1953).
10. Baron, M. L., et al, "The Design of Lined Underground Cavities Subjected to Nuclear Blasts," Bull. 32, U.S. Naval Research Laboratory, 32nd Symposium on Shock, Vibration and Associated Environments: Protective Construction, Part III, pp 133-158 (December 1963).

11. Salmon, M. A., Investigation of Silo Linings, Technical Report AFSWC-TR-59-57, Armour Research Foundation, Chicago, Ill. (September 1959).
12. Robinson, R. R., "Investigation of Silo and Tunnel Linings," AFSWC-TDR-62-1 (March 1962).
13. Costantino, C. J.; Robinson, R. R. and Salmon, M. A., "A Simplified Soil/Structure Interaction Model to Investigate the Response of Buried Silos and Cylinders," Proc. Symp. on Soil/Structure Interaction, Univ. Ariz. (September 1964).
14. Welch, R. E., "Soil/Structure Interaction Computer Codes," IITRI, DASA 2355-1, Contract DASA 01-68-C-0075 (October 1969).
15. Costantino, C. J., "Study of Advanced Missile Support Isolation Systems," AFBSD Contract AF04(694)-569, IITRI Report M6091 (January 1965).
16. Robinson, R. R. "Effects of Site Peculiar Variations in Ground Shock Environment on SAFEGUARD PAR Power Plant Structure Response," IITRI Report J6173, Contract DACA 87-68-C-0012 (March 1970).
17. Robinson, R. R., "Comparison of a Soil/Structure Interaction Formulation with Experimental Data for the SAFEGUARD Power Plant," IITRI Progress Report 12, Contract DACA-39-C-70-0020 (February 1971).
18. Welch, R. E., "SPARTAN Launch Station Dynamic Analysis," Contract DASA-01-70-C-0018, (October 1969).
19. "Sentinel: A Briefing on Analyses of the Dynamic Responses of the MSCB, Spartan LS and EDC," Presented to the Sentinel Airblast and Shock Vulnerability Working Group, the Ralph M. Parsons Company, Los Angeles, Calif. (March 4, 1969).
20. Nishimura, G. and Jimbo, Y., "A Dynamical Problem of Stress Concentration--Stresses in the Vicinity of a Spherical Matter Included in an Elastic Solid," J. Faculty Engr. XXIV(3), Univ. Tokyo.
21. Ying, C. F. and Truell, R., "Scattering of a Plane Longitudinal Wave by a Spherical Obstacle in an Isotropically Elastic Solid," J. Appl. Phys. 27(9) (September 1956).
22. Anderson, V. C., "Sound Scattering from a Fluid Sphere," J. Acoust. Soc. Am. 22(4) (July 1950).
23. Mow, C. C., "On the Transient Motion of a Rigid Spherical Inclusion in an Elastic Medium and Its Inverse Problem," J. Appl. Mech. 33(E4) (December 1966).

24. Mow, C. C., "Transient Response of a Rigid Spherical Inclusion in an Elastic Medium," J. Appl Mech. 33(3) (September 1965).
25. Mow, C. C., "On the Effects of Stress Wave Diffraction on Ground-Shock Measurements; Part I," Rand Corp. RM-4341-PR (January 1965)
26. Peek, J. C. and Miklowitz, J., "Shadow-Zone Response in the Diffraction of a Plane Compressional Pulse by a Circular Cavity," Intl J. Solids and Structures 5(5), pp 437-454 (May 1969).
27. Paul, S. L. and Robinson, A. R., "Interaction of Plane Elastic Waves with a Cylindrical Cavity," AFWL, RTD TDR-63-3021 (June 1963).
28. Baron, M. L. and Mathews, A. T., "Diffraction of a Pressure Wave by a Cylindrical Cavity in an Elastic Medium," J Appl. Mech., Trans ASME 28(3), pp 347-354 (September 1961).
29. Baron, M. L. and Parnes, R., "Displacements and Velocities Produced by the Diffraction of a Pressure Wave by a Cylindrical Cavity in an Elastic Medium," J. App. Mech 29(2) (June 1962).
30. Pao, H. L., "Dynamical Stress Concentration in an Elastic Plate," J. Appl. Mech. 29(2) (June 1962).
31. Peralta, L. A.; Carrier, G. F. and Mow, C. C., "An Approximate Procedure for the Solution of a Class of Transient Wave Diffraction Problems," J. Appl. Mech 34(1) (March 1966).
32. Baron, M. L. and Parnes, R., "Diffraction of a Pressure Wave by a Cylindrical Shell in an Elastic Medium," Proc. 4th U.S. Natl. Congress Appl. Mech. 1, pp 63-75 (June 1962)
33. Yoshihara, T.; Robinson, A. R. and Merritt, J. L., "Interaction of Plane Elastic Waves with an Elastic Cylindrical Shell," Civil Engr. Studies, Struc, Res. Ser. 261, Univ. Ill. (January 1963).
34. Mindlin, R. D. and Bleich, H. H., "Response of an Elastic Cylindrical Shell to a Transverse Step Shock Wave," J. Appl. Mech., Trans. ASME 20(2), pp 189-195 (June 1953).
35. Baron, M. L., "The Response of a Cylindrical Shell to a Transverse Shock Wave," Proc. 2nd U.S. Natl. Congress Appl. Mech. ASME (1954).
36. Miles, J. W., "Motion of a Rigid Cylinder Due to a Plane Elastic Wave," J. Acous. Soc. Am. 32(12) (December 1964).
37. Pao, Y. H., "Dynamic Stress Concentrations in an Elastic Plate with Rigid Circular Inclusion," MITRE Corp. SR-41 (December 1961).
38. Mow, C. C. and McCabe, W. L., "Dynamic Stresses in an Elastic Cylinder," J. Engr. Mech. Div., Proc. 89 ASCE (EM3), pp 21-41 (June 1963)

39. Mente, L. J. and French, F. W., "Response of Elastic Cylinders to Plane Shear Waves," J. Engr. Mech. Div., Proc. ASCE 90(EM5) (October 1964).
40. Parnes, R. and Baron, M. L., "Moving Loads on the Surface of a Cylindrical Bore in an Infinite Elastic Medium: Part III--Some Applications of the Theory," Rand Corp. RM-4420-PR (May 1965).
41. Ali-Akbarian, M. and Johnson, J., "Oblique Incidence of Plane Stress Waves on a Thick Cylindrical Shell," Univ. Ill, AFWL-TR-69-56 (July 1969).
42. Bycroft, G. N., "Forced Vibrations of a Rigid Circular Plate on a Semi-Infinite Elastic Space and on an Elastic Stratum," Phil. Trans. Roy. Soc. London 248(A948), pp 327-368 (1956).
43. Arnold, R. N.; Bycroft, G. N. and Warburton, G. B., "Forced Vibrations of a Body on an Infinite Elastic Solid," J. Appl. Mech., Trans. ASME 22, pp 391-400 (September 1955).
44. Thomson, W. T. and Kobori, T., "Dynamical Compliance of Rectangular Foundations on an Elastic Half-Space," J. Appl. Mech. 30(4) (December 1963).
45. Isenberg, J., "Interaction between Soil and Nuclear Reactor Foundation During Earthquakes," Agbabian-Jacobsen Assoc., Report J6915-1200, for Univ. Toledo Res. Foundation (June 1970).
46. Farhoomand, I. and Wilson, E. L., "A Nonlinear Finite Element Code for Analyzing the Blast Response of Underground Structures," WES Report N-70-1 (January 1970).
47. Welch, R. E., "Three-Dimensional Structure/Media Interaction--DYNAX Development and Applications," IITRI, DASA 2442-1, Contract DASA 01-69-C-0028 (May 1970).
48. Belytschko, T.; Chiapetta, R. L.; and Rouse, J., "A Computer Code for Dynamic Stress Analysis of Media-Structure Problems with Nonlinearities (SAMSON)," AFWL-TR-72-104, IIT Research Institute (February 1973).
49. Crawford, R. E.; Higgins, C. J. and Bultmann, E. H., "The Air Force Manual for Design and Analysis of Hardened Structures," Air Force Weapons Laboratory, AFWL-TR-74-102 (October 1974).
50. Burn, J. Q. and Richards, R. M., "Attenuation of Stresses for Buried Cylinders," Proc. Symp. on Soil-Structure Interaction, Univ. Ariz. (September 1964).
51. Hoeg, Kaare, Pressure Distribution on Underground Structural Cylinders, Technical Report AFWL TR-65-98, Massachusetts Inst. Tech. (April 1966).

52. Hoeg, Kaare, "Stresses Against Underground Structural Cylinders," J. Soil Mech. and Foundations Div., ASCE 94(SM4), pp 833-858 (July 1968).
53. Flugge, W., Stresses in Shells, 2nd Ed., Springer Verlag (1973).
54. Bathe, K.; Wilson, E. L. and Peterson, F. E., "SAP IV, A Structural Analysis Program for Static and Dynamic Response of Linear Systems," Report EERC 73-11, Univ. Calif.(Berkeley)(June 1973).
55. Bartel, H. D. and Cole. D. M., "User Manual for SAMSON and Family," AFWL Tech. Note DE-TN-74-009 (December 1974).
56. Chiapetta, R. L., "A Computer Code for Dynamic Stress Analysis of Media-Structure Problems with Nonlinearities (SAMSON) Volume IV, Analysis of GRABS Phase 1 Tests," AFWL-TR-72-104, 4, Pt 1, IIT Research Institute (February 1973).
57. Cole, D. M., "SMI Analysis of MX Buried Structures," AFWL. Facility Branch, Memo for Record/BH/Sept. 12, 1975.
58. Dorris, A. F., "Response of Horizontally Oriented Buried Cylinders to Static and Dynamic Loading", WES Tech. Rept. I-682, July 1965.
59. Albritton, G. E., et al "The Elastic Response of Buried Cylinders Critical Literature Review and Plot Study", WES Tech. Rept. I-720, April 1966.
60. Dorris, A. F. and Albritton, G. E., "Response of a Buried Prototype Communications Conduit to Static and Dynamic Loading", WES Tech. Rept. I-750, December 1966.

APPENDIX A

FREE FIELD VERTICAL STRESS WAVE INVESTIGATIONS

The results of the SAMSON dynamic finite element solutions indicated that when the cylindrical tunnel liner was buried under two tunnel diameters of overburden, relatively drastic reductions in the SSI tunnel loadings occurred. The free field stress wave study presented in this appendix was undertaken to quantify the source of these reduced loadings and to ensure the adequacy of the finite element model used to represent the soil. This investigation used both one- and two-dimensional finite element meshes of the soil. In an effort to see whether the basic soil mesh used in the buried tunnel liner dynamic solutions was creating some of the attenuation and distortion of the soil stress wave, the two-dimensional finite element mesh was made up by filling in the tunnel cavity with an appropriate mesh of soil elements.

Table A1 gives the essential parameters for the 14 free field cases discussed herein. The results of this study are presented in figures A1 through A9 and show that the primary source of the reduced SSI liner loadings is the free field peak stress attenuation with depth for the two nonlinear soil models (materials A and B) employed in this project. That is, the hardening material stress-strain variation coupled with the stiff unloading-reloading rate creates rather drastic changes in the airblast pressure waveform as it propagates downward into the soil media. The most pronounced reduction in the peak vertical free field stress with depth occurs for the short duration (0.015 sec) surface loading case.

The finite element soil meshes were made up as follows. First, the representation of the concrete liner was removed from the two-dimensional plane strain finite element model and the resulting void filled in by 126 soil elements as illustrated in figure A1, thus producing a two-dimensional soil model composed of 803 rectangular and triangular soil elements. In addition, a simplified one-dimensional model was constructed which consists of 48 rectangular elements representing a vertical column of soil.

Table A1
FREE FIELD STUDY RUN MATRIX

Case	Mesh*	P_o (psi)	t_d	Soil	Stress-Strain Rates (psi)		Load-Unload Rates (psi)	
					K_{L1}	K_{L2}	K_{L3}	K_u
FF1	5DSFF	500	0.015	B	16700	38900	166700	166700
2	5DSFF	1500	0.060	B	16700	38900	166700	166700
3	6	500	0.015	B	16700	38900	166700	166700
4	6	1500	0.060	B	16700	38900	166700	166700
5	6	500	0.015	B-2 Load	16700	38900	-	166700
6	6	1500	0.060	B-2 Load	16700	38900	-	166700
7	6	500	0.015	B-1 Load	16700	-	-	166700
8	6	1500	0.060	B-1 Load	16700	-	-	166700
9	6	500	0.015	-	16700	38900	-	38900
10	6	1500	0.060	-	16700	38900	-	38900
11	6	500	0.015	Elastic	16700	-	-	16700
12	6	1500	0.060	Elastic	16700	-	-	16700
13	6	500	0.015	A	16700	38900	166700	166700
14	6	1500	0.060	A	16700	38900	166700	166700

* Mesh 5DSFF - Same as Mesh 5DS ($h/R=4$) with cavity filled in with soil media elements

Mesh 6 - One-dimensional mesh with 48 elements

1 psi = 6.895 kPa

Identical load cases were applied to both of the models and the results evaluated. Results from the two models compare more closely for the low overpressure ($P_o=500$ psi), short time duration ($t_d=0.015$ sec) loading than for the higher overpressure ($P_o=1500$ psi), long time duration ($t_d=0.60$ sec) case. However, the wave shapes and peak stress values obtained using the detailed two-dimensional mesh for the soil are generally in good agreement with results obtained using the simplified 48 element one-dimensional model as illustrated in figures A2 and A3. This indicates that the detailed model does provide a reliable description of the soil response due to dynamic loading.

The soil characteristics provided by the ROCKMT3 soil model for soil B has three progressively steeper compressive loading rates and an unloading rate equal to the steepest loading rate. The response of the soil using the simplified 48 element one-dimensional mesh and the ROCKMT3 soil description is shown in figure A4. For the load cases considered ($P_o=500$ psi and $P_o=1500$ psi) the resulting stress magnitudes are not high enough to require use of the third loading rate. Consequently, if only the first two loading rates and the same steep unloading rate are used to describe the material, the soil response is virtually unaltered, as indicated by figure A5.

By using the first two loading rates and an unloading rate equal to the second loading rate instead of the steeper third rate, considerably less attenuation of the stress wave occurs as illustrated in figure A7. This result indicates that the steeper unloading rate used by the soil A and B models is primarily responsible for the decay of the propagating stress wave.

Figure A6 illustrates the result of using only the first loading rate and the steep unloading rate. For the case of low overpressure ($P_o=500$ psi) only the first load rate is required; therefore, the results are not altered from the $P_o=500$ psi results shown in figures A4 and A5. For the higher overpressure, the second loading rate is utilized; and as expected, a greater attenuation of the stress wave is realized when only a single loading rate is used.

Figure A8 shows the one-dimensional results for soil A. This material model is identical to soil B except the yield surface passes through the origin, i.e., there is no cohesion for soil A. The results for soils A and B are essentially identical as seen by comparing figures A4 and A8.

Figure A9 gives the results for an elastic soil with a bulk modulus equal to that used for the first loading rate of soil B. The damping parameters for this material are also the same as those used for soil B. The results indicate that there is very little attenuation of the peak stress with depth, especially for the high

overpressure load case FF12. There is also a smaller amount of "shocking-up" or overshoot of the peak stress at shallow depths (near the ground surface) in comparison to the soil B solutions as seen by comparing figures A4 and A9.

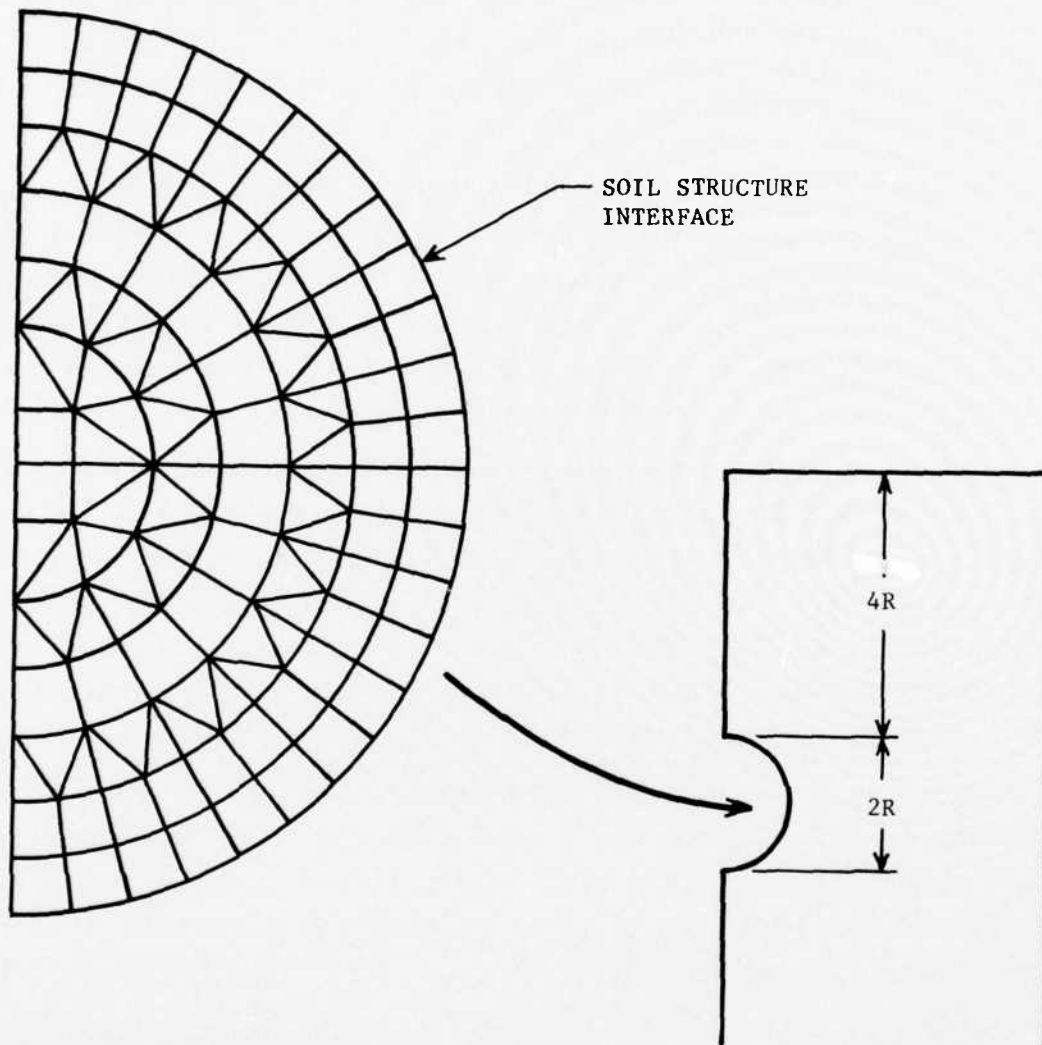
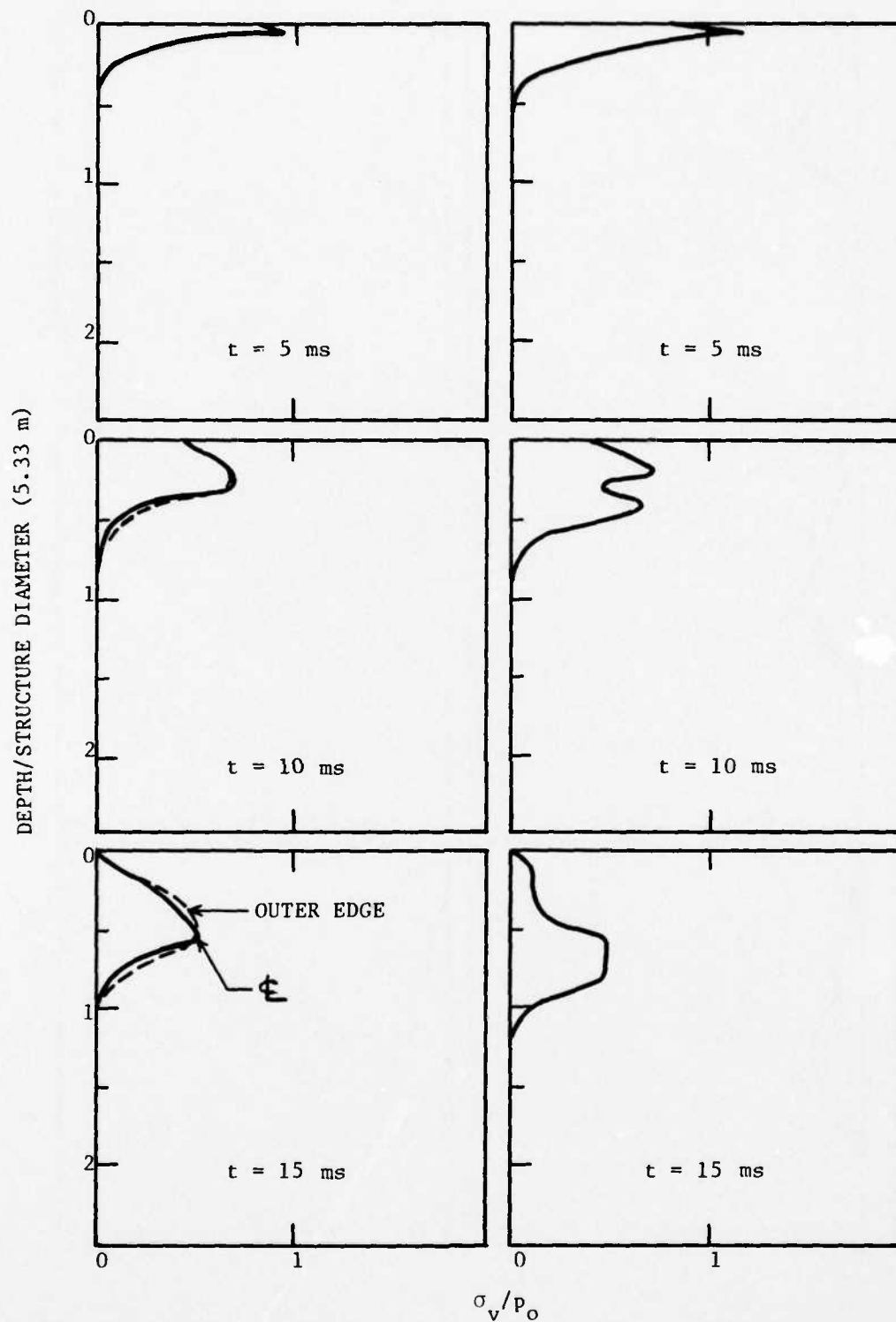


Figure A1. Soil Media Mesh to Fill In Tunnel Liner Cavity

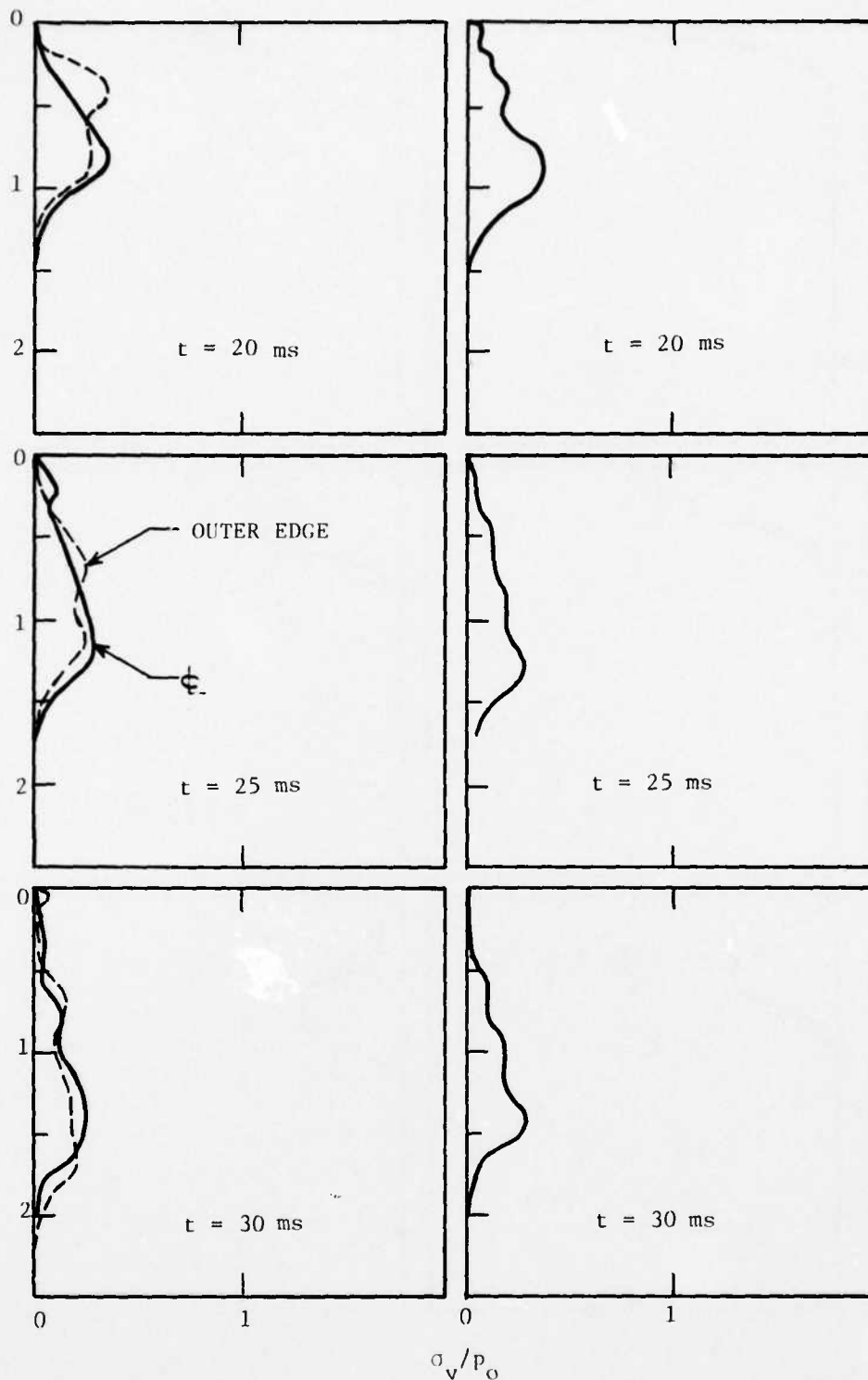


(a) 2D Results Case FF1

(b) 1D Results Case FF3

Figure A2. Comparison of 2D and 1D Free Field Vertical Stress Waves
Soil B, $p_o = 500$ psi, $t_d = 0.015$ sec

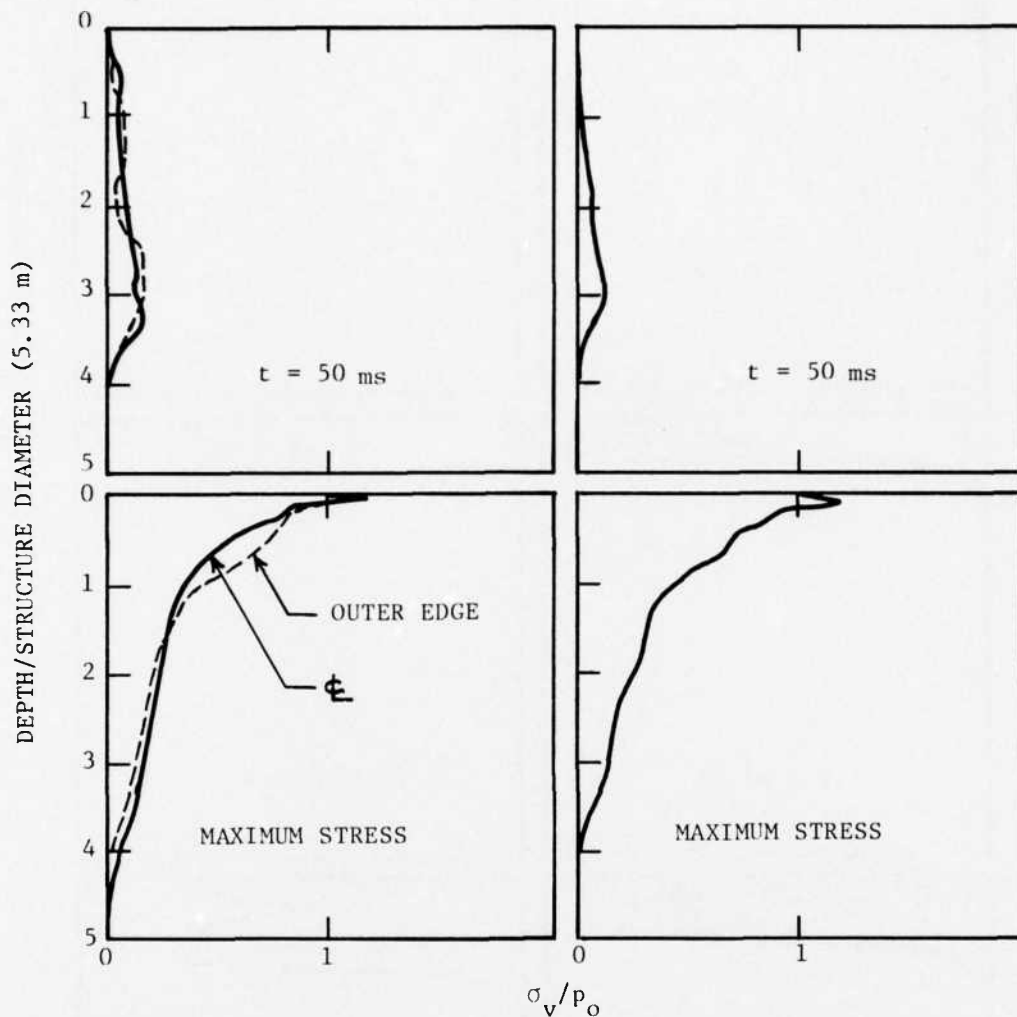
DEPTH/STRUCTURE DIAMETER (5.33 m)



(c) 2D Results Case FF1

(d) 1D Results Case FF3

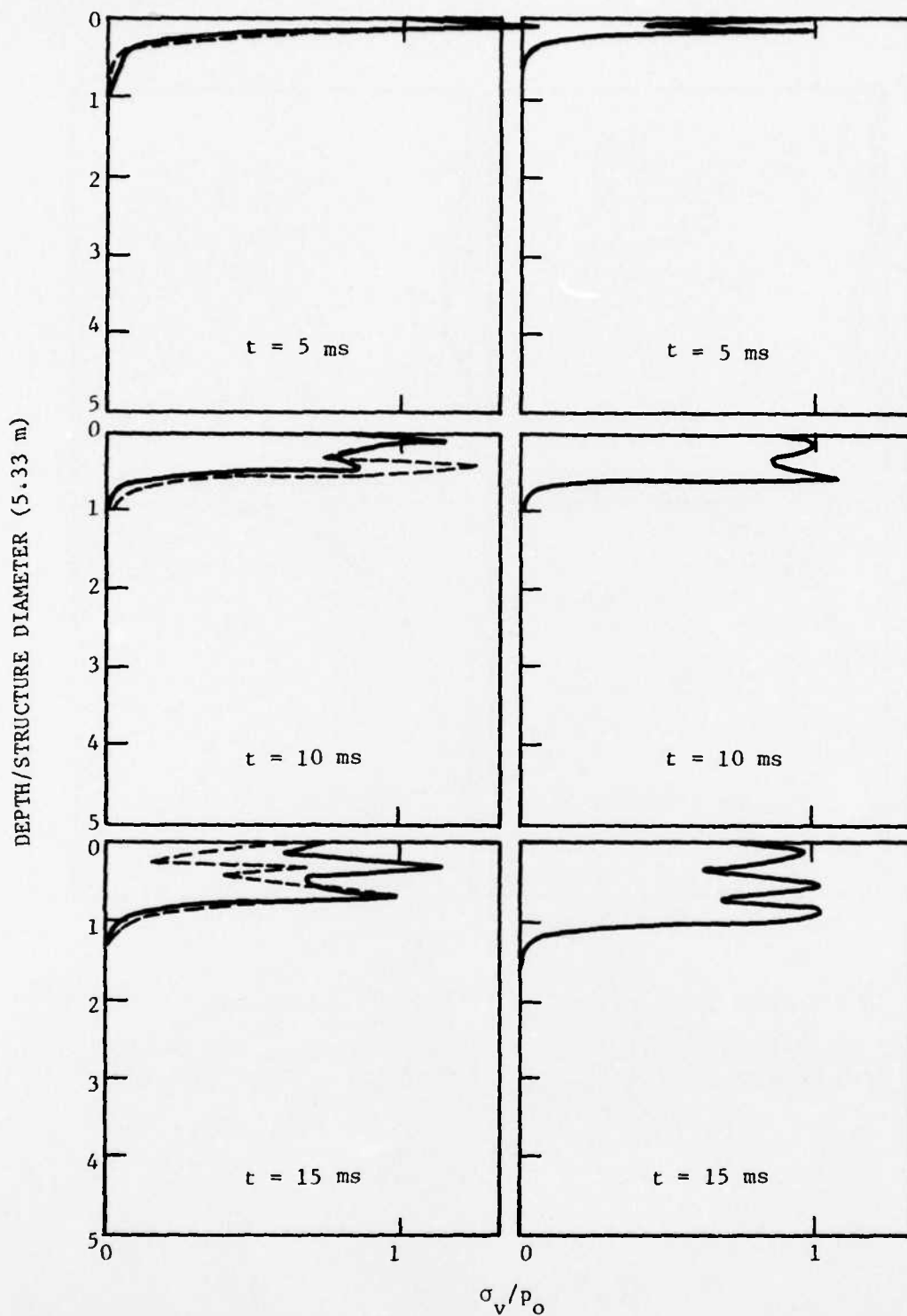
Figure A2 (contd). Comparison of 2D and 1D Free Field Vertical Stress Waves, Soil B, $p_0 = 500$ psi, $t_d = 0.015$ sec



(e) 2D Results Case FF1

(f) 1D Results Case FF3

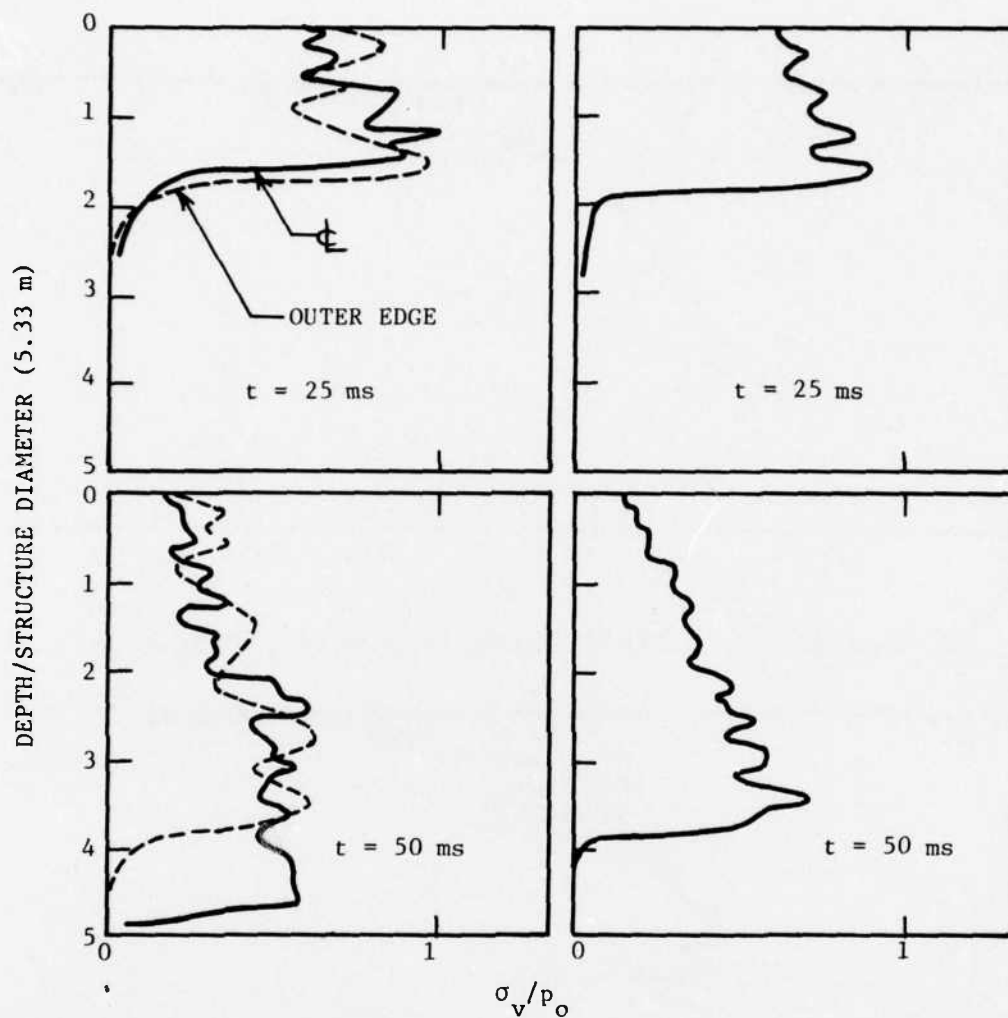
Figure A2 (concl). Comparison of 2D and 1D Free Field Vertical Stress Waves, Soil B, $p_o = 500 \text{ psi}$, $t_d = 0.015 \text{ sec}$



(a) 2D Results Case FF2

(b) 1D Results Case FF4

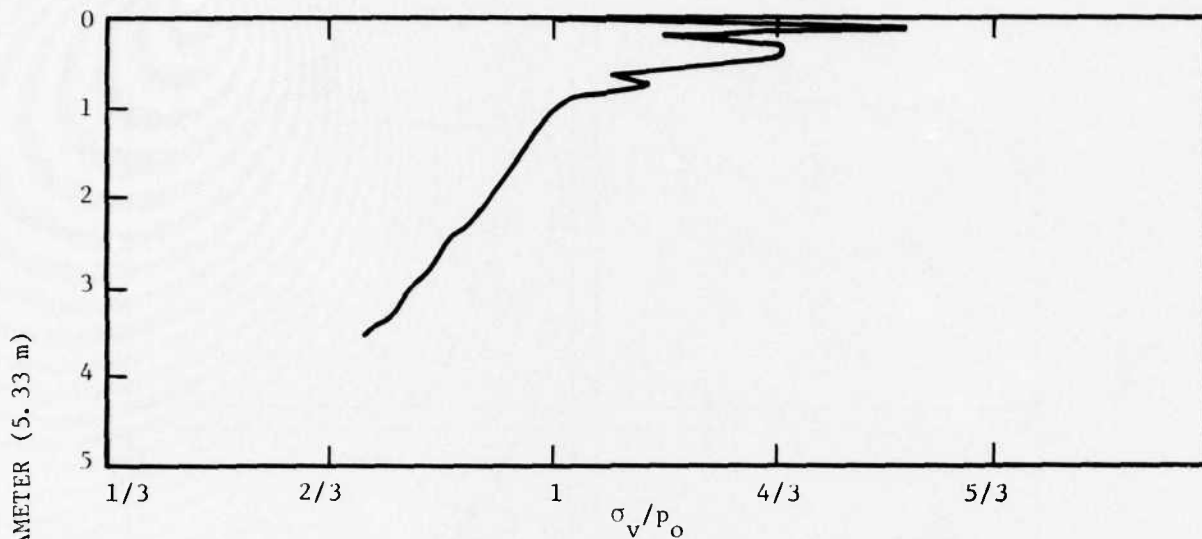
Figure A3. Comparison of 2D and 1D Free Field Vertical Stress Waves
Soil B, $p_o = 1500$ psi, $t_d = 0.06$ sec



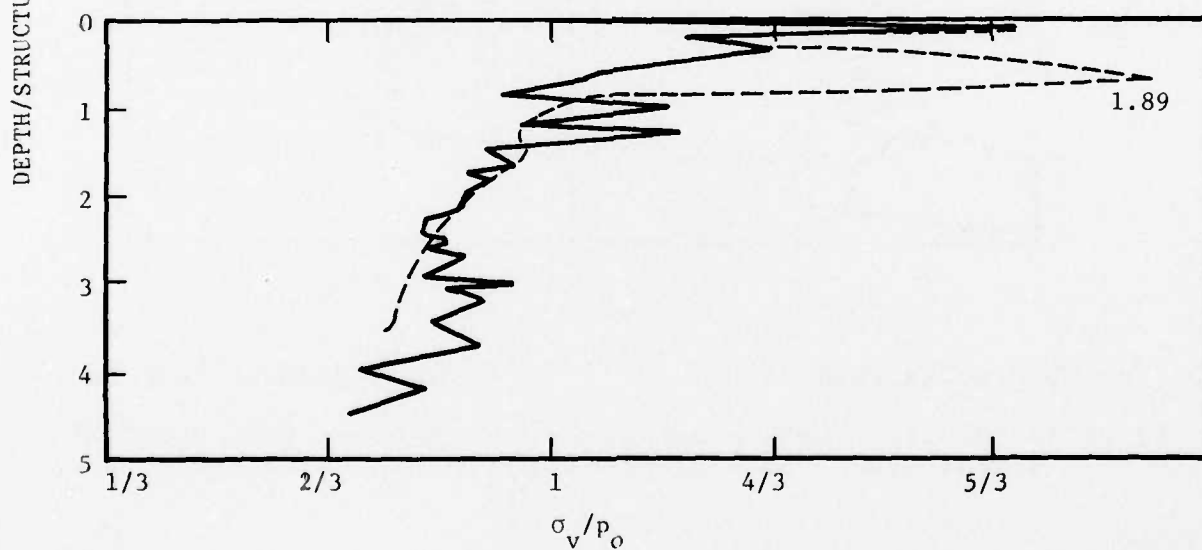
(c) 2D Results Case FF2

(d) 1D Results Case FF4

Figure A3 (contd). Comparison of 2D and 1D Free Field Vertical Stress Waves, Soil B, $p_o = 1500$ psi, $t_d = 0.06$ sec



(e) Maximum Free Field Vertical Stress, 1D Results



(f) Maximum Free Field Vertical Stress, 2D Results

Figure A3 (concl). Comparison of 2D and 1D Free Field Vertical Stress Waves, Soil B, $p_o = 1500$ psi, $t_d = 0.06$ sec

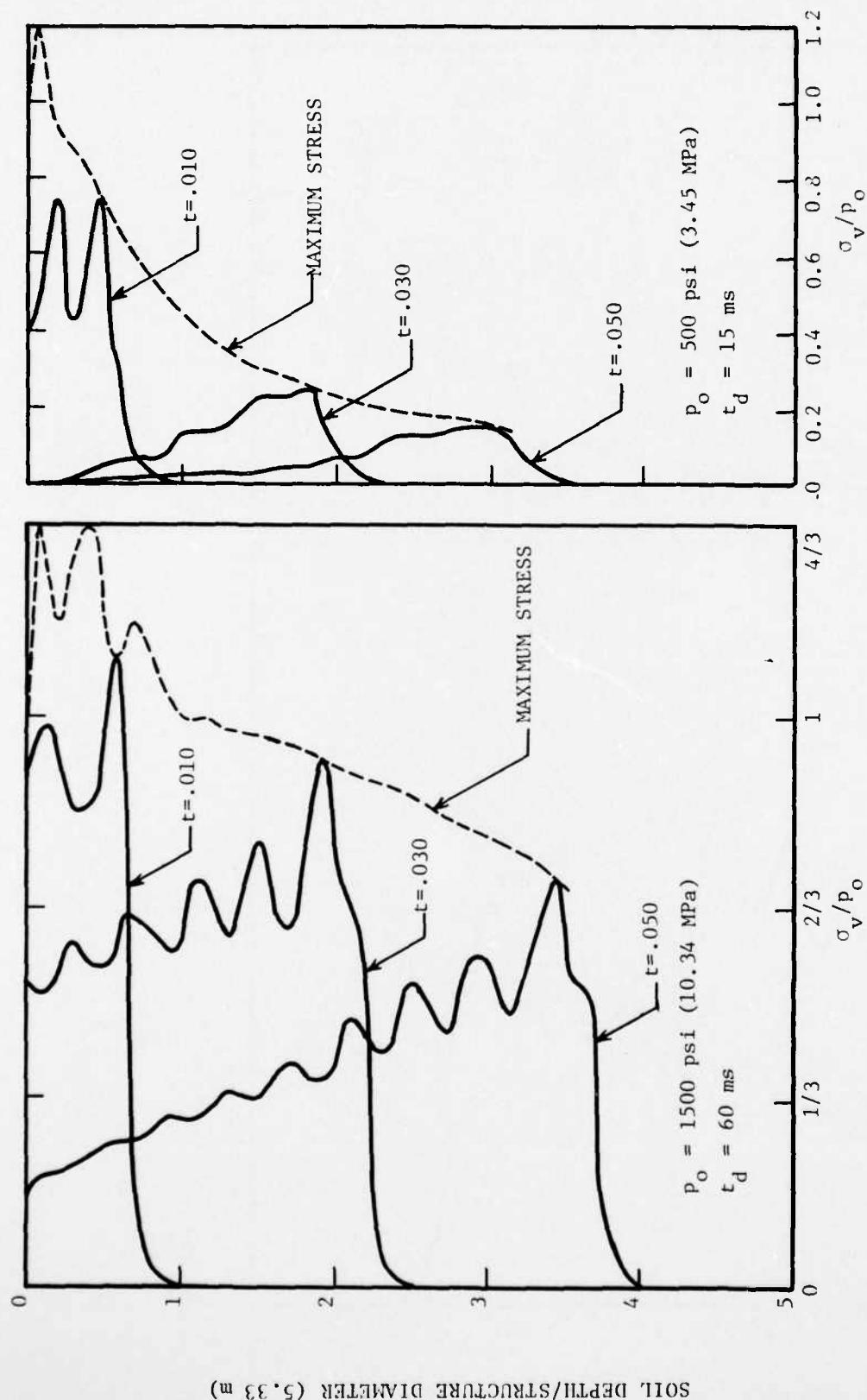


Figure A4. Response of Trilinear Loading ROCKMT3 Soil B
 $(K_{L1} = 16,700 \quad K_{L2} = 38,900 \quad K_{L3} = K_u = 166,700) \text{ 1D Finite Element Model}$

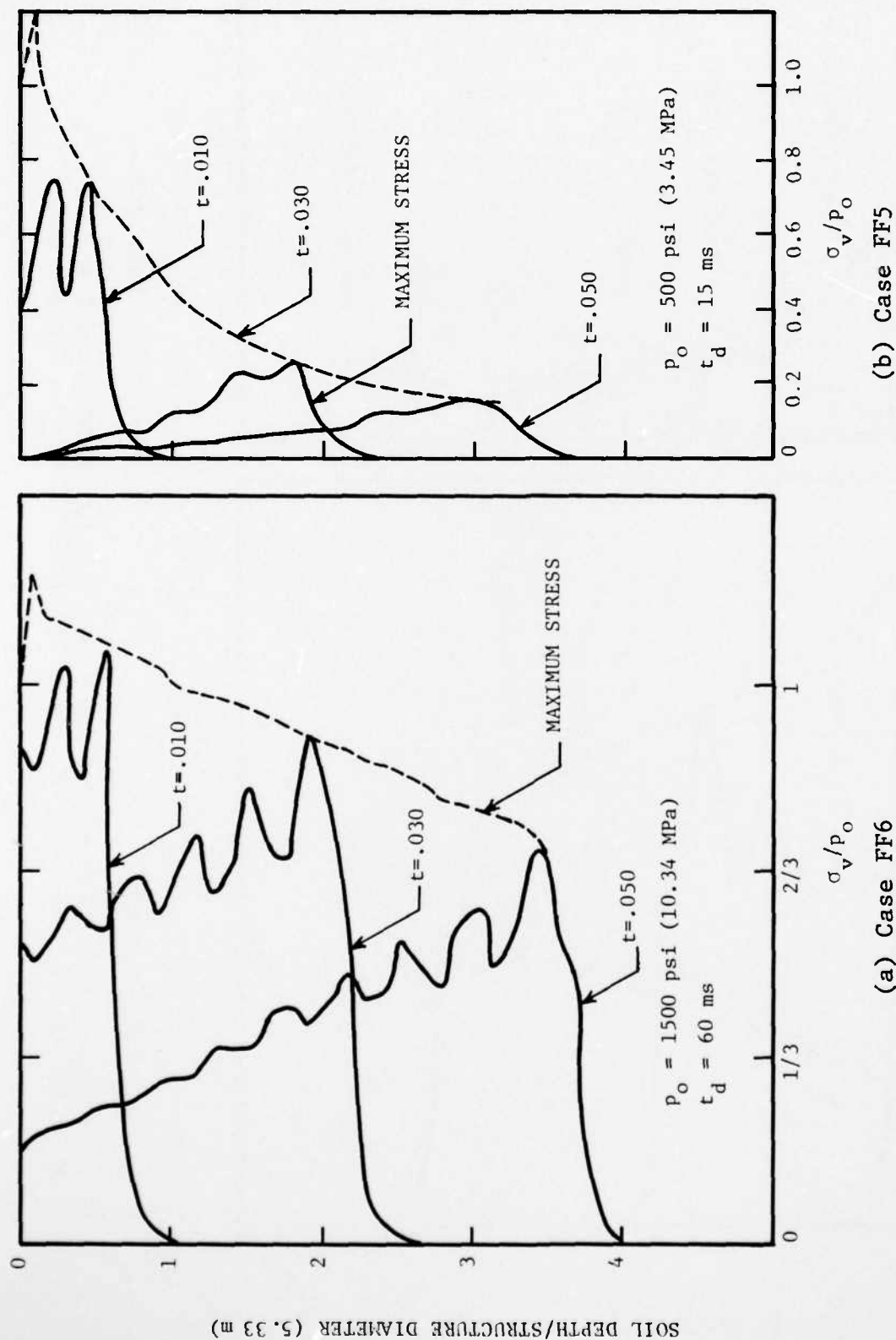
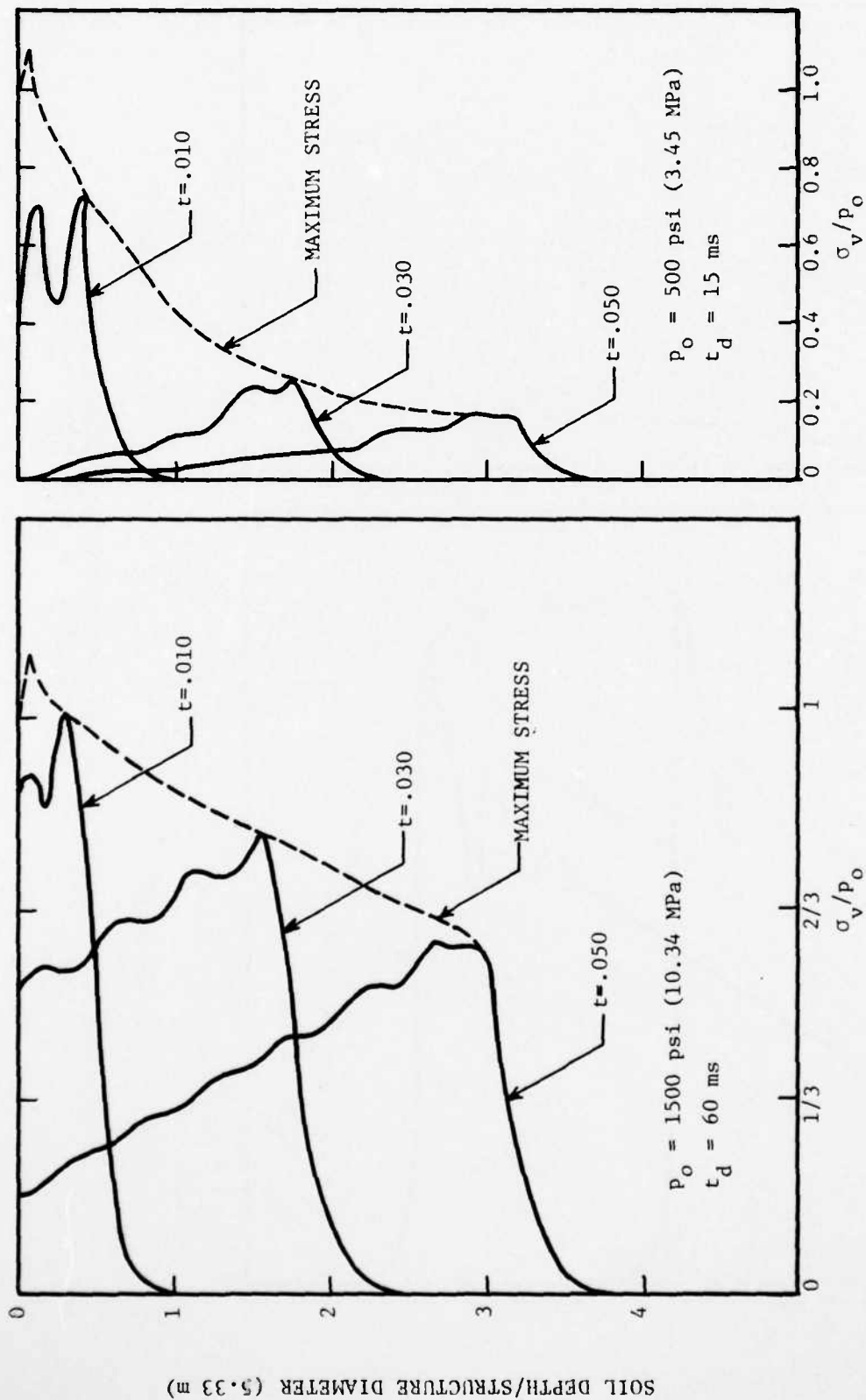


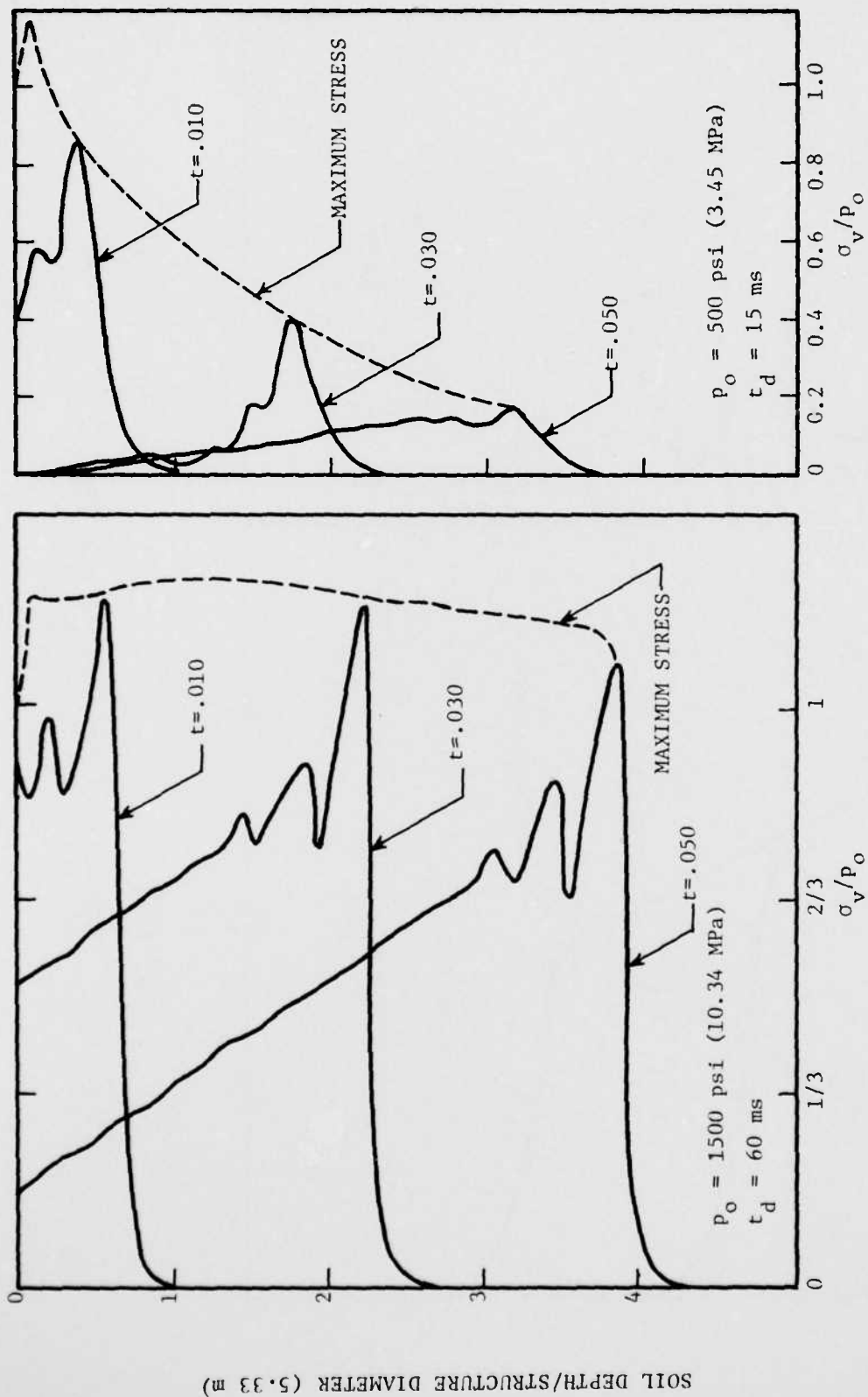
Figure A5. Response of Bilinear Loading ROCKMT3 Soil
 $(K_{L1} = 16,700 \quad K_{L2} = 38,900 \quad K_u = 166,700)$



(b) Case FF7

(a) Case FF8

Figure A6. Response of Linear Loading ROCKMT3 Soil
 $(K_L = 16,700 \quad K_u = 166,700)$



(a) Case FF10

(b) Case FF9

Figure A7. Response of Bilinear Loading, ROCKMT3 Soil
 $(K_{L1} = 16,700 \text{ } K_{L2} = 38,900 \text{ } K_u = 38,900)$

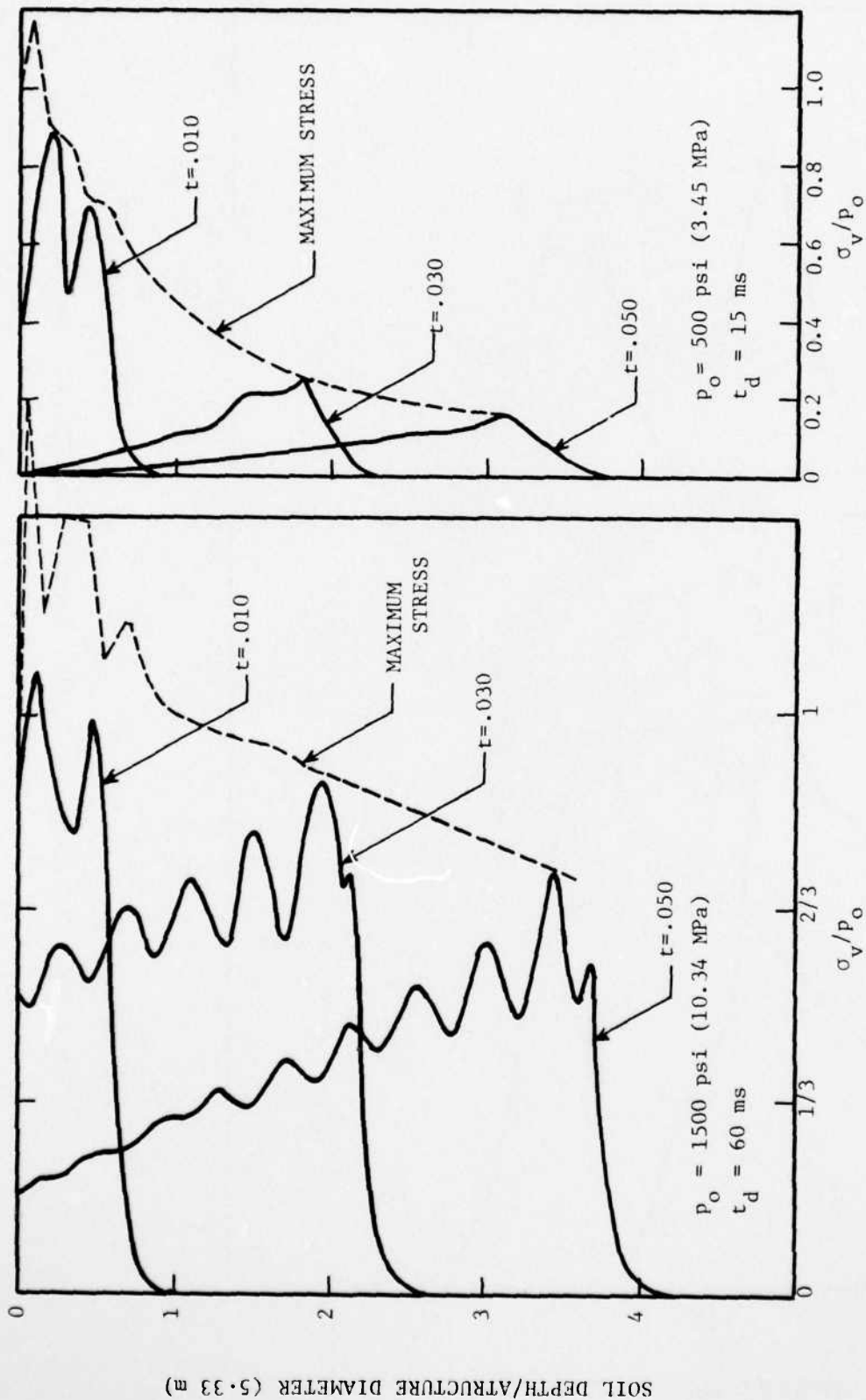


Figure A8. Free Field Response of Trilinear Loading ROCKMT3 Soil A
 $(K_{L1}=16,700, K_{L2}=38,900, K_{L3}=K_u=166,700)$ 1D Finite Element Model

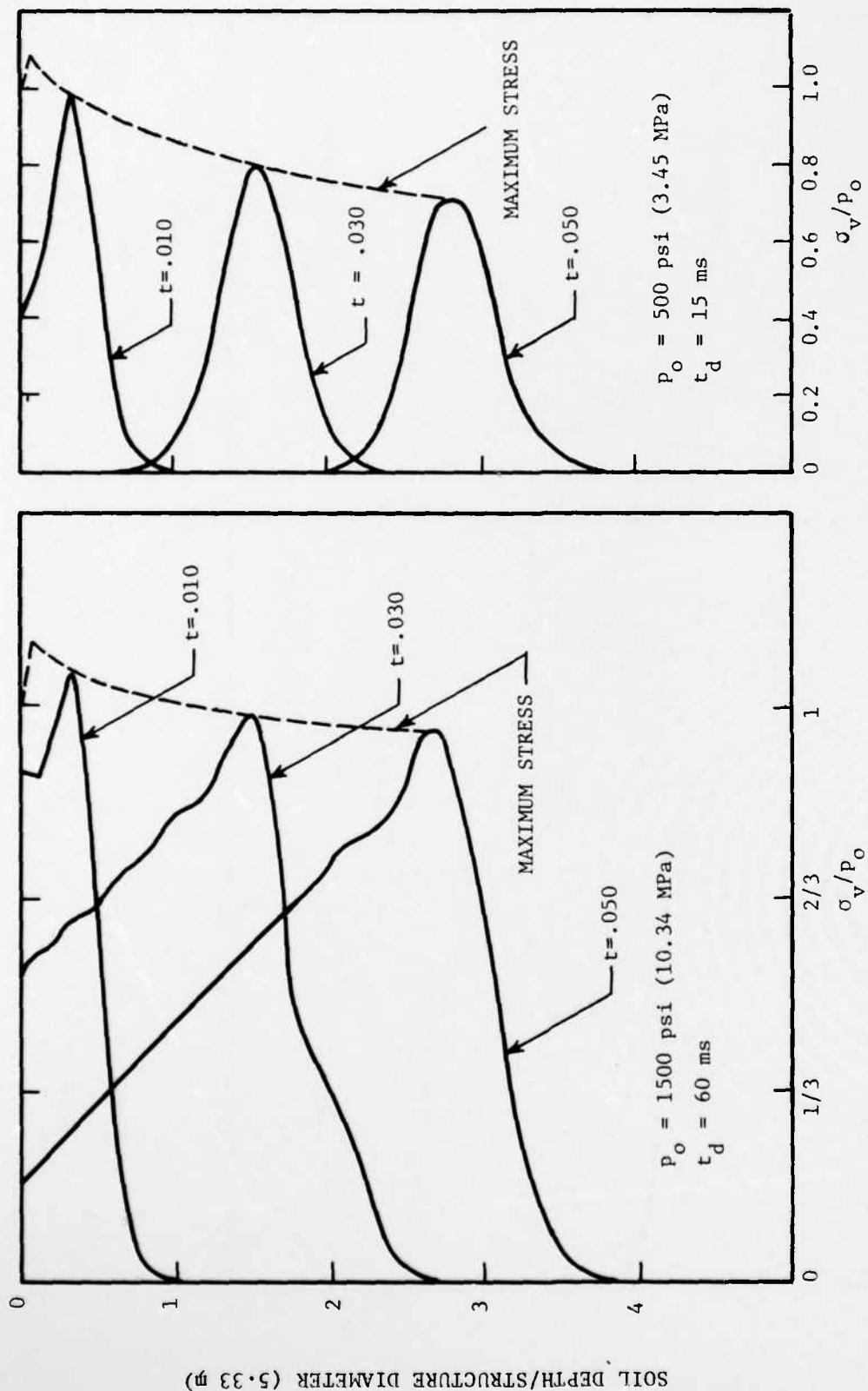


Figure A9. Response of Linear Elastic Soil with Damping

AD-A061 464

IIT RESEARCH INST CHICAGO ILL

F/G 18/3

THEORETICAL INVESTIGATION OF LOADS ON BURIED STRUCTURES. VOLUME--ETC(U)

AUG 78 R R ROBINSON

F29601-76-C-0124

UNCLASSIFIED

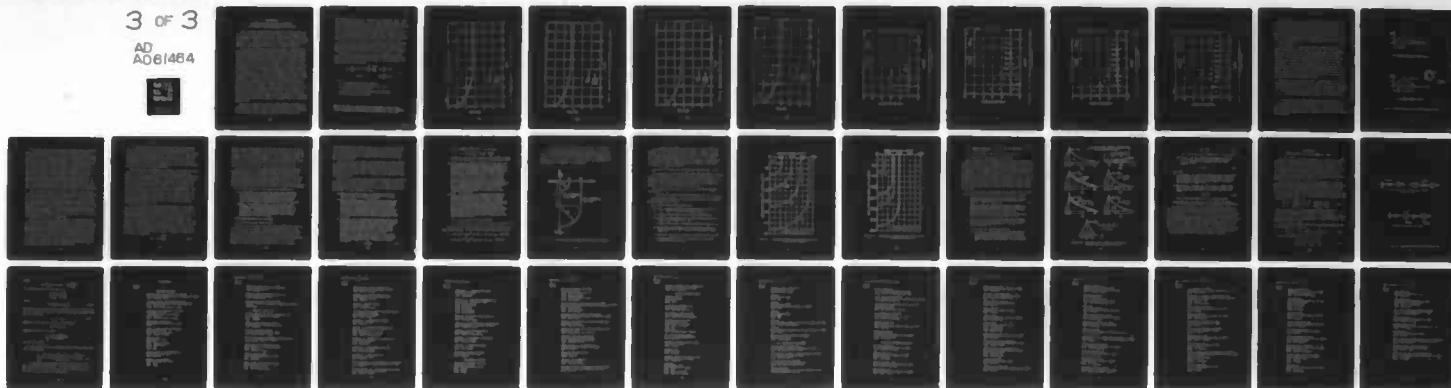
IITRI-J6378-VOL-1

AFWL-TR-78-6-VOL-1

NL

3 OF 3

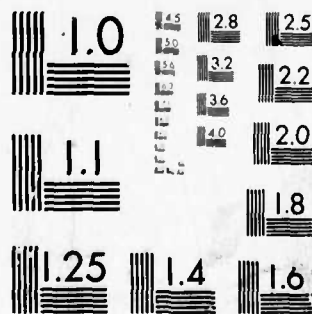
AD
A061464



END
DATE
FILMED

2 - 75
DOC

06146



MICROCOPY RESOLUTION TEST CHART
NATIONAL BUREAU OF STANDARDS-1963-A

APPENDIX B

LOADING FUNCTIONS ON BURIED CYLINDERS

by N. M. Newmark Consulting Engineering Services

As an airblast wave propagates across the ground surface, it induces a pressure pulse in the soil which, as it impinges upon and engulfs an underground cylinder, produces loads (pressures) on the cylinder. Clearly, as this soil stress wave traverses a buried cylinder, the pressures produced by it on the cylinder vary non-uniformly, both spatially and in time, around the cylinder.

It is not now possible to define these soil-cylinder interface pressures with a high degree of confidence. Qualitatively, they should be influenced by a number of parameters that include, possibly among others, the depth of burial of the cylinder, the stiffness of the cylinder (in both flexure and in radial compression), the properties of the surrounding soil (including local nonuniformities in it around the cylinder), the period (or periods) of vibration of the cylinder (or cylinder-soil system), and the size (diameter) of the cylinder in relation to length of the free field pressure pulse. Intuition and judgment alone provide some insight into the general nature of the influences of some of these parameters. For example, as the depth of burial increases, the blast-induced pressures on a buried cylinder should be reduced; as the stiffness of the soil increases relative to that of the cylinder which it surrounds, a larger proportion of pressure that would otherwise be resisted by the cylinder should be taken by arch action in the soil around the cylinder; as the periods of vibration of the cylinder become longer, the nature of the imposed dynamic load pulse should approach, in effect, that of a statically applied load.

While it is possible to discuss these probable influences in a qualitative fashion, they are not yet sufficiently well understood to permit one to define them quantitatively with a high level of confidence. This problem is presented more graphically

in the data plots (Ref. 1) of figures B1 through B8. These data were taken from small model cylinder tests (generally steel) conducted under controlled conditions, generally when buried in dense sand. Inspection of these data plots confirms the general influences of some of the parameters discussed above, but the scatter of the data, even under these controlled test conditions, is so great that any quantification of these effects is almost impossible, especially insofar as flexure-producing loads are concerned.

Figures B1 through B4 indicate a general reduction in circumferential thrust with increasing depth. However, similar plots, which are not reproduced herein, fail to show any significant relationship between circumferential thrust and cylinder stiffness.

Although the data shown in figures B1 through B4 are quite scattered, one can draw a curve as shown on these figures that attempts to reflect an approximate average of the data points. The curve shown has the equation

$$C_a = \frac{T_r}{p_z r} = 0.65 + 0.25 \left(1 - \frac{h_z}{D} \right)^2 \quad \text{for } \frac{h_z}{D} < 1.0$$

$$= 0.65 \quad \text{for } \frac{h_z}{D} \geq 1.0$$
(B-1)

in which

- T_r = circumferential thrust, lb/inch
- p_z = free field pressure at depth $z = h_z$, psi
- r = radius of cylinder, inch
- h_z = depth of soil cover over crown of cylinder
- $D = 2r$, diameter of cylinder

¹ Taken from "Design of Cylindrical Reinforced Concrete Tunnel Liners to Resist Air Overpressure", NCEL Report 68.010, prepared by N. M. Newmark Consulting Engineering Services, June 1968.

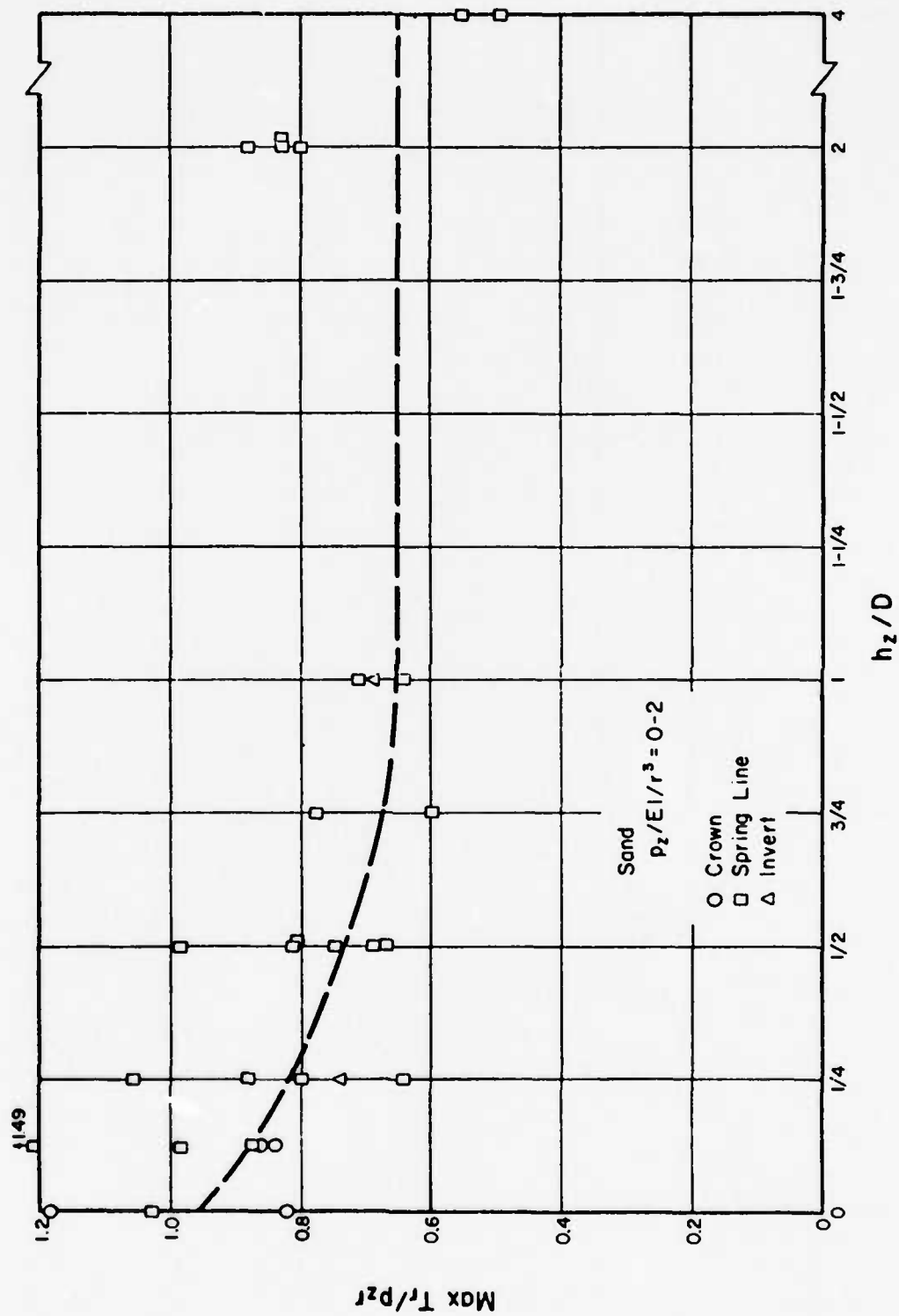


Figure B1. Maximum Thrust Versus Depth of Burial in Sand, $p_z r^3/EI=0-2$

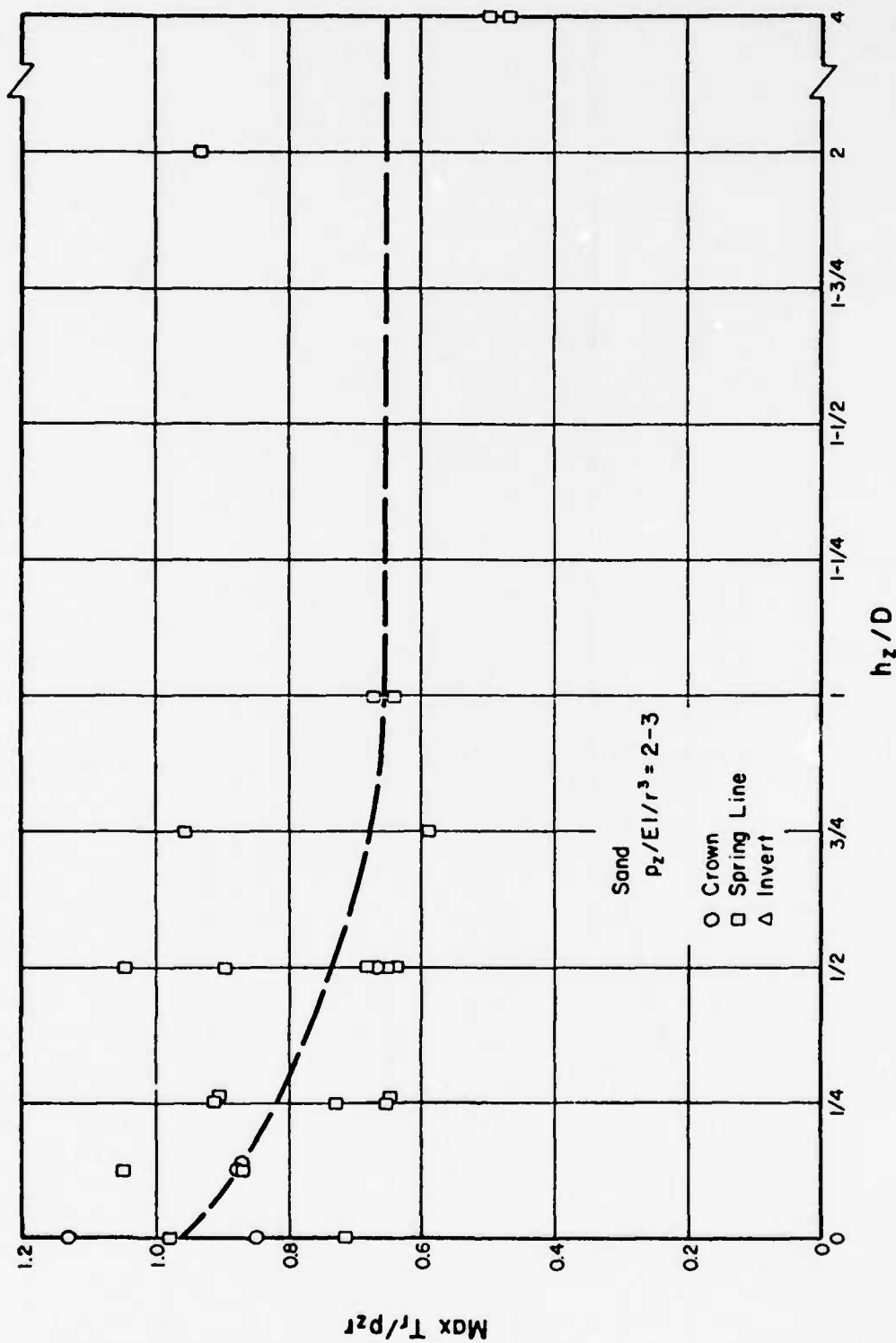


Figure B2. Maximum Thrust Versus Depth of Burial in Sand, $p_2r^3/EI=2-3$

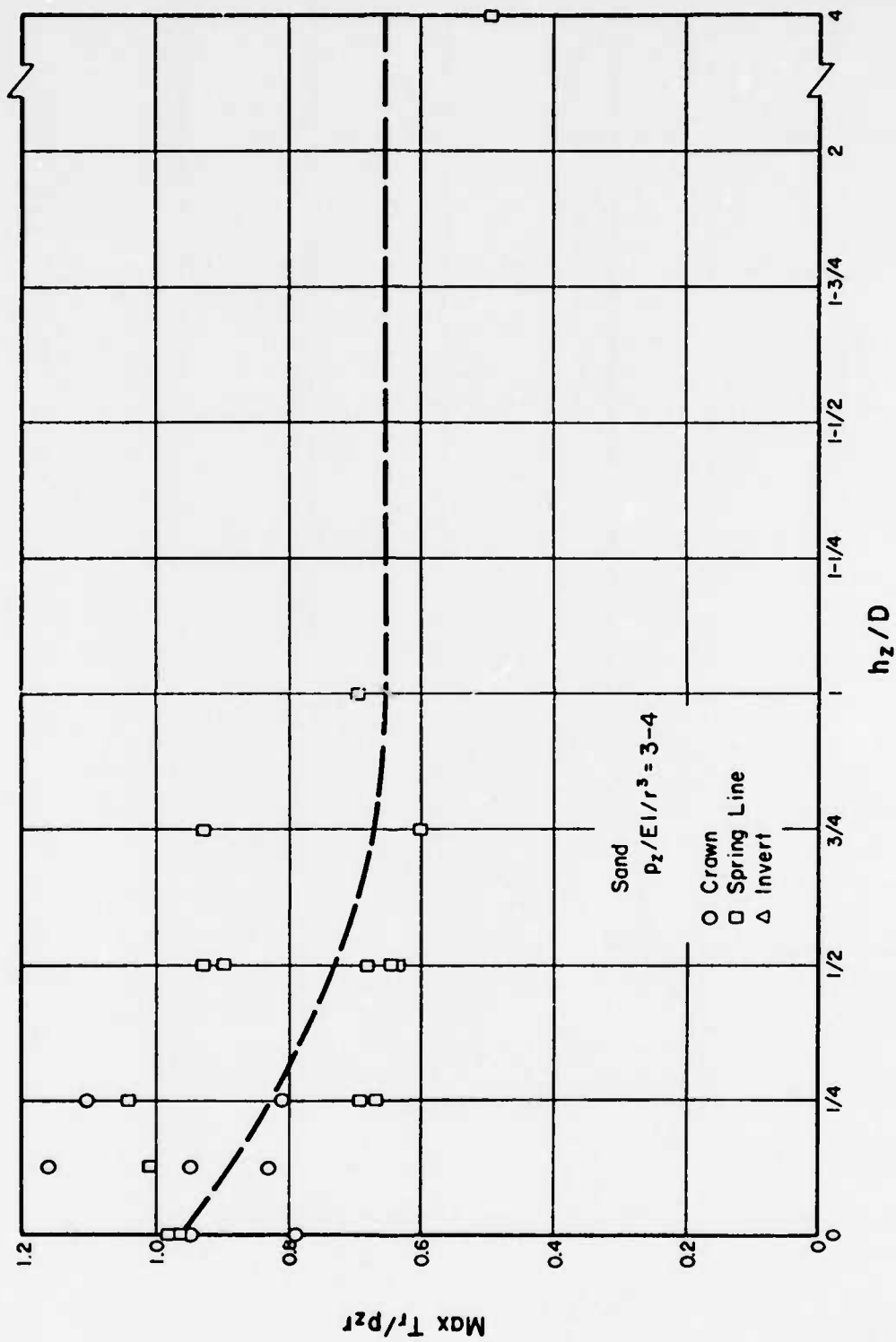


Figure B3. Maximum Thrust Versus Depth of Burial in Sand, $p_z r^3/EI=3-4$

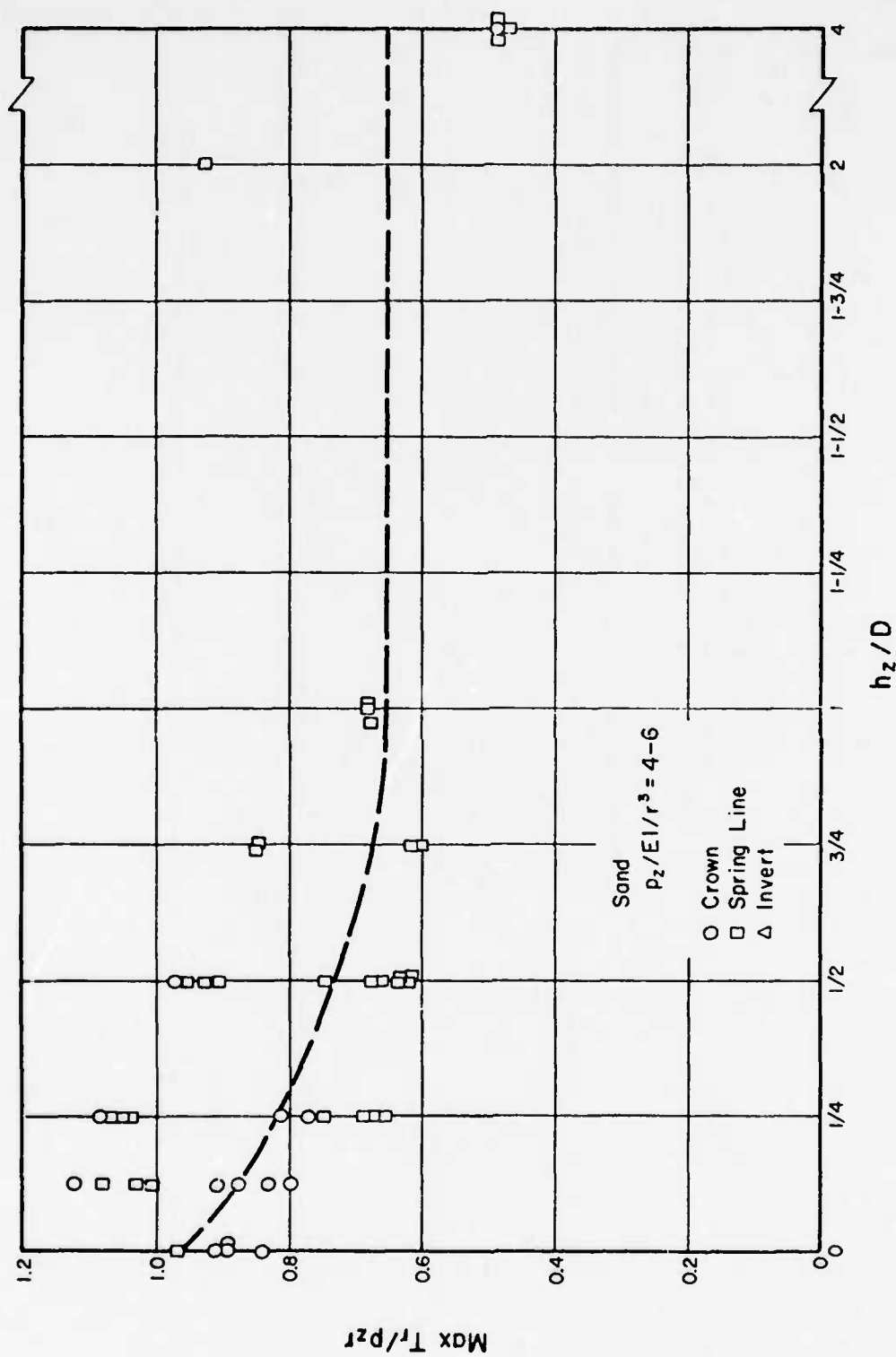


Figure B4. Maximum Thrust Versus Depth of Burial in Sand, $p_z r^3/EI=4-6$

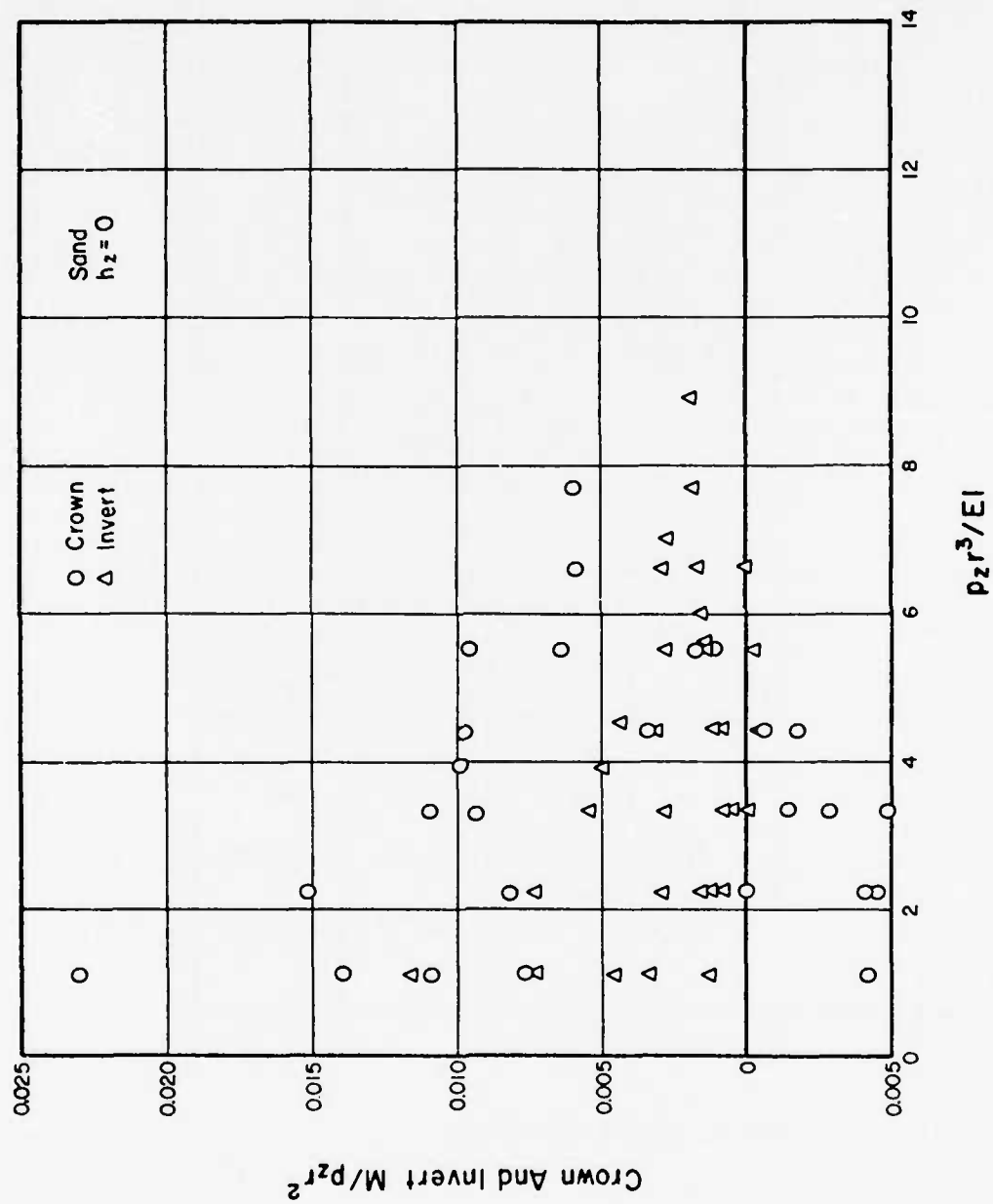


Figure B5. Crown and Invert Moments Versus Normalized Overpressure, $h_z=0$ in Sand

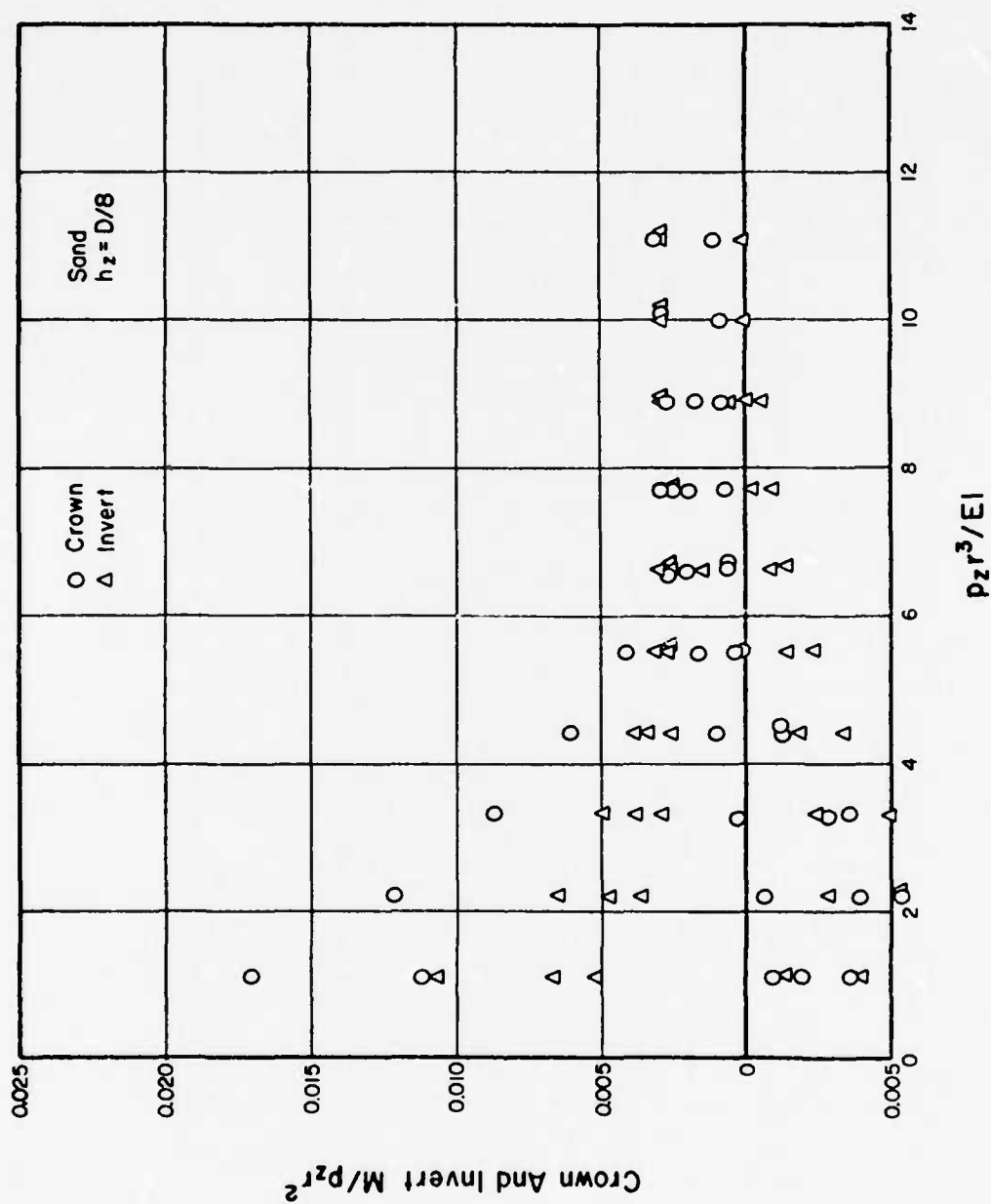


Figure B6. Crown and Invert Moments Versus Normalized Overpressure, $h_z = D/8$ in Sand

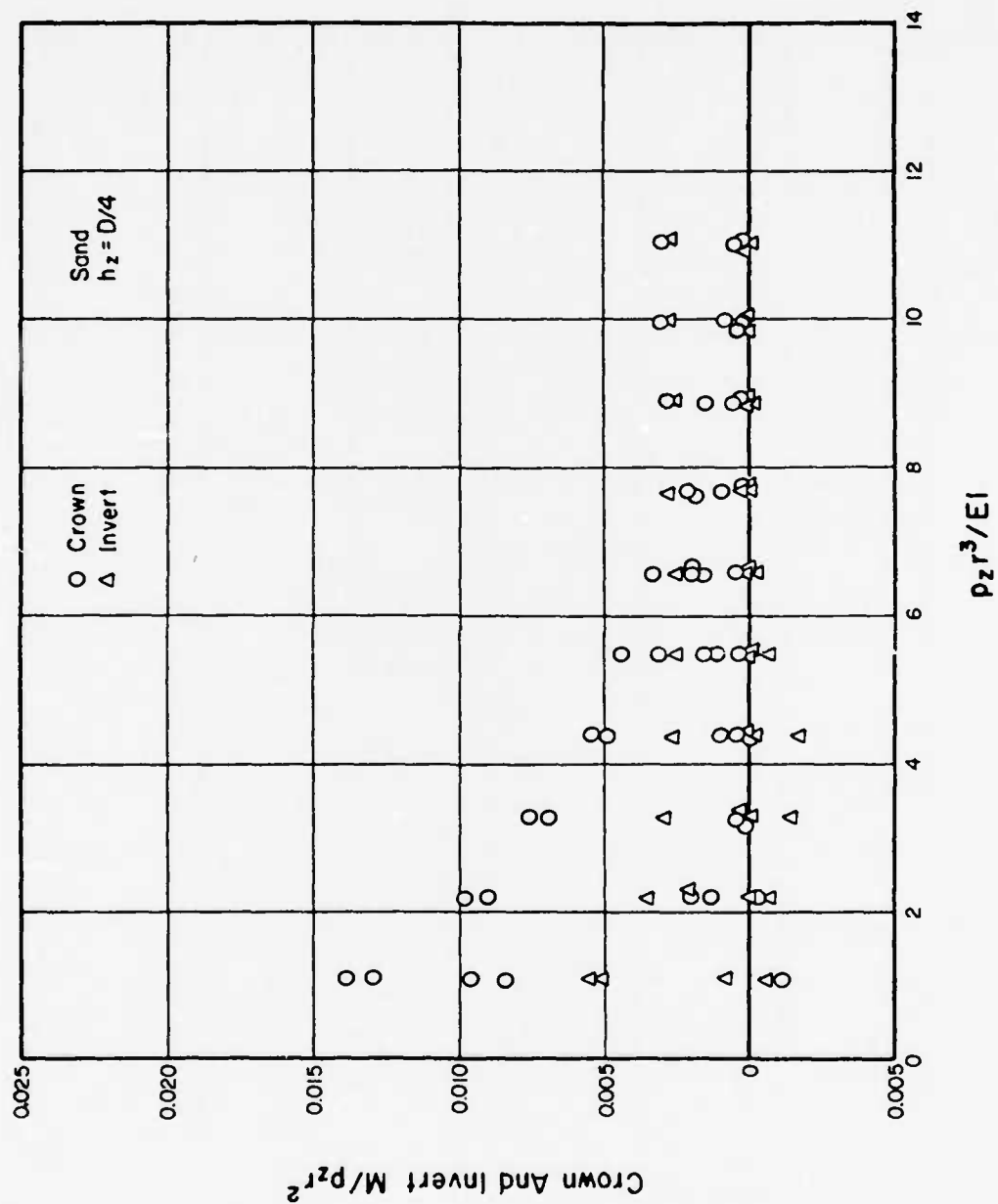


Figure B7. Crown and Invert Moments Versus Normalized Overpressure, $h_z = D/4$ in Sand

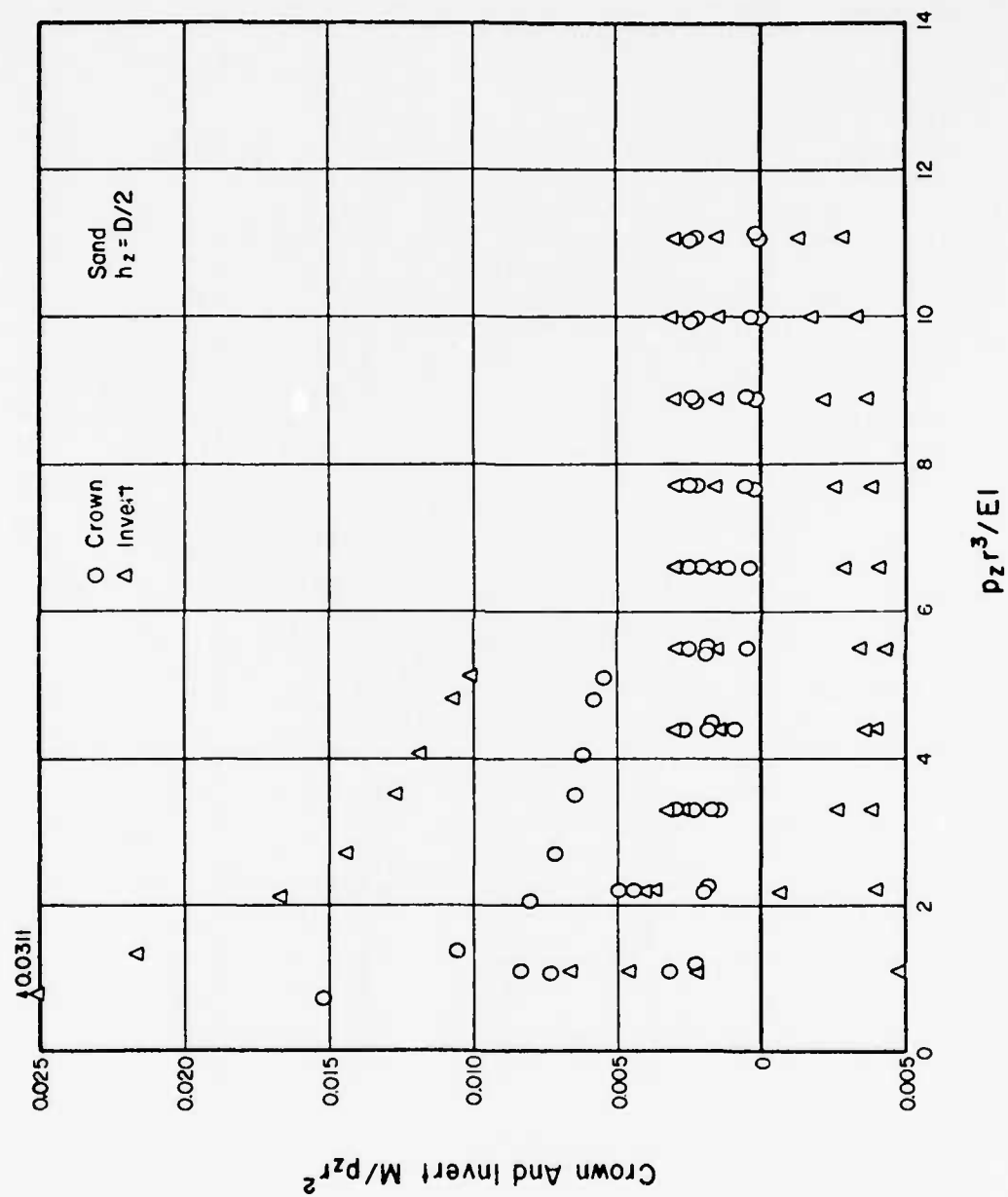


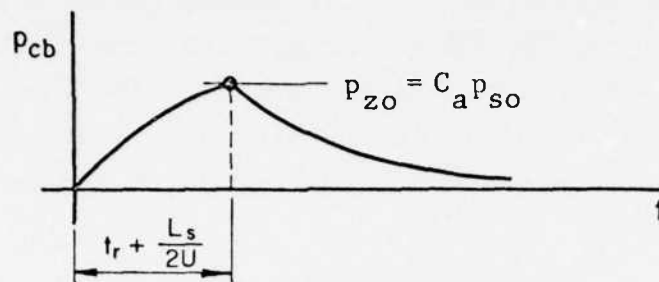
Figure B8. Crown and Invert Moments Versus Normalized Overpressure, $h_z = D/2$ in Sand

The thrust is $p_c r$ for a uniform radial pressure, p_c , acting on the cylinder; thus, the ratio $(T_r/p_z r)$ is, effectively, a soil arching factor. This equation is obviously inadequate since, for a cylinder of any given diameter, it reflects only the effects of depth of cover over the cylinder. It neglects the influences of cylinder stiffness or, perhaps more properly, the relative stiffnesses of the cylinder and the surrounding soil. As noted earlier it seems extremely unlikely that these neglected parameters should, in fact, be negligible.

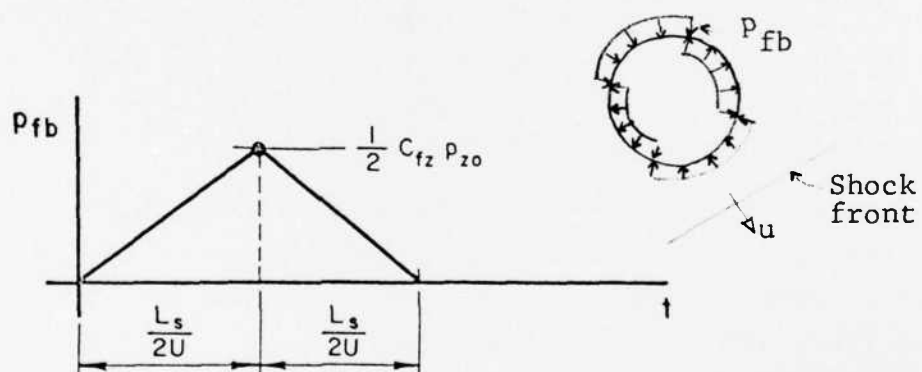
The prediction of the maximum bending moments that might be experienced by a buried cylinder and, hence, the prediction of the loads that would produce these maximum moments is fraught with even more uncertainty than was the prediction of the maximum thrusts. These greater uncertainties are in evidence in the extremely wide scatter of the experimental data shown in figures B5 through B9. Because of specialized nature of these data, one should be extremely careful about drawing conclusions from them. Indeed, they may show little more than judgment would tell us to expect; namely, that for flexible cylinders in dense materials only modest amounts of earth cover are required to reduce bending moments to relatively negligible amounts.

Despite the scatter of these data, it does appear that the moment diminishes quite rapidly as the cylinder flexural stiffness (EI/r^3) decreases and that, for the range of data points available, the moments are all relatively quite small. Furthermore, although not a clearly defined relationship, there is, for the stiffer cylinders, a trend toward reduction in moment with increasing depth.

As suggested by the above observations, one of the primary deficiencies of the data contained in these figures is the absence of data for flexurally stiff cylinders, i.e., for normalized pressure values less than 1.0, in which domain it is noted from the plots that the normalized moments appear generally to be increasing quite rapidly.



(a) Uniform Compression Mode Loading



(b) Flexural Mode Loading

Figure B9. Loading Functions for Underground Cylinders

These data were obtained either from static tests or from dynamic tests in which the air pressure was uniformly applied on the ground surface above the cylinders. Hence, these data do not properly reflect the moments that would be induced in an antisymmetrical flexural mode during passage of an airblast wave across a cylinder, thereby loading one side of the cylinder before the other side is loaded. There is reason to suspect, especially for very shallow buried cases, that moments associated with an antisymmetrical, flexural deformation mode (which would, or might, result from the horizontal passage of an airblast wave across the ground surface above a buried cylinder) may be greater than the moments in the symmetrical flexural mode (shortening of the vertical diameter and lengthening of the horizontal diameter). Because of the manner in which the cylinders were tested, the data of figure B5 through B8 contain primarily symmetric flexural modes.

In an attempt to provide a basis for a more rational representation of the influence of the surrounding soil on the behavior of a buried cylinder, studies were made of a half-cylinder (i.e., an arch) in which the soil was represented as a series of radial springs and added masses which would respond compatibly with the cylinder (or arch) as it deforms under load. Unfortunately, these studies were unsuccessful. Results obtained therefrom were in substantial disagreement with the known dominance of the uniform compression mode of response for fully buried flexible arches and, as a consequence, must be disregarded.

However, on the basis of these studies, it appears that the soil effects on the loading and response of an underground arch (or cylinder) cannot be represented simply, at least not as direct modifications of the structural arch mass and stiffness. Indeed, additional studies suggest that a more reasonable approach may be to model the soil as a soil arch which surrounds the structural arch and whose deformations must be compatible with those of the structural arch. However, to define such a structural arch-soil arch model rationally and simply requires major research that is substantially beyond the scope of this effort.

It is clear that the present inadequate state of knowledge will not permit analysis of a buried cylinder comprehensively, taking into account properly and rationally the interaction of the cylinder with the surrounding soil. Consequently, it seems most reasonable to adopt a procedure which has at least the virtue of simplicity and which yields results that, in the limit, appear to be reasonable and which are in general agreement with the limited amount of test data that are available.

Consistent with this simplistic approach, an underground cylinder can be assumed to respond to two primary modal loadings, namely, a uniform compression mode and an antisymmetrical flexural mode. For the compression mode, the pressure on the cylinder can be taken to be uniform and equal in intensity to the free field vertical pressure p_{so} at depth h_{av} , where h_{av} is approximately $(h_z + 0.2r)$, except that the rise time, t_r , is increased by one-half the transit time of the blast wave across the cylinder. This transit time is equal to L_s/U , where $L_s = D$, diameter of the cylinder and U is the shock wave velocity. The resulting function is shown in figure B9(a). These pressures are reduced to account for the arching effect of the soil by the factor C_a , which may be estimated from equation (B-1).

For the flexural mode, the pressure distribution is assumed to be antisymmetrical, with uniform inward pressures on the upper windward and lower leeward quarters of the cylinder, and equal uniform outward pressures on the other two quarter segments. The pressure intensity on each of the four quarter segments is the same, and is assumed to vary in time as shown in figure B9(b). The factor C_{fz} , which appears in this pressure-time function, is introduced to provide for an orderly reduction in this flexural mode loading as soil resistance to structural deformation in this mode increases with increasing depth of cover. Somewhat arbitrarily, this factor is taken as

$$C_{fz} = 1.2 - 4 \left(\frac{h_z}{r} \right) \quad (B-2)$$

which is never taken greater than 1.0 nor less than zero. As is evident from this expression, the flexural mode is not considered to exist if h_z/r is greater than 0.3. This is clearly an arbitrary judgment which fails to acknowledge that the resistance offered by the soil to structural deformation in this mode must be a function not only of the depth of soil cover but also of the soil type, density, and stiffness, or resistance to deformation.

As noted earlier, these suggested modal loadings are obvious simplifications of a very complex problem. Much more research involving, perhaps, finite-element solutions of the highly non-linear and inelastic soil-structure continuum is needed to assess the reasonableness of this approximation. Desirably, in view of the known difficulties involved in modeling such a system, the results of such theoretical studies should be checked experimentally.

A few final comments in this regard seem appropriate:

- (1) The conditions of interest are those that correspond to failure of the cylinder, recognizing that failure is, itself, difficult to define in many cases. But almost certainly, we are interested in the behavior of the cylinder, and probably of the surrounding soil, well beyond the range of linear elastic response.
- (2) Unless the cylinder is quite long relative to its diameter, the effects of the ends of the cylinder on its behavior under applied external loads should be considered. Limited studies have indicated that the shell effects of closed cylinder ends can increase markedly the ability of a relatively short cylinder to withstand flexural loading.

1. UNDERGROUND PRESSURE-TIME FUNCTIONS

a. General Philosophy and Concepts

There is now no rational basis on which to define the detailed character of the air-induced, underground pressure pulse shape. It is clear that, as a given surface overpressure pulse is propagated vertically downward through a soil medium, its shape will be changed; both theoretical wave propagation studies in nonelastic materials and field test data confirm this. It is not yet possible to define the highly variable in-situ soil dynamic

properties within the limits needed, nor is it possible to represent the wide variety and the infinite possible combinations of soil types and conditions with a mathematical model that would permit the development of a theoretically rigorous underground pressure pulse shape.

Similarly, while the nuclear field tests have provided useful information in regard to these pulse shapes, the data scatter to such an extent, even in repeated tests in the same soil, and are available in only a few relatively atypical soils, that detailed underground pulse shapes cannot be predicted with confidence from this source either.

Nevertheless, pressure pulse shapes must be known (or estimated) in order to investigate the vulnerability of buried structures to ground surface airblast loadings; hence, it is suggested that they be approximated on the basis of the following criteria which are defensible, at least in general terms:

- (1) The soil is assumed to be a uniform medium of infinite depth. No attempt is made here to account for the effects of a layered system.
- (2) The total impulse that is applied to the ground surface must be propagated without diminution through the underlying soil medium. Hence, the iso-impulse curves (discussed subsequently), which were developed using a pseudostatic computational technique on the basis of impulse conservation, can be used to identify the total impulse that should exist under the vertical pressure-time function at any depth for any given weapon yield and surface overpressure level or range.
- (3) The peak vertical pressure must attenuate with depth of penetration. The mechanism by which this pressure attenuation takes place is not fully understood, although it clearly must be influenced by the shape of the surface overpressure pulse, the level and distribution of pressures over the ground surface, and probably the soil properties. The first two effects are represented by the α factor of equation (B-3). The latter effect is not yet well-defined, but evidence indicates that it will generally be relatively small in comparison to the other two effects; hence no effort was made to include it herein.

$$\alpha = \frac{1}{1+z/L} \quad (B-3)$$

where z = depth below ground surface, and

$$L = 2300 (W_{MT})^{1/3} p_{so}^{-0.5} \left(\frac{C}{622}\right)$$

in which C , in feet per second, is the seismic velocity of the soil and W_{MT} is the nuclear weapon yield in MT.

- (4) As the pressure pulse penetrates into the soil, its rise time to peak pressure increases, but neither the duration of this rise time nor the shape of the pulse during this period of time can be predicted closely. It is suggested, in the absence of better information, that the rise time to peak pressure at a given depth be taken as 1 msec plus half the transit time of the peak pressure to that depth.

Rather arbitrarily, the shape of the pulse during its rise is taken to be parabolic. This is done in an attempt to recognize the extreme improbability of the occurrence of a linear rise to maximum pressure. Available acceleration test data support the argument that during rise the shape of the velocity pulse and, hence, of the pressure pulse is in fact nonlinear.

- (5) There being virtually no information available in regard to the shape of the pressure pulse beyond maximum pressure, it seems reasonable to assume that the total duration of the pulse, excluding the rise time just discussed, be taken as nearly as possible to be equal to the positive phase duration of the surface overpressure pulse. Hence, the duration of the pulse beyond maximum pressure may be taken equal to the surface overpressure duration except when forced to vary from this in order to comply with the previously stated criteria of impulse conservation, peak pressure attenuation, and rise time pulse shape.

b. Overpressure-Induced Vertical Impulse

(1) Positive Phase Overpressure Impulse on Ground Surface

The overpressure impulse produced on the ground surface is given approximately, but adequately, by the following equation.

$$\begin{aligned} I &= 1.739 p_{so}^{0.5} W_{MT}^{1/3} \text{ psi-sec, for } 0 \leq p_{so} \leq 1000 \text{ psi} \\ &= 4.125 p_{so}^{0.375} W_{MT}^{1/3} \text{ psi-sec, for } p_{so} > 1000 \text{ psi (B-4)} \end{aligned}$$

(2) Vertical Free Field Impulse Below Ground Surface

For a surface overpressure impulse of 200 psi-sec or greater (for $W = 1$ MT), the iso-impulse curve is approximated closely by a circle, as shown in figure B10, whose center is at ground zero and whose radius is equal to the ground range, R_n , determined to correspond to the impulse, I , of interest.

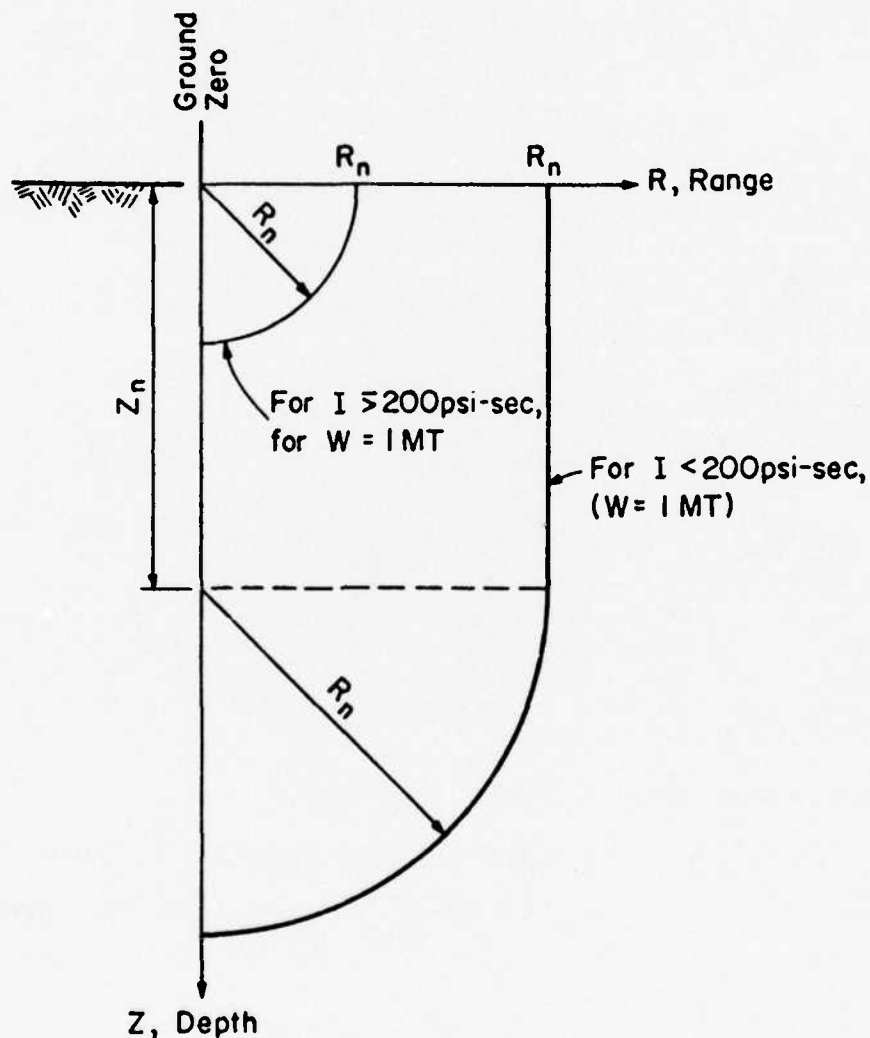


Figure B10. Representation of Underground Iso-Impulse Curves

For a surface overpressure impulse equal to or less than 200 psi-sec (for $W=1$ MT) the iso-impulse curve is adequately represented, as shown in figure B10, by a vertical straight line segment from the ground surface and a circular arc. The straight line extends from the ground surface at a range R_n (corresponding to the surface range as determined for the impulse of interest) to a depth, z_n , that is given by

$$z_n = 200 I^{-4/3}, \text{ for } 5 \leq I \leq 200 \text{ psi-sec for } W=1 \text{ MT} \quad (\text{B-5})$$

The lower part of this iso-impulse curve is represented closely by a circle whose center is directly below ground zero ($R=0$) at a depth of z_n , and whose radius is equal to R_n for the impulse of interest. Thus, the circular arc is tangent to the straight line segment at a point whose coordinates are R_n, z_n .

These approximate iso-impulse curves are plotted in figures B11 and B12.

(3) Notation Used for Underground Pulse Shape Determinations

The following notation is used in the description of the underground pressure pulse shapes:

p_{so} = peak surface overpressure, psi

$p_z = \alpha p_{so}$ = attenuated peak vertical pressure at depth z , psi
where α is given by equation (B-3)

t_s = surface overpressure positive phase duration, sec

t'_s = positive phase duration of a surface overpressure pulse having a peak value of p_z , sec

t_t = travel time of pulse from ground surface to depth z , sec

t_r = rise time to peak value of pressure pulse at depth z
(taken here as $[0.001 + (1/2)t_t]$, but no greater than $(1/2)t_s$)

I = positive overpressure impulse on ground surface, psi-sec

I' = positive impulse under a surface overpressure pulse of peak value p_z , psi-sec

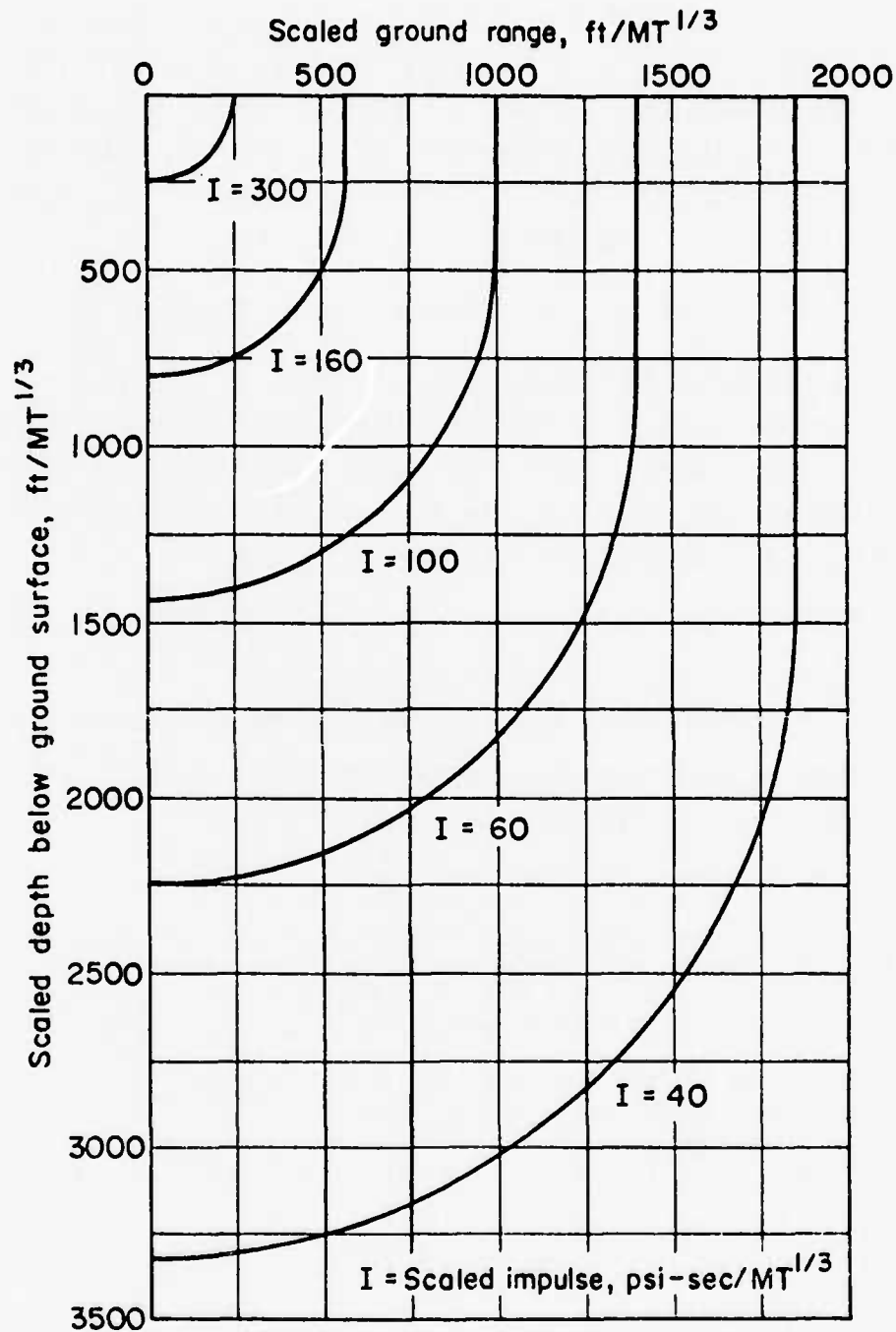


Figure B11. Approximate Underground Iso-Impulse Curves (High Impulse Region)

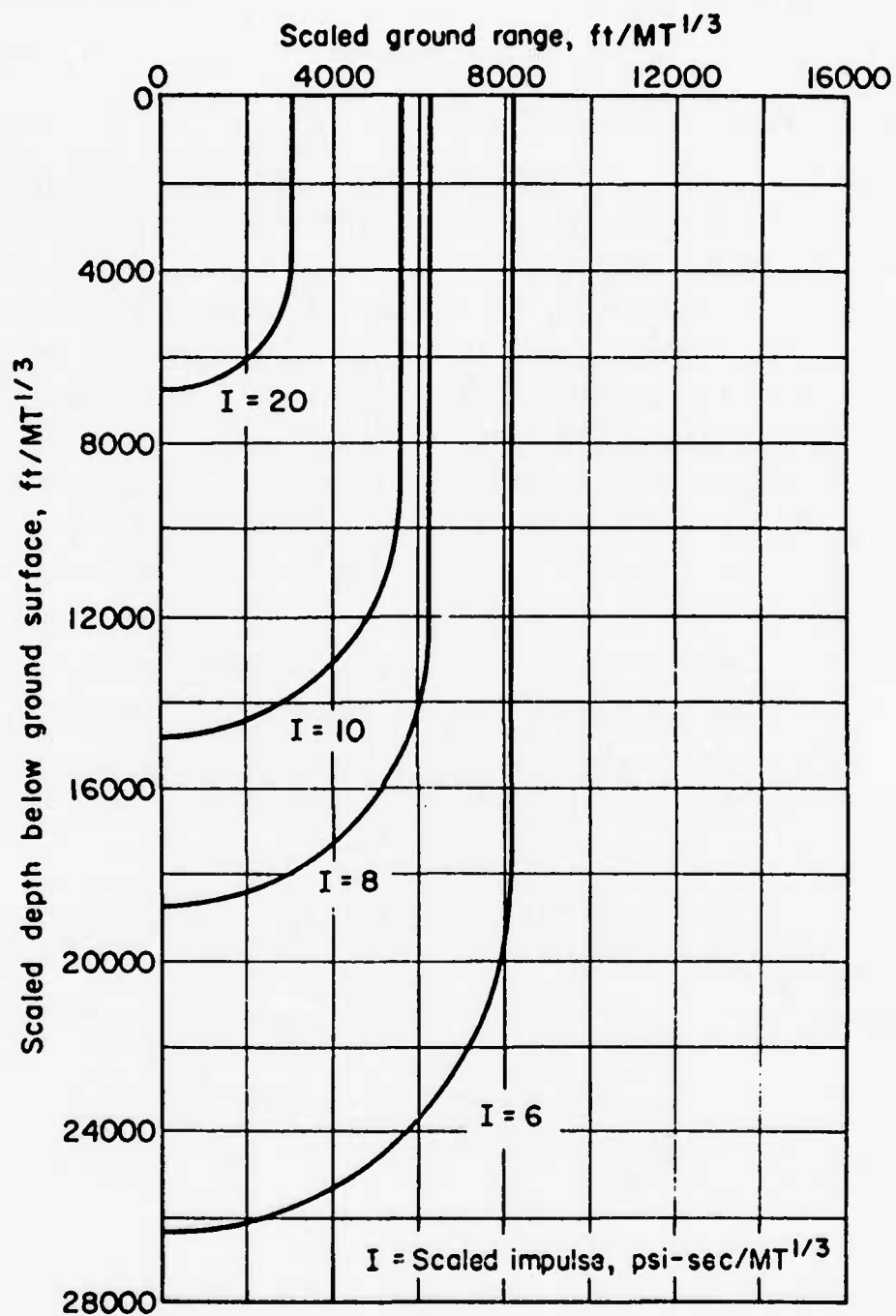


Figure B12. Approximate Underground Iso-Impulse Curves
(Low Impulse Region)

I_r = impulse under rise time portion of underground pressure pulse, psi-sec

I_z = positive phase impulse at depth z , psi-sec

c. Definition of Underground Pulse Shapes

For individual or hand-computational purposes, an adequate underground pulse could be approximated or sketched for a particular case on the basis of the criteria stated above, but such a procedure is not satisfactory for a general computerized program of analysis. For a computer analysis, it is essential that the underground pulse shapes be so described that, for a given set of conditions, it is uniquely defined. Consequently, the following procedure was developed for computer solution to define underground pulse shapes consistent with the general criteria stated above and which are uniquely defined by a specific set of given conditions.

For a given surface overpressure level, weapon yield, depth below ground surface, and soil profile, proceed as follows:

1. Assume a parabolic rise in the underground pressure from zero to a maximum pressure of $p_z = \alpha p_{so}$ in a time t_r . Then $I_r = 2/3 p_z t_r$. (B-6)
2. Assume the pulse to decay from its peak pressure to zero in a manner defined by a surface overpressure pulse having a peak pressure equal to p_z , a corresponding duration of t'_s and an impulse of I' .
Steps 1 and 2 yield a pulse as shown in figure B13(a). This pulse is satisfactory when $(I_r + I') = I_z$.
3. If $(I_r + I') < I_z$, add a parabola as shown in figure B13(b) to the decay portion of the pulse to yield the pulse shown in figure B13(c), for which the total impulse is I_z .
4. If $(I_r + I') > I_z$, proceed as follows:
 - (a) For $I_r < I$, use a parabolic rise time portion as defined in step 1, which is followed by a decay from peak pressure as defined in step 2 except that the decay duration is $\beta t'_s$ instead of t'_s , in which β is less than 1.0 and is given by

Note: In all cases, ordinate is pressure (psi) and abscissa is time (sec.)

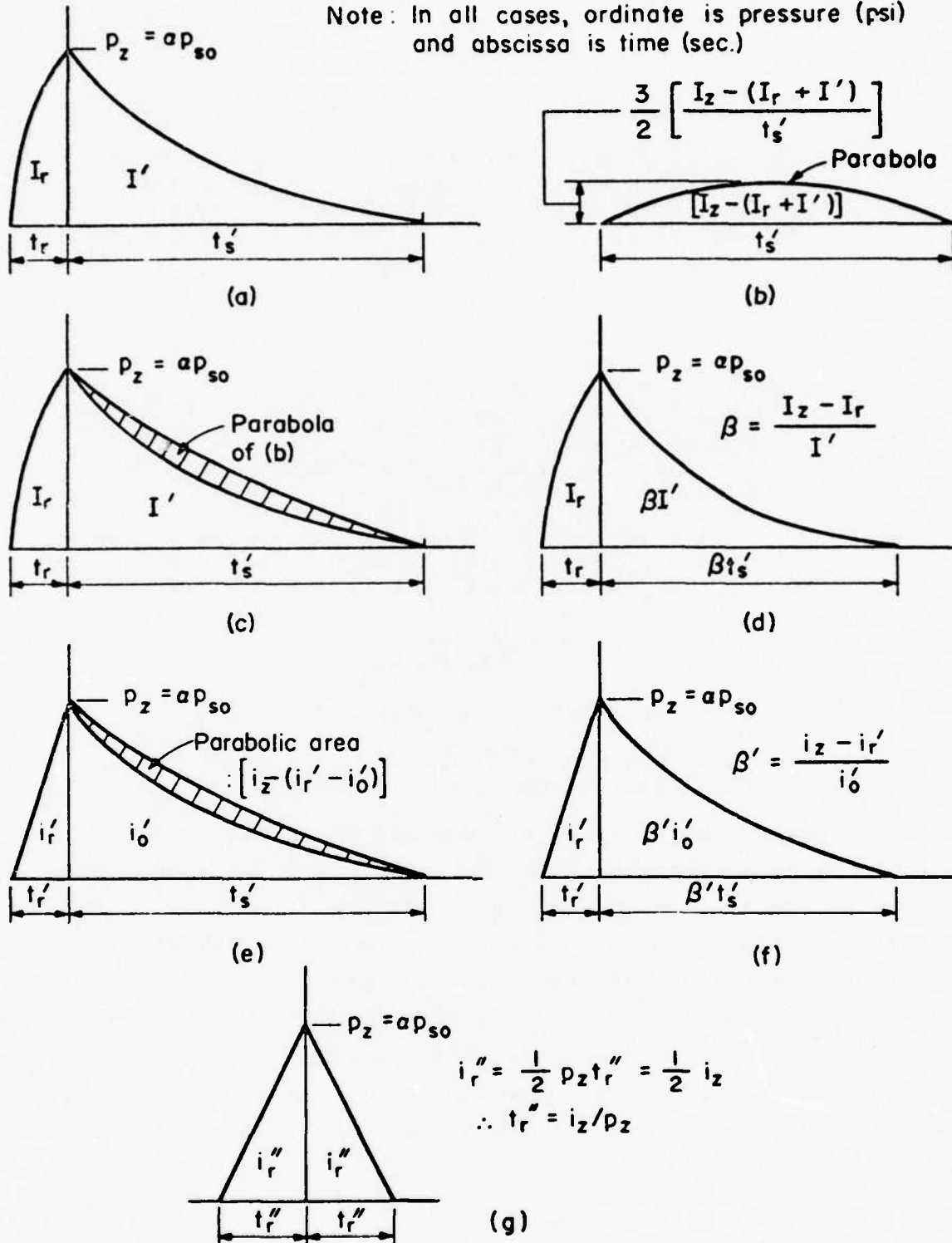


Figure B13. Representation of Underground Vertical Airblast-Induced Pressure Pulses

$$\beta = \frac{I_z - I_r}{I_r} \quad (B-7)$$

This yields the pulse illustrated in figure B13(d).

- (b) For $I_r > 1/2 I_z$, arbitrarily assume a rise time $t_r' = 1/2 t_r$, and use a straight line increase to p_z . Compute the corresponding rise time impulse to be

$$I_r' = \frac{1}{2} p_z t_r' \quad (B-8)$$

For step 4(b):

- (1) If $(I_r' + I_r) < I_z$ assume the decay portion of the curve to be defined by steps 2 and 3, except that the parabolic segment of step 3 has an area of $[I_z - (I_r' + I_r)]$ instead of $[I_z - (I_r + I_r)]$. This produces the pulse illustrated in figure B13(e).
- (2) If $(I_r' + I_r) > I_z$, but $I_r' < 1/2 I_z$, use a linear rise time portion of duration t_r' as above, followed by a decay from peak pressure to zero in a time $\beta' t_s$, in which

$$\beta' = \frac{I_s - I_r'}{I_r'} \quad (B-9)$$

This yields the pulse depicted in figure B13(f).

- (3) If $(I_r' + I_r) > I_z$, but $I_r' \geq 1/2 I_z$, assume the pulse to be triangular in shape, as illustrated in figure B13(g).

The detailed character of the outlined procedure should not be interpreted as implying that the resulting pulse shapes are precise in the sense that they represent the correct pulse shapes. As stated earlier, correct pulse shapes cannot now be predicted with a high degree of confidence by any method. The procedure presented here is considered to yield pulse shapes that are as correct as can be developed conveniently for computer solution on the basis of currently available data. The rather complex character of this procedure results solely from the necessity of specifying uniquely defined pulses for computer solution.

APPENDIX C

DYNAMIC INTERACTION BETWEEN ELASTIC MEDIA

In this appendix a simplified problem of dynamic interaction between two elastic media is considered. The objective of this analysis is to determine the relative influence of the soil and the structure discrete mass distribution on the SSI forces. For the dynamic finite element solutions described in Section III, the stresses in the soil elements adjoining the tunnel liner structure were used as the SSI loads. The analysis given herein addresses the adequacy of this approach.

To study the problem, the structure is modeled by a single-degree of freedom system with mass m_1 and stiffness k_1 . The soil element adjoining the structure is modeled by two lumped masses of m_2 each, and an element stiffness of k_2 joining the two mass points as shown in figure C1(a). The combined soil structure system is shown in figure C1(b). The undamped equations of motion of the combined system is given by

$$\begin{bmatrix} m_1+m_2 & 0 \\ 0 & m_2 \end{bmatrix} \begin{Bmatrix} \ddot{u}_1 \\ \ddot{u}_2 \end{Bmatrix} + \begin{bmatrix} k_1+k_2 & -k_2 \\ -k_2 & k_2 \end{bmatrix} \begin{Bmatrix} u_1 \\ u_2 \end{Bmatrix} = \begin{Bmatrix} 0 \\ F \end{Bmatrix} \quad (C-1)$$

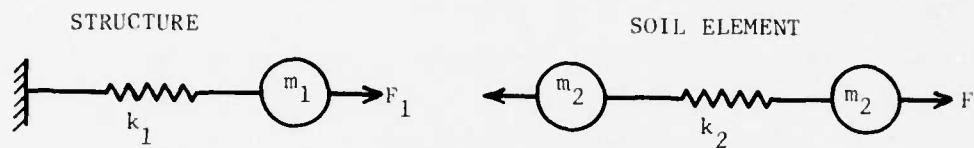
where u_1 and u_2 are the translational degrees of freedom as shown in figure C1, superscript dot represents time derivative, and F is the force applied to the mass m_2 . To simplify the analysis presented here, it is assumed that F is applied suddenly and remains constant with time.

The two combined frequencies of the simplified system are given by the characteristic equation

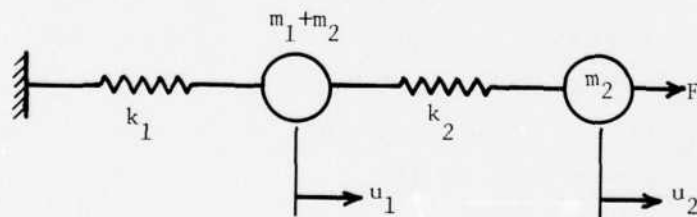
$$\left[k_1 + k_2 - \omega^2 (m_1 + m_2) \right] \left[k_2 - m_2 \omega^2 \right] - k_2^2 = 0 \quad (C-2)$$

For each mode the normalized mode shapes are

$$\begin{Bmatrix} \phi_1 \\ \phi_2 \end{Bmatrix} = \begin{Bmatrix} (k_2 - m_2 \omega^2) / D \\ k_2 / D \end{Bmatrix} \quad (C-3)$$



(a) FREE BODY DIAGRAM OF THE IDEALIZED STRUCTURE AND SOIL ELEMENT



(b) COMBINED STRUCTURE AND SOIL MODEL

Figure C1. Simplified Soil Structure Finite Element Model.

where

$$D = \left[(m_1 + m_2) (k_2 - m_2 \omega^2)^2 + m_2 k_2^2 \right]^{1/2}$$

The response of the system is given by

$$\begin{Bmatrix} u_1 \\ u_2 \end{Bmatrix} = P \begin{Bmatrix} \phi_1 \\ \phi_2 \end{Bmatrix} \quad (C-4)$$

where

$$P = (F k_2 / D) (1 - \cos \omega t) \quad (C-5)$$

The force that is applied to the structure (F_1) is the force that mass m_2 transmits to mass m_1 at the soil-structure interface. This force is given by

$$F_1 = F_2 - m_2 \ddot{u}_1 \quad (C-6)$$

where F_2 is the force in the soil element (k_2)

$$F_2 = k_2 (u_2 - u_1) \quad (C-7)$$

Equations (C-3) to (C-7) yield

$$\frac{F_1}{F_2} = \frac{1 - (2 - \omega^2 / \omega_2^2) \cos \omega t}{1 - \cos \omega t} \quad (C-8)$$

in which $\omega_2^2 = k_2 / m_2$

If the applied force is a periodic function like $F \cos \Omega t$, the above ratio becomes

$$\frac{F_1}{F_2} = \frac{\left[1 + \left(\frac{\Omega}{\omega} \right)^2 - \left(\frac{\Omega}{\omega_2} \right)^2 \right] \cos \Omega t - \left[2 - \left(\frac{\omega}{\omega_2} \right)^2 \right] \cos \omega t}{\cos \Omega t - \cos \omega t} \quad (C-9)$$

It is apparent from equations (C-8) and (C-9) that F_1 and F_2 can be substantially different. Therefore, in general it is not desirable to use the soil stresses in the elements adjacent to the structure (F_2) as the SSI stresses (F_1).

DISTRIBUTION

No. of
Copies

Department of Defense

1	Director, Defense Advanced Rsch Proj Agency Architect Bldg., 1400 Wilson Blvd., Arlington, VA 22209 ATTN: Technical Library
1	Director, Defense Civil Preparedness Agency Asst. Director for Research, Washington, DC 20301 ATTN: Admin Officer
1	ATTN: Staff Dir Resr George N. Sisson
1	Director, Defense Communications Agency Washington, DC 20305 (ADR CNWDI: ATTN: Code 240 For)
1	ATTN: Code 930
1	ATTN: CCTC/C672 Franklin D. Moore
2	Defense Documentation Center Cameron Station, Alexandria, VA 22314 ATTN: TC
1	Director, Defense Intelligence Agency Washington, DC 20301 ATTN: DB-4C2, Timothy Ross
1	ATTN: Technical Library
2	Director, DNA Washington, DC 20305 ATTN: SPSS
3	ATTN: TITL Tech Library
1	ATTN: TISI Archives
2	ATTN: SPAS
1	ATTN: DDST
1	Director, Defense Rsch & Engineering DOD, Washington, DC 20301 ATTN: S&SS (OS)
1	Commander, Field Command DNA, Kirtland AFB, NM 87115 ATTN: FCPR
1	ATTN: FCTMOF

Department of Defense, cont'd.

No. of
Copies

1	Director, Interservice Nuclear Weapons School Kirtland AFB, NM 87115 ATTN: Tech Lib
1	Director, Joint Strat Tgt Planning Staff JCS Offutt AFB, Omaha, NB 68113 ATTN: STINFO Library
1	Chief, Livermore Div, Fld Command DNA Lawrence Livermore Laboratory, P. O. Box 808, Livermore, CA 94550 ATTN: FCPRL

Department of the Army

1	Director, BMD Adanced Tech Ctr, Huntsville Office P. O. Box 1500, Huntsville, AL 35807 ATTN: CRDABH-S
1	ATTN: 1CRDABH-X
1	Program Manager, BMD Program Office 1300 Wilson Blvd., Arlington, VA 22209 ATTN: CRDABM-NE
1	Commander, BMD System Command P. O. Box 1500, Huntsville, AL 35807 ATTN: BDMSC-TEN Noah J. Hurst
1	Director, Construction Engineering Research Laboratory P.O. Box 4005, Champaign IL 61820 ATTN: CERL-SL
1	Dep Chief of Staff or Rsch Dev & Acq Dept of the Army, Washington DC 20310 ATTN: DAMA(CS)
1	ATTN: Technical Library
1	Chief of Engineers, DOA Forrestal Bldg., Washington DC 20314 ATTN: DAEN-MCE-D
1	ATTN: DAEN-RDM
1	Deputy, Chief of Staff for Ops & Plans DOA, Washington, DC 20310 ATTN: Technical Library
1	ATTN: Dir of Chem & Nuc Ops

Department of the Army, cont'd.

No. of
Copies

1	Chief, Engineer Strategic Studies Group 6500 Brooks Lane, N.W., Washington DC 20315 ATTN: DAEN-FES LtC Hatch
1	Commander, Harry Diamond Laboratories 2800 Powder Mill Rd., Adelphi, MD 20783 ATTN: DRXDO-TI Tech Lib
1	ATTN: DRXDO-NP
1	Commander, Picatinny Arsenal Dover, NJ 07801 ATTN: Technical Library
1	Commander, Redstone Scientific Information Center U. S. Army Missile Command Redstone Arsenal, AL 35809 ATTN: Chief, Documents
1	Commander, U. S. Army Armament Command Rock Island, IL 61202 ATTN: Tech Lib
1	Director, U. S. Army Ballistic Research Labs Aberdeen Proving Ground, MD 21005 ATTN: W. Taylor
1	ATTN: DRXBR-X Julius J. Meszaros
2	ATTN: Tech Lib, Edward Baicy
1	Commander, U. S. Army Comb Arms Combat Dev Acty Ft Leavenworth, KS 66027 ATTN: LTC G. Steger
1	ATTN: LTC Pullen
1	Commander, U. S. Army Communications CMD Fort Huachuca, AZ 85613 ATTN: Technical Library
1	Commander, U. S. Army Engineer Ctr Fort Belvoir, VA 22060 ATTN: ATSEN-SY-L
1	Division Engineer, U. S. Army Engineer Div Huntsville P. O. Box 1600, West Station, Huntsville, AL 35807 ATTN: HNDED-SR
1	Division Engineer, U. S. Army Engineer Div Ohio River P. O. Box 1159, Cincinnati, OH 45201 ATTN: Technical Library

Department of the Army, cont'd.

No. of
Copies

	Commandant, U. S. Army Engineer School Ft. Belvoir, VA 22060
1	ATTN: ATSE-TEA-AD
1	ATTN: ATSE-CTD-CS
	Director, U. S. Army Engr Waterways Exper Sta P. O. Box 631, Vicksburg, MS 39180
1	ATTN: John N. Strange
1	ATTN: Technical Library
1	ATTN: Guy Jackson
1	ATTN: Leo Ingram
1	ATTN: William Flathau
1	ATTN: James Ballard
	Commander, U S Army Mat & Mechanics Rsch Ctr Watertown, MA 02172
1	ATTN: Technical Library
	Commander, U S Army Materiel Dev & Readiness Cmd 5001 Eisenhower Ave., Alexandria, VA 22333
1	ATTN: Technical Library
	Commander, U S Army Missile Command Redstone Arsenal, AL 35809
1	ATTN: DRSMI-XS Chief Scientist
	Commander, U S Army Mobility Equip R&D Ctr Fort Belvoir, VA 22060
1	ATTN: Technical Library
	Commander, U S Army Nuclear Agency Ft. Bliss, TX 79916
1	ATTN: Tech Library
	Commandant, U S Army War College Carlisle Barracks, PA 17013
1	ATTN: Library

Department of the Navy

	Chief, Naval Operations, Navy Dept. Washington, DC 20350
1	ATTN: Code 604C3 Robert Piacesi
1	ATTN: OP 03EG
1	ATTN: OP 981
1	ATTN: OP 982

Department of the Navy, cont'd.

No. of
Copies

	Chief, Naval Research, Navy Dept. Arlington, VA 22217
1	ATTN: Code 464 Jacob L. Warner
1	ATTN: Technical Library
1	ATTN: Nicholas Perrone
1	ATTN: Code 464 Thomas P. Quinn
1	ATTN: John Haycock
	Officer-in-Charge, Civil Engineering Laboratory Naval Construction Battalion Center, Port Hueneme, CA 93041
1	ATTN: R. J. Odello
1	ATTN: Technical Libray
1	ATTN: Stan Takahashi
	Commander, Naval Electronic Systems Command Naval Electronic Systems Cmd Hq, Washington DC 20360
1	ATTN: PME 117-21A
	Commander, Naval Facilities Engineering Command Hqs Washington DC 20390
1	ATTN: Technical Library
	Superintendent (Code 1424), Naval Postgraduate School Monterey, CA 93940
1	ATTN: Code 2124 Tech Rpts Librarian
	Commander, Naval Surface Weapons Ctr White Oak, Silver Spring, MD 20910
1	ATTN: Code WA501 Navy Nuc Prgms Off
1	ATTN: Code WX21 Tech Lib
	Commander, Naval Surface Weapons Ctr Dahlgren Laboratory, Dahlgren, VA 22448
1	ATTN: Tech Lib
	President, Naval War College Newport, RI 02840
1	ATTN: Tech Lib
	Commander, Naval Weapons Ctr China Lake, CA 93555
1	ATTN: Code 533 Tech Lib
	Commanding Officer, Naval Weapons Evaluation Facility Kirtland Air Force Base, Albuquerque, NM 87117
1	ATTN: Tech Lib

Department of the Navy, cont'd.

No. of
Copies

1 Director, Strategic Systems Project Office
Navy Dept., Washington, DC 20376
ATTN: NSP-43 Tech Lib

Department of the Air Force

1 Commander, ADC/XP
Ent AFB, CO 80912
ATTN: XPQDQ
1 ATTN: XP

1 AF Geophysics Laboratory, AFSC
Hanscom AFB, MA 01731
ATTN: SUOL AFCRL Rsch Lib

1 AF Institute of Technology, AU
Wright-Patterson AFB, OH 45433
ATTN: Library AFIT Bldg 640 Area B

1 AF Weapons Laboratory, AFSC
Kirtland AFB, NM 87117
ATTN: DES, M. A. Plamondon
1 ATTN: DES, L. S. Melzer
1 ATTN: SUL
1 ATTN: DEO
12 ATTN: DES Capt Stanton A. Chang

1 HQ, Air Force Systems Command
Andrews AFB, Washington DEC 20331
ATTN: Tech Lib

1 Commander, Armament Dev & Test Center
Eglin AFB, FL 32542
ATTN: Tech Lib

1 Commander, ASD
WPAFB, OH 45433
ATTN: Tech Lib

1 Commander, Foreign Technology Div, AFSC
Wright-Patterson AFB, OH 45433
ATTN: TD-BTA Lib

1 HQ USAF/RD
Washington DC 20330
ATTN: RDQRM Col S. C. Green
1 ATTN: RDPM
1 ATTN: RDPS LTC A Chiota
1 ATTN: RDQPN Maj F. Vajda

Department of the Air Force, cont'd.

No. of
Copies

1	Commander, Rome Air Dev Ctr, AFSC Griffiss AFB, NY 13440 ATTN: EMTLD Doc Library
1	SAMSO/DE Norton AFB, CA 92409 ATTN: DEB
1	SAMSO/DY Post Office Box 92960 Worldway Postal Ctr, Los Angeles, CA 90009 ATTN: DYS
1	SAMSO/MN Norton AFB CA 92409 ATTN: MNNH
1	SAMSO/RS P. O. Box 92960, Worldway Postal Ctr, Los Angeles, CA 90009 ATTN: RSS/Col Donald Dowler
1	SAMSO/XR P. O. Box 92960, Worldway Postal Ctr, Los Angeles, CA 90009 ATTN: XRTB
1	Commander in Chief, Strategic Air Command Offutt AFB, NB 68113 ATTN: NRI-Stinfo Lib
<u>U. S. Energy Rsch and Dev Admin</u>	
1	Division of Military Application US Energy Rsch & Dev Admin, Washington, DC 20545 ATTN: Doc Control for Test Office
1	University of California, Lawrence Livermore Laboratory P. O. Box 808, Livermore, CA 94550 ATTN: Tech Info Dept L-3
1	Los Alamos Scientific Laboratory P. O. Box 1663, Los Alamos, NM 87545 ATTN: Doc Control for Reports Lib
1	Sandia Laboratories Livermore Laboratory, P. O. Box 969, Livermore, CA 94550 ATTN: Doc Control for Tech Lib

U.S. Energy Rsch and Dev Admin, Cont'd.

No. of
Copies

1	Sandia Laboratories P. O. Box 5800, Albuquerque, NM 87115 ATTN: Doc Con for 3141 Sandia Rpt Coll
1	U. S. Energy Rsch & Dev Admin Albu. Operations Office, P. O. Box 5400, Albu., NM 87115 ATTN: Doc Con for Tech Lib
1	U.S. Energy Rsch & Dev Admin, Div of HQ Services Library Branch G-043 Washington, DC 20545 ATTN: Doc Con for Class Tech Lib
1	U. S. Energy Rsch & Dev Admin Nevada Operations Office P. O. Box 14100, Las Vegas, NV 89114 ATTN: Doc Con for Tech Lib
1	Dept of the Interior Bureau of Mines Bldg 20, Denver Federal Center, Denver, CO 80225 ATTN: Tech Lib
1	Dept of the Interior US Geological Survey 345 Middlefield Rd., Menlo Park, CA 94025 ATTN: Cecil B. Raleigh
1	ATTN: J. H. Healy

Department of Defense Contractors

2	Aerospace Corporation P. O. Box 92957, Los Angeles, CA 90009 ATTN: Tech Info Services
1	Agbabian Associates 250 N. Nash St., El Segundo, CA 90245 ATTN: M. Agbabian
1	ATTN: Carl Bagge
1	Analytic Services, Inc. 5613 Leesburg Pike, Falls Church, VA 22041 ATTN: George Hesselbacher
1	Applied Theory, Inc. 1010 Westwood Blvd., Los Angeles, CA 90024 ATTN: John G. Trulio

Dept of Defense Contractors, Cont'd.

No. of
Copies

1	Artec Associates, Inc. 26046 Eden Landing Road, Hayward CA 94545 ATTN: Steven Gill
1	Avco Research & Systems Group 201 Lowell Street, Wilmington MA 01887 ATTN: Research Lib A830 Rm 7201
1	Battelle Memorial Institute 505 King Ave., Columbus OH 43201 ATTN: Tech Lib
1	BDM Corporation 1920 Aline Ave., Vienna VA 22180 ATTN: Tech Lib
1	Ted Belytschko 6304 No. Hiawatha Ave., Chicago IL 60646 ATTN: Ted Belytschko
1	Boeing Company P.O. Box 3707, Seattle WA 98124 ATTN: R. H. Carlson
1	ATTN: Aerospace Lib
1	ATTN: Robert Dyrdahl
1	Brown Engineering Co., Inc. Cummings Research Park, Huntsville AL 35807 ATTN: Manu Patel
1	California Institute of Technology 1201 E. California Blvd., Pasadena CA 91109 ATTN: Thomas J. Ahrens
1	California Research & Technology, Inc. 6269 Variel Ave., Woodland Hills CA 91364 ATTN: Ken Kreyenhagen
1	ATTN: Tech Lib
1	ATTN: Sheldon Shuster
1	Calspan Corporation P.O. Box 235, Buffalo NY 14221 ATTN: Tech Lib
1	Civil/Nuclear Systems Corp. 1200 University Blvd., N.E., Albuquerque NM 87102 ATTN: Tech Lib

Dept of Defense Contractors, Cont'd.

No. of
Copies

1	Dayton, University of Industrial Security Super KL-505 300 College Park Ave., Dayton, OH 45409 ATTN: Hallock F. Swift
1	University of Denver Colorado Seminary Denver Research Institute P. O. Box 10127, Denver, CO 80210 ATTN: Sec Officer for Tech Lib
1	EG&G, Inc. Albuquerque Division P. O. Box 10218, Albuquerque, NM 87114 ATTN: Tech Lib
1	Electric Power Research Institute 3412 Hillview Ave., Palo Alto, CA 94303 ATTN: George Sliter
1	Engrg Decision Analysis Co., Inc 2400 Michelson Dr., Irvine, CA 92715 ATTN: R P Kennedy
1	Franklin Institute 20th Street and Parkway, Philadelphia, PA 19103 ATTN: Zenons Zudans
1	General Electric Co., TEMPO-Center for Advanced Studies 816 State St., (P. O. Drawer QQ), Santa Barbara, CA 93102 ATTN: DASIAAC
1	General Research Corporation P. O. Box 3587, Santa Barbara, CA 93105 ATTN: Benjamin Alexander
1	H-Tech Laboratories, Ind. P. O. Box 1686, Santa Monica, CA 90406 ATTN: B. Hartenbaum
1 5	IIT Research Institute 10 West 35th St., Chicago, IL 60616 ATTN: Tech Lib ATTN: R. R. Robinson
1	Institute for Defense Analyses 400 Army-Navy Dr., Arlington, VA 22202 ATTN: IDA Librarian Ruth S. Smith

Dept of Defense Contractor, Cont'd.

No. of
Copies

1	J. H. Wiggins, Co., Inc. 1650 S. Pacific Coast Highway, Redondo Beach, CA 90277 ATTN: John Collins
1	Kaman Avidyne, Division of Kaman Sciences Corp. 83 Second Ave., Northwest Industrial Park, Burlington, MA 01803 ATTN: Norman P. Hobbs
1	ATTN: Tech Lib
1	ATTN: E. S. Criscione
1	Kaman Sciences Corporation P. O. Box 7463, Colorado Springs, CO 80933 ATTN: Library
1	Karagozian and Case 6330 N. Figueroa St., Los Angeles, CA 90042 ATTN: John Karagozian
1	Lockheed Missiles & Space Co., Inc. P. O. Box 504, Sunnyvale, CA 94088 ATTN: Tech Lib
1	Martin Marietta Aerospace, Orlando Div P. O. Box 5837, Orlando, FL 32805 ATTN: G. Fotieo
1	McDonnell Douglas Corp 5301 Bolsa Ave., Huntington Beach, CA 92647 ATTN: Robert W. Halprin
1	Merritt Cases, Inc. P. O. Box 1206, Redlands, CA 92373 ATTN: Tech Lib
1	ATTN: J. L. Merritt
1	Newmark, Nathan M., Consulting Engineering Services 1211 Civil Engineering Bldg, Rm B106A, Univ. of Illinois Urbana, IL 61801 ATTN: Nathan M. Newmark
1	ATTN: W. J. Hall
1	ATTN: J. Haltiwanger
1	Pacifica Technology P. O. Box 148, Del Mar, CA 92014 ATTN: R. Bjork
1	ATTN: G. Kent

Dept. of Defense Contractors, Cont'd.

No. of
Copies

	Physics International Co. 2700 Merced St., San Leandro, CA 94577
1	ATTN: Doc Con for Tech Lib
1	ATTN: Doc Con for Coye Vincent
	R & D Associates P. O. Box 9695, Marine Del Rey, CA 90291
1	ATTN: Jerry Carpenter
1	ATTN: Henry Cooper
1	ATTN: J. G. Lewis
1	ATTN: Tech Lib
1	ATTN: R. J. Port
	Rand Corporation 1700 Main St., Santa Monica, CA 90406
1	ATTN: C. C. Mow
1	ATTN: Tech Lib
	Science Applications, Inc. 2201 San Pedro NE, Albuquerque, NM 87110
1	ATTN: J. L. Bratton
	Science Applications, Inc. P. O. Box 2351, La Jolla, CA 92038
1	ATTN: Tech Lib
	Southwest Research Institute P. O. Drawer 28510, San Antonio, TX 78284
1	ATTN: Wilfred E. Baker
1	ATTN: A. B. Wenzel
	Stanford Research Institute 333 Ravenswood Ave., Menlo Park, CA 94025
1	ATTN: Carl Peterson
1	ATTN: George R. Abrahamson
	Systems, Science and Software, Inc. P. O. Box 1620, La Jolla, CA 92038
1	ATTN: Donald R. Grine
1	ATTN: Tech Lib
1	ATTN: J. Sweet
	Terra Tek, Inc. 420 Wakara Way, Salt Lake City, UT 87108
1	ATTN: Tech Lib
1	ATTN: Sidney Green

Dept. of Defense Contractors, Cont'd.

No. of
Copies

1	Tetra Tech, Inc. 630 North Rosemead Blvd., Pasadena, CA 91107 ATTN: Tech Lib
1	TRW Systems Group One Space Park, Redondo Beach, CA 90278 ATTN: Tech Info Center/S-1930
1	ATTN: Peter K. Dai R1/2170
1	ATTN: Norm Lipner
1	TRW Systems Group, San Bernardino Operations P. O. Box 1310, San Bernardino, CA 92402 ATTN: E. Y. Wong 527/712
1	TRW Systems Group Room 712, Bldg 527, Norton AFB, CA 92409 ATTN: Gregory D. Hulcher
1	Universal Analytics, Inc. 7740 W. Manchester Blvd., Playa Del Rey, CA 90291 ATTN: E. I. Field
1	URS Research Co 155 Bovet Rd., San Mateo, CA 94402 ATTN: Tech Lib
2	Eric H. Wang Civil Engineering Rsch Fac, University Station Box 188, University of NM, Albuquerque, NM 87121 ATTN: Jerry Berglund
1	Weidlinger Assoc Consulting Engineers 110 East 59th St., New York, NY 10022 ATTN: Melvin L. Baron
1	Weidlinger Associates Consulting Engineers Suite 245, 3000 Sand Hill Road, Menlo Park, CA 94025 ATTN: J. Isenberg
1	ATTN: F. S. Wong

END

DATE
FILMED

2 - 75

DDC